CRANFIELD UNIVERSITY

TONGYU WU

INVESTIGATION OF THE FRACTURE BEHAVIOUR OF EPOXY-BASED WATER BALLAST TANK COATINGS UNDER STATIC AND FATIGUE LOADINGS

SCHOOL OF AEROSPACE, TRANSPORT, AND MANUFACTURING
Materials and Manufacturing

PhD
Academic Year: 2011 - 2015

July 2015

CRANFIELD UNIVERSITY

SCHOOL OF AEROSPACE, TRANSPORT, AND MANUFACTURING
Materials and Manufacturing

PhD

Academic Year 2011 - 2015

TONGYU WU

Investigation of the fracture behaviour of epoxy-based water ballast tank coatings under static and fatigue loadings

Supervisors:
Professor Phil Irving
Dr David Ayre
Dr Giuseppe Dell'Anno

July 2015

This thesis is submitted in partial fulfilment of the requirements for the degree of PhD

ABSTRACT

The fracture of water ballast tank (WBT) coatings due to thermal stresses is widely recognised as an issue. Upon coating fracture, rapid corrosion of the tanker steel structure will occur, leading to expensive structure repairs or even tanker scrapping. In this project, the fracture behaviour of two experimental WBT coatings, referred to as A and B, in the forms of free film and substrated coatings was investigated. Static tensile tests and fatigue tests of the substrated coatings were performed. A finite element model of coating cracking was developed. Thermal stress and J-integral of surface cracking defects in substrated coatings were calculated using the model, in which the effects of defect size, coating thickness, and thermal strain on coating fracture were investigated. For the first time, fracture mechanics was used to explain WBT coating fracture behaviour. The J-integral of surface defects was used to predict the onset strain of coating cracking under mechanical strains in laboratory and under thermal strains in service. A theoretical comparison between the cracking drive forces in terms of J-integrals in WBT coatings under thermal strains and mechanical strains was performed.

Tensile testing of coating free films showed that the tensile strength of coatings A and B were 30 and 17 MPa respectively, with corresponding fracture strains of 0.67% and 0.34%. The measured fracture toughness values of coatings A and B were 1.09 and 0.64 $MPa\sqrt{m}$. During tensile testing of substrated coatings, the coatings developed the first surface crack at a critical nominal strain, and further increases in mechanical strain led to the propagation and initiation of new parallel cracks, lying perpendicularly to the loading direction, and the crack number saturated as straining continued. The nominal strain to first crack of substrated coatings A and B were found to be 1.04% and 0.64%, which was much greater than the ductility of the free films, despite of the presence of thermal residual strains. Predictions of failure strains of the coatings A and B made using the J-integral of surface cracking defects and coating fracture toughness were found to be within 10% and 30% of the experimental values. Coating A was found to be more fatigue resistant than coating B in terms of both life to first 2 mm long fatigue crack and total

crack growth rate. It was found that the total crack growth rate had a Paris' Law-like correlation with strain range and with J-integral range.

The results show the static ductility and fatigue life of the coatings strongly depend on toughness, defect size, coating thickness and residual stress. To achieve long life, coating formulations should possess high toughness and low residual stress, and in application coatings should be as thin as allowed for sufficient anti-corrosion capability.

Keywords:

Fracture mechanics, DIC, FEA, Thermal stress, Fatigue

ACKNOWLEDGEMENTS

I would like to express my very great appreciation to my supervisors, Professor Phil Irving, Dr David Ayre, and Dr Giuseppe Dell'Anno. They generously offered me patient guidance, valuable encouragement, and constructive recommendations throughout my PhD study.

I am also grateful for the intellectual and financial support from International Paint, particularly for Dr Paul Jackson and Dr Fangming Zhao for the preparation of my samples and other helpful technical advice for this project. Also many thanks to Dr Paul Dooling and Dr Trevor Willis at International Paint for their intellectual contributions throughout the period.

My thanks shall be also extended to the technicians as well as other academic staff and fellow research students at both Cranfield University and International paint. Special thanks to Mr Barry Walker, Mr Ben Hopper, Dr Isidro Durazo-Cardenas, Mr Andrew Dyer, Dr Xianwei Liu and Dr Danny Gagar at Cranfield University for their kind support in mechanical testing and microscopy.

Finally, I would like to thank my friends and family for their priceless emotional support that made my life at Cranfield a marvellous experience.

TABLE OF CONTENTS

ABBREVIATIONS

WBT	Water ballast tank
CTE	Coefficient of thermal expansion
PVC	Pigment volume content
CHE	Coefficient of hygroscopic expansion
RH	Relative humidity
SERR	Strain energy release rate
PMMA	Poly(methyl methacrylate)
PC	Polycarbonate
DIC	Digital image correlation
FEA	Finite element analysis
FEM	Finite element method
PTFE	Polytetrafluoroethylene
TMA	Thermal mechanical analysis

NOMENCLATURE

E	Young's modulus
α^T	Coefficient of thermal expansion
α^H	Coefficient of hygroscopic expansion
T_g	Glass transition temperature
t	Time
σ^S	Solidification stress
σ^T	Thermal stress
σ^H	Hygroscopic stress
σ^{Mec}	Mechanical stress
σ^{Tot}	Total stress
σ_y	Yielding stress
ε	Strain
ε_f	Fracture strain
ε_{EXT}	Extensometer nominal strain
ε_{local}	Local strain
Δl	Change of local displacement
υ	Poisson's ratio
h	Coating thickness
R	Radius or radius of curvature
D_{max}	Maximum deflection of bi-layer beams
e	Total energy stored before fracture
Π	Potential energy available for fracture
W_S	Surface energy of fracture surface
W_e	Elastic energy
W_p	Plastic energy
A	Area of fracture surface
a	Defect depth
γ_s	Surface energy density
σ_f	Fracture stress

γ_p	Plastic energy density
G	Strain energy release rate
K	Stress intensity factor
G_C	Critical Strain energy release rate/Fracture toughness
K_C	Critical stress intensity factor/Fracture toughness
J	J-integral
J_C	Critical J-integral/Non-linear Fracture toughness
Δ	Displacement
Δd	Change of surface crack opening displacement
w	Strain energy density
σ_{ij}	Stress tensor
ε_{ij}	Strain tensor
T_i	Traction vector
u_i	Displacement vector
α	Dundur's parameter
β	Dundur's parameter
μ	Shear modulus
s	Stress singularity exponent
L	Surface crack length
L_{total}	Sum of all surface cracks
L_{avg}	Average length of all surface cracks
G_p	Strain energy release rate for crack penetration
G_{ch}	Strain energy release rate for crack channelling
G_d	Strain energy release rate for interfacial delamination
J_p	J-integral for crack penetration
J_{ch}	J-integral for crack channelling
l_r	Reference length
H	Inter-crack distance
Γ	Fracture energy
ΔK	Stress intensity range

ΔG	Strain energy release rate range
ΔJ	J-integral range
N	Cycle number
N_{crack}	Number of cracks
C and m	Empirical parameters in Paris' Law
F_Q	Critical load
K_Q	Critical stress intensity factor/Provisional fracture toughness
W	Sample width within gauge length
H'	Height
$\delta(y)$	Local crack opening
Δ'	Collective crack opening
W'	Energy consumed for crack opening
de	Change of energy due to cracking
θ	Yielding offset in Ramberg-Osgood equation
n	Hardening exponent in Ramberg-Osgood equation
$\bar{r}$	Reference plastic region size

LIST OF FIGURES

LIST OF TABLES

1. INTRODUCTION

In recent years, crude oil tankers (COTs) have been required to adopt a double-hulled structure to avoid oil leakage due to accidental tanker collision [1,2]. Sandwiched by the inner and the outer hull is a water ballast tank (WBT), where sea water is stored as ballast when the tanker is free of cargo. In order to protect the tanker steel structure from corrosion, organic coatings, normally heavily filled epoxy coatings are applied on the inner surface of WBTs. However, it has been observed that sometimes these coatings fail before the desired service life of the tanker [3], which leads to the corrosion of the tanker structure and poses potential danger to the tanker integrity. Repair of the coating is expensive, and sometimes severe corrosion leads to scrapping of the tanker [2].

The causes of the failure of WBT coatings are widely known to be stresses developed internally such as thermal, hygroscopic and curing stresses due to the mismatch between the volumetric changes of coating and substrate subjected to environmental changes, as well as stress applied externally such mechanical stress due to tanker hull deformation [4,5]. It is also known the thermal stress has the largest contribution [6]. Figure 1 illustrates 4 major types of stress WBT coatings endure after curing and in service.

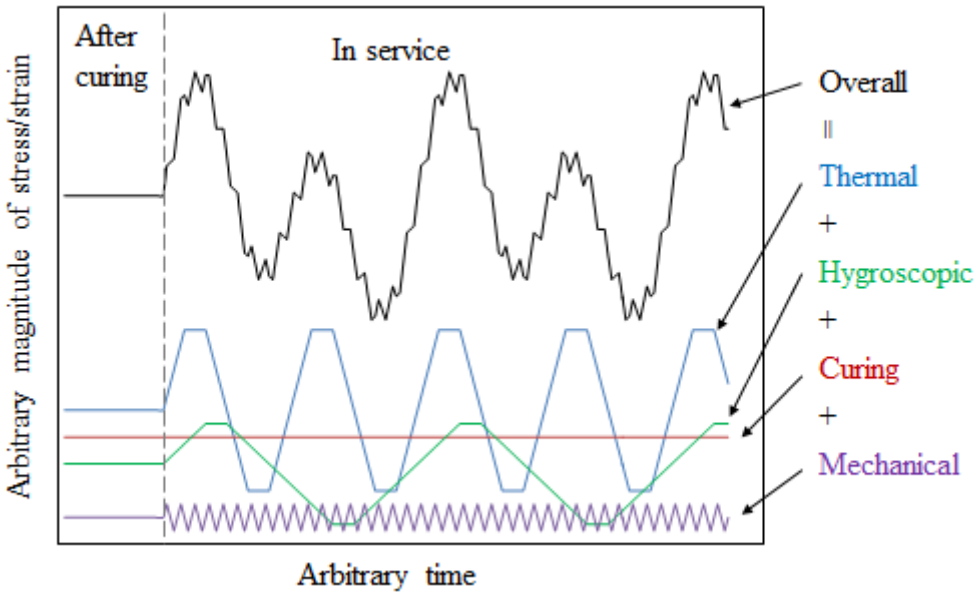

Figure 1. Illustration of major types of stress/strain in WBT coatings

After curing and before being in service, WBT coatings are in a stable environment, and the all types of stresses are constant. During service, the temperature and humidity inside WBTs start to vary periodically, and the tanker hull is cyclically deformed by sea wave motions, the resultant stresses in WBT coatings become cyclic. Due to this cyclic nature of the stresses, the failure of WBT coatings could be caused by fatigue.

The best way to avoid this problem is to apply suitable coatings in the very beginning. Therefore a model that is capable of predicting the life of WBT coatings in the service environment would be highly desirable. In order to build the model, an understanding of the fracture behaviour of WBT coatings is essential. Therefore, this project was established with an aim to understand better the fracture behaviour of WBT coatings under both static and cyclic strains. In this work, coating failure was induced by large deformation of steel substrate that exceeded the substrate yielding stress. Considering that the generation of thermal stress in WBT coatings in service would not cause substrate yielding, how experimental characterisation of coating performance can be related to service performance was also explored in this work.

To fulfil the aim, the following objectives had to be performed during this project:

1) Characterisation of the mechanical and thermal properties of two types of coatings provided by International Paint as individual materials;
2) Observation and quantification of the fracture behaviour of the coatings on substrate under both static and cyclic strains;
3) Thermal stress analysis and fracture mechanics analysis of the coatings on substrate using finite element (FE) analysis;
4) Explanation of the observed fracture behaviour using theoretical predictions;
5) Prediction of the fracture behaviour of the coatings in service conditions using experimental and theoretical results.

A literature review of the current understanding in the development of stress and the coating fracture behaviour is given first. After that, the materials and methods used for

the experimental observation are described, followed by the results of the experimental investigations. Then, the procedures as well as the results of the FE investigation are presented before the discussion, in which the fracture behaviour of coatings in the laboratory condition will be explained in detail. Subsequently, the prediction of the fracture behaviour of the coatings in service condition is presented in an independent chapter before the conclusions.

2. LITERATURE REVIEW

Coating fracture is a common problem encountered in various applications [7]. The fracture of polymeric coatings in automotive [8,9] and marine industry [6,10], metallic coatings in electronics industry [11–13], and thermal barrier coatings in aerospace industry [14–16] has been observed and investigated. The conditions leading to the fracture of different coatings vary depending on the configuration of each coating/substrate system, but the similarities in the fracture processes analysis should remain. This chapter summarises the previous research relevant to the current investigation, including both the fundamental and recent developments. However, considering the scope of this work, it focuses on WBT coatings.

A brief introduction to the composition of WBT coatings and its relationship with the material properties is given firstly. Following that, the development of internal stresses and other influences are introduced. And then, the focus will move on to the fracture behaviours and the mechanics of coatings. And finally, the recent developments in the research of fatigue behaviour of coatings is summarised. WBT coatings are essentially materials in the form of thin films, and thus this literature review includes the knowledge of particulate filled epoxy resins. The significantly unique characteristics of coatings are highlighted along the way wherever appropriate.

2.1. Coating Composition and Main Properties

In WBTs, organic coatings are usually used for anti-corrosion purposes. These coatings use polymers as binders, in which various types of particulate pigments are dispersed. Note that fillers in the organic coating industry are normally referred to as pigments. Organic coatings are normally diluted by solvents to reduce the viscosity for the convenience of application. After application, the coatings solidify by either solvent evaporation or a chemical curing reaction or both, and eventually form a solid layer or multiple layers. In WBTs, epoxy resins are widely adopted as the binder as epoxies offer excellent adhesion to metals, chemical stability and water resistance [17,18]. For better

corrosion resistance, various particles are used as pigments [19,20]. Micaceous iron oxide, lamellar aluminium pigments, and glass flake pigments [21–23] are used as barrier pigments which impede the transport of water molecules by forming a tortuous path for diffusion. Besides the anti-corrosive functions, the pigments also modify the original properties of the epoxy resins and influence the final properties of the coating systems [24].

WBT coatings are essentially particulate-filled epoxy resins in the form of thin layers. Therefore, one would expect that the influence of the pigments on the properties of epoxy coatings to be the same as particulate fillers on epoxy resins. The effects of the particulate fillers on the properties of such composites have been studied intensively. Many text books such as Landel [25] and Rothon [26], as well as many review papers provide comprehensive summaries of relevant developments [27–29]. Perera [30] has summarised the effects of pigmentation on organic coating characteristics. Considering the integrity of the coatings, the most important mechanical and thermo-mechanical properties are Young's modulus $\boldsymbol{E}$, coefficient of thermal expansion (CTE) $\boldsymbol{\alpha_C^T}$, glass transition temperature $\boldsymbol{T_g}$ and fracture toughness. The first three properties determine the magnitude of thermal stress in the coating for imposed temperature changes, while fracture toughness is a measure of the resistance of a material to crack propagation and will be described in detail later. This section will briefly introduce the effects of pigments only on the first three properties, and the effects of them on the development of thermal stress are introduced in the section regarding thermal stress. The effect of pigments on fracture toughness will be introduced in the section summarising fracture mechanisms of filled epoxy resins.

As polymeric thermosetting materials, the physical properties of the epoxy resins vary depending on the crosslink density. Normally, the modulus is proportional to the crosslink density, while the flexibility is inversely proportional to the crosslink density. Generally speaking, cross-linked epoxy resins have a Young's modulus ranging from 2 to 5 GPa at room temperature, while the strain to failure is about 3%, and the CTE is about

100×10^{-6} /°C. Compared to this, pigments are normally metals and metallic oxides with higher Young's moduli, much less flexibility and smaller CTEs. Pigments in epoxy resins cause the properties of the resins to deviate from the initial properties towards the properties of the pigments. As a result, the filled epoxy coatings normally possess higher Young's moduli, smaller strain to failure, and smaller CTEs compared to their pristine state. Perera and Eynde [31] reported the increase of Young's modulus of a thermoplastic polymer coating with increasing volume content of various types of fillers. Zosel [32] studied the elastic modulus of a polyacrylate coating with different volume content of titanium oxide pigments, and found similar results. Figure 2 shows the trend of pigment reinforcement on an acrylate filled with four types of pigments. The drop in the moduli of the acrylate coating filled with talc and yellow iron oxide was due to the excessive pigment volume content (PVC), which hindered the formation of a continuous resin phase.

Perera [30] has also reported the significant influence pigments have on the CTE of polymeric coatings. In general, the CTEs of polymeric coatings studied decreased with the increase of PVC. Figure 3A shows the reduction of CTE of an epoxy coating filled with various PVC of TiO_2. In the same paper, it is also emphasised that due to the heterogeneity of many pigments, such as lamellar shape pigments, the CTE of a filled coating can be anisotropic. Figure 3B demonstrates the discrepancy of the CTEs of a filled polypropylene coating measured in different directions. CTE is of great importance when determining the magnitude of the thermal stress developed inside coatings, and more details are to be introduced in the later section regarding internal stress development.

The glass transition temperature T_g is the temperature of the transition between the glassy and rubbery state of polymeric materials [33]. Below T_g a polymeric material behaves like a glass mechanically with high stiffness and brittle nature, and above T_g the material behaves like a rubber with low stiffness and high flexibility. The influence of pigments on the T_g of polymeric coatings is rather complicated, and it depends on the strength of the "inter-phase" between binder and pigment, which is the surface layer of

the pigment with binder absorbed [34–36]. If the T_g of the inter-phase is higher than the binder, the T_g of the pigmented coating will be increased, and vice versa. It has been found that in some cases pigments do not have any influence on the T_g [37,38], or have a negative influence on the T_g [39,40]. However, it is widely considered that pigments would increase the T_g of pigmented coatings [41–43]. T_g also possesses great importance in determining the magnitude of the internal stress in organic coatings, and the details are described in the next section.

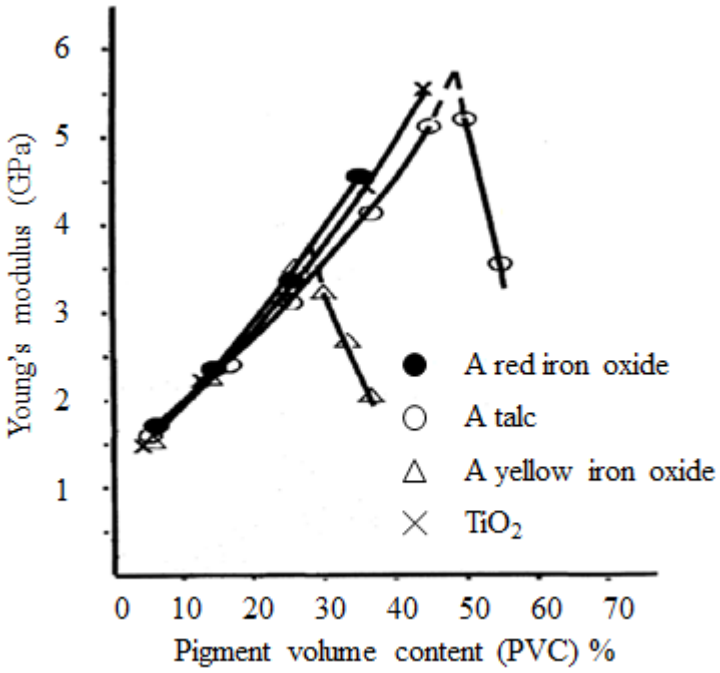

Figure 2. Reinforcing effect of inorganic pigments on an acrylate coating, adapted from reference [30].

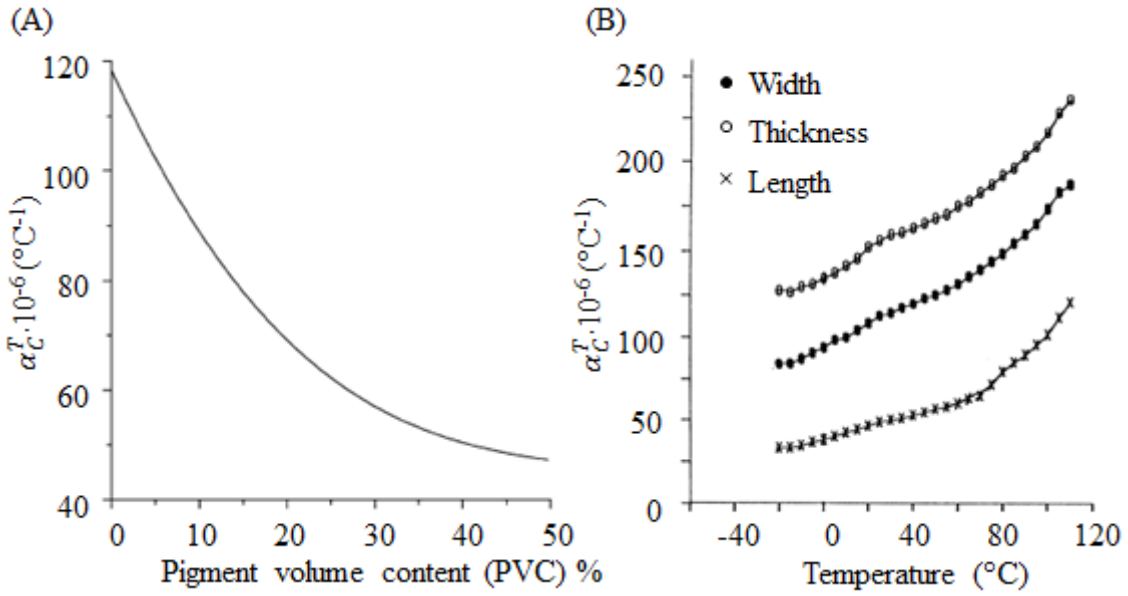

Figure 3. (A) Coefficient of thermal expansion (CTE) of an epoxy coating containing various volume content of a TiO2 pigment at 21 °C. (B) Coefficient of thermal expansion (CTE) of a polypropylene coating containing wolastonite (50 wt%) as a function of temperature measured in three direction. Both figures are adapted from reference [30].

2.2. Development of Stresses in Organic Coatings

The primary development of the stress comes from the solidification of the coatings, which causes volumetric shrinkage. Due to the adhesion to stiff substrates, the shrinkage is constrained, which in result generates an internal stress in the coating. For coatings with thermosetting binders such as WBT coatings with epoxy resins as binder, the solidification includes the evaporation of solvents and the crosslink reaction of monomers into a densely packed structure. Both processes introduce volumetric shrinkage over time $\boldsymbol{t}$. Croll [44] used T_g to define the solidification point. When the T_g of a solidifying coating reaches the curing temperature, the coating is considered as solidified. The beginning of significant stress development starts when the solidification point is reached and the coatings develop sufficient modulus. In fact, solidification does not cease after the solidification point is reached, and the loss of any residual solvent and/or the reaction of unreacted monomers will cause further shrinkage, and thus generate even more stress. The development of coating stress due to either solvent evaporation [45–48] or chemical

curing [49–56] has been studied intensively. Reviews [57,58] of the stress development in organic coatings can also be found. Typical stress development due to solvent loss over time and chemical curing has been reported by Vaessen [45] and Stolov [49] respectively. Essentially, the magnitude of internal stress developed during solidification $\boldsymbol{\sigma_C^S(t)}$ has two time-dependent contributions, the shrinkage strain $\boldsymbol{\varepsilon_C(t)}$ and the Young's modulus of the coating $\boldsymbol{E_C(t)}$.

$$\sigma_C^S(t) = \frac{E_C(t)}{1 - \upsilon_C} \cdot \varepsilon_C(t) \tag{1}$$

Here, $\boldsymbol{\upsilon_C}$ is the Poisson's ratio of the coating, and equation (1) depicts a biaxial stress away from the edge of the coating [59–61].

For thermosetting coatings such as epoxy coatings, several factors influence the magnitude of the internal stress, namely crosslink density, solvent type, curing rate, and coating thickness. It is easy to understand why crosslink density plays a role. As the crosslink density increases, the final modulus of thermosetting coatings and the amount of shrinkage strain will increase [50–52], which would result in a higher internal stress as depicted by equation (1).

The influences of solvent type, curing rate, and coating thickness need to be discussed together, as the stress development is a result of their competition. Normally the solvent content of thermosetting coatings/solvent solutions is about 20% to 30% [62], which generates a very large shrinkage after evaporation. Solvents inside the coatings need to diffuse through the thickness to the surface in order to escape from the coating solution. If the rates of solvent diffusion and evaporation, as well as chemical curing allow the solvent to escape from the system before the densely cross-linked structure is formed, the shrinkage due to solvent loss will happen at very low coating modulus [63]. In this case, further coating curing, generating little shrinkage, will not lead to the development of large internal stress. However if the crosslink reaction finishes while much solvent still remains, subsequent slow evaporation of the trapped solvent paired with the already

developed high modulus will generate a much greater internal stresses. A thicker coating tends to trap more solvent, because it slows down the evaporation as the solvent molecule has a longer path to diffuse to the surface. In a solvent-less system, it has been found that a slower curing rate would lead to a smaller internal stress, because a longer curing time allows the relaxation of the internal stress over time, and vice versa [53]. Generally speaking, to avoid undesired high internal stress, the formulation of the coating should allow fast solvent evaporation and slow curing rate if possible.

The internal stress of organic coatings can be measured using the observation of the deflection of coated substrates [58]. The earliest analysis of internal stress measurement was from Stoney [64] using beam theory. Later, based on Stoney's analysis intensive studies were performed for thin coatings on thick substrates [65–67] and coatings on substrate with equal thickness [68–70]. The most widely adopted method to measure the internal stress of coatings is to measure the deflection of a bi-layer strip of a coating and a substrate. When the internal stress is developed in the coating, both the ends of the strip will deflect symmetrically towards the centre. If a tensile or a compressive stress is developed in the coating, the strip will defect towards the coating or substrate side respectively. The deflection will stabilise when the stress and moment equilibrium of the coating/substrate system is reached. Assuming perfect curvature, the deflection of the strip can be converted to a radius of curvature, and using this value the internal stress of the coating on a non-deflecting strip $\boldsymbol{\sigma_C^0}$ can be calculated by the equation as follows [68].

$$\sigma_C^0 = \frac{E_S h_S^2}{6h_c(1-\upsilon_S)R} \cdot \frac{1}{1+R_E R_H} \times \left[1 + R_H(4R_E - 1) + {R_H}^2\left[{R_E}^2(R_H - 1) + 4R_E + \frac{(1+R_E)^2}{1+R_H}\right]\right] \quad (2)$$

$$R_E = \frac{E_C(1-\upsilon_S)}{E_S(1-\upsilon_C)}, \qquad R_H = \frac{h_C}{h_S} \quad (3)$$

$$R = \frac{L^2}{8D_{max}} \tag{4}$$

Here, $\boldsymbol{h}$ is the the thickness, the subscripts $\boldsymbol{C}$ and $\boldsymbol{S}$ represent coating and substrate respectively. $\boldsymbol{v_S}$ is the Poisson's ratio of the substrate. $\boldsymbol{R}$ is the radius of curvature of the deflected strip, and it can be calculated using $\boldsymbol{L}$, the length of the strip, and $\boldsymbol{D_{max}}$ the maximum deflection of the ends of the strip with respect to the centre. It is important to bear in mind that during the deflection some internal stress is released by the shape change of the coating, due to which the equation estimates an internal stress greater than when a coating is attached on a deflected substrate. In most of realistic organic coating/metal substrate systems, the substrate is not able to be deflected due to their much greater thickness and modulus than the coating, therefore this estimation made by equation (2) is appropriate.

In WBTs of crude oil tankers, the failure of commercial protective coatings was observed normally after some years in service, and some "inferior" coatings only last 3 years [71] while the life of WBT coatings is expected to be 15 years or even longer [1,62]. One cause of the failure is believed to be the fatigue cracking of the coatings under cyclic loadings, which are introduced by changes of temperature and humidity inside WBT during service, and sea wave induced tanker structure deformation. Crude oil is normally heated up to about 60 °C to reduce the viscosity for the convenience of transport [3], the cyclic charging and discharging of hot oil along with discharge and charge of cold sea water as ballast, there is a temperature cycle and a humidity cycle. Due to the discrepancy in the CTEs and the coefficient of hygroscopic expansion (CHEs) of the coating and the steel substrate, the changes of temperature and humidity modify the volumetric mismatch between the coating and the substrate, and hence influence the magnitude of the internal stress originally generated by curing. During service, the tanker hull structure responds to the sea wave motions and deforms cyclically at a frequency of 0.05 to 0.5 Hz. This deformation is transferred into the coatings as mechanical stress $\boldsymbol{\sigma_C^{Mec}}$, and adds to

the internal stress. These types of the stress contributing to the final total WBT coatings stress $\boldsymbol{\sigma_C^{Tot}}$, can be expressed mathematically as follows [72].

$$\sigma_C^T = \int_{T_2}^{T_1} \frac{E_C(T)}{1-\upsilon_C}(\alpha_C^T - \alpha_S^T)dT \tag{5}$$

$$\sigma_C^H = \int_{RH_2}^{RH_1} \frac{E_C(RH)}{1-\upsilon_C}(\alpha_C^H - \alpha_S^H)dRH \tag{6}$$

$$\sigma_C^{Tot} = \sigma_C^S + \sigma_C^T + \sigma_C^H + \sigma_C^{Mec} \tag{7}$$

Here, σ_C^T is thermal stress, σ_C^H is hygroscopic stress, σ_C^S is curing stress, T and RH are temperature and relative humidity respectively, α_C^H and α_S^H are the hygroscopic expansion coefficients of coating and substrate respectively, α_C^T and α_S^T are the thermal expansion coefficients of coating and substrate respectively. Due to the cyclic nature of the environmental change driven stresses and the sea wave-induced stresses, σ_C^{Tot} is cyclic. Among these environmental stresses, the thermal stress is considered as the biggest contribution to the low-life cycle fatigue failure of the coatings [6], and is the one considered in this research. The moisture inside WBT in fact reduces the magnitude of the stress in the coating by serving as a plasticiser that expands the coating and decreases the modulus. The earliest WBT coating failure is normally observed at the fillet welded "T" joints of the tanker structure [2], see Figure 4. In such a structure two steel plates were perpendicularly joined forming two corners, where the mechanical deformation is believed to be small, and therefore the mechanical stress should not be considered a dominant factor of the coating failure [6]. The place most likely to have coating failure is the welded joint with big changes in temperature from very high to very low and a relatively low humidity.

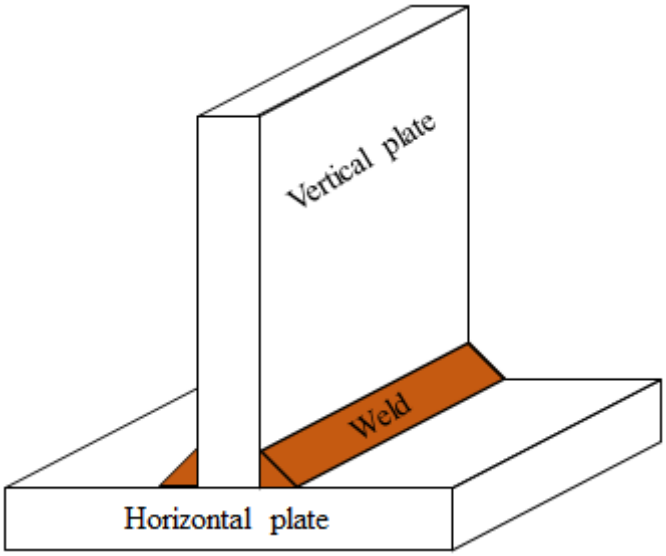

Figure 4. Illustration of a fillet welded T joint formed by a vertical and a horizontal plate.

It has been introduced previously that the pigments influence the mechanical and the thermo-mechanical properties of the coatings, which results in internal stress of the coatings being affected by the type and the amount of pigments involved. For example, the incorporation of inorganic pigments usually increase the modulus, which according to equation (1) will increase the internal stress. However, pigments also reduce the shrinkage of the coatings, such as the reduction of CTE due to pigments, which decrease the internal stress. Therefore, to determine whether pigments lead to an undesired internal stress one must consider the effects of the pigments on both modulus and shrinkage.

Another crucial factor influencing the properties of organic coatings as well as the internal stress is physical ageing, which is due to the molecular re-arrangement of binders in a non-equilibrium state, as the binder molecular structure is not in the most compact conformation [73–75]. Physical ageing is different from chemical ageing, in which molecular configuration is changed permanently, while physical ageing is merely conformational changes that can be thermally reversed by reheating the material to a temperature greater than T_g for a sufficiently long time. This also means that physical ageing only occurs below T_g, and the rate of physical ageing increases as the ageing

temperature approaches T_g but not exceeds it. Perera [76] systematically summarised the effects of physical ageing on organic coatings. Briefly speaking, the modulus of organic coatings increases with physical ageing, while the CTE decrease with physical ageing however its effect is well exceeded by the former [77]. The initial phenomenon of physical ageing is stress relaxation, meaning that the internal stress that a coating experiences drops. The internal stress evolution in organic protective coatings has been reported by Hare [78]. It was reported that the internal stress reduces due to stress relaxation in months after the solidification of the coatings, then stabilises for years in service, and eventually increases due to further physical ageing-caused modulus rise, see Figure 5.

In addition, the most detrimental effect of physical ageing on the structural integrity of organic coatings is that of embrittlement of the materials [79–84]. Truong and Ennis [84] characterised the effect of physical ageing on the fracture toughness of epoxy resin, and they found the fracture toughness of an aged epoxy had a 40 – 50 % reduction compared to the un-aged resin. This, along with the increase in the internal stress, indicates that the failure of WBT coatings could be caused by the time-dependent physical ageing, which degrades the cracking resistance of the coatings to a level exceeded by the internal stress [10].

In summary, the failure of WBT coatings may be caused by either fatigue damage due to cyclic stresses or static failure due to physical ageing induced fracture toughness degradation or both. Irrespective of the failure mechanism, the knowledge of coating fracture mechanics and fracture mechanisms of filled epoxies are essential if coating fracture is to be investigated further, and it will be introduced in the following section.

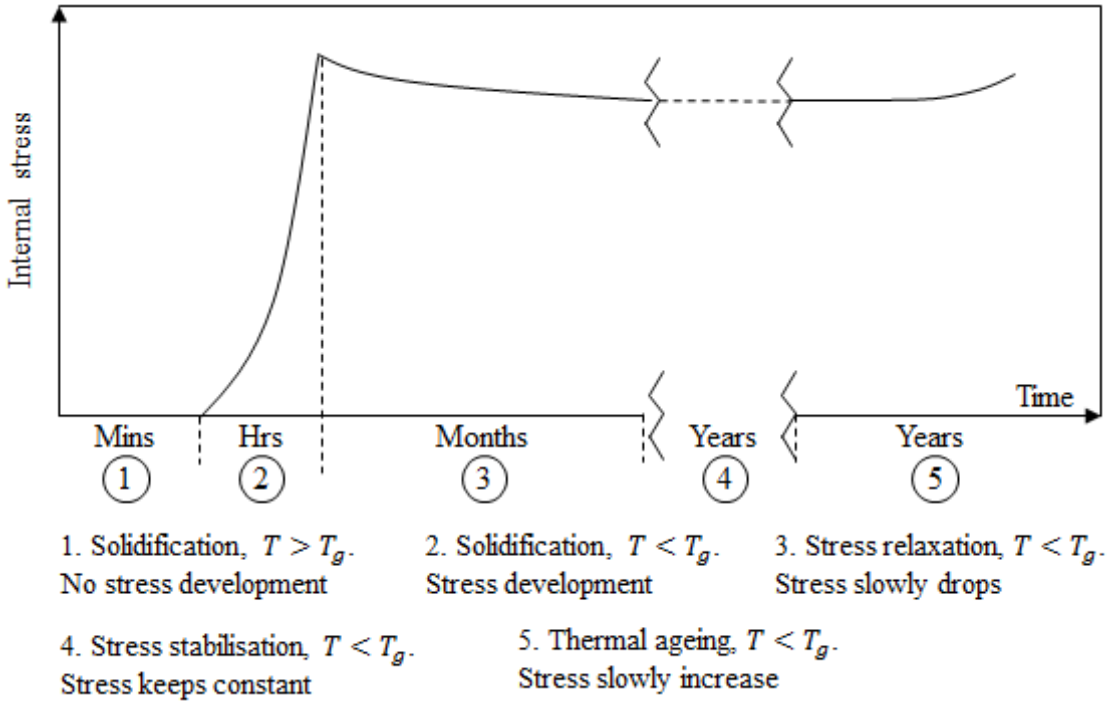

Figure 5. Illustration of the Evolution of internal stress in organic coatings. This is adapted from [78].

2.3. Fracture of Epoxies

2.3.1. Brief description of fracture mechanics

Before getting into the fracture of epoxies, the fracture mechanics of general materials will be briefly reviewed first.

The onset of the failure of a material from a pre-existing flaw obeys physical rules. The most fundamental rule is that of linear elastic fracture mechanics (LEFM). Initially, Griffith [85] applied the First Law of Thermodynamics and treated the fracture of material as a process from non-equilibrium to equilibrium. Any fracture can occur only if the process leads the total energy $\boldsymbol{e}$ of the system to reduce or remain constant. In Griffith's theory, an existing flaw can increase in size only when the sufficient potential energy $\boldsymbol{\Pi}$ is available in the material to supply the surface energy $\boldsymbol{W_S}$ required for the new surface created due to cracking. For an increment in the crack area $\boldsymbol{dA}$, the equilibrium can be expressed by the equation below.

$$\frac{de}{dA} = \frac{d\Pi}{dA} + \frac{dW_S}{dA} = 0 \tag{8}$$

For a through-thickness flaw with a length of $2\boldsymbol{a}$ in a purely elastic thin plate with width much greater than $2a$ and a thickness much smaller than a, and given the surface energy density of the plate material as γ_s and the plate is loaded in the direction normal to the crack, the solution of the fracture stress $\boldsymbol{\sigma_f}$ can be expressed by the equation below. Note here γ_s is the energy required to create a surface with a unit area.

$$\sigma_f = \left[\frac{2E\gamma_s}{\pi a}\right]^{0.5} \tag{9}$$

Griffith's theory is only valid for purely elastic materials, and to expand the theory to metals, Irwin [86] and Orowan [87] independently modified Griffith's solution to take the plastic deformation at the crack tip into consideration. In addition to the surface energy require for cracking, the energy $\boldsymbol{\gamma_p}$consumed due to plastic deformation during cracking was introduced into equation (9) for a solution for the same problem with the consideration of plasticity confined in a small area around crack tip, see equation (10).

$$\sigma_f = \left[\frac{2E(\gamma_s + \gamma_p)}{\pi a}\right]^{0.5} \tag{10}$$

For convenience in solving engineering problems Irwin [88] further developed Griffith's model by introducing energy release rate, $\boldsymbol{G}$, as a measure of the energy available for an increment of cracking. For a wide thin plate in plane stress with a crack with a length of $2a$ under a remote stress $\boldsymbol{\sigma}$perpendicular to the crack, $\boldsymbol{G}$ can be written as below. Essentially $\boldsymbol{G}$ is the sum of the required surface energy γ_s and the required plastic energy γ_p.

$$G_I = \frac{\pi\sigma^2 a}{2E} \tag{11}$$

In addition to the energy approach, the fracture of materials can also be expressed from the aspect of the stress field at a crack tip [89–92]. Consider a sample being loaded

in a direction normal to a pre-existing crack, the stress in the sample at the crack tip is infinite and decreases on moving away from the crack tip. In this case, the mode I stress intensity factor $\boldsymbol{K_I}$ was employed to quantify the magnitude of a crack tip singularity. For the $2a$ crack in the thin plate under normal stress, the stress intensity factor at the crack tip can be approximated by equation (12). For an edge crack with a length of a in a semi-infinite thin plate, its K_I at the crack tip can be approximated by equation (13) below.

$$K_I = \sigma\sqrt{\pi a} \tag{12}$$

$$K_I = 1.12\sigma\sqrt{\pi a} \tag{13}$$

In LEFM, the mode I stress intensity factor has a unique relationship with the energy release rate G. In equation (14) below, E is replaced by $E/(1-\upsilon^2)$ for the plane strain condition.

$$G = \frac{{K_I}^2}{E} \tag{14}$$

When the sample with a pre-existing crack failed in mode I at a critical remote stress σ_c, the stress intensity factor reaches a critical value $\boldsymbol{K_{IC}}$, which is also known as the fracture toughness of the material. It is a material property, and independent from the size and geometry of the cracked body. Based on equation (14), a critical value of the energy release rate $\boldsymbol{G_{IC}}$ can be obtained as an alternative form of the fracture toughness. These critical values serve as criteria for the onset of fracture. Consider a cracked body with a crack length of a loaded with a mode I stress of σ, if the K or the G values calculated from the crack length and the stress exceed the K_{IC} or the G_{IC} respectively, the body will fracture.

In LEFM the plasticity of material is required to be confined in a small area at the crack tip, when large plastic deformation takes place in the bulk of material before fracture, LEFM will not hold anymore [93]. In order to express the crack-driving force of a defect in such materials, J-integral (J) was developed [94]. If unloading is not considered, elastic-plastic behaviour can be approximated using non-linear elasticity. Figure 6 illustrates the

load-displacement relationship of a purely elastic and a non-linear elastic body extended and kept at a constant displacement (Δ). In the case where a pre-existing defect grows at the constant displacement, the load-displacement relationship is altered and shown by the dashed curves.

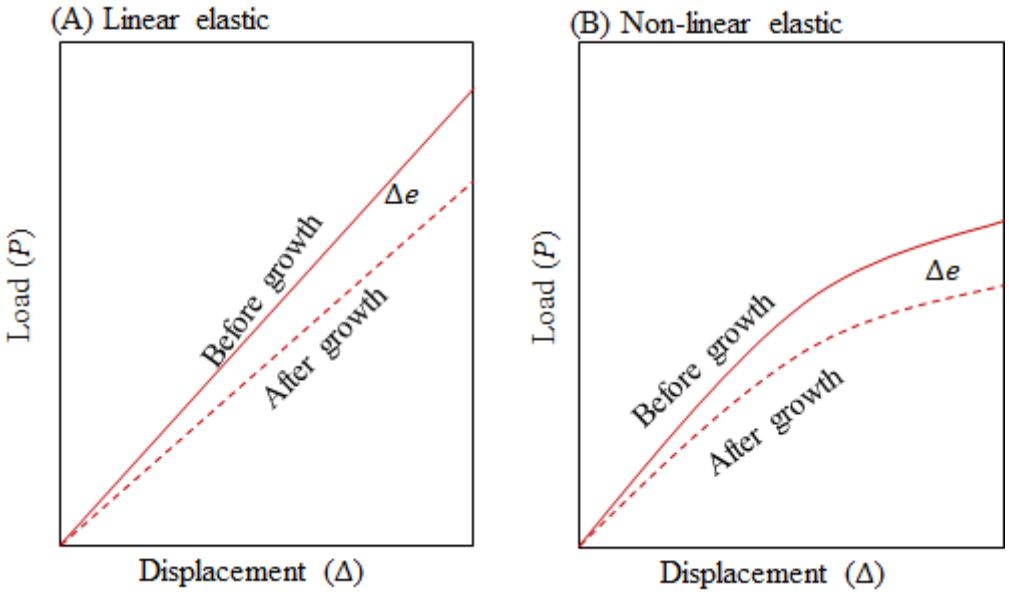

Figure 6. Load-displacement relationship before and after crack growth at a constant displacement in a (A) linear elastic and a (B) non-linear elastic material [93].

The potential energy released (Δe) can be seen as the area confined by the load-displacement curves before and after the growth of the defect. If the defect growth create new crack surfaces with an area of A, the linear elastic energy release rate G can be described as equation (15) below. In the non-linear case, the non-linear energy release rate is replaced with J, which is described by equation (16).

$$G = \frac{\Delta e}{A} \tag{15}$$

$$J = \frac{\Delta e}{A} \tag{16}$$

Essentially, G and J both represent the rate of energy release due to a unit crack growth. In fact, J is a more generic form of energy release rate, while G does not account for non-linear or plastic material behaviour, and it can be measured by converting the

measured stress intensity factor K using equation (14). In linear elastic materials, J is equal to G. As the term J-integral implies, J can be described using the integral of a contour (Γ) around a crack tip, of which a schematic is shown in Figure 7.

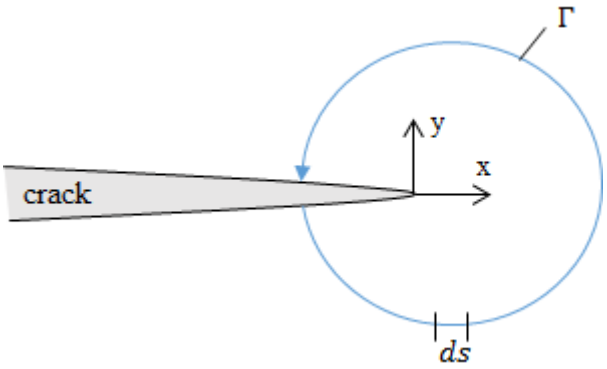

Figure 7. Arbitrary contour Γ around a crack tip [93].

Using the coordinate system shown in Figure 7, the J-integral of the crack under a remote stress normal to the crack can be expressed by equation (17) as below [93].

$$J = \oint (wdy - T_i \frac{\partial u_i}{\partial \mathrm{x}} ds) \tag{17}$$

$$w = \int_0^{\varepsilon_{ij}} \sigma_{ij} d\varepsilon_{ij} \tag{18}$$

$$T_i = \sigma_{ij} n_j \tag{19}$$

In equation (17), w is strain energy density, shown by equation (18), in which σ_{ij} and ε_{ij} are stress and strain tensors. T_i is the traction vector, shown by (19), in which n_j are the components of the unit vector normal to the contour, and T_i essentially is the normal stresses along the contour. Also in equation (17), u_i are displacement vector components, and ds is a unit length increment along the contour. The first half term in equation (17) describes the total energy stored in the contour, while the second half describes the energy dissipated by the deformation of the contour. Rice [94] has showed that the value of the J is independent from the contour shape as long as the path starts at one side the crack and ends at the other. With the advances in computer-aided numerical analysis, the calculation of J-integral is now performed routinely by

commercial software packages directly incorporating equation (17) and its derivatives [95].

Despite the similarity between G for linear elastic material and J for non-linear elastic materials, when the plasticity is considered one would bear in mind that the plastic deformation will not recover upon cracking or unloading, thus plastic crack wake will be generated and plastic deformation in the un-cracked region will remain. In this case, J related energy changes should not be seen as the energy released only, but also the energy dissipated by plastic deformation. The J-integral can also be used as a fracture criterion, the fracture toughness of a body with a certain crack length in a given geometry can be found as a critical J value, J_C. If the body is under a stress producing a J greater than the J_C, fracture will commence and vice versa. Special caution needs to be taken here. J_C is influenced by sample geometry and defect configuration. In a case that the sample geometry and defect configuration allow more plasticity before fracture, a greater J_C will be measured than in the case that allows less plasticity.

2.3.2. Deformation and fracture of epoxy resins

As a type of polymeric material, epoxy resins share similarities in their mechanical behaviour with the rest of polymers. Several textbooks [96–99] systematically summarised the deformation and the fracture characteristics of polymers. It is widely understood that, due to the viscoelasticity of polymeric materials, the mechanical behaviour of polymers is highly influenced by strain rate and temperature [99]. Polymers tend to deform in a more ductile manner when loaded at high temperature or tested at a sufficiently low strain rate, while they behave in a brittle fashion in the opposite conditions. However, due to the polydisperse nature of macromolecules sizes, the boundary between the brittle region and the ductile region can be obscure. Lee and Kim [3] experimentally demonstrated the influence of temperature on the deformation of an epoxy based WBT coating, see Figure 8.

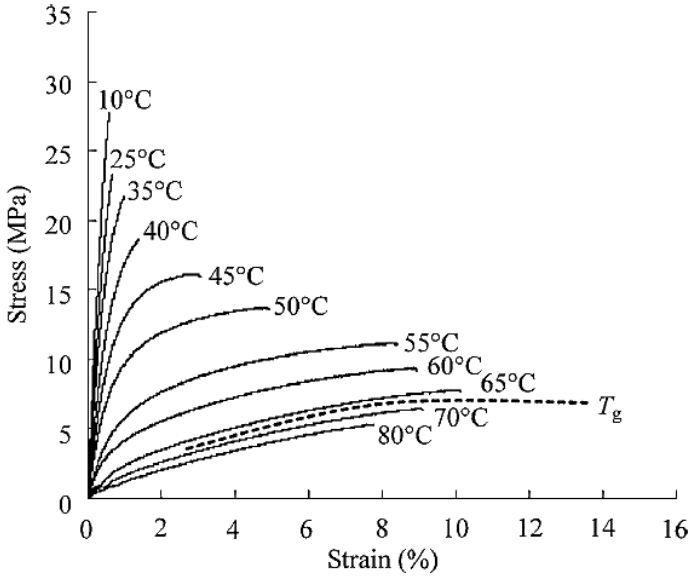

Figure 8. Temperature dependence of the stress-strain behaviour of an epoxy-based WBT coating. This figure is adapted from [3].

As shown in Figure 8, the samples tested at temperatures less than 25 °C exhibited rather high moduli and low strain to failure, while with the increasing testing temperature, the material exhibited much more ductility before failure and the modulus was reduced.

In terms of the fracture of epoxy resins, several publications [100–105] comprehensively reviewed the microscopic and macroscopic aspect of both pristine and filled epoxy resins. Based on the fracture surface of two types of pristine epoxy resins and the observation of craze fibrils at the crack tips, Morgan and co-workers [106–108] suggested that the initiation of cracking in epoxy resins was derived from local crazing and the failure of the craze fibrils. Following the initiation, the crack grows slowly with a plastic zone at the crack tip due to local stress concentration, and when the crack grows to a critical length the epoxy resin will fail with fast and unstable crack growth. Shear band deformation rather than crazing was also observed at the crack initiation in epoxy resins by Morgan *et al.* [106] and other researchers [109,110]. The temperature and loading rate can strongly influence the initiation mechanism. At higher testing temperature or lower loading rate, the initiation tends to be caused by shear band deformation, and at

lower testing temperature or higher loading rate the crazing mechanism will prevail [100]. In some works [109–111], the crazing phenomenon was not observed, which might be due to the fine size of craze fibrils (about 1 μm) being difficult to observe optically [112].

The crack propagation in epoxy resins has been intensively investigated using notched test samples, tapered double-cantilever-beam (TDCB) samples that allows a constant crack growth rate are widely used [113–117]. Depending on test temperature, loading rate, and the presence of toughening particles, the crack propagation in TDCB specimens exhibits three major types of modes. Figure 9 shows the schematics for the load-displacement behaviour of the macroscopic fracture of pristine epoxy resins in the form of TDCB specimens. Figure 9(A) shows the load-displacement behaviour of the first type of crack propagation mode characterised by a continuous crack propagation at a constant load [100,118]. In this mode, the crack will initiate when the load produces a stress intensity factor K_I that reaches the fracture toughness K_{IC}, and propagate at the same load till complete fracture. Epoxy resins can also exhibit the second type of crack propagation mode demonstrated by Figure 9B. In this mode, a crack initiates when K_I reaches K_{IB}, which is greater than the K_{IC} of the material, then grows rapidly with a falling load, and eventually arrested at a load producing a K_I approximately equal to K_{IC}. Further crack propagation requires the load to increase and produce a K_I that reaches K_{IB} again [100,118]. This crack-jump phenomenon is believed to be caused by crack tip blunting due to local plastic deformation. Once the crack is initiated the energy stored in the material is much higher than that needed for continuous crack propagation, the crack will advance very rapidly, and be arrested when the crack tip lose the energy enough for further propagation. The second type of crack growth is shown with low strain rate and/or high testing temperature, which favour plastic deformation in the material.

Figure 9C shows the load-displacement behaviour of the third type of crack propagation mode. This was observed in the failure of rubber-toughened epoxy resins [119,120]. In this mode, a crack propagates slowly and continuously with the requirement

of further load input. The reason of this phenomenon is believed to be a progressive increase of K_{IC} at the crack tip. Kinloch and William [121] argued that one epoxy resin can fail by all these modes depending on how much the testing condition favours the crack tip blunting. They correlated the K_{IB}/K_{IC} ratio with the yielding stress $\boldsymbol{\sigma_y}$, of which a lower value indicates higher degree of crack tip blunting, and they found that the epoxies with σ_y greater than 110 MPa tend to fail in a brittle fashion with fast and continuous crack growth, and those with σ_y lying between 50 and 110 MPa tend to fail in a stick-slip mode, and lastly those with σ_y less than 50 MPa tend to fail in a slow continuous mode.

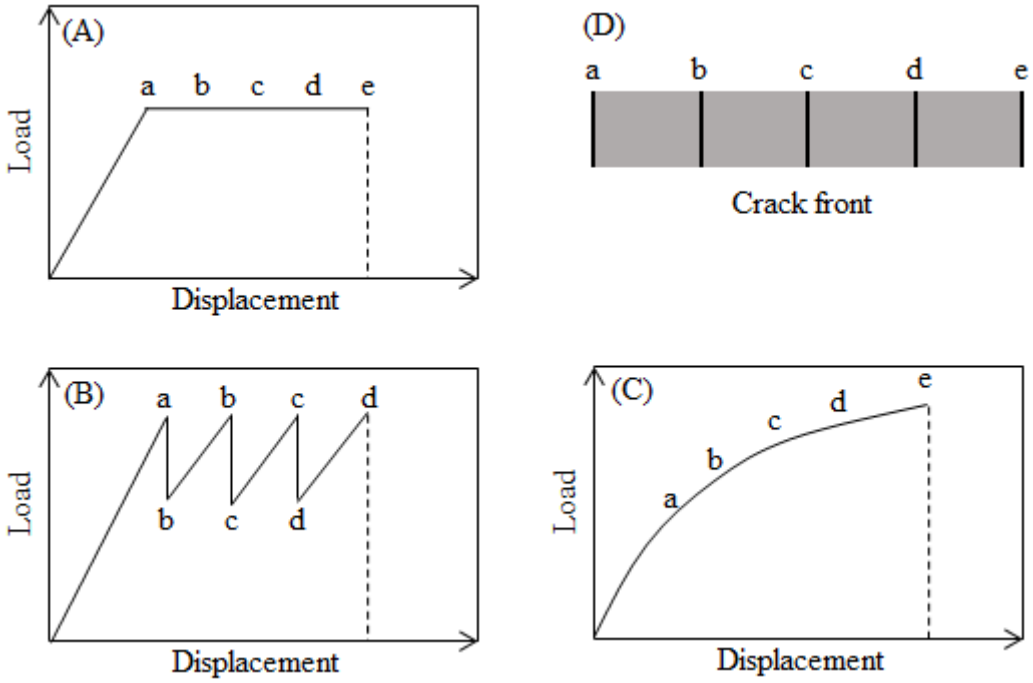

Figure 9. (A) Load-displacement relationship of fast continuous crack growth in epoxy; (B) Load-displacement relationship of stick-slip type crack growth in epoxy; (C) Load-displacement relationship of slow continuous crack growth with increasing $\boldsymbol{K_{IC}}$; (D) Illustration of crack front on a cross section of a fracture surface. This figure is adapted from [100].

Pristine epoxies are widely considered as brittle materials at room temperature (~23 °C), and to toughen epoxy resins, soft rubber particles and rigid inorganic fillers are incorporated. In WBT coatings, rigid inorganic fillers are normally added as pigments for anti-corrosive purposes, and therefore only the toughening mechanisms of inorganic

fillers are briefly summarised here. Three major mechanisms are normally considered as the toughening mechanisms [105,122,123]. (1) Crack deflection: By this mechanism, crack growth is deflected by the fillers and thus it leads to more surface area created due to cracking, causing an increase in the toughness. (2) Plasticity: By this mechanism, fillers encourage local shear banding and causes localised yielding and crack tip blunting when interacting with the fillers, thus increase the energy requirement for cracking. (3) Cracking pinning: By this mechanism the advancing of the crack tip is pinned by an array of fillers which act as barriers for crack growth. It has been widely recognised that crack deflection mechanism does not offer obvious improvement in toughness, but the plasticity and the crack pinning mechanisms sometimes together significantly increase the fracture toughness [124,125].

2.4. Fracture Mechanics of Coatings

Normally, the coating failure produces surface cracks originating from surface flaws, which penetrate towards and arrest at the interface, see Figure 10A. Due to the dispersion of the flaws, the surface cracks are observed discretely on the coating surface. The surface cracks can then propagate across the width of the coatings, and form channels, see Figure 10B. The channel cracks do not stop advancing until they get close to another channel or an edge. In addition, in the presence of a very tough substrate, the coating crack can be deflected and induce de-bonding at the interface, see Figure 10C. Throughout this work, a represents the depth of defect or crack into the thickness, l represent the length of crack appeared on coating surface, and h stands for coating thickness.

Different from monolithic materials, the fracture behaviour of coatings is strongly influenced by the elastic mismatch of material properties of the coating and the substrate. The magnitude of this mismatch is usually quantified by Dundurs' parameters [126] for plane strain problems, see equation (20) and (21).

$$\alpha = \frac{\bar{E}_c - \bar{E}_s}{\bar{E}_c + \bar{E}_s}, \left(\bar{E} = \frac{E}{1 - v^2}\right) \tag{20}$$

$$\beta = \frac{\mu_c(1 - 2v_s) - \mu_s(1 - 2v_c)}{2\mu_c(1 - v_s) + 2\mu_s(1 - v_c)} \tag{21}$$

$\bar{E}_c$, $\bar{E}_s$ are the plane strain moduli of the coating and the substrate respectively;
μ_c, μ_s are the shear moduli of the coating and the substrate respectively;
v_c, v_s are the Poisson's ratios of the coating and the substrate respectively.

In equation (20) α varies from -1 to 1. For a compliant coating and stiff substrate combination, α approaches to -1 and for an opposite combination , α approaches to 1. It has been found that for most practical materials combinations, β typically varies from 0 to $\alpha/4$ [127]. For WBT coatings, the coatings are more compliant than the substrate, and therefore in this review only the case of compliant coating/stiff substrate combination ($\alpha \leq 0$) is considered.

2.4.1. Penetration of coating cracks

The earliest solutions, for a vertical crack propagating from coating surface to interface, were provided by Gecit [128], and later the solutions were then modified by Beuth [129] with an intention of expanding their applications. Zak and Williams [130] firstly derived a stress singularity exponent $\boldsymbol{s}$, which allowed the traction, just ahead of a coating crack tip at the interface, to be expressed. The stress singularity exponent s, along with Dundurs' parameter α and β satisfy the relationship as below.

$$\cos(s\pi) - 2\frac{\alpha - \beta}{1 - \beta}(1 - s)^2 + \frac{\alpha - \beta^2}{1 - \beta^2} = 0 \tag{22}$$

In the linear-elastic case, for a coating/substrate combination of certain Dundurs' parameters α and β, the stress intensity factor at the tip of a vertical crack K_I is found to be dependent only on the relative crack depth a/h.

$$K_I = \sigma(\pi h)^{0.5} \cdot f\left(\alpha, \beta, \frac{a}{h}\right) \tag{23}$$

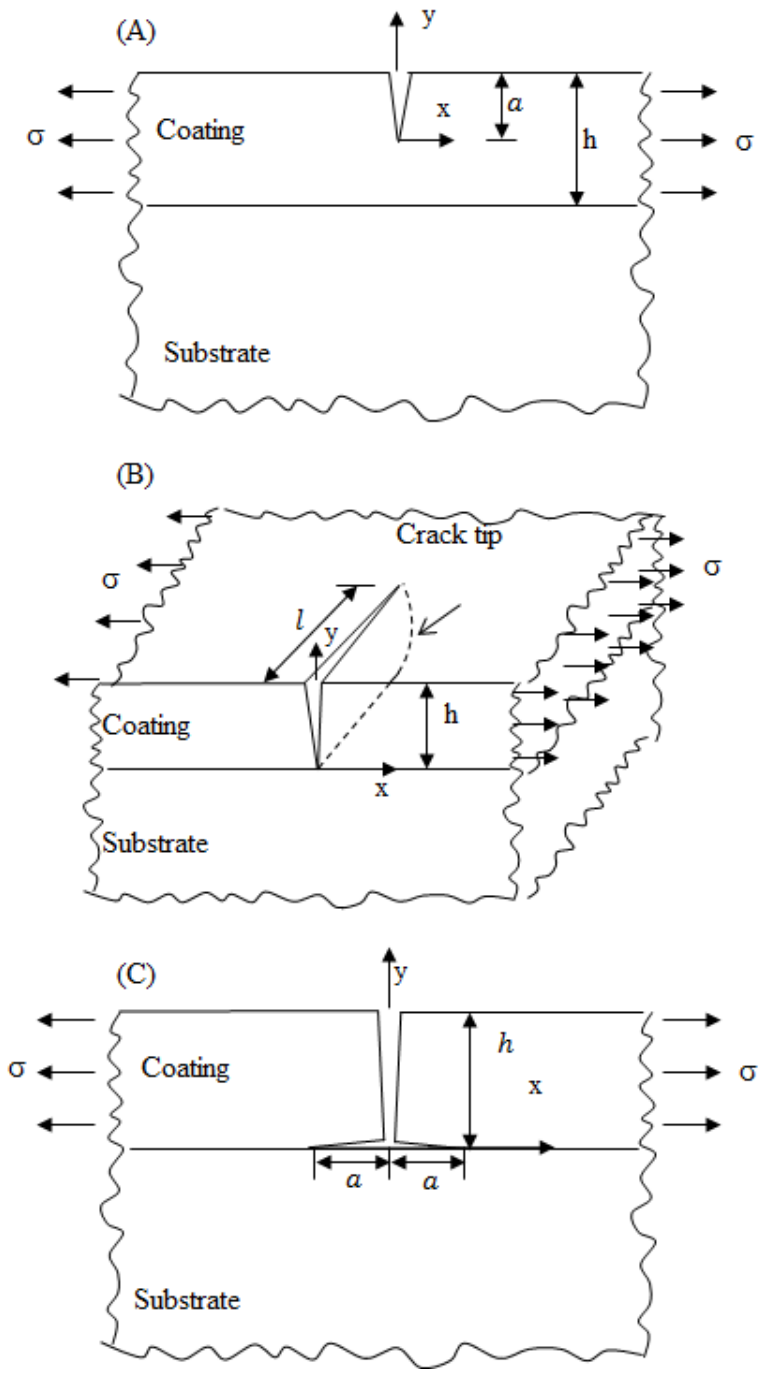

Figure 10. (A) A surface defect propagates towards interface; (B) a vertical crack channel across the width; (C) a fully grown vertical crack deflects at interface and causes debonding.

Here, $f\left(\alpha, \beta, \frac{a}{h}\right)$ is a non-dimensionalised value which reflects the material dissimilarity and crack depth, and can also be treated as a non-dimensionalised stress

intensity factor. The exact value of $f\left(\alpha,\beta,\frac{a}{h}\right)$ can be obtained numerically. For the ease of application, Beuth [129] approximated his numerical results with a closed form expression. Essentially, $f\left(\alpha,\beta,\frac{a}{h}\right)$ can be treated as a non-dimensionalised stress intensity factor.

$$f\left(\alpha,\beta,\frac{a}{h}\right)=\frac{K_I}{\sigma(\pi h)^{0.5}}=1.1215\left(\frac{a}{h}\right)^{0.5}\left(1-\frac{a}{h}\right)^{0.5-s}(1+\lambda\frac{a}{h}) \tag{24}$$

Here, $\boldsymbol{\lambda}$ is a parameter adopted to increase the accuracy of the fitting and can be found in [129] for different α, and it is rather small over the whole range of α, β and a/h, thus has little influence on $f\left(\alpha,\beta,\frac{a}{h}\right)$. s is the same as that shown in equation (22). Equation (24) demonstrates that when $a/h\to 0$, meaning a very shallow flaw, K_I is dominated by $\left(\frac{a}{h}\right)^{0.5}$, and it is similar to a defect in a monolithic material and the crack propagation is hardly influenced by the presence of the substrate. As a/h increases, meaning that the crack tip grows closer to the interface, K_I becomes more dependent on $\left(1-\frac{a}{h}\right)^{0.5-s}$, which demonstrates that the influence of substrate significantly increases as the crack tip approaches the substrate.

Based on equation (14) under linear elastic condition the energy release rate of penetrating crack propagation $\boldsymbol{G_p}$ in plane strain can be derived with the K_I, and $\bar{E}_C$ is the plane strain modulus of the coating.

$$G_p=\frac{K_I^2}{\bar{E}_C}=\frac{\pi\sigma^2 h}{\bar{E}_c}f\left(\alpha,\beta,\frac{a}{h}\right)^2 \tag{25}$$

2.4.2. Channelling of coating cracks

The problem of channel cracks in coatings has been treated by a number of researchers. The earliest was Gille [131], who tackled the problem theoretically using the numerical method at the time. Subsequently, Hu and Evans [132] treated the problem by calculations and experiments. The treatment of this problem considers a single through-

thickness defect with a surface crack, of length exceeds a few times the coating thickness, channelling across the coating plane in a steady state, in which the crack front maintain constant shape. Recent finite element analysis by Nakamura [133] as well as Xia and Hutchinson [134] show that in compliant coating/stiff substrate systems the steady-state condition is achieved when the channel crack length reaches roughly twice the coating thickness.

The basic concept to calculate the energy release rate of crack channelling in steady state is based on the energy balance of channelling process. The energy release rate at the crack front is treated as two plane problems, the planes far ahead and far behind the crack tip, see Figure 11. It is calculated by subtracting the energy stored far behind the crack tip from that far ahead.

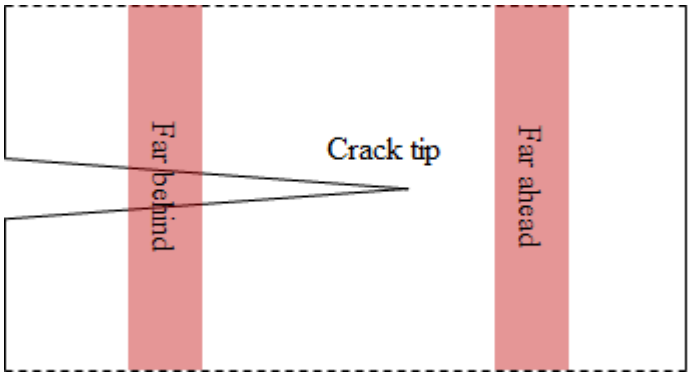

Figure 11. Illustration of an overview of a channelling crack on a coating surface.

The energy release rate for coating crack channelling under steady state $\boldsymbol{G_{ch}}$ can be described by equation (26) below [129]. Like $f\left(\alpha,\beta,\frac{a}{h}\right)$, $g\left(\alpha,\beta,\frac{a}{h}\right)$ is a non-dimensionalised value which reflects the material dissimilarity and crack depth.

$$G_{ch} = \frac{1}{2}\frac{\pi\sigma^2 h}{\bar{E}_c} g\left(\alpha,\beta,\frac{a}{h}\right) \tag{26}$$

Beuth [129] further demonstrated the cracking channelling in dissimilar bi-layer structures using numerical methods, and approximated $g\left(\alpha,\beta,\frac{a}{h}\right)$ result as follows.

$$g\left(\alpha,\beta,\frac{a}{h}\right)=\frac{2G_{ch}\bar{E}_c}{\pi\sigma^2 h}$$
$$=-\frac{2h}{a}(1.1215)^2[b^{2-2s}\left(\frac{1+2\lambda+\lambda^2}{2-2s}\right.$$
$$\left.-\frac{1+4\lambda+3\lambda^2}{3-2s}b+\frac{2\lambda+3\lambda^2}{4-2s}b^2-\frac{\lambda^2 b^3}{5-2s}\right)]_{b=1}^{b=1-a/h} \quad (27)$$

Here, the parameters λ and s are the same as those shown in equation (25). Beuth [129] treated $f\left(\alpha,\beta,\frac{a}{h}\right)^2$ as a non-dimensionalised energy release rate $g_p\left(\alpha,\beta,\frac{a}{h}\right)$ for crack penetration, and plotted it and the non-dimensionalised energy release rate $g_{ch}\left(\alpha,\beta,\frac{a}{h}\right)$ (equation (27))for crack channelling against the relative crack depth a/h, see Figure 12.

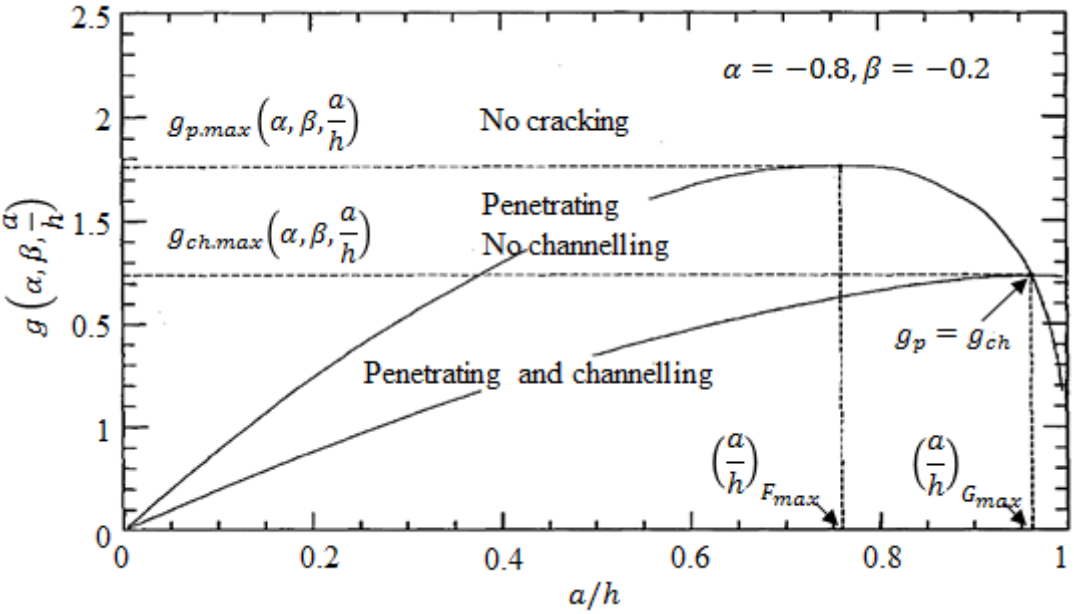

Figure 12. Non-dimensionalised energy release rates for both crack penetration and crack channelling as a function of relative crack depth. This example uses a compliant coating/stiff substrate combination with $\boldsymbol{\alpha=-0.8,\beta=\alpha/4}$. This figure is adapted from [129].

Figure 12 demonstrates that the energy release rate for either the crack penetrating or channelling vary with the relative depth of the defect. The biggest energy release rates for both processes can be found before the crack penetrates fully through the thickness, and $g_p\left(\alpha,\beta,\frac{a}{h}\right)$ drastically drops after the peak to zero, which indicates that the crack

penetration will never reach the interface in theory. In addition, before the intercept of the plots $g_p\left(\alpha,\beta,\frac{a}{h}\right)$ is greater than $g_{ch}\left(\alpha,\beta,\frac{a}{h}\right)$, which indicates that the crack penetration is more prone to occur, in other words it requires less stress.

2.4.3. Interfacial failure

When a penetrating crack reaches the interface, the crack can either be deflected into the interface or carry on penetrating into the substrate, which are two processes in competition [135]. Numerous research works have focused on this problem. Mechanics solution of interfacial failure was investigated by Malyshev and Salganik [136]. Cook and Erdogan [137] as well as Erdogan and Biricikoglu [138] were the earliest to analyse a crack in a medium propagating through the interface into the other medium of the same material. Goree and Venezia [139] later investigated a crack penetrating through and deflected by an interface. Solutions regarding a crack penetrating and deflected by an interface joining two dissimilar materials were summarised by He and Hutchinson [140].

Failure of the interface is a mixed mode failure due to the asymmetry of the material properties. Whether a vertical crack is penetrating into the substrate or being deflected and propagating at the interface depends on the relative magnitudes of the tendencies of these two processes. The energy release rate for interfacial delamination $\boldsymbol{G_d}$ can be expressed as follows [135]

$$G_d = \frac{1-\beta^2}{2}\left(\frac{1}{\bar{E}_c}+\frac{1}{\bar{E}_s}\right)(K_I + K_{II}) \tag{28}$$

The criterion for delamination to take place, G_d needs to satisfy the following requirement.

$$\frac{G_{Ic.s}}{G_{c.d}} < \frac{G_d}{G_p} \tag{29}$$

Here, $\boldsymbol{G_{Ic.s}}$ and $\boldsymbol{G_{c.d}}$ are the mode I fracture toughness of the substrate and the fracture toughness of the interface respectively. He and Hutchinson [140] numerically

demonstrated that the $\frac{G_d}{G_p}$ ratio in compliant coating/stiff substrate combinations is much higher than that of stiff coating/compliant substrate combinations. This means that the interfacial delamination is more prone to take place when the coating is more compliant than the substrate, and this is the case for epoxy based WBT coatings. The effect of delamination on the crack channelling process was also studied, Mei *et al.* [141] analysed the energy release rate of channelling crack with delamination behind the crack tip, and found the energy release rate was increased. This means delamination promotes further channelling.

2.4.4. Multiple cracking and crack interaction

Multiple cracking of films under unidirectional loading is widely observed. Xia and Hutchinson [134], based on the energy approach applied to crack channelling, derived the energy release rate of a crack tip among the first array of parallel multiple cracks $\boldsymbol{G_{first}}$ simultaneously advancing towards the same direction in mode I.

$$G_{first} = \frac{l_r \sigma^2}{\bar{E}_C} \tanh\left(\frac{H}{2l_r}\right), \qquad l_r \equiv \frac{\pi}{2} G(\alpha, \beta) h \tag{30}$$

Here, $\boldsymbol{H}$ is the distance between two parallel cracks, l_r is a reference length that reflects the elastic mismatch between the film and the substrate, which increases with increasing film stiffness and film thickness. For the second array of parallel multiple cracks initiated in the centres of un-cracked film segments, the energy release rate is as follows.

$$G_{second} = \frac{l_r \sigma^2}{\bar{E}_C} \left[2 \tanh\left(\frac{H}{2l_r}\right) - \tanh\left(\frac{H}{l_r}\right)\right] \tag{31}$$

Xia and Hutchinson [134] plotted the relationship between the normalised energy release rates for the occurrence of the multiple cracks. Figure 13 demonstrates that the reference length l_r has a strong influence on the driving force of the multiple cracking. With constant H, bigger l_r means that a lower driving force for the multiple cracking under a given stress. This figure also clearly shows that a higher stress is required for the

second array of multiple cracks. It is important to notice that in Xia and Hutchinson's solution, it is assumed that the multiple cracks initiate and propagate simultaneously, which in reality is not true. Hsueh *et al.* [142,143] based on energy equilibrium in the cracking process of strained coating/substrate systems and a shear-lag model, developed an analytical model which describes the relationship between the applied strain and the crack density. It also predicts the initiation of the first crack.

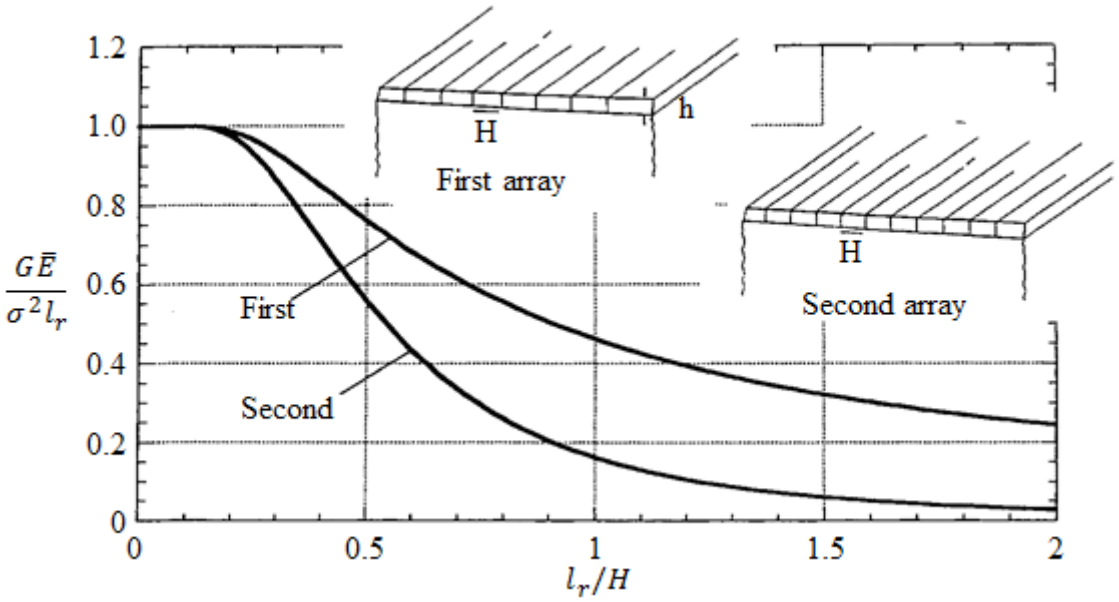

Figure 13. Normalised energy release rate of each crack in the first array and the subsequently initiated second array. This is adapted from [134].

In Hsueh's model, the relationship between the applied strain to the first crack $\boldsymbol{\varepsilon_c}$ and the fracture energy $\boldsymbol{\Gamma}$ stored in a strained coating is as (32) below [142]. Γ is essentially fracture toughness in the form of G_{IC}. Here, $\boldsymbol{h_s}$ is the thickness of the substrate, and $\boldsymbol{\Delta\varepsilon}$ is the residual stress. In equations (32) and (33), $\boldsymbol{l}$ is the half of the inter-crack distance, which equals $H/2$.

$$\Gamma = \frac{E_c}{2\alpha(1-\upsilon_c)(1-\upsilon_c\upsilon_s)^2} \times \left[\frac{(1-\upsilon_c\upsilon_s)\varepsilon_c}{1+\upsilon_c} - \frac{\Delta\varepsilon}{1+\frac{h(1-\upsilon_c\upsilon_s)E_c}{h_s(1-\upsilon_c)E_s}}\right]^2 \times \left[\frac{3P_1}{2} - \frac{P_2\Delta\varepsilon}{\frac{(1-\upsilon_c\upsilon_s)\varepsilon_c}{1+\upsilon_c} - \frac{\Delta\varepsilon}{1+\frac{h(1-\upsilon_c\upsilon_s)E_c}{h_s(1-\upsilon_c{}^2)E_s}}}\right] \quad (32)$$

$$\alpha = \left[\frac{3}{2hh_s(1+\upsilon_s)}\left(\frac{h}{h_s} + \frac{(1-\upsilon_c{}^2)E_s}{(1-\upsilon_c\upsilon_s)E_c}\right)\right]$$

$$P_1 = (1+\upsilon_c)(1-2\upsilon_c\upsilon_s+\upsilon_s{}^2)$$

$$P_2 = -2\upsilon_s(1+\upsilon_c)(1-\upsilon_c{}^2)Q$$

$$= \frac{-3P_1}{2}\left[\frac{1}{1+\frac{h(1-\upsilon_c\upsilon_s)E_c}{h_s(1-\upsilon_c{}^2)E_s}} - \frac{(1-\upsilon_c\upsilon_s)\varepsilon_c}{(1-\upsilon_c{}^2)\Delta\varepsilon}\right]^2 - P_2\left[\frac{1}{1+\frac{h(1-\upsilon_c\upsilon_s)E_c}{h_s(1-\upsilon_c{}^2)E_s}} - \frac{(1-\upsilon_c\upsilon_s)\varepsilon_c}{(1-\upsilon_c{}^2)\Delta\varepsilon}\right]$$

The relationship between the applied strain ε_a and the inter-crack distance $2l$ is as below [142].

$$\varepsilon_a = \frac{-(1+\upsilon_c)\Delta\varepsilon}{1-\upsilon_c\upsilon_s}\left\{\frac{-1}{1+\frac{h(1-\upsilon_c\upsilon_s)E_c}{h_s(1-\upsilon_c)E_s}} + \frac{-P_1R_1 + [(P_2R_2)^2 - 4P_1R_1Q]^{0.5}}{2P_1R_1}\right\} \quad (33)$$

$$R_1 = 4\tanh\left(\frac{\alpha l}{l}\right) - \frac{e^{\alpha l} - e^{-\alpha l} + 2\alpha l}{e^{\alpha l} + e^{-\alpha l} + 2} - 2\tanh(\alpha l) + \frac{1}{2}\frac{e^{2\alpha l} - e^{-2\alpha l} + 4\alpha l}{e^{2\alpha l} + e^{-2\alpha l} + 2}$$

$$R_2 = 2\tanh\left(\frac{\alpha l}{2}\right) - \tanh(\alpha)$$

$$Q = \frac{-3P_1}{2}\left[\frac{1}{1+\frac{h(1-\upsilon_c\upsilon_s)E_c}{h_s(1-\upsilon_c{}^2)E_s}} - \frac{(1-\upsilon_c\upsilon_s)\varepsilon_c}{(1-\upsilon_c{}^2)\Delta\varepsilon}\right]^2 - P_2\left[\frac{1}{1+\frac{h(1-\upsilon_c\upsilon_s)E_c}{h_s(1-\upsilon_c{}^2)E_s}} - \frac{(1-\upsilon_c\upsilon_s)\varepsilon_c}{(1-\upsilon_c{}^2)\Delta\varepsilon}\right]$$

2.5. Fatigue of Materials

Materials also fail by fatigue, and comprehensive knowledge regarding the fatigue behaviour of materials has been well documented by several well-known textbooks by authors such as Suresh [144] and Schijve [145]. Essentially, fatigue is a process where cyclic loading causes progressive failure at stresses less than those to cause static failure. Stresses that cause fatigue failure are normally much smaller than the ultimate tensile strength of material or even the yielding strength. However, stress can be locally magnified by a stress concentration and eventually form micro-cracks. In a structural material, fatigue failure starts with the changes in sub-structural and microstructural features, and the changes lead to nucleation of permanent damage, which further develops into microscopic cracks. The growth and the coalescence of the microscopic cracks form dominant cracks, which undergo a stable propagation to a size whereby the propagation becomes unstable and eventually leads to complete rupture.

The classic approach to fatigue of materials is based on total life of materials. In this approach, laboratory characterisation of the number of cycles or life to the failure in terms of a given cyclic stress/strain range of a sample is carried out [144]. The result normally includes the cycle number to the crack initiation and the cycles of crack propagation until the catastrophic failure of a test sample. Based on the proportion of the cycles to crack initiation within the total life, one can determine if the fatigue failure of the material is predominantly controlled by the crack initiation or the propagation. Figure 14 illustrates a maximum stress/strain to the cycle life (S-N) curves of a specimen under arbitrary stress/strain ranges.

Another common approach to the fatigue problem is a defect-tolerant approach. In this approach, a critical crack size is defined according to the in-service load of a structure. The fatigue life of the substructure is defined as the cycle number to propagate an initial crack to the critical crack size. This approach requires the characterisation of the crack growth rate, and empirical crack growth laws such as the Paris' law [146] have been developed to allow the prediction of fatigue life, and its expression is as follows,

$$\frac{da}{dN} = C\Delta K^m, \Delta K = K_{max} - K_{min} \tag{34}$$

where, $\boldsymbol{C}$ and $\boldsymbol{m}$ are empirical constants and functions of material properties, test sample geometry and test configurations; $\boldsymbol{\Delta K}$ is the change of stress intensity factor at the crack tip, and is the difference of the stress intensity factors at the maximum and the minimum loads.

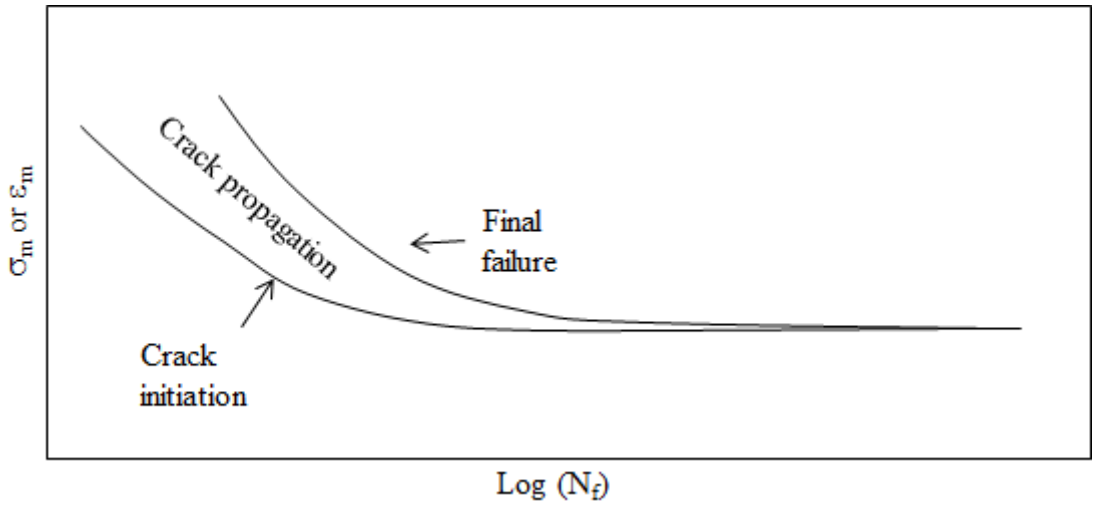

Figure 14. Arbitrary illustration of S-N curve of crack initiation and propagation to the final failure in a normal smooth specimen. Adapted from reference [144].

Paris' law shows that the crack growth per cycle is a function of ΔK, and recall that K is a function of far-field stress and crack length, and hence the crack growth rate is also a function of the quantities. Figure 15 shows the general shape of a $log(\frac{da}{dN})$ vs. $log(\Delta K)$ curve. The Paris' law only describes the regime B in Figure 15, where the logarithmic crack growth rate increases linearly with the increase of the logarithmic change of stress

intensity factor. In the regime A, when the ΔK is greater than a critical value, the crack growth rate endures a steep increase, and in the regime C the crack growth rate is further accelerated and eventually reaches the fracture toughness of the material and causes the complete failure.

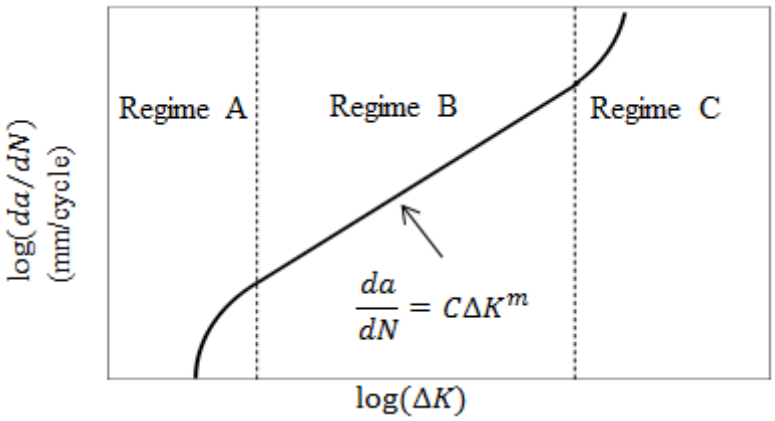

Figure 15. Schematics of a bi-logarithmic relationship between crack growth rate and change of stress intensity factor. Adapted from reference [144].

2.6. Experimental Observations of Coating Fracture

Coating fracture has been widely observed experimentally [14,16,147–155]. Although the aforementioned theories clearly demonstrate that the fracture of coatings includes the vertical crack penetration and the lateral crack channelling, still experimentally observed failure normally is the lateral crack channelling and the multiple cracking phenomenon. This is understandable as the coatings are usually very thin, from several tens of nanometres to several hundreds of microns, the vertical crack penetration is very difficult to observe. Nairn and Kim [147] observed the cracking of uni-directionally strained poly(methyl methacrylate) (PMMA) coatings on polycarbonate (PC) substrate using optical microscopy. They found that the applied strain to first crack decreases with the increase of the coating thickness, which can be explained as the increased coating thickness causes an increase in the energy release rate for the crack to channel, see equation (26). They also found that at higher applied strains the density of multiple cracks also decreases with the increase of the coating thickness. This can be explained by a shear-lag model where the stress in a coating segment confined by two adjacent cracks

is smaller in a thick coating than in a thinner coating. Similar observations have been reported by Yanaka *et al* [149] and Hu and Evans [132].

To date, most of the coating cracking is observed visually using either camera or microscope. A few papers reported coating crack detection using Digital Image Correlation (DIC) [14,153] or/and acoustic emission technique [16,155]. Wu *et al.* [153] used DIC to record the in-situ strain evolution over the surface of a ceramic coating on a steel substrate subjected to tensile straining. They found that when cracking occurred, the local strain at the crack increased drastically compared with the global strain. Further, they monitored the side view of the coating under tension, and observed the cracks initiated from the coating surface. Similar observation has been reported by Zhou *et al*. [14] who also observed the interfacial debonding of a ceramic coating from its steel substrate using DIC. Xu and Mellor [154,155] studied the fracture of an epoxy coating on steel substrate subjected to four point bending using acoustic emission. They claimed that they established the failure modes from different acoustic emission characteristics. However, no evidence has been shown that their technique is capable of accurately measuring the applied strain to the first crack.

Some research [3,62,156] regarding the internal stress of organic WBT coatings has been found. Lee and Kim [3] performed probably the most systematic study. They characterised the Young's moduli and the CTEs of two commercial WBT coatings, and evaluated the internal stress in these coatings on welded joints due to curing and temperature change using a finite element method (FEM). They found that the internal stress in the coatings on these structures are much higher that measured on flat strips. They evaluated the internal stress induced by curing shrinkage independently, and the result indicated that the failure of the coatings was not caused by internal stress prior to service. The following evaluation of thermally induced internal stress yielded stresses 3 fold greater than the curing-induced stress in the coatings of the same thickness, and an increasing thickness of the coatings was found to increase the thermally induced internal

stress as well. They concluded that if the coatings were applied too thick, the thermally induced internal stress would cause the coating failure.

Fatigue failure of coatings has also been dealt with, however mainly in the field of metallic thin films on polymeric substrates [11–13,157–159]. Similar to the research in the static failure of coatings, the fatigue failure of coatings are observed indirectly through other physical responses of the coatings. Eve *et al.* [11] investigated gold and aluminium thin films supported by PMMA and PC substrates under cyclic mechanical and thermal stresses. They adopted an optical method to monitor the fatigue failure, in which the dispersion of laser light shining on the coating surface was monitored, and the reduction in the reflected laser intensity indicated the appearance of coating cracks. Kim *et al*. [157], Kraft *et al*. [158] and Zhang *et al*. [12] investigated the fatigue behaviours of several metallic coatings on polymeric substrates by monitoring the change of the compliance of the coating/substrate systems. When the coating starts to develop fatigue crack(s), the load-bearing capability of the coating will reduce. As a macroscopic result, the compliance of the coating/substrate system will start to drop and finally becomes the compliance of uncoated substrates. The onset of the compliance reduction was used to define the point of fatigue failure.

In addition, the fatigue failure of metallic coatings was also investigated using the electrical responses of the coatings. Sim et al. [13,159,160] put silver and copper coatings supported by polymeric substrates under cyclic mechanical stresses, and in-situ measured the electrical resistance of the coatings. Upon fatigue cracking, the electrical resistance of the coating will increase, and the onset of the resistance increase was defined as the failure point. They also measured the following increase of the electrical resistance after the failure point, and qualitatively correlated it with the number of fatigue cracks as a function of cycle number. All these studies found that the strain-life relationship of the metallic coatings satisfied a Coffin-Manson type of relationship, in which the life of the coatings increase with the reduction of strain amplitude following power-law relationships. Importantly, it has also been observed that thicker coatings tend

to have less fatigue resistance [12,13,158]. This is in agreement with the fracture mechanics, in which the increase of coating thickness raises the energy release rate of cracking.

The fatigue behaviour of WBT coatings is rarely investigated, the only work found by the author was performed by Zhang et al. [156] and Kim and Lee [3]. They simulated the temperature cycle in WBTs on 5 types of epoxy based coatings on T-girders that simulate the geometry of a welded fillet joint, which is a structure with two steel plate perpendicularly joint by welding. The WBT coatings with different thickness from 300 μm to 1200 μm were sprayed onto the corner of the joints. They found that the coating thickness played a very crucial role in determining the life of the coatings. The thicker the coatings were, the shorter the life to cracking. For the coatings with thickness about 300 μm, no cracking was observed in all types of coatings after 128 cycles, which is roughly about 5 years of service time, and for the coating with a thickness about 1200 μm, coating fatigue failure was observed in 4 types of the coating at different cycle numbers from 6 to 128.

2.7. Summary

In the current research into the durability study of WBT coatings, factors such as internal stress, physical ageing, and thermal fatigue are widely appreciated. However, the investigations seem only to use the strength of the coating materials as a criterion of the coating failure. The application of fracture mechanics and the adoption of fracture toughness are not rooted in the basic methodology of this research yet. Relevant research performed by Zhang et al. [156] and Kim and Lee [3] are typical examples of this. For the investigation of the effects of coating thickness on the internal stress, Kim and Lee [3] deliberately kept the radius of the curvature of the coating surface constant. However, this is not the case, the radius of curvature of a coating surface on the welded joint varies due to applications and uncured coating rheology, the variation of the curvature could introduce more dramatic scenarios. To date, no research addressing this

matter has yet been found. In addition, Lee and Kim used the strength of the coatings obtained from the tensile tests of free films as the failure criterion of the coatings on substrate. It is not be a rigorous treatment, as it has already been found that epoxy coatings on substrate will have a different ductility from the free films [161]. There is a need to develop their FE model further with fracture mechanics incorporated.

The fatigue study of the WBT coatings as well can only provide limited information. In the research of Zhang et al. [156] and Kim and Lee [3], they merely found that the WBT coatings with bigger thicknesses tended to be less fatigue resistant, but no more insights regarding the effect of the material properties were proposed. To have more accurate prediction of the fatigue failure of WBT coatings, the correlation between the fatigue behaviours and the material properties ought to be established. In addition, quantitative research regarding the fatigue of polymeric coatings on stiff substrates has not been found yet. Even in the published fatigue research of stiff metallic coatings, the crack growth was only indirectly measured by other physical responses of the coatings. A quantitative coating fatigue crack growth needs investigating.

3. CHARACTERISATION OF MATERIAL PROPERTIES

This chapter will present the characterisation of the material properties of two grades of experimental WBT coatings and one type of steel substrate. The substrates were designed and manufactured at Cranfield University, and all coatings were prepared at International Paint. The experimental work to characterise coating fracture on substrate under static and cyclic strains will be described in the next chapter.

3.1. Materials and Sample Preparation

3.1.1. Coating materials and samples manufacture

For this project, two grades of epoxy-based experimental water ballast tank coating were provided by International Paint, and will be referred to as coating A and coating B in this thesis. Both coatings were heavily filled with various types of inorganic particulate pigments/fillers. The pigment volume contents in the dry state of coatings A and B were 25% and 29% respectively. Before curing, the coatings contained a high solvent content and therefore were in the form of a viscous liquid, and once applied they solidified by solvent evaporation and chemical curing. The fully cured coatings A and B possessed similar Young's moduli of about 5 GPa.

Free film sample for tensile tests

Free film samples of both coatings with a dog bone shape and a nominal thickness of 300 μm were made for the characterisation of the stress-strain behaviour of the coatings, see Figure 16, which shows the dimensions. To manufacture the free films, sheets of the coating materials were initially prepared by spraying the uncured coatings on polytetrafluoroethylene (PTFE) coated glass plates. After two days of curing at ambient temperature, the sheets were partly cured into a form of rubbery solid with low stiffness, and then peeled off from the PTFE surface and cut into the dog bone shape by a punch mould. After cutting, the free films samples were further cured at ambient temperature for another 5 days followed by a post-cure step at 100 °C for another 2 days. The coating

spraying was performed at International Paint, the coating thickness was controlled using different spraying times, and final coating thicknesses were determined by measuring 15 samples of each coating in a fully cured state using a micrometre. The average thickness coating of coating A free films were 0.29 ± 0.04 mm, and that of coating B free films were 0.29 ± 0.02 mm. The errors shown here and all errors of mean values to be shown are the standard deviations.

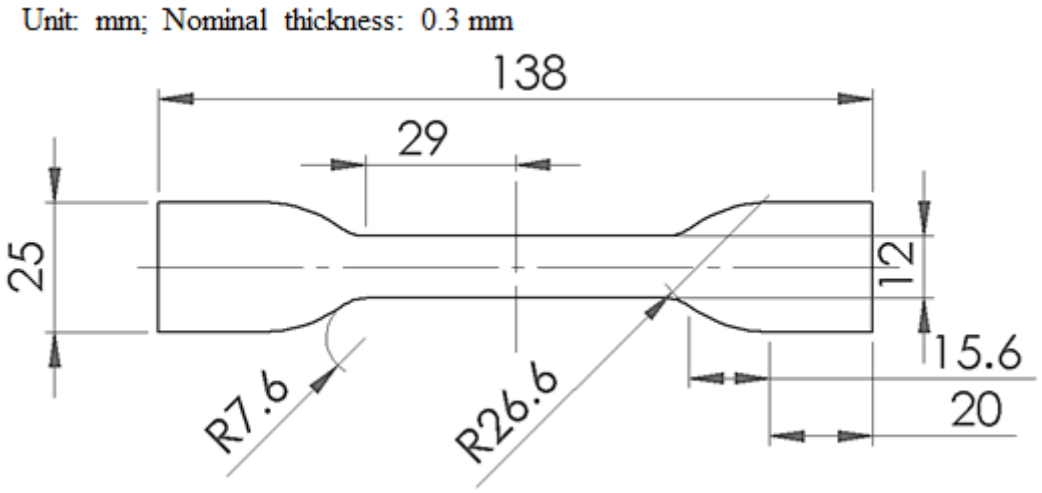

Figure 16. Dimensions of free film samples

Double edge notched free films for fracture toughness measurement

For the measurement of mode I fracture toughness, double notched free film samples have been used previously [162]. A pair of notches with nominally equal lengths (a) from 1 to 4 mm were introduced on the edges of each sample on a 100 °C hot plate using a razor blade, see Figure 17. The lengths of the notches were measured under an optical microscope with a calibrated stage, and the crack tips were found sharp under optical microscope. A light intensity image showing a typical edge notch tip produced using a confocal optical microscope is shown in Figure 18 using a coating B sample as example. Defining the crack tip sharpness as the radius of the crack tip, the sharpness of the edge notch tips was below 500 nm. Difference between the lengths of the two notches on each sample was found to vary from 0.01 to 0.35 mm, and the average of the notch

lengths of each sample were used for fracture toughness calculation. The detailed sample dimensions and corresponding notch depths are shown in Appendix i.

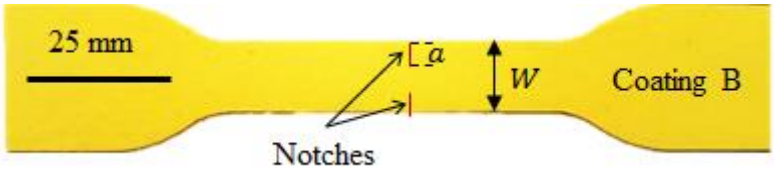

Figure 17. Photo of free films of coating A and coating B. the red markings illustrates the locations of pre-cracks in double notched free film samples.

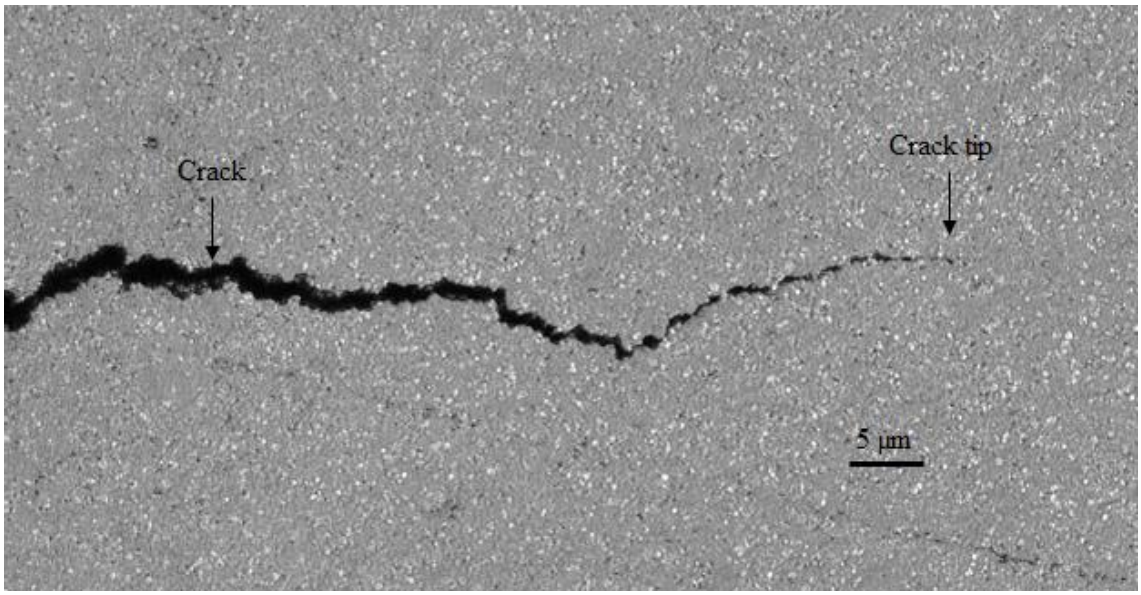

Figure 18. Typical light intensity map of an edge crack tip produced using a con-focal microscope of a coating B sample.

Cylindrical tablets for thermal property measurement

For the measurement of the thermal expansion coefficients (CTEs) and glass transition temperature (T_g) of the coating materials, cylindrical tablets made of the coating materials were prepared, see Figure 19. The tablets were made by casting the uncured coatings into a silicon mould. Due to the high solvent content, the casting was done layer by layer, and between each casting the solvent was allowed to evaporate at room temperature for 1 day. After casting, the samples were cured at room temperature for 7 days and then at 100 °C for 2 days. For each tablet 5 layers were cast, which gave a final

thickness of about 5 mm. Due to the uneven top surface, the samples were cut short to provide a flat surface. The samples eventually used for CTE measurement had a diameter of 6.27 ± 0.03 mm and a height of 2.79 ± 0.44 mm.

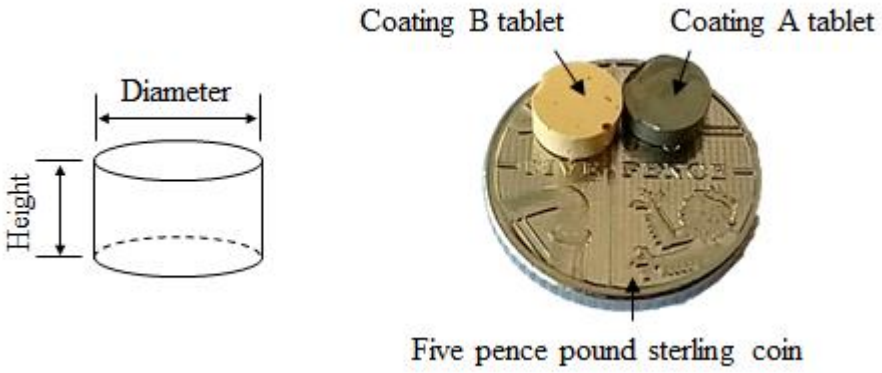

Figure 19. Photo of the coating material tablets for thermal mechanical analyses.

3.1.2. Substrate material and sample manufacture

The substrate material was a steel to standard EN 10025-2:2004 and was of S355K2+N grade. Based on Lloyd's rules for the classification of offshore units (includes double hulled oil tankers) [163], this steel satisfies as structural material for marine structures. The substrate steel was purchased in the form of a 6 mm thick sheet. The ladle analysis results are shown in Table 1 below. Also given by the manufacture, the minimum values of yield stress, ultimate tensile strength, and failure strain of this type of steel were 355 MPa, 470 MPa, and 20% respectively.

Table 1. Ladle analysis results of S355K2+N steel to standard EN 10025.

Elemental Analysis (wt.%)						
C	Si	Mn	P	S	N	Al
0.17	0.33	1.12	0.007	0.003	0.004	0.033
Cr	Ni	Mo	V	Ti	Nb	Cu
0.04	0.22	0.01	0.001	0.001	0.03	0.21

Substrate dog-bone samples for tensile tests

For the characterisation of substrate stress-strain behaviour, substrates tensile samples were made. The samples were machined from the steel sheet into dog-bone shape tensile bars based on ASTM E8/E8M [164] standard and the dimensions are shown in Figure 20.

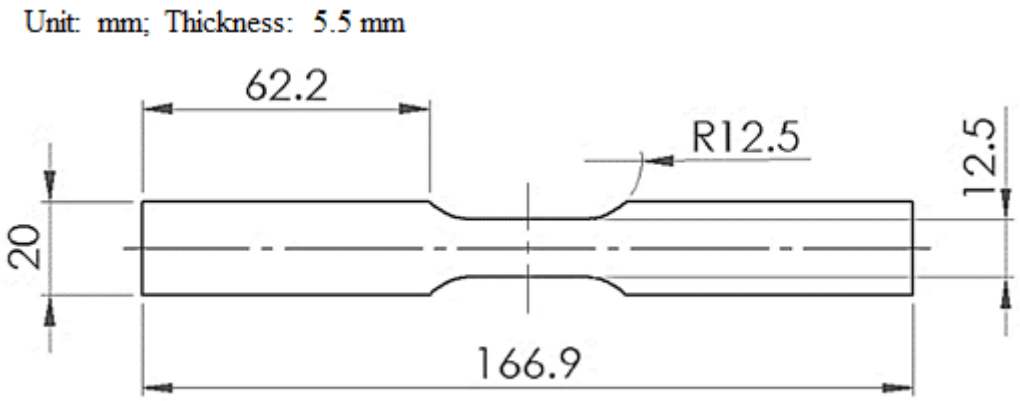

Figure 20. Dimensions of the substrate samples for static tensile tests.

3.2. Test Procedures

3.2.1. Tensile tests of coating free films

The static mechanical properties of the coating free films were characterised by static tensile tests using an INSTRON 5500R screw-driven machine with a 250 N load cell. All tests were performed at a crosshead speed of 5 mm/min. The tests were run at temperatures of -10, 23, 50 and 70 °C achieved by an environmental chamber with a temperature controlling error of ± 1 °C attached to the test machine. The extension was measured by an INSTRON video extensometer with a measuring resolution of 0.001 mm, and the gauge length monitored was 25 mm. Prior to test, all the samples were heat treated in an oven at 100 °C for 30 minutes, and cooled down to ambient temperature at ambient temperature.

The Young's modulus of the free film (E_C) was determined using the stress-strain curves. Based on ISO 527-1 [165], the slope of a least-square regression line fit of the data between strains of 0.05% and 0.2% was used as modulus, which is the same as a secant modulus as the stress-strain curve within this range was linear.

3.2.2. The measurement of fracture toughness of free films

For the fracture toughness measurement, the double notched free film samples were tested at ambient temperature using the INSTRON 5500 screw-driven test machine with a load cell of 100 N capacity. All tests were performed at a crosshead speed of 5 mm/min to failure. The load and cross-head displacement to fracture of each sample was recorded. Considering that the loads to fracture were small, and thus unlikely to cause large displacement in the grips, the cross-head displacement should serve well as the displacement of the samples between the two gripping points.

The determination of fracture toughness followed ASTM D5045 [166]. The load-displacement relationship was used to determine load that initiated crack growth (F_Q). Using F_Q, the failure stress (σ_f) was calculated by incorporating the cross-section area of the samples. The critical stress intensity factor (K_Q) at fracture for the double edge notched samples was determined using equations (35) and (36) [167] . Here, $2W$ and a are the width of the sample and the average of 2 notch lengths.

$$K_Q = \sigma_f \sqrt{\pi a} f\left(\frac{a}{W}\right) \tag{35}$$

$$f\left(\frac{a}{W}\right) = \left[1.12 - 0.561\left(\frac{a}{W}\right) - 0.205\left(\frac{a}{W}\right)^2 + 0.471\left(\frac{a}{W}\right)^3 - 0.19\left(\frac{a}{W}\right)^4\right] / \sqrt{1 - \frac{a}{W}} \tag{36}$$

3.2.3. Measurement of free film Poisson's ratio

The Poisson's ratio ($\boldsymbol{\nu}$) of the free films at ambient temperature was measured using tensile testing of 5 free film samples of each coating using an INSTRON 5500 screw-driven

machine with a 5 kN load cell. The coating deformation during testing was recorded by a Dantec DIC system at an acquisition rate of 5 frames per second. Figure 21 shows the DIC configuration for this measurement. The two cameras had an angle of about 30° between them, and their distance to the sample set to cover a length of about 73 mm within 1616 pixels. The surface of the free film samples were sprayed with a thin layer (about 0.02 mm) of white primer paint (see Figure 50 on page 91), on top of which black paint dots were speckled to form a random pattern. Given the much smaller thickness of the primer paint, the primer paint does not affect the properties of the coatings. The strain measurement in these tests had an error of ± 0.02%. A description of the DIC system can be found in Appendix vii. Note that the maximum load recorded was about 100 N, which was about 2% of the capacity of the load cell, thus the recorded load was not used to produce the stress response of the coatings.

According to IS0 527-1 [165] the Poisson's ratio υ can be determined using the equation below.

$$\upsilon = -\frac{\Delta\varepsilon_t}{\Delta\varepsilon_l} \tag{37}$$

Here, $\Delta\varepsilon_t$ and $\Delta\varepsilon_l$ are the change of strain in transverse and longitudinal direction in a longitudinal strain increment.

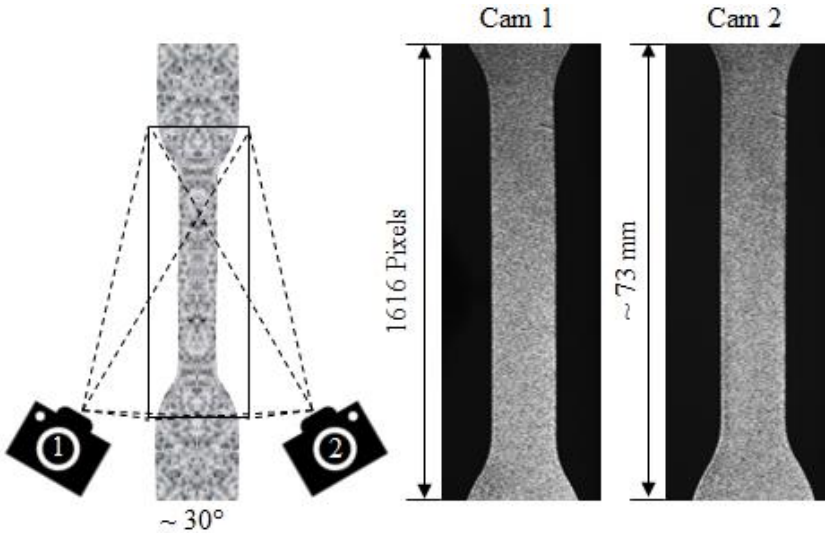

Figure 21. Configuration of DIC system for the measurement of free film Poisson's ratio.

3.2.4. Measurement of coating thermal properties

The glass transition temperatures (T_g) and coefficient of thermal expansion (CTE) of the coating materials were measured using thermal mechanical analysis (TMA) based on ISO 11359-2 standard [168].

The coating tablet samples, 5 samples of each coating, were tested using a TA TMA 2940 thermo-mechanical analyser. The samples were firstly conditioned at 150 °C for 5 min and then tested in temperature cycle from 150 °C to -50 °C and back to 150 °C at a rate of 5 °C/min. The development of sample height with temperature changes was recorded, and used to determine the T_g and CTE based on procedures described in ISO 11359-2.

3.2.5. Free film fracture surface observation

Free film samples, 3 of each type of coatings were bent to fracture by hand at room temperature. For coating A they are referred to as A1, A2 and A3 for coating, and for coating B they are referred to as B1, B2, and B3. Under bending the largest tensile stress will be on the coating surface, and crack will initiate from that surface. The fracture surface of the hand-broken free films were then sputtered with thin Au/Pd coating and observed under a Philips XL 30 SFEG Scanning Electron Microscopy under a 10 kV accelerating voltage. In addition to the bent free films, the fracture surface of fracture toughness measurement samples were also observed.

3.2.6. Tensile tests of substrates

The tensile tests of the substrate samples were performed at ambient temperature using an INSTRON 5500R screw-driven machine with a 100 kN load cell. Five samples were tested under a cross-head speed of 0.5 mm/min. The strain was recorded using an INSTRON clip-on extensometer with a gauge length of 25 mm. One sample was initially tested to fracture, and then 4 samples were tested to a strain of 3%, which is well below

the ductility of the substrate provided in the manufacturer's data sheet. The surface of the substrate sample within the gauge length during test was also recorded by the Dantec DIC system with an image acquisition rate of 1 frame per second. The load and extensometer strain at each image acquisition were also recorded by the DIC system via 2 analogue channels from the tensile test machine. The strain distribution of the substrate surface was then calculated by ISTRA 4D software. The digital images had 1195 pixels in the vertical direction, and the distances between the cameras and samples were adjusted to contain roughly the central part of the sample with a length of about 36 mm. An example of a pair of digital images of a sample surface is also shown in Figure 22. The strain measurement using DIC had an error of ± 0.02%, and the measurement of displacement using had an error of ± 0.04 mm.

The Young's modulus of each sample was determined based on ASTM E111-04 standard [169], the slope of the linear regression of the stress-strain curve between 0% and 0.15% strain was defined as the modulus.

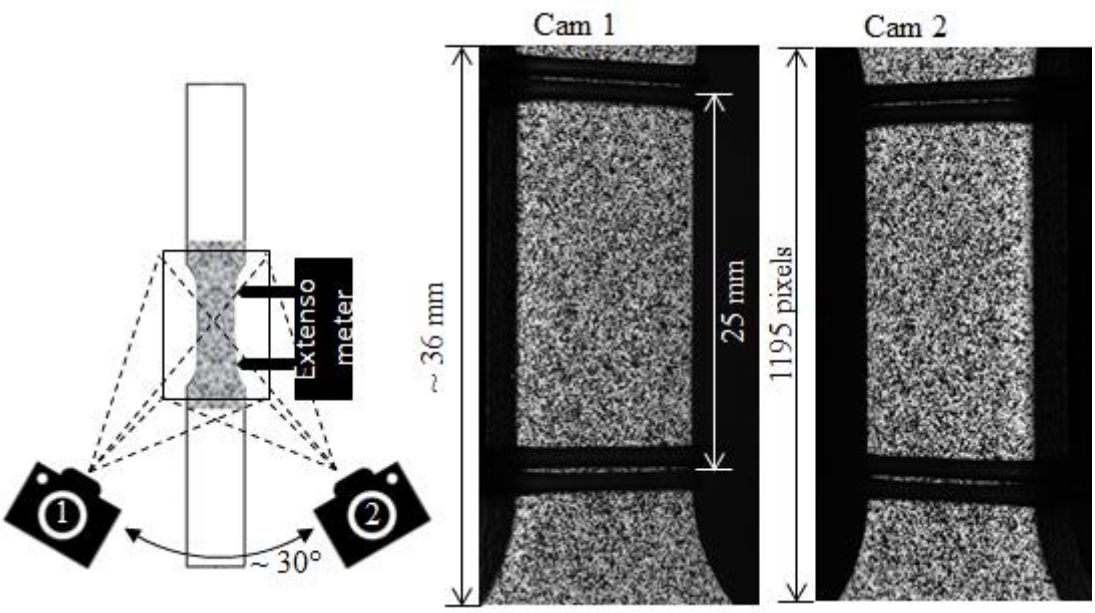

Figure 22. DIC system configuration for the observation of coating fracture on substrate.

3.3. Results

3.3.1. Coating material properties

Tensile properties of free films under tensile stress

The failure of coating free films under static tensile load was unstable, as soon as the ultimate strength or the ultimate strain to failure was reached the sample instantaneously failed completely. Figure 23 shows the typical stress-strain behaviour of coatings A and B in the form of free films at 4 different testing temperatures from -10 to 70 °C. For each temperature, 5 samples were tested. Full sets of free films mechanical properties at these temperatures can be found in Appendix ii.

The stress-strain curves at all temperatures exhibit non-linearity, and the closest to linear stress-strain behaviour occurred in the tests at -10 °C. As the testing temperature increases, the curves tend to be more non-linear. The temperature dependence of coating modulus E_C is shown in Figure 24A, each data point is an averaged value of 5 samples, and the error bar represents the standard deviation. The moduli of coatings A and B were almost equal at temperature below 23 °C, and increased with the reduction of the testing temperature from about 5 GPa at 23 °C to about 6.2 GPa at -10 °C. The moduli of the coatings reduced with the increasing testing temperature, and the modulus reduction of coating B was greater than that of coating A. The modulus of coating A at 70 °C was about 3 GPa, while the modulus of coating B at the same temperature was about 1.7 GPa. The moduli of the free films at 23 °C calculated using the average of 5 samples of each coating are shown in Table 2. In Figure 24, the temperature dependence of the stress to failure and strain to failure of the free films are also shown in B and C. Similar to the modulus, the stress to failure also increased with the decreasing temperature, while the strain to failure increased with the increase of the temperature. At 23 °C, the stress to failure of the free films of coatings A and B was 30 and 17 MPa respectively, while the strain to failure of coatings A and B free films was 0.67% and 0.34% respectively.

The value of each data point is also an average of the values obtained from 5 samples. The figures show that both stress and strain to failure of coating A at almost all testing temperatures are greater than coating B. In general, the stress to failure reduced with increasing temperature, while the strain to failure increased. The stress and strain to failure of 5 free films of each coatings at 23 °C have been averaged and shown in Table 2.

Table 2. Mechanical properties of coatings at 23 °C

	E (GPa)	σ_f (MPa)	ε_f (%)
Coating A	5.2 ± 0.4	29.7 ± 3.0	0.67 ± 0.06
Coating B	5.2 ± 0.4	17.2 ± 2.2	0.34 ± 0.06

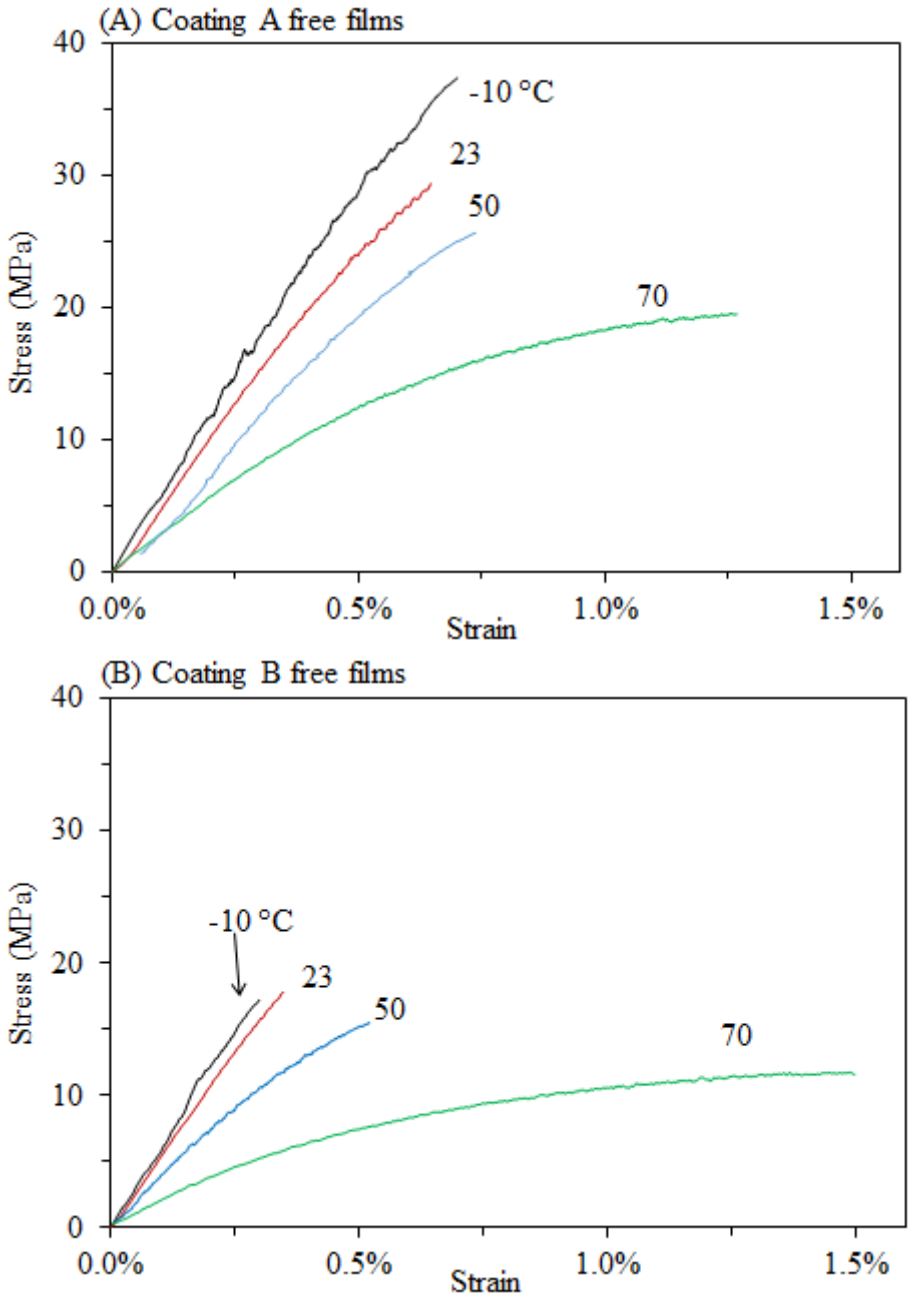

Figure 23. Stress-strain behaviour of the coatings in the form of free films at 4 different testing temperatures. In (A), sample number of each curve at each temperature in the order of increasing temperature: No.3, No.5, No. 3, and No.1; In (B), sample number of each curve at each temperature in the order of increasing temperature: No.3, No.2, No.5, and No.2.

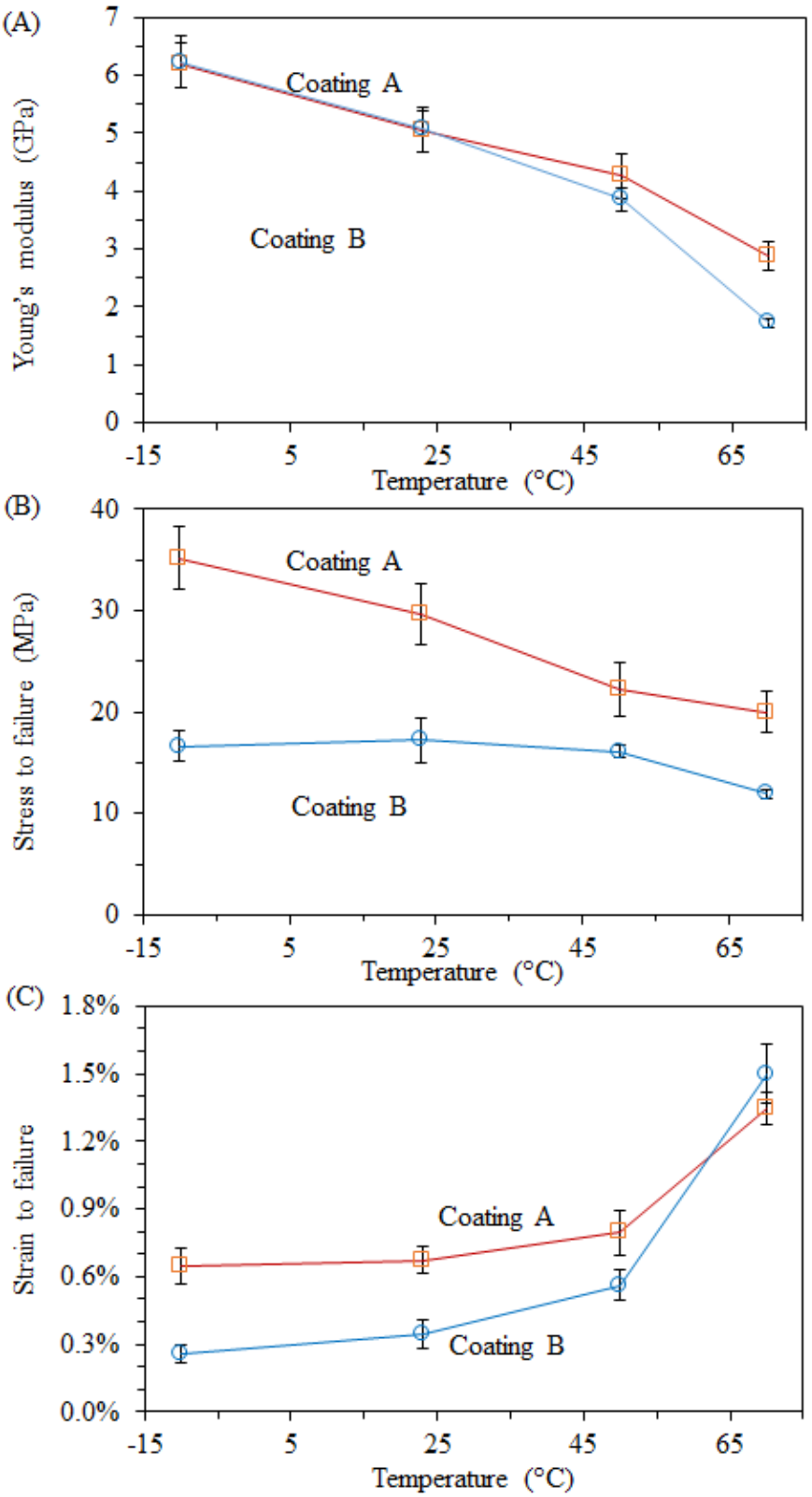

Figure 24. Temperature dependence of (A) Young's modulus, (B) stress to failure, and (C) strain to failure of free films of the coatings.

Fracture toughness of free films at ambient temperature

For each coating, 10 samples with different notch lengths from 1 to 4 mm were tested. Full sets of data including both sample dimensions and fracture loads can be found in Appendix i. The load-displacement relationship of one coating A sample (TA – 1) and one coating B sample (TB – 1), both with two 1 mm long edge notches, is shown in Figure 25 by the solid black lines. The load-displacement relationship of both samples is linear, and the right ends of the plots represent the fracture point. The dashed lines plotted in the figure are the 95% stiffness lines, which was produced based on ASTM D5045 [166] and they do not intersect with the load-displacement plots over the entire displacement ranges. This indicates that during the test neither slow crack growth nor large scale yielding took place before fracture. The loads at fracture were used as load to initiate crack growth (F_Q), which were converted into fracture stresses (σ_f) to calculate a critical stress intensity factors to fracture.

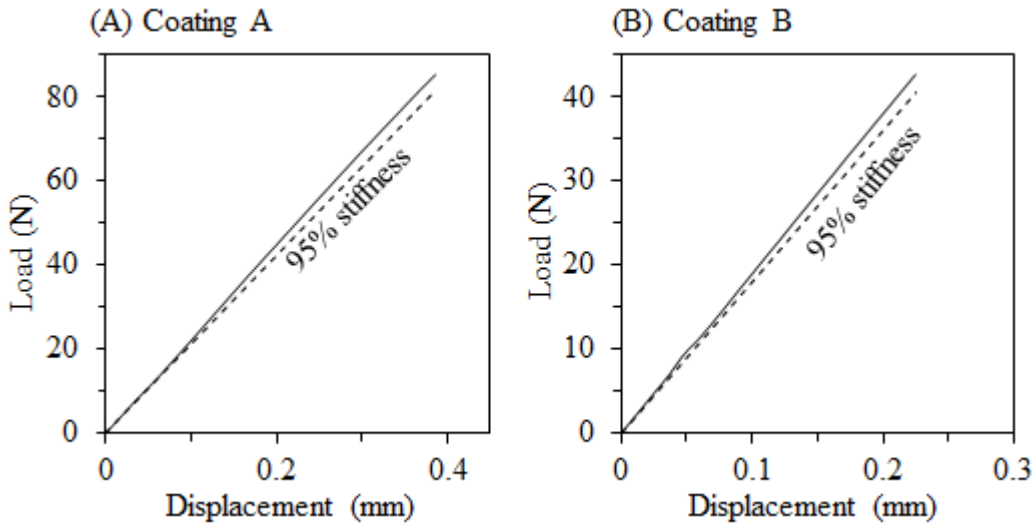

Figure 25. Load-displacement curves of fracture toughness samples with notch depth of about 1 mm for coatings A (TA – 1) and B (TB – 1). The 95% stiffness plots for each sample are also shown.

Table 3. Critical stress intensity factor of the coating free films at ambient temperature (~ 23 °C).

	K_Q $(MPa\sqrt{m})$
Coating A	1.09 ± 0.07
Coating B	0.64 ± 0.05

According to ASTM D5045 [166] standard test methods of fracture toughness of polymers, for the provisional critical stress intensity factor (K_Q) to be a linear elastic plane strain fracture toughness (K_{IC}), the dimensions of the specimen, including thickness (h), notch length (a), and ligament length ($W - 2a$), need to be sufficiently larger than the size of plastic zone, characterized by a length $\bar{r}$, around the crack tip. The yielding stress σ_Y is fracture stress of the un-notched free films [166].

$$\bar{r} = \frac{{K_Q}^2}{\sigma_Y^2} \tag{38}$$

$$h,\ a, \text{ and } (W - 2a) > 2.5 \times \bar{r} \tag{39}$$

The $2.5\bar{r}$ value for both coatings A and B was found to be about 3.4 mm. As the thickness of the samples was only about 0.3 mm, the test samples were closer to be in plane stress. As the nominal width (W) of the samples was 12 mm, for sample with a = 4 mm, the notch length satisfied the criterion, but the ligament length failed to satisfy; while for samples with $a \leq$ 3 mm, the ligament length satisfies the criterion, but the notch length failed satisfy the criterion. Judging from the linear load-displacement lines of the notched samples shown in Figure 25 (page 54), there is very little plasticity. The K_Q can then be considered as a critical stress intensity factor in mode I close to plane stress. For both coatings, a critical strain energy release rate/fracture toughness G_C was deduced from K_Q using equation (14) (page 17). For coatings A and B, the G_C was 228 ± 34 J/m^2 and 79 ± 14 J/m^2 respectively. The errors are standard deviations, which were produced with the consideration of the standard deviations of both K_Q and modulus using the error propagation laws that can be found in a textbook [170].

Poisson's ratio of free films at ambient temperature

The transverse and longitudinal strain distributions of free film samples can be directly obtained from DIC post-processing. For example, Figure 26 shows the distribution of strain in longitudinal (Y) and transverse direction (X) of a coating B free film under a load of 105 N in the longitudinal direction. Within the gauge area the sample has an overall strain of about 0.48% in Y direction, with some of the area of slightly higher strains to about 0.6% maximum; while the overall strain in X direction was about -0.13%. An representative examples of the development of strain in Y and X directions as a function of time of 1 coating B free film sample out of 5 samples in total is shown in Figure 27, which shows that after loading started at about 2 s, the strain in Y direction increases linearly with time, while the strain in X direction decreases linearly.

The Poisson's ratio was determined using equation (37). A representative example of the development of Poisson's ratios as a function of strain in Y direction of a coating A and a coating B free film sample out of 5 samples of each coating are shown in Figure 28. It can be seen that the Poisson's ratios of the free films decreases slightly with an increasing strain. The Poisson's ratio of the free film of each coating was estimated using the average of 5 samples, and it is shown in Table 4.

Table 4. Thermal and thermomechanical properties and Poisson's ratio of coatings and substrate

	ν (at 23 °C)	T_g (°C)	CTE (× 10^{-6})	
			$<T_g$	$>T_g$
Coating A	0.30 ± 0.01	65 ± 3	5.7 ± 0.4	12.4 ± 0.1
Coating B	0.31 ± 0.02	69 ± 2	6.0 ± 0.4	15.0 ± 0.4
Substrate	0.3 [171]	-	1.2 [171]	

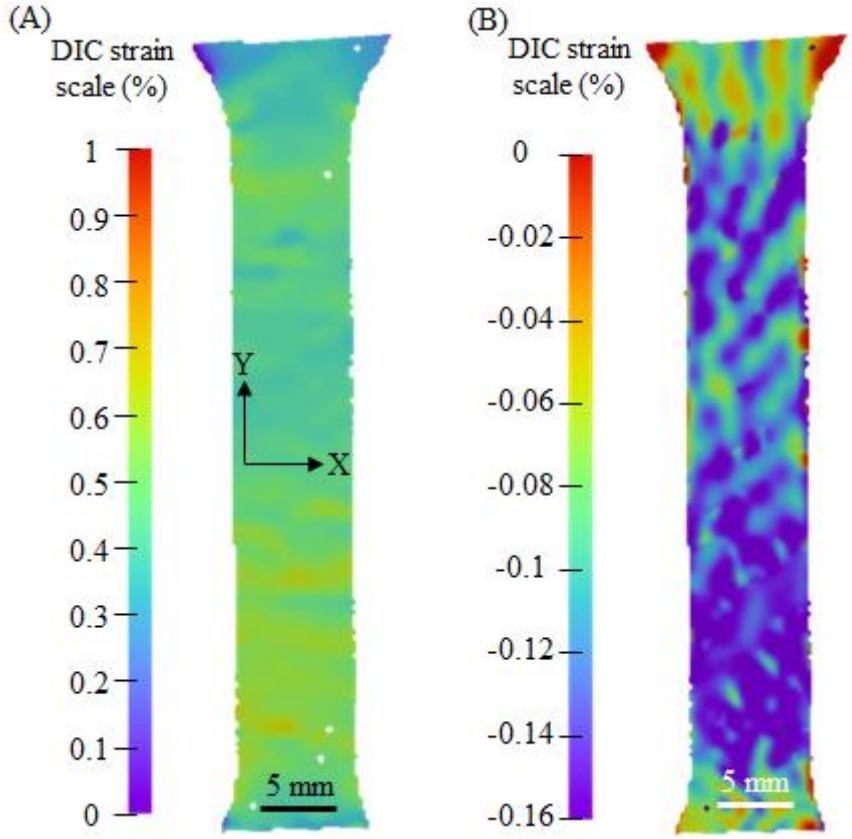

Figure 26. DIC mapping of strain in Y (A) and X (B) direction a coating B free film under a load of 105 N.

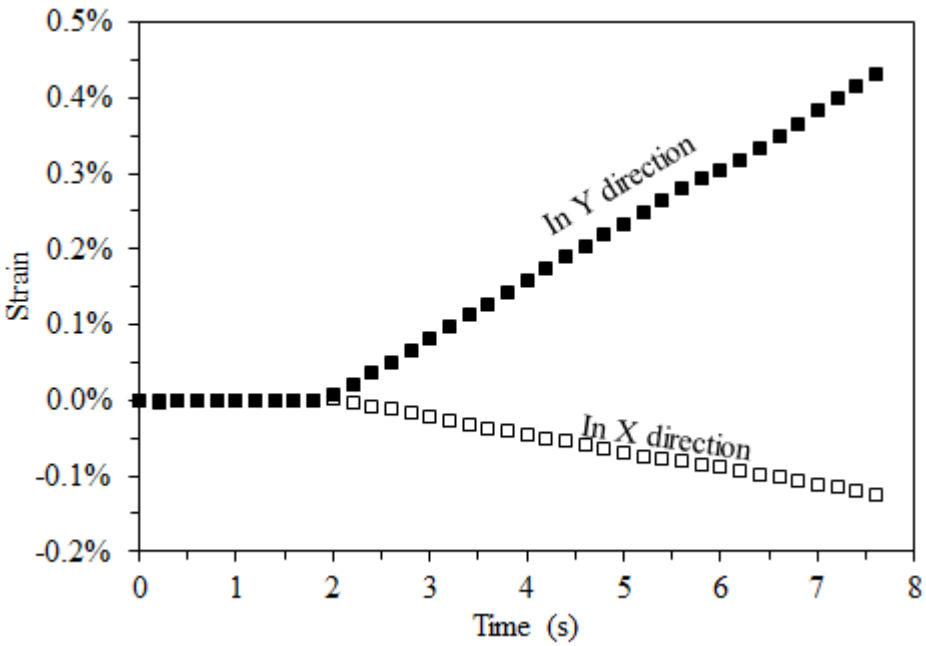

Figure 27. Strain in Y and X direction of a coating B free film as a function of time produced using DIC.

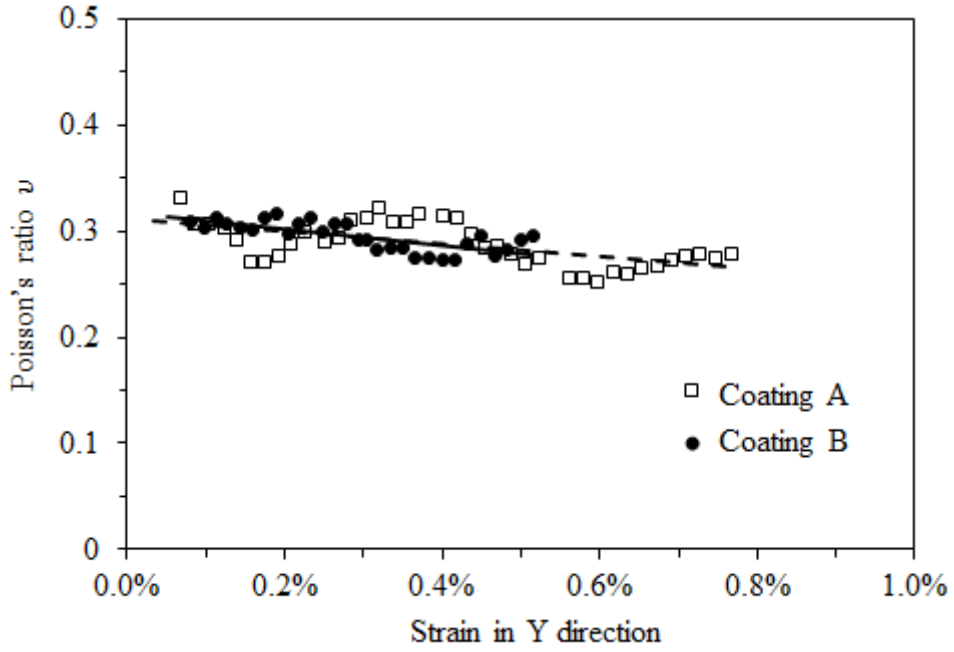

Figure 28. Development of Poisson's ratio of free films as a function strain in Y direction.

Glass transition temperature and thermal expansion coefficient

The thermal properties of the coatings, mainly the glass transition temperature T_g and thermal expansion coefficient CTE were characterised using TMA, which measured the change of sample height $\Delta H'$ as a function of temperature. A typical example of ΔH – temperature plots of the coatings tested within -50 to 150 °C can be found in Figure 29.

For both coatings, the height increases as the temperature increases. Both plots exhibit a transition of the height change, before and after which the height change is linear to the temperature change, and after the transition the slopes of the plots are greater than before the transition. The transition of the plots was due to the glass transition of the materials. As described in ISO 11359-2, the glass transition temperature is measured using the intersect of the linear fits of the plot before and after the transition, and the slopes of the linear fits can be used to calculate the linear thermal expansion coefficient before and after the glass transition using the equation below, in which H'_0 is the original height of the sample at 23 °C.

$$CTE = \frac{Slope}{H'_0} \tag{40}$$

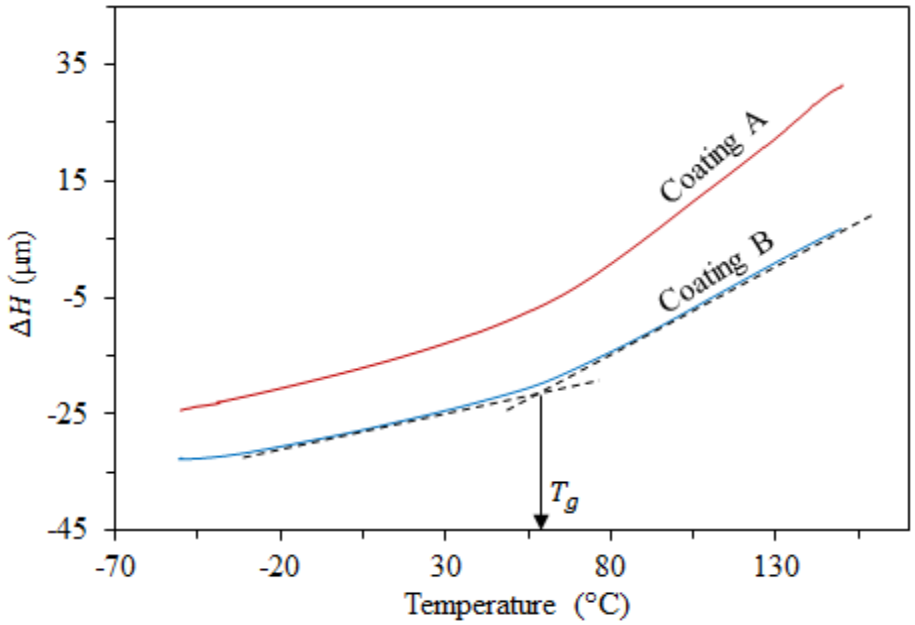

Figure 29. Change of the height ΔH of the TMA samples of the coatings as a function of temperature.

The T_g and CTE were measured from 5 samples for each coating, and the averaged results are shown in Table 4. The CTE of the steels substrated was cited from [171]. Note, the CTEs of the coatings were greater than that of the steel substrate, which means if the coatings were attached the steel substrate, a thermal residual stress will be developed.

Observation of fracture surfaces of free films

Figure 30 shows the fracture surface of a coating A and a coating B free film sample broken by tension. In Figure 30A, lamellar features (indicated by yellow arrows) aligning perpendicular to the plane can be found to be sandwiched by a different phase. These lamellar features had smooth surface, and the gaps between these features and the surrounding phase can be easily seen. In Figure 30B, angular features (indicated by yellow arrows) with sharp edges dispersed in an apparently amorphous phase can be found.

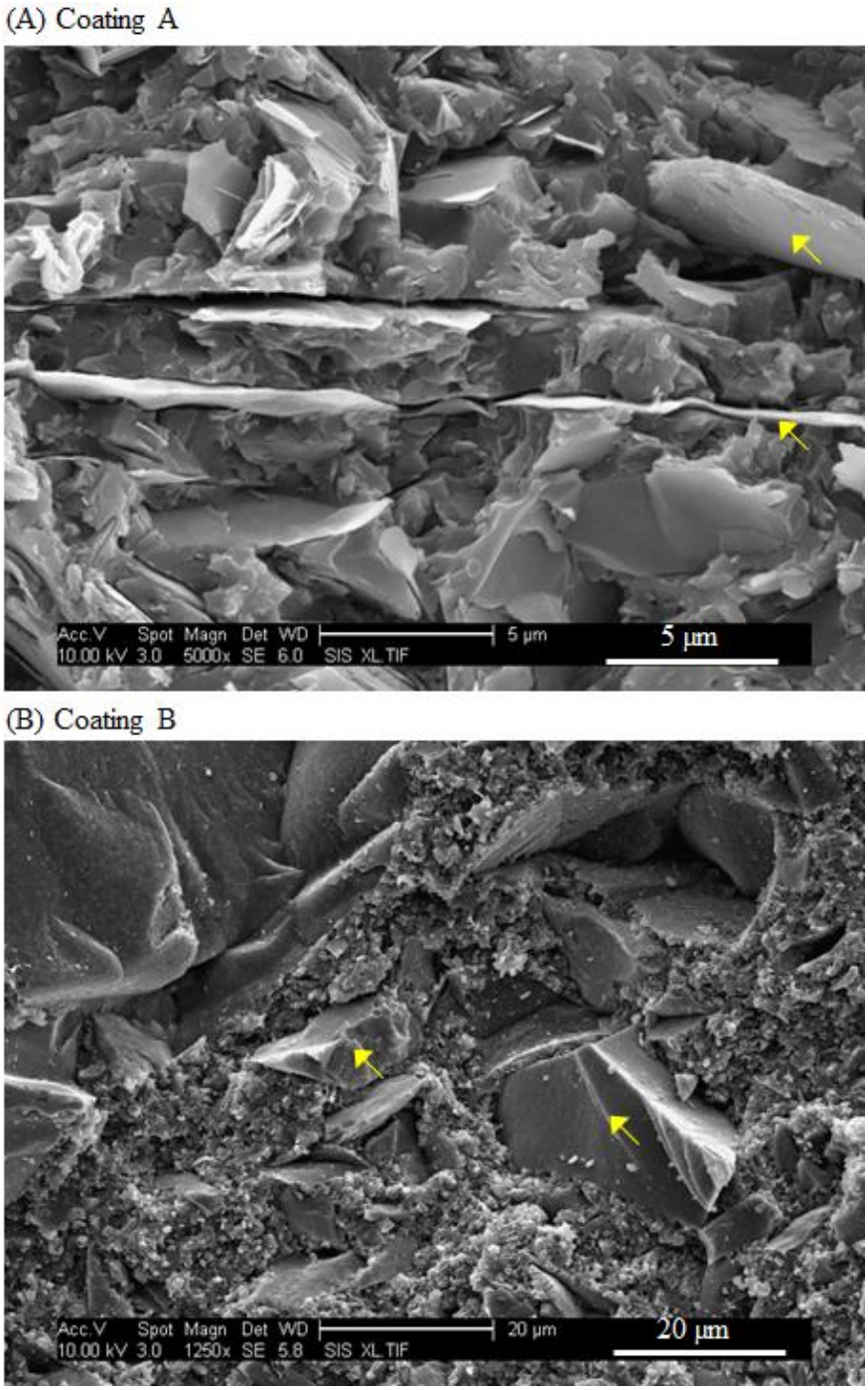

Figure 30. SEM images of fracture surface of coating A and B. (A) coating A sample No.1 tested at 23 °C; (B) coating B sample No.1 tested at 23 °C.

These angular features were also found to have a rather clean surface. The clean surface of the features in both coatings indicate that the bonding between them and the surrounding phases was not optimal as it allowed fracture paths to propagate along the

interface. It is known that these coatings contain large amount of particulate fillers, and these features should be the fillers.

Figure 31 A and B shows the fracture surfaces of two coating A free film samples broken by bending. Surface breaking thumb-nail shape features located on the tensile sides of the samples (see dashed yellow curves) can been seen in both of these figures. The height of the planes of these thumb-nail features appeared to be lower than the surrounding fracture surface plane. The thumb-nail feature in Figure 31A comprised of smaller lamellar features (see yellow arrows) in a common plane, and collectively they defined the origin of the thumb-nail feature. Similarly, the thumb-nail feature in Figure 31B contained one large lamellar feature (see yellow arrow) with clean surface, which aligned roughly in the plane of the fracture surface.

Figure 32 A and B shows the fracture surfaces of two coating B free film samples broken by bending. Similar to coating A, surface breaking thumb-nail shaped features (see yellow dashed lines) comprised of smaller features with clean surface (see yellow arrows) were also found in these samples. Within these features, smaller features (> 50 μm) were found to align almost perpendicular to the surface and either merge or be close to the surface, see arrowed features in Figure 31 and Figure 32. Such particles in coating A have their plane almost in parallel to the fracture surface. These features were widely observed in all manually bent samples. In coating B samples, voids with smooth surface area were also found (see blue arrows in Figure 32). In comparison to the angular-shaped particles, the effect of the voids on crack initiation will be benign, thus should not be crack initiating source with the presence of the angular particles.

A closer view of these small features (indicated by small arrows) can be found in Figure 33. Figure 33A shows two of such features each with a size of about 50 μm closely positioned, and the top one merges with the coating surface. Figure 33B shows a feature which seems to be the imprint of a large angular particle with a depth of about 60 μm from the surface. In a situation where the interface between the particle and resin fails by a small energy, the de-bonded interface may act as crack initiation sites. The sizes of

such particles in each coating were measured. The average of 10 measurements in coating A and B was 60 ± 8 μm and 70 ± 17 μm respectively.

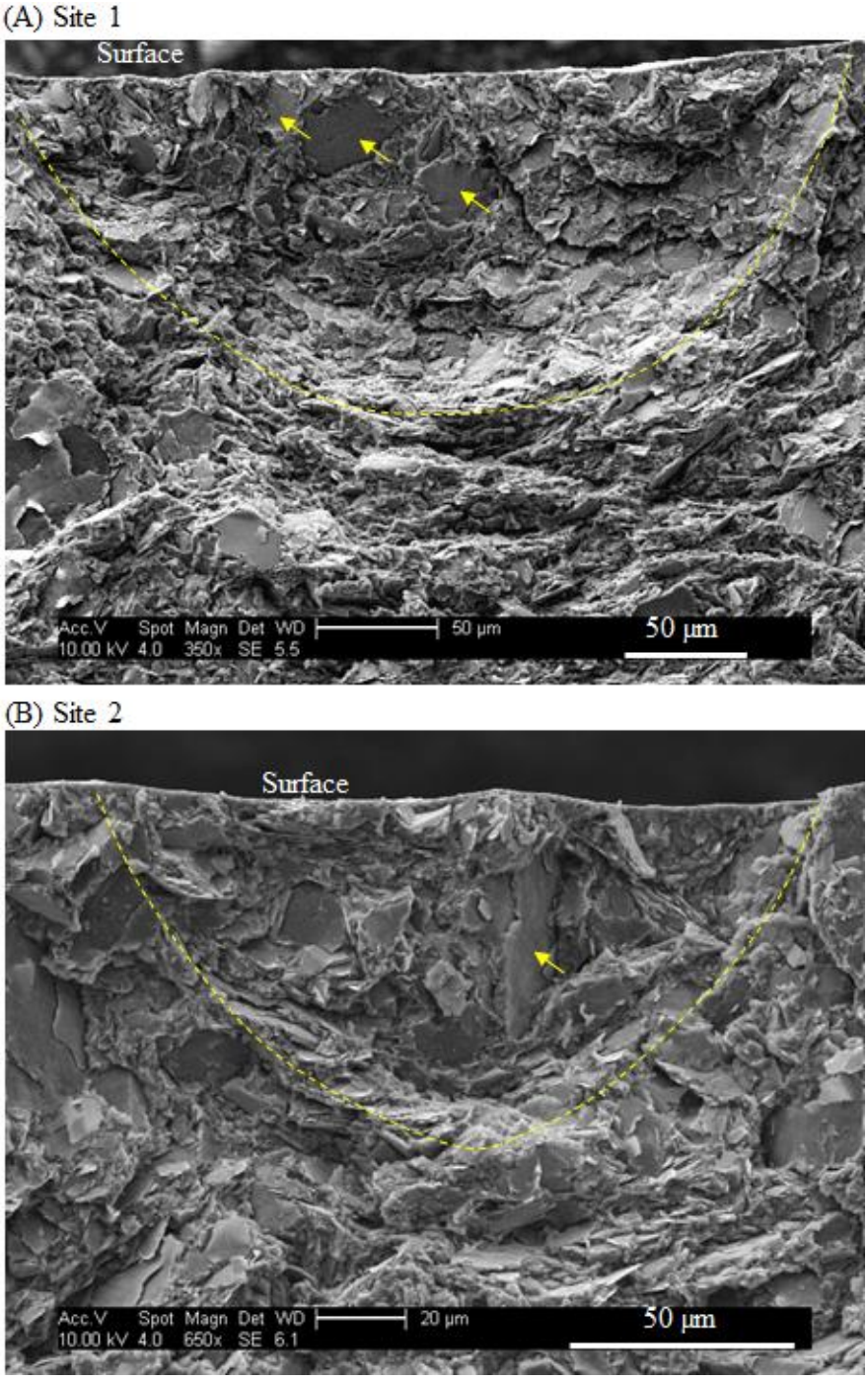

Figure 31. Fracture surface of coating A free films broken by manually bending. The images show the areas beneath the surfaces under tension. (A) Manually bent sample A1; (B) Manually bent sample A2.

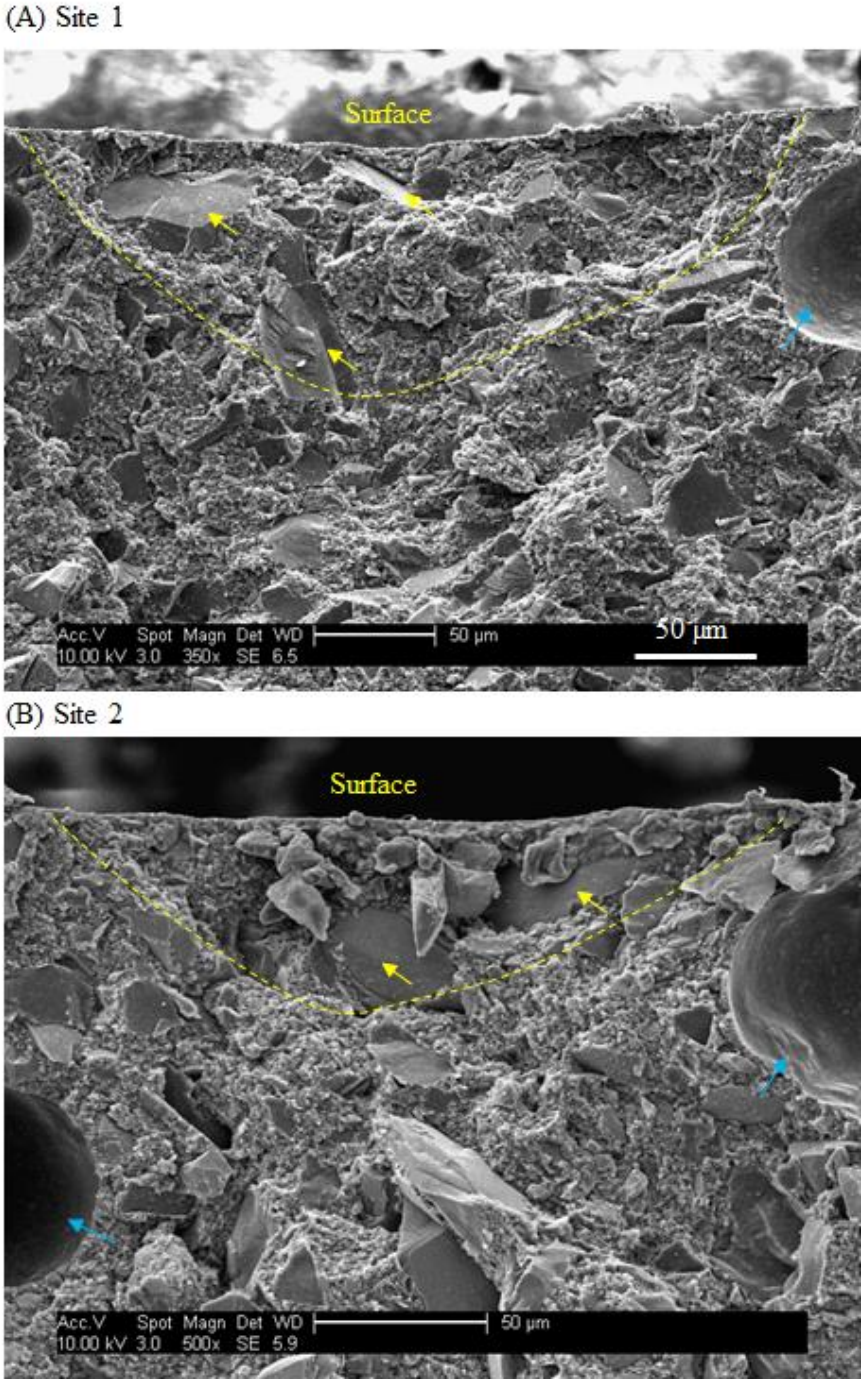

Figure 32. Fracture surface of coating B free films broken by manually bending. The images show the areas beneath the surfaces under tension. (A) Manually bent sample B1; (B) Manually bent sample B2.

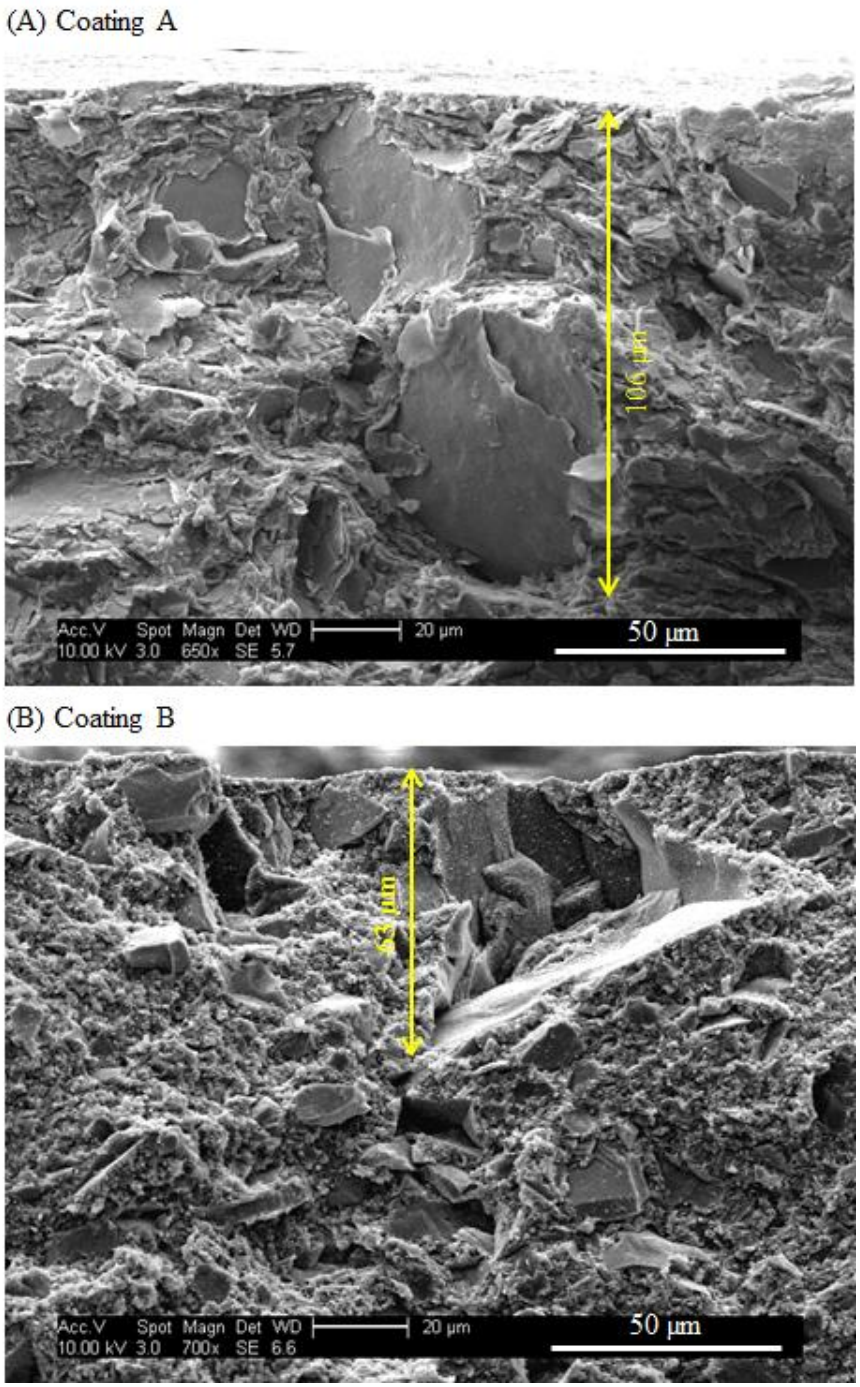

Figure 33. SEM images of the fracture surface of free films of each coating broken by manual bending. The images show the areas beneath the surfaces under tension. (A) Manually bent sample A3; (B) Manually bent sample B3.

3.3.2. Stress-strain behaviour of substrate

The stress-strain behaviour of the steel substrate sample tested to failure is shown in Figure 34. The substrate exhibited a sharp yielding at a stress of about 420 MPa, an ultimate tensile strength of about 560 MPa, and a strain to fracture of about 45%, which satisfied the minimum values supplied by the manufacturer. After yielding at about a strain of 0.2%, the deformation continued at a constant stress of about 400 MPa until a strain of 1.7%, after which the work hardening commenced. The modulus of the substrate was determined by the linear fit of the stress-strain curve from 0 to 1.5% strain. The averaged modulus based on 5 samples was 200 ± 12 GPa.

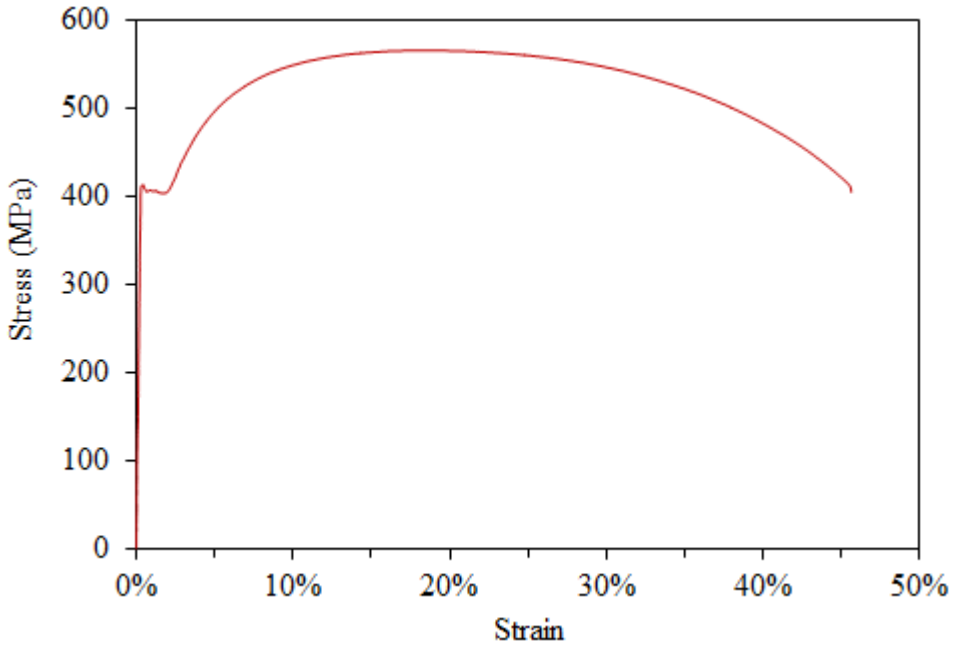

Figure 34. Stress-strain curve of substrate material.

The strain distribution in the samples between yielding and the start of work hardening was revealed using DIC. As an example of 5 samples tested, Figure 35 shows the typical surface strain distribution from extensometer strain of 0.7 to 1.7% of a substrate sample. In the figure, the extensometer strain of each frame is shown on the top. The white spots shown in the frames are the locations where the DIC system failed

to analyse due to large speckle dots, and considering the small number of such spots, the results are still good to represent the overall trend.

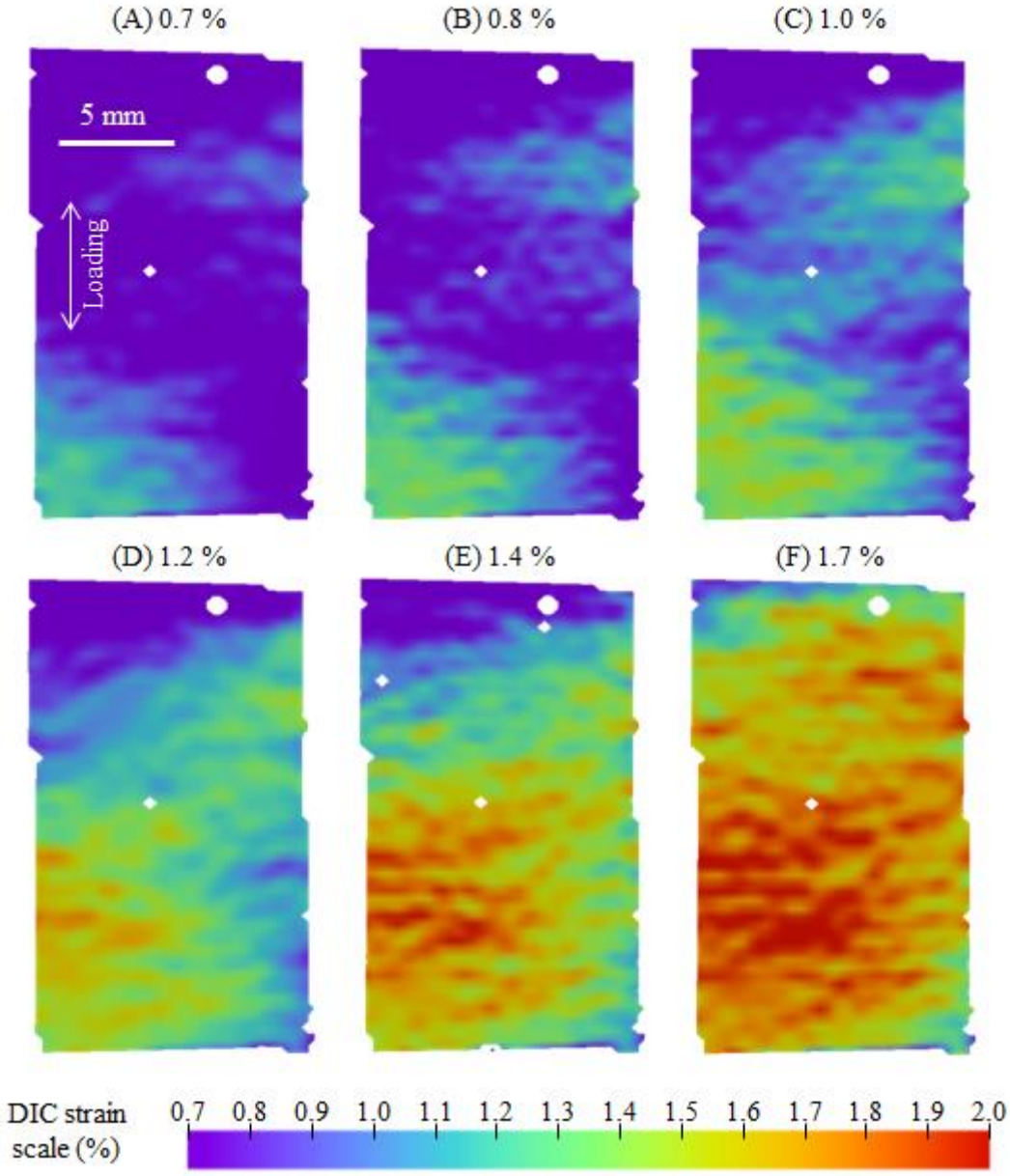

Figure 35. The distribution of strain in loading direction of a substrate sample (sample No.1) at extensometer strains from 0.7 to 1.7%.

As Figure 35 shows, at 0.7% extensometer strain the substrate developed high strain regions with greater local strains of about 1.2%. As the extensometer strain increases, the regions expanded, and gradually covered the most of the surface at an extensometer

strain of 1.7%. During this period, the local strains within the high strain regions were up to 0.3 to 0.5% greater than the extensometer strain of each frame. Some regions outside of the regions remained 0.7% or below, while the high strain regions achieved local strains in excess of 2% at extensometer strains from 1.4 to 1.7%. This high strain region is likely to be Lüder's band [170], the DIC results revealed the expansion of the band with increasing strain. For a coating attached on the surface of this type of substrate, the coating will have strains imposed by the substrate deformation, thus it is expected that this uneven deformation process of substrate could affect the fracture behaviour of the coating.

A group of 5 substrate samples were pre-strained to 3% strain, and the tests were repeated and the results are also shown here. To distinguish between the pre-strained substrates, the substrates without pre-straining are referred to as original substrates. Figure 36 shows the typical stress-strain curves of substrates in the pre-strained condition to a maximum strain of 3%. In the same figure the stress-strain curve of the original substrate is also shown for comparison.

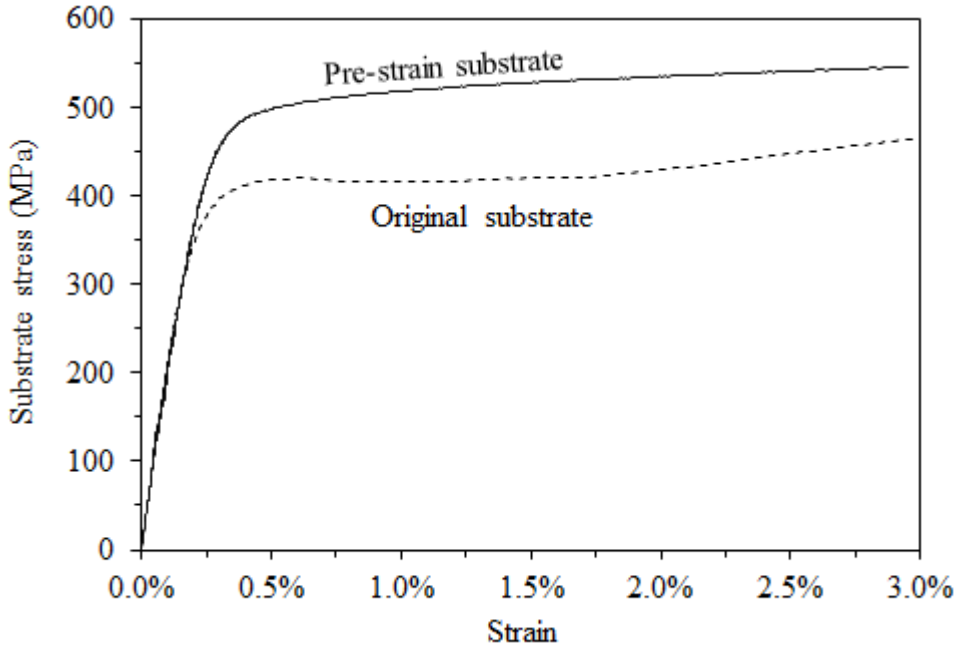

Figure 36. Stress-strain curves of substrate in the original and 3% pre-strained conditions up to 3% of strain.

The pre-strained substrate yielded at a greater stress of about 500 MPa, and work hardening commenced immediately afterwards. This means the post yielding deformation with reduced stress was completely eliminated by pre-straining. The strain distribution of the pre-strained substrates also differed from that of the original substrates. Figure 37 shows the typical surface strain distribution from extensometer strain of 0.7 to 1.7% of a pre-strained substrate sample. In the figure, the extensometer strain of each frame is shown on the top.

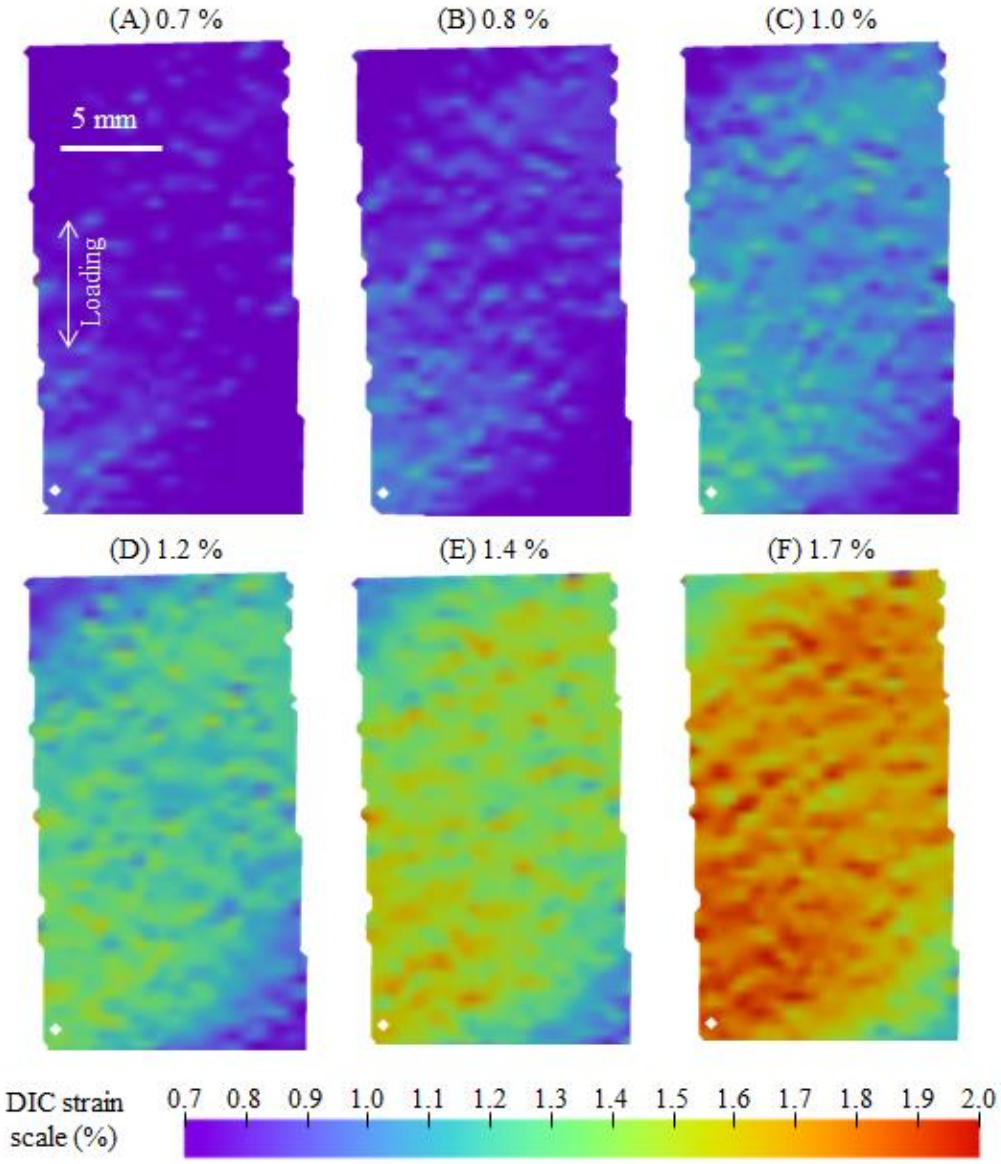

Figure 37. The distribution of strain in loading direction of a pre-strained substrate sample at extensometer strains from 0.7 to 1.7%.

In contrast to the original substrates, the deformation behaviour of the pre-strained substrate was uniform across the entire gauge length, and the extensometer strains were close to the local strains indicated by DIC. This means that the uneven deformation of the original substrate was completely consumed by pre-straining. The difference in the strain distribution of substrates in the original and pre-strained states was found to have an effect on the fracture behaviour of coatings under static strains, of which the details will be presented in the next chapter.

4. TENSILE AND FATIGUE BEHAVIOUR OF SUBSTRATED COATINGS

As mentioned previously in Chapter 1, the failure of WBT coatings in service is mainly caused by thermal stresses. Considering that thermal cycling test of WBT coatings normally takes weeks or even months to perform, and the results are usually qualitative, in this work mechanical strains were applied to substrated coatings by mechanically straining the substrates. The purpose of this was to simulate thermal stresses in service using mechanical stresses. The advantage of using mechanical strain is that the environment of the test is isothermal, where the coating properties would stay constant throughout the tests. However, mechanical tests of substrated coatings introduces large substrate deformation that exceeds the elastic limits of the substrate, which is not the same as the thermal stresses in service condition. This section details the test samples and procedures adopted, as well as the resultant substrated coating failure behaviour under static and cyclic strains. Whether or not mechanical strain is a good substitute for thermal strain that WBT coatings experience in service will be discussed later.

It is important to mention here that thermal residual stress developed in both substrated coating samples for static tensile and fatigue tests due to the temperature reduction after curing. Thus, the initial stress prior to the test inside the coating samples was non-zero. The thermal residual stresses of the substrated coatings at ambient temperature (~ 23 °C) were also measured. The details will also be described first in this chapter. After that the tensile and fatigue tests of substrated coatings as well as the results will be described in detail.

4.1. Measurement of Thermal Residual Stress and Results

4.1.1. Materials and sample manufacture

Thermal stress as one of the internal stresses in coatings can be measured using bi-layer strips consists of a coating layer and a substrate layer. Coating/steel bi-layer strip samples were prepared at International Paint for the measurement of thermal residual stresses of coatings A and B. Steel shims with a length of 267 mm and a width of 12.5 mm

were used as the substrate of the bi-layer strips. Before coatings were sprayed onto the shims, the surface of the shims was roughened by sand paper. For each coating, 3 samples were manufactured. The average coating thickness of coating A samples was 0.24 ± 0.05 mm, and the average coating thickness of coating B samples was 0.29 ± 0.01 mm. The average thickness of the shims of all 6 samples was 0.21 ± 0.003 mm. The errors are standard deviation. A photo of these samples can be seen in Figure 38. These samples were cured at ambient temperature for 7 days, followed by post-curing at 100 °C for 2 days. After curing, thermal residual stress developed, and caused the deflection of the samples, which can be easily noticed in Figure 38.

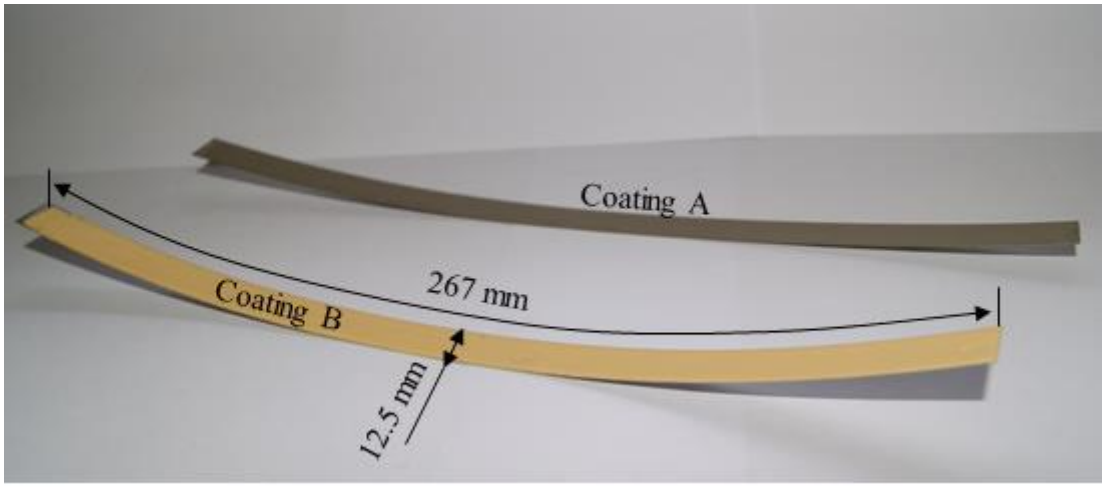

Figure 38. Bi-layer strips of Coatings A and B for thermal residual stress measurement.

4.1.2. Test procedures

To measure the thermal residual stresses, the coating/steel bi-layer strip samples of both coatings were reheated to 100 °C first in an oven for 1 hour. After that the samples were removed from the oven and placed on a flat desk to cool down at ambient temperature for 15 minutes. Due to the development of thermal residual stress, these samples deflected towards the coating side. The deflected samples were then placed on a HP commercial office scanner, and the longitudinal sides were scanned, see Figure 39. The deflection of the samples was determined optically with image processing software

ImageJ. An example of the scanned images can be found in Figure 40. A 1 pound GBP coin (22.5 mm in diameter) was scanned at the same time with the samples as reference.

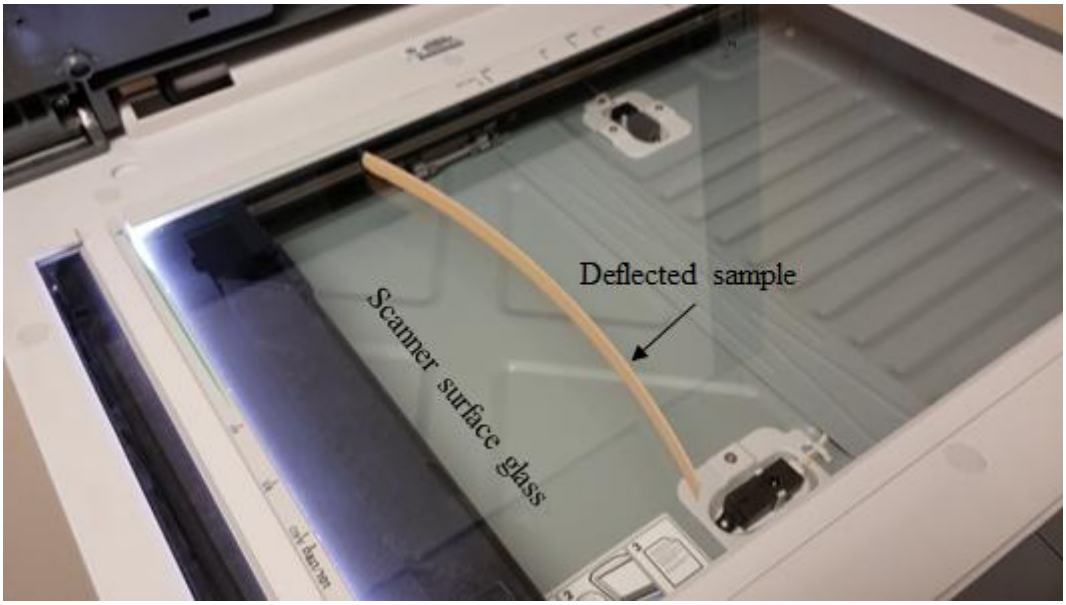

Figure 39. A deflected coating B bi-layer strip sample standing on the longitudinal side on a scanner.

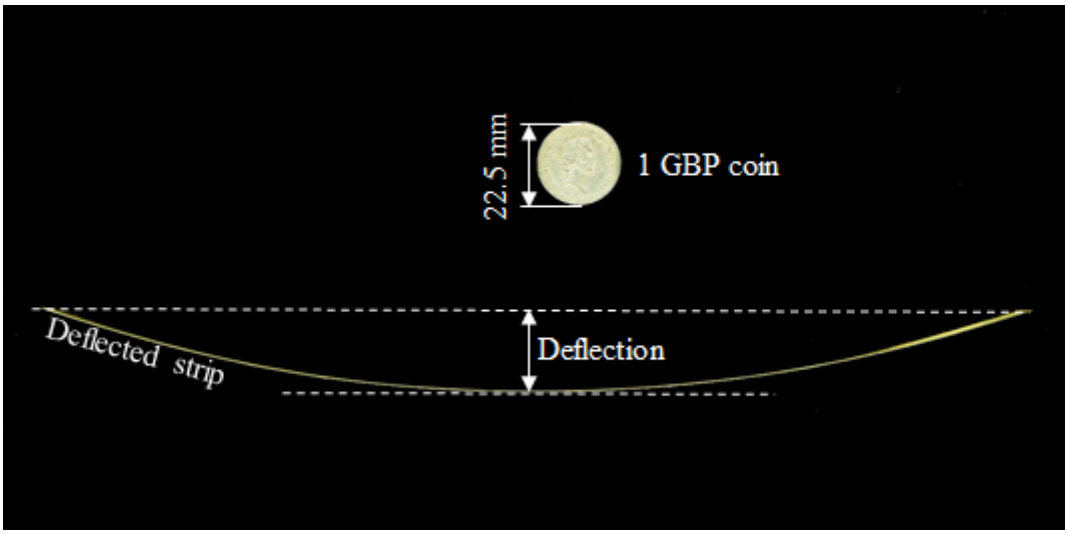

Figure 40. Scanned image of a deflected bi-layer strip with coating B at ambient temperature.

The ends of the deflected sample served as a reference level, see the long dashed line. A parallel line was then used to meet the tangent point of the strip that had the longest distance from the long dashed line, see the short dashed line. The distance between these two parallel lines was used as the deflection of the sample. The thermal

residual stress of each test sample was calculated using equations (2) to (4) incorporating the measured deflection, coating modulus, and thicknesses of the coating and steel shim.

4.1.3. Results

The results including the measured deflection as well as the calculated thermal stresses are shown in Table 5. Both coatings developed tensile residual stresses, about 11 MPa and 14 MPa for coatings A and B respectively. Note the thermal residual stress calculated using equations (2) to (4) represent the stress in the coatings as if the samples were forced to return to a non-deflected state. In other words, the thermal stresses shown in Table 5 represent the thermal stresses in the coatings in thick non-deflecting substrates such those used in the current work.

Table 5. Deflections and thermal residual stresses and strains of coatings A and B at ambient temperature caused by a temperature reduction of about 77 °C. The modulus of both coatings at ambient temperature was 5.2 GPa.

Coating type	Sample number	Thickness (mm)		Deflection (mm)	Coating thermal residual stress on non-deflected substrate (MPa)	Coating thermal residual strain (%)
		Coating	Substrate			
A	1	0.187	0.205	13.60	11.43	0.15
	2	0.234	0.210	16.40	11.04	0.15
	3	0.285	0.210	18.01	10.31	0.14
			Average	16.00	10.93	0.15
			Standard Deviation	2.23	0.57	0.01
Coating type	Sample number	Thickness (mm)		Deflection (mm)	Coating Thermal stress on non-deflected substrate (MPa)	Strain (%)
		Coating	Substrate			
B	1	0.272	0.214	27.52	15.55	0.21
	2	0.291	0.205	24.82	13.35	0.18
	3	0.295	0.212	26.00	13.85	0.19
			Average	26.11	14.25	0.19
			Standard Deviation	1.35	1.15	0.02

In Table 5, the coating thermal residual strain is defined as the strain generated by the part of coating volumetric shrinkage constrained by the substrate. This strain is also equivalent to the thermal strain mentioned throughout this work. It can be calculated by dividing the thermal stress by the biaxial modulus $E/(1-\nu)$, here, E and ν are the Young's modulus and Possion's ratio of the coatings, which can be found in Table 2. This results indicates that before the substrated coating samples were even tested, they have already developed 0.15% and 0.19% equivalent mechanical strain in coatings A and B respectively.

4.2. Mechanical test samples and procedures

4.2.1. Sample manufacture

Substrated coating tensile test samples

For the substrated coating tensile test samples, coating materials were sprayed on steel substrates with the dimensions shown in Figure 20 in the last chapter. Considering the uneven deformation of the substrate in the original state, some substrates were pre-strained to 3% strain in the longitudinal direction, of which the purpose was to fully consume the uneven deformation after yielding. Here the substrates which did not undergo pre-straining will be referred to as original substrates.

Prior to spraying, the surface of the substrates was shot-blasted to Sa2.5 standard [172] in order to cleanse the surface and enhance adhesion. The coating materials were sprayed onto one side of substrate at International Paint. The thickness was controlled by the same way for the free film spraying mentioned earlier, see 3.1.1 in page 41. The nominal thickness of the substrated films was 300 μm. The samples were initially cured at room temperature for 7 days and then post-cured at 100 °C for 2 days.

Substrated coating fatigue test samples

For the substrated coating fatigue test samples, fatigue substrates were designed based on ASTM E606 [173] standard, and the dimensions are shown in Figure 41. The spraying of coatings was also performed at International Paint following the same procedures to prepare the substrated coating samples for static tensile tests. Some fatigue test substrates were also pre-strained to 3% strain, and they were coated only with coating B. The curing programme of all fatigue test samples was also the same as the substrated tensile samples.

Including the substrated tensile test samples, the actual coating thickness after curing was measured at International Paint using a coating thickness gauge with an accuracy of ± 2.5 μm. Despite substrate geometry, the average thickness of 50 coating A samples was 300 ± 30 μm, and the average thickness of 50 coating B samples was 350 ± 30 μm, the errors are the standard deviation for the set of measurements. Also including the substrated tensile samples, before testing, all samples were reheated at 100 °C for 30 min in order to eliminate any property change due to physical ageing. All samples were then tested within 6 hours after reheating.

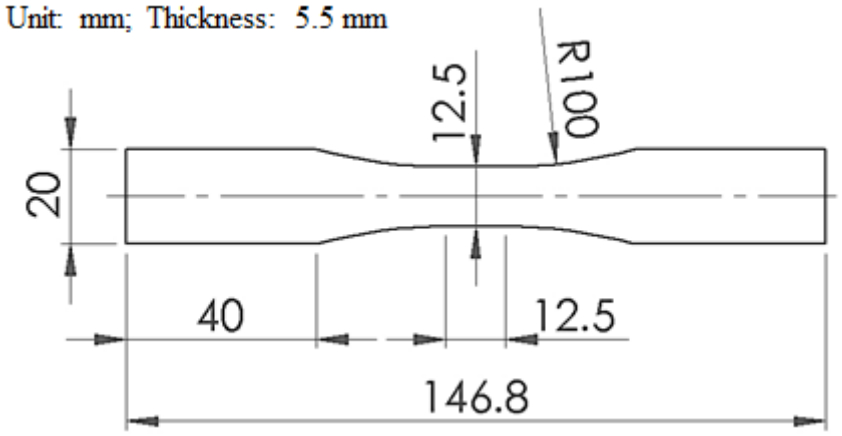

Figure 41. The dimensions of coating fatigue test substrates

4.2.2. Test Procedures

Tensile tests

The substrated coating tensile test samples were tested using the same test setup as the tensile tests of substrates shown in section 3.2.6. The tests were run at a crosshead speed of 0.5 mm/min to a strain of 3% monitored by a clip-on extensometer with a gauge length of 25 mm on the side of the samples, see Figure 22 in page 49. The coating side of the samples were covered by a thin layer (<<0.3 mm) of white primer paint finely speckled with black paint on the top. During each test, the coating side was monitored by a Dantec Digital Image Correlation (DIC) system, which then identified coating cracking in post processing. The DIC system configuration was also the same as that described in section 3.2.6.

In total, 5 samples of each coating with pre-strained substrate and 3 samples of each coating with original substrate were tested. Among all the samples, 2 coating A samples, one with pre-strained substrate and the other with original substrate, and 2 coating B samples, one with pre-strained substrate and the other with original substrate, had the substrate sides recorded simultaneously by another identical DIC system. For these samples, the strain distributions of both coating and substrate sides were compared. In addition to all of these, another coating B sample on pre-strained substrate was tested and the test was terminated at 0.85% strain. The DIC analysed strain distribution of this sample was compared to the surface cracking feature. This was used to find out the strain distribution that is characteristic of a coating crack.

The details of coating crack detection will be introduced in the result section. After tests, 2 samples of each coating were cross-section along the longitudinal direction using an automatic precision saw. The cross-sectioned samples were then potted in clear epoxy resin. The cross-section surfaces were polished then observed under an optical microscope.

Fatigue Tests

The substrated coating fatigue test samples were tested using a servo-hydraulic machine with a load cell of ± 50 kN capacity. The machine was controlled by an INSTRON 8500+ controller. The tests were run under strain control using a dynamic INSTRON clip-on extensometer with a gauge length of 10 mm. The samples of both coatings were tested under both fully-reversed cycles (R = $\varepsilon_{min}/\varepsilon_{max}$ = -1) and zero-tension cycles (R = 0) with a series of selected strain ranges. A full testing matrix for coating A and coating B samples can be found in Tables 6 and 7 repectively.

Table 6. Coating A fatigue test matrix

Sample type and R ratio	Sample label	Strain range (%)	Total number of sample tested
Coating A $\boldsymbol{R}$ = -1	FFA – 1	-0.45 ~ +0.45	7
	FFA – 2	-0.45 ~ +0.45	
	FFA – 3	-0.5 ~ +0.5	
	FFA – 4	-0.5 ~ +0.5	
	FFA – 5	-0.5 ~ +0.5	
	FFA – 6	-0.55 ~ +0.55	
	FFA – 7	-0.6 ~ +0.6	
Coating A $\boldsymbol{R}$ = 0	FTA – 1	0 ~ 0.80	8
	FTA – 2	0 ~ 0.85	
	FTA – 3	0 ~ 0.90	
	FTA – 4	0 ~ 1.00	
	FTA – 5	0 ~ 1.00	
	FTA – 6	0 ~ 1.05	
	FTA – 7	0 ~ 1.05	
	FTA – 8	0 ~ 1.10	

Table 7. Coating B fatigue test matrix

Sample type and R ratio	Sample label	Strain range (%)	Number of sample tested
Coating B R = -1	FFB – 1	-0.16 ~ 0.16	12
	FFB – 2	-0.2 ~ 0.2	
	FFB – 3	-0.22 ~ 0.22	
	FFB – 4	-0.23 ~ 0.23	
	FFB – 5	-0.24 ~ 0.24	
	FFB – 6	-0.24 ~ 0.24	
	FFB – 7	-0.25 ~ 0.25	
	FFB – 8	-0.25 ~ 0.25	
	FFB – 9	-0.30 ~ 0.30	
	FFB – 10	-0.32 ~ 0.32	
	FFB – 11	-0.35 ~ 0.35	
	FFB – 12	-0.45 ~ 0.45	
Coating B R = 0	FTB – 1	0 ~ 0.40	9
	FTB – 2	0 ~ 0.425	
	FTB – 3	0 ~ 0.425	
	FTB – 4	0 ~ 0.45	
	FTB – 5	0 ~ 0.45	
	FTB – 6	0 ~ 0.48	
	FTB – 7	0 ~ 0.48	
	FTB – 8	0 ~ 0.50	
	FTB – 9	0 ~ 0.58	
Coating B on pre-strained substrate R = 0	FTBP – 1	0 ~ 0.40	6
	FTBP – 2	0 ~ 0.40	
	FTBP – 3	0 ~ 0.50	
	FTBP – 4	0 ~ 0.50	
	FTBP – 5	0 ~ 0.55	
	FTBP – 6	0 ~ 0.60	

The test frequencies varied from 0.5 to 3 Hz depending on the strain amplitude. At small strain amplitudes, higher frequencies were adopted, and vice versa. The

temperature at the coating surface of some samples were monitored using a thermocouple, it was found that at greater testing frequencies or strain amplitudes the temperature was slightly greater than ambient with a maximum 2 °C increase. This means the effect of temperature change on the coatings during the fatigue tests can be ignored as the small temperature variation would not introduce coating property changes.

The load and corresponding strain were recorded using a National Instrument data acquisition device with a recording rate of 1000 data points per second. The data was later used to produce the hysteresis loops and cyclic stress-strain curves of the substrates. The development of surface cracks were recorded at various cycle intervals from 10 to 5000 by a Microset RT101 surface replication compound, and the cracking development was then measured using optical microscopy with a measuring error of ± 2μm (standard deviation from 10 measurements of standard length references). For each surface feature recording to be taken, the tests had to be paused at the mean strain, and then the surface replication compound was applied and cured for 5 minutes. After that, cycling was resumed. The surface replicas were observed under an optical microscope, and the crack lengths were measured, of which the details will be described in the results.

4.3. Results of Tensile Testing of Substrated Coatings

4.3.1. Fracture process

As the load bearing capacity of the coatings was almost negligible compared to the substrate, the stress in the coatings and its changes due to coating cracking during the tests were not able to be measured. The behaviour of the coatings were characterised in terms of the overall strain measured by extensometer, and locally in terms of DIC strain distribution. In all the measurements, coating cracks initially were detected as the extensometer strain reached a critical value. Coating cracks were found to align perpendicular to the load axis and grew in both length and number as the extensometer strain increased. An example of crack development with increasing extensometer strain

is given for a coating B sample with a pre-strained substrate under extension to an extensometer strain of 0.85%, see Figure 42, in which the extensometer strains are indicated at the top of each image.

Images A to E in Figure 42 were produced using the DIC system and show the development of high strain bands with increasing extensometer strain. These high strain bands had local strains greater than 2% in the centre, and about 1% at the ends. On either side of each high strain band are regions roughly 0.5 mm wide, which had strains less than 0.6%, the smallest in the contour shown and even smaller than the extensometer strain. Image F is a photograph of the actual surface the same area at the same extensometer strain (0.85%) as image E. Coating cracks, features enhanced by blue ink, were in image F. The close correspondence of cracks and DIC high strain pattern can be seen, which provided evidence that the high strain bands observed by DIC were indication of surface cracks.

In reality, a crack does not really possess any strain, but a big displacement given by the opening of the crack. As DIC interpreted such crack opening as displacement on the surface, the high strain bands were produced. It is important to bear in mind that the high strains shown at the cracks are not “true”, and only served as an indication of crack opening. For this sample the first crack initiation was observed at 0.68% of extensometer strain, and as the strain increased the length and number of the cracks increased, and eventually grew into a multiple crack pattern. Similar crack development of coating A up to an extensometer strain of 1.6% and 1.7% can be found in Figure 43 and Figure 44. It is worth noting here that the images show a progressive, rather than unstable, crack growth in the coatings on substrate under increasing static tensile strains. In other words, the cracks did not propagate across the entire length of the sample immediately after initiation.

4.3.2. Coating crack pattern on different substrate types

The DIC strain distribution mapping also revealed the difference between the distribution of coating cracks in coatings on the original and pre-strained substrates. Figure 43 and Figure 44 also show the development of coating cracks in increasing extensometer strain of coatings on an original and a pre-strained substrate respectively.

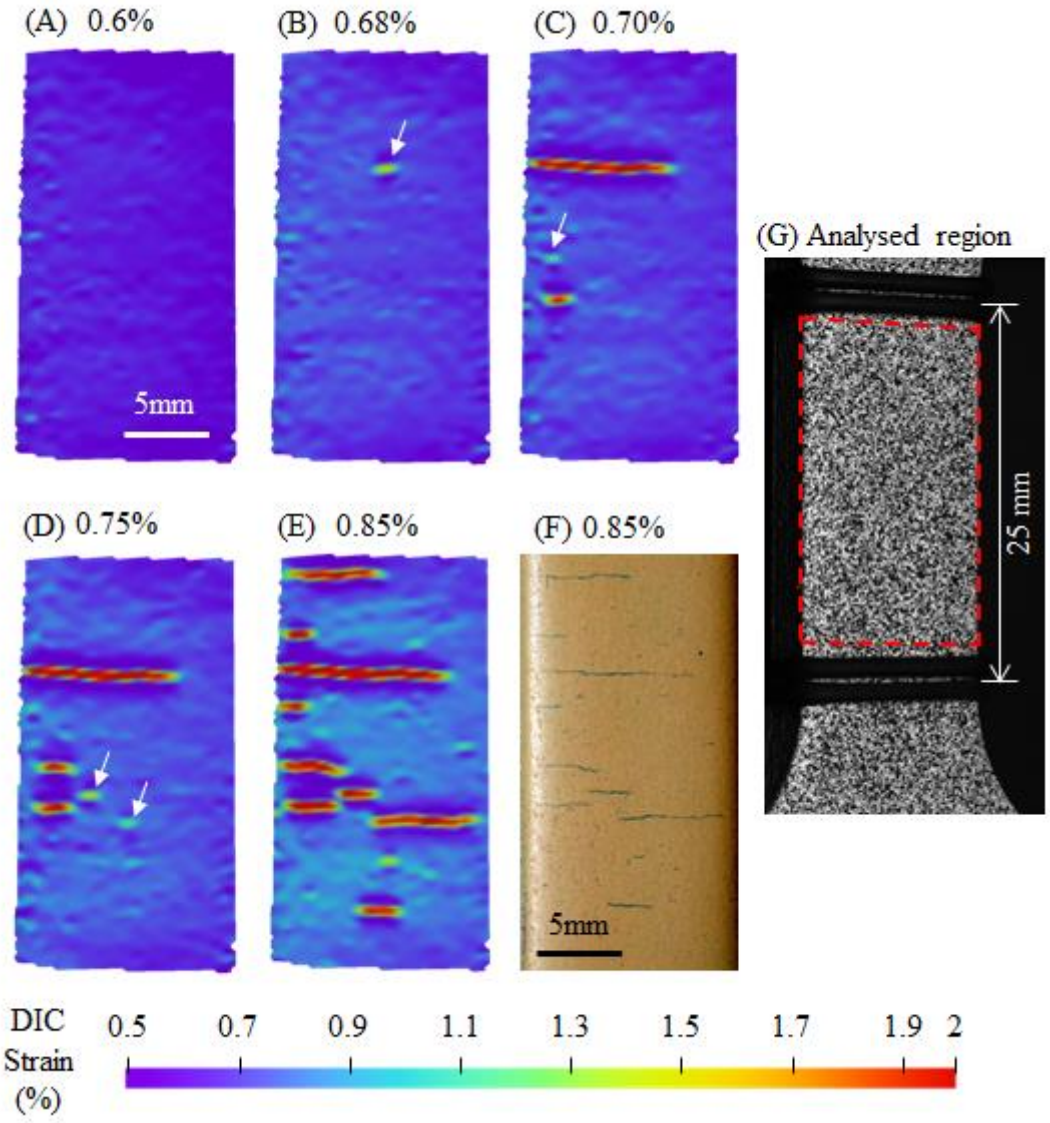

Figure 42. DIC Strain distribution mapping of a coating B substrated coating sample with a pre-strained substrate extended 0.85% strain (A to E). The photograph of the actual surface of the coating at 0.85% with features enhanced by blue ink (F). Photograph (G) shows the part of the sample within gauge length being analysed.

The coating on the original substrate developed high strain regions corresponding directly to the high strain regions developed in the substrate. The first cracks in the coating initiated within the high strain region, for example in the lower right region in Figure 43. As the substrate yielding band spreads with the increasing extensometer strain, more cracks were initiated and mainly within the high strain regions. Before coating cracks completely covered the entire coating surface, the distribution of the cracks resembled the strain distribution of the substrate.

In contrast, as shown by Figure 44 the substrate did not develop high strain regions, and the strain distribution in the coating was also rather even in comparison to that in Figure 44. Consequently, the initiations of coating cracks in the coating on the pre-strained substrate did not locate within a particular high strain region. The wide spread cracks with lengths shorter than 2 mm shown on the central top image at an extensometer strain of 1.2% in Figure 44 is a good demonstration. Eventually the cracks cover the entire gauge area by joining with other cracks.

4.3.3. Determination of strain to first crack

The ductility of substrated coatings is defined as the strain to the onset of the first coating crack observed within the sample gauge length. Both extensometer and DIC gave strain measurements; the former provided the overall strain over the gauge length and the latter provided the local strains surrounding the cracks.

The locations of first cracks can be found in DIC strain distribution, such as Figure 42B. Using ISTRA 4D software, two points, P_1 and P_2, 0.5 mm apart were located on the opposite sides of the crack, as shown by Figure 45A. A second identical pair of points (P_1' and P_2') were assigned on the rear substrate surface of the sample opposite to the first pair of points as shown in Figure 45B. The change of displacement (Δd) between the pair of point on the coating surface and opposite substrate surface of a coating B sample can be found in Figure 46B.

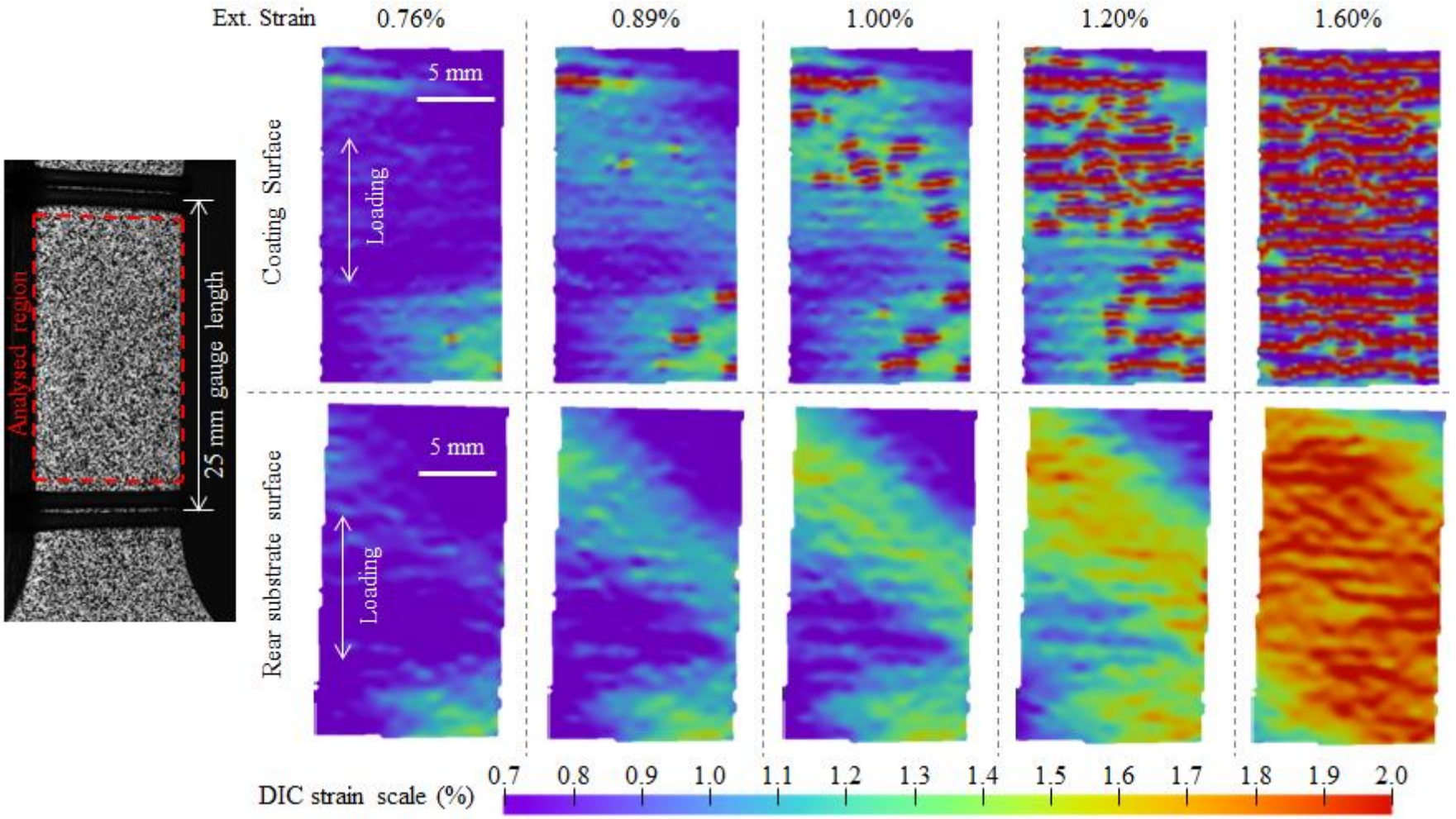

Figure 43. DIC strain distribution mapping of coating surface and the corresponding substrate surface at rear of a substrated coating A sample with the original substrate at various extensometer strains. The photograph on the left shows the part of the sample within gauge length being analysed.

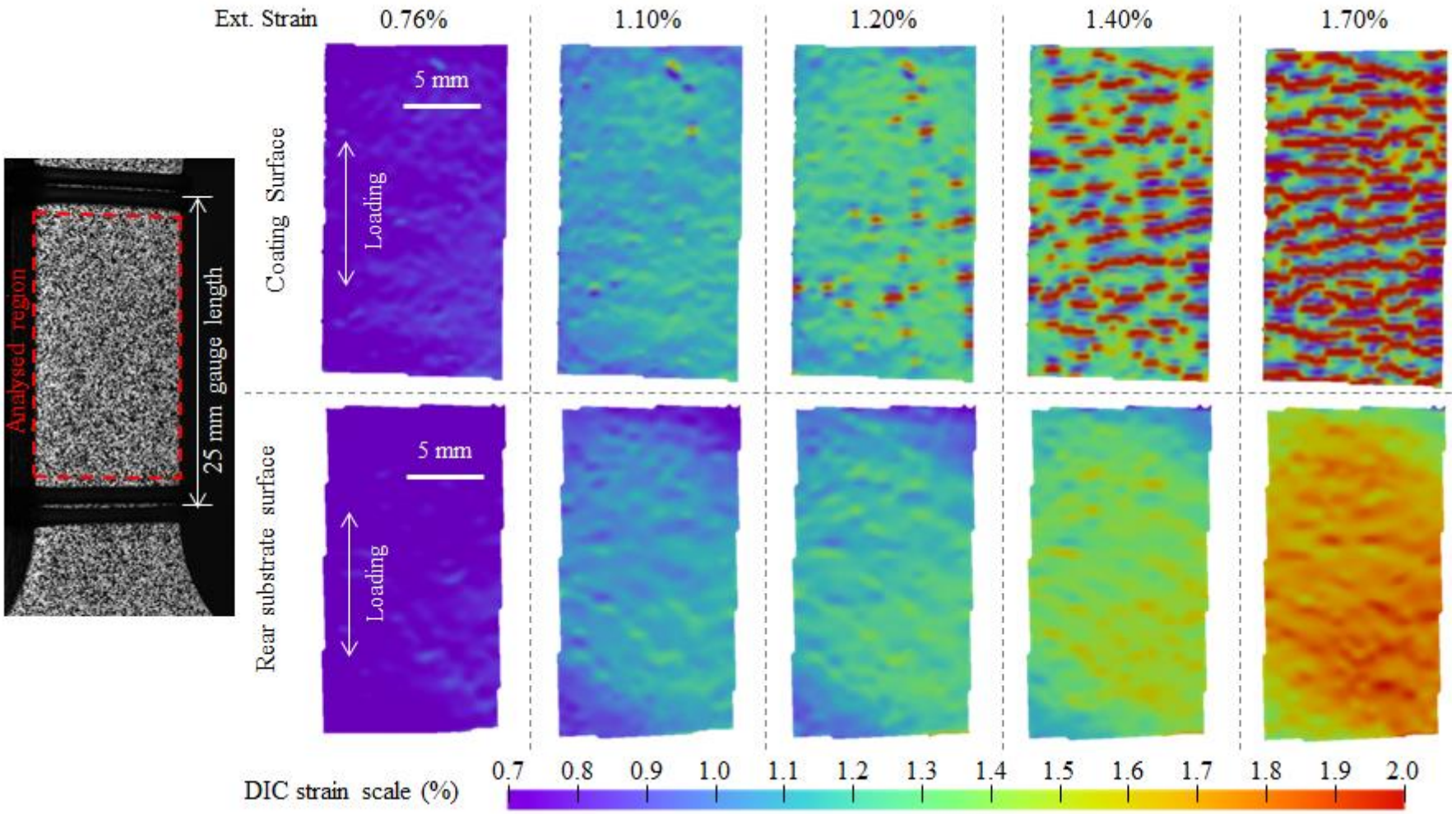

Figure 44. DIC strain distribution mapping of coating surface and the corresponding substrate surface at rear of a substrated coating A sample with the pre-strained substrate at various extensometer strains. The photograph on the left shows the part of the sample within gauge length being analysed.

An abrupt change of gradient was observed at an extensometer strain of about 0.6%. A comparison with Figure 42B, this shows that this corresponds to the appearance of a coating crack. The strain at the onset of the crack can be accurately found at this sharp transition. For coating A sample, see Figure 46A the transition of coating side displacement across the first crack was less pronounced, but using a gradient fitting construction shown the strain at the onset of crack can be identified.

Having defined the start point of deviation, hence the onset of cracking is defined, the strain to the onset of first crack can be produced. For an onset, an extensometer strain ($\boldsymbol{\varepsilon_{EXT}}$) and a Δd can be recorded from the extensometer and DIC analysis respectively. The DIC produced Δd was used to calculated a local strain (ε_{Local}) to the onset of first crack by dividing the Δd at the start of deviation using the original virtual gauge length (d_0).

$$\varepsilon_{Local} = \frac{\Delta d}{d_0} \times 100\% \tag{41}$$

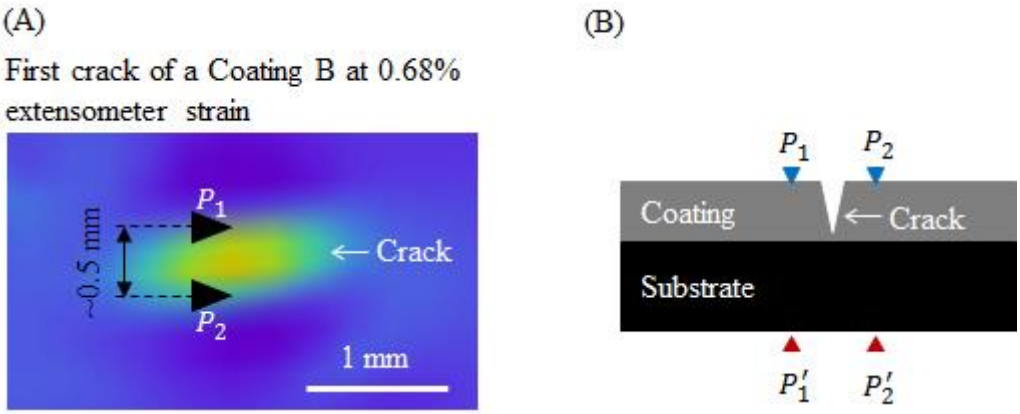

Figure 45. (A) Illustration of two points 0.5 mm apart located across a coating crack; (B) Illustration of an identical pair of points on the substrate side directly opposite to the pair on the coating side.

For each coating, 5 samples with pre-strained substrate and 3 samples with original substrate were used for the calculation of averaged extensometer strain and local strain

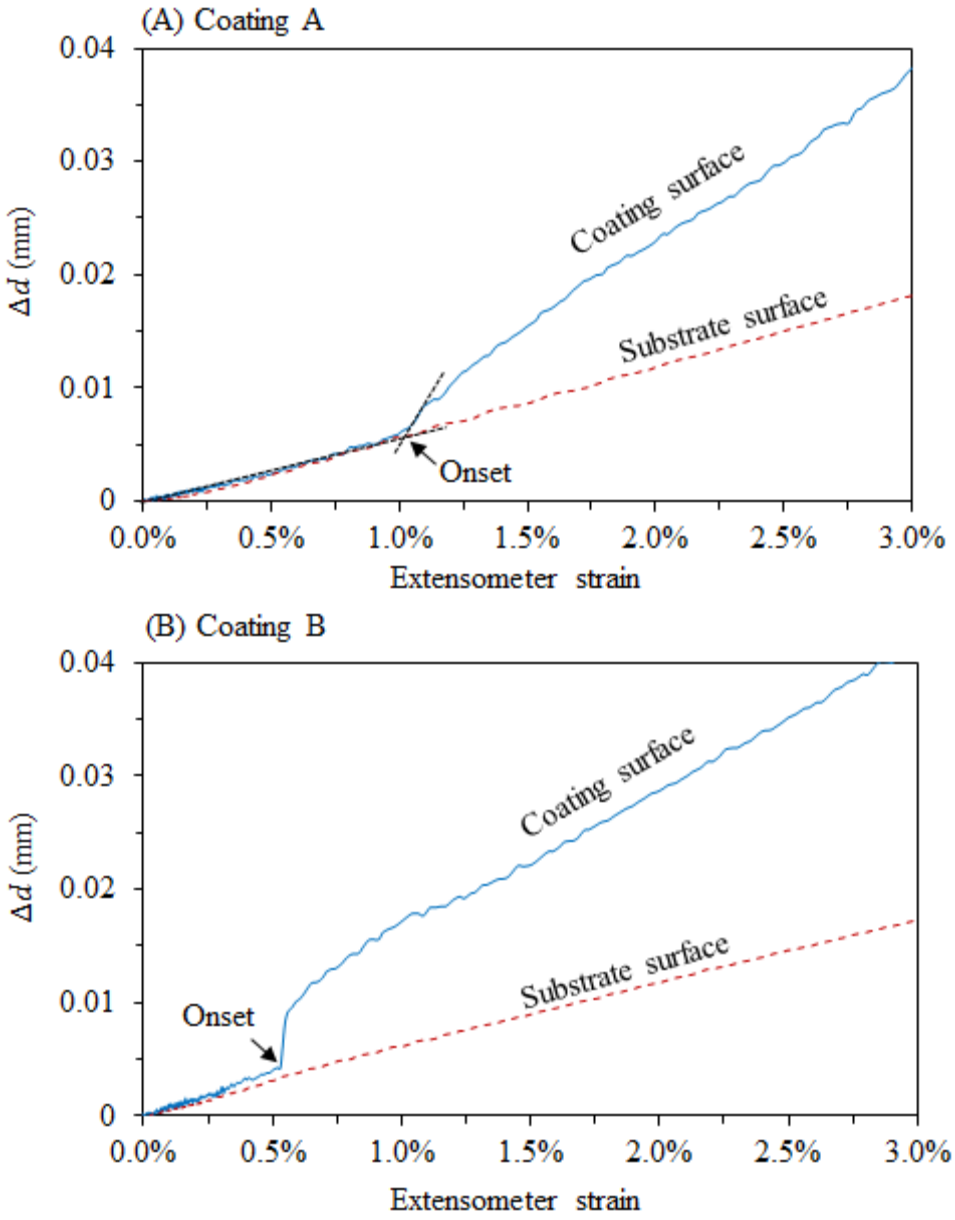

Figure 46. Change of displacement of the point pair across coating first crack and the second pair of points opposite to the former on the substrate side. (A) A coating A sample (STAP-4) and (B) a coating B sample (STBP-1).

to the onset of first crack. The results are also shown in Table 8, in which the free film strain to failure was also shown for comparison. Coating A had greater strains to first crack than coating B. The samples on pre-strained substrate had the same strain to first crack irrespective of the strain determination method, while strain to first crack of coatings on the original substrate depended on the strain determination method. In fact,

DIC local strains to first crack were the same for coating on both substrate states. This indicates that local strain determined the onset of cracking rather than extensometer strains. The strain to first crack of each sample measured can be found in Appendix iii. The strain to first crack of both coatings were also found greater than the failure strains of their free films. In fact, the free film failure strains were about half of the DIC local strains to first crack in substrated coatings.

Table 8. Strain to first crack of the substrated coatings on both original and pre-strained substrate measured by both extensometer and DIC technique.

Strain to first crack onset (%)	Coating A		Coating B	
Substrate state	Original	Pre-strained	Original	Pre-strained
ε_{EXT}	0.70± 0.09	1.04 ± 0.05	0.49 ± 0.16	0.64 ± 0.10
ε_{Local}	1.21 ± 0.11	1.21 ± 0.05	0.66 ± 0.07	0.73 ± 0.06
Free film	0.67 ± 0.06		0.34 ± 0.07	

4.3.4. Determination of coating crack spacing

The spacing between each of the multiple parallel cracks was quantified. As the coating crack opening generated a local high strain band, the number of cracks along the loading direction was determined by counting the number of high strain regions. Figure 47A shows the DIC strain distribution of a coating B sample on a pre-strained substrate under an applied strain of 3%. Three paths marked as 'L', 'M' and 'R', which refer left, middle and right respectively are shown in Figure 47A. Each peak in Figure 47B corresponds to a high strain region that the M path in Figure 47A lies over. The number of cracks along all the paths can be counted by counting the number of peaks similar to those shown in Figure 47B. The reason three paths rather than one are defined here is that many coating cracks did not cross the entire sample width, and for a more accurate measurement, three paths increase the sampling number from each coating sample.

It was found that the number of coating cracks increased with increasing strain. As an example, Figure 48 shows the development of the number of coating cracks along the M path of 5 samples of coating A and coating B on pre-strained substrate under an

increasing extensometer strain. For both coatings, the number of cracks increased roughly linearly with strain once the first crack was initiated. The number of cracks eventually reached a maximum value and remained unchanged till the end of test at 3% extensometer strain, which can be seen as the horizontal portion of the plots in Figure 48. This behaviour of reaching a maximum number of cracks reflected the saturation of crack number, and the extensometer strain at the start of saturation for each coating was calculated by averaging the results from the 5 samples shown in Figure 48. It was 1.94 ± 0.22 % for coating A and 1.42 ± 0.20 % for coating B.

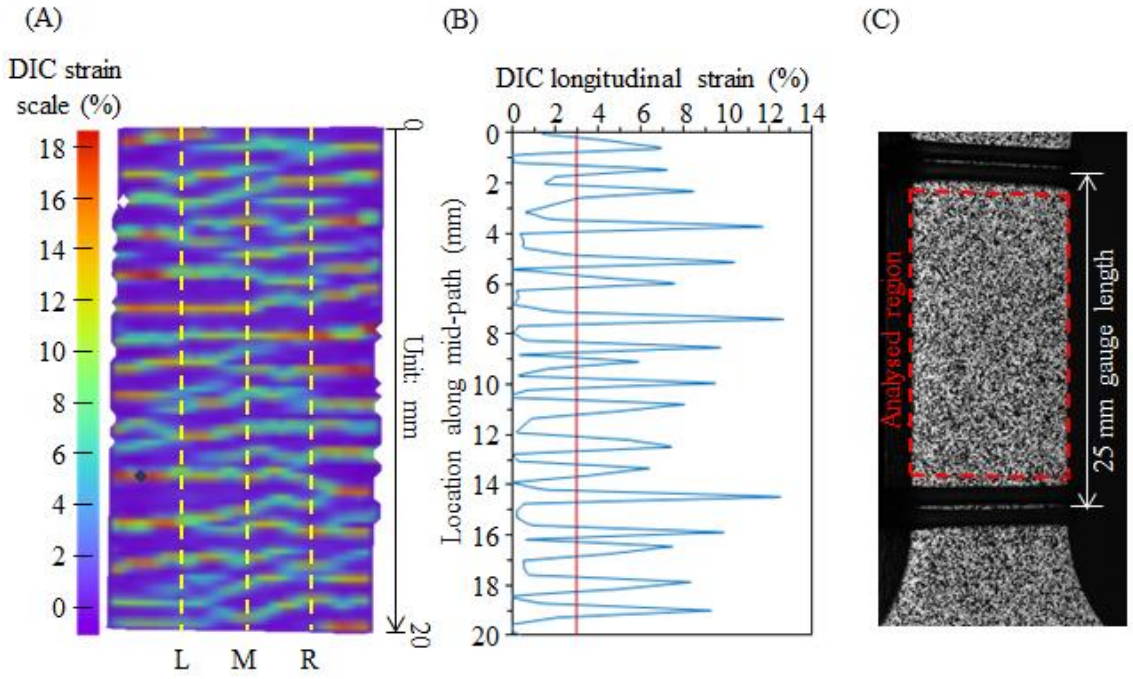

Figure 47. (A) Distribution of longitudinal strain within a 20 mm gauge region of a coating B substrated on a pre-strained substrate under an extensometer strain of 3%. (B) Plot of DIC longitudinal strain along the middle path marked 'M' in (A). Photograph (C) shows the part of the sample within gauge length being analysed..

The saturation of crack numbers shown in Figure 48 indicates that there was a minimum spacing between each pair of adjacent cracks in coating A and B with a thickness of about 0.3 mm under tensile strain. The crack numbers after saturation of coating A and B were counted using the DIC strain distribution at 3% of extensometer

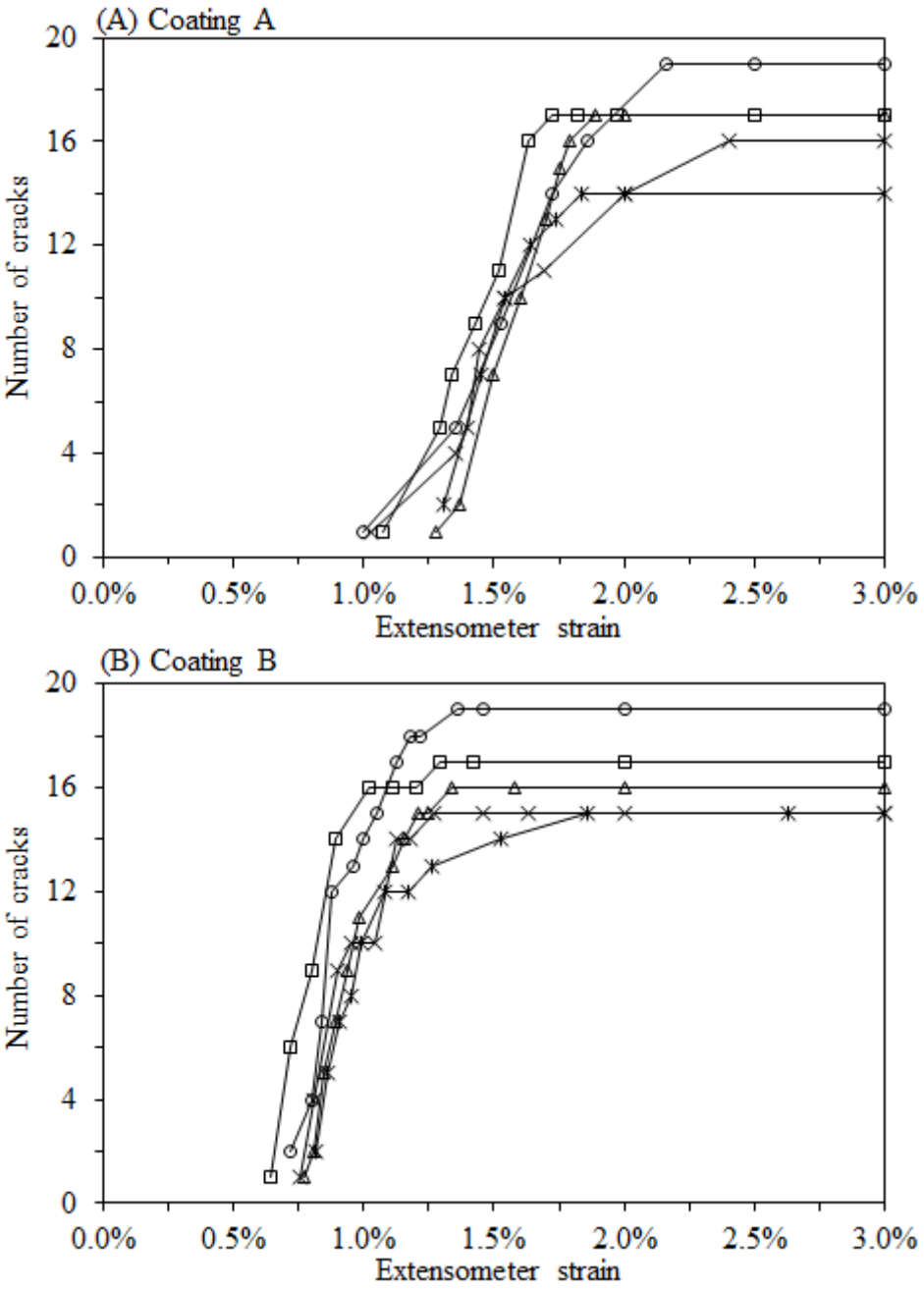

Figure 48. Number of cracks along the mid-paths of a coating A and a coating B substrated sample under increasing applied strain. Each graph shows the response of 5 samples of each coating.

strain. The number of cracks along all three paths of 5 samples of both coatings was counted and averaged to produce the results. For coating A, the critical crack number was 17 ± 3 and for coating B it was 17 ± 2. Consider a situation where each crack is confined in a region with a width equal to d, and the crack lies in the centre of the region,

see the regions defined by the dash lines in Figure 49. Thus the critical crack numbers translate to a d of 1.25 mm. This can be interpreted as that the cracks grow in separate but adjacent regions with equal size, which in this case would be 1.25 mm. As this value was calculated using the crack number after saturation, the value defines the minimum crack spacing for coatings A and B with a nominal thickness of 0.3 mm under static strains.

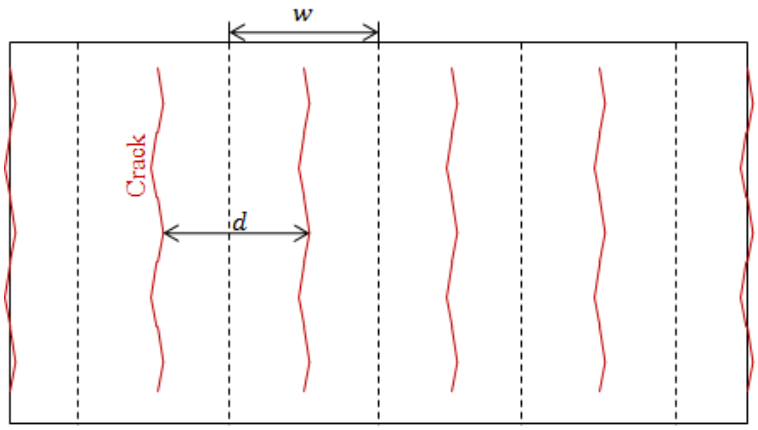

Figure 49. Illustration of a gauge area divided into 5 equally sized regions by 6 cracks.

4.3.5. Cross section of coating static cracks

The longitudinal cross-sections of substrated coatings with static cracks at the end of a test were observed using optical microscopy. For each coating, 2 samples were observed.

Within the same type of coating, one sample had the original substrate and the other had the pre-strained substrate. No difference in the crack cross-sections was found due to the different states of substrate. The typical cross-sections of coating cracks in coatings A and B after being tested to 3% of strain are shown in Figure 50.

The layer in white on the surface of the coatings is the primer paint used as background for DIC image capturing. The thickness of the primer paint shown in these figures is less than 10% of the coating thicknesses. The images in Figure 50 show a vertical crack penetrating from the coating surface towards the interface, where crack deflection

occurred. These deflections indicate that coating debonding from existing cracks took place in both coatings. Some voids are shown near the interface of coating B samples, in fact such voids were seen at other sites of coating B, while nearly no voids were found in coating A.

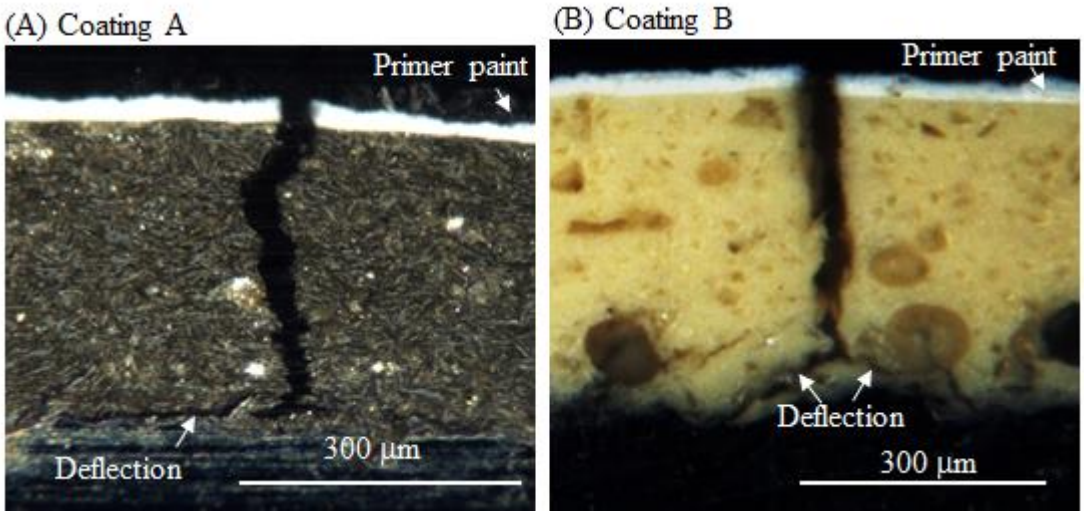

Figure 50. Coating cracks shown in the longitudinal cross sections of substrated coating A and B samples subjected to 3% of substrate strain.

4.4. Results of Fatigue testing of Substrated Coatings

During the fatigue tests, the coatings were subjected to cyclic strains imposed by the substrates. The largest strains of the strain cycles were below the static strain to first crack of the coatings, and fatigue cracks were observed on coating surface when sufficient number of cycles was achieved. Similar to the observation of coating cracking during the static tests of substrated coating samples, the coating stress and its change due to cracking could not be directly measured. In the current work, the fatigue cracking of coating was recorded mainly by surface replication, and for a small number of samples by a digital camera with a resolution of 1.4M Pixels. A typical coating cracking process under cyclic strains is demonstrated by Figure 51, which shows digital images of the evolution of surface cracks of a coating B sample (FFB – 5) with the original substrate under a fully reversed cycle with amplitude of ± 0.24%. Also to be noted here is that

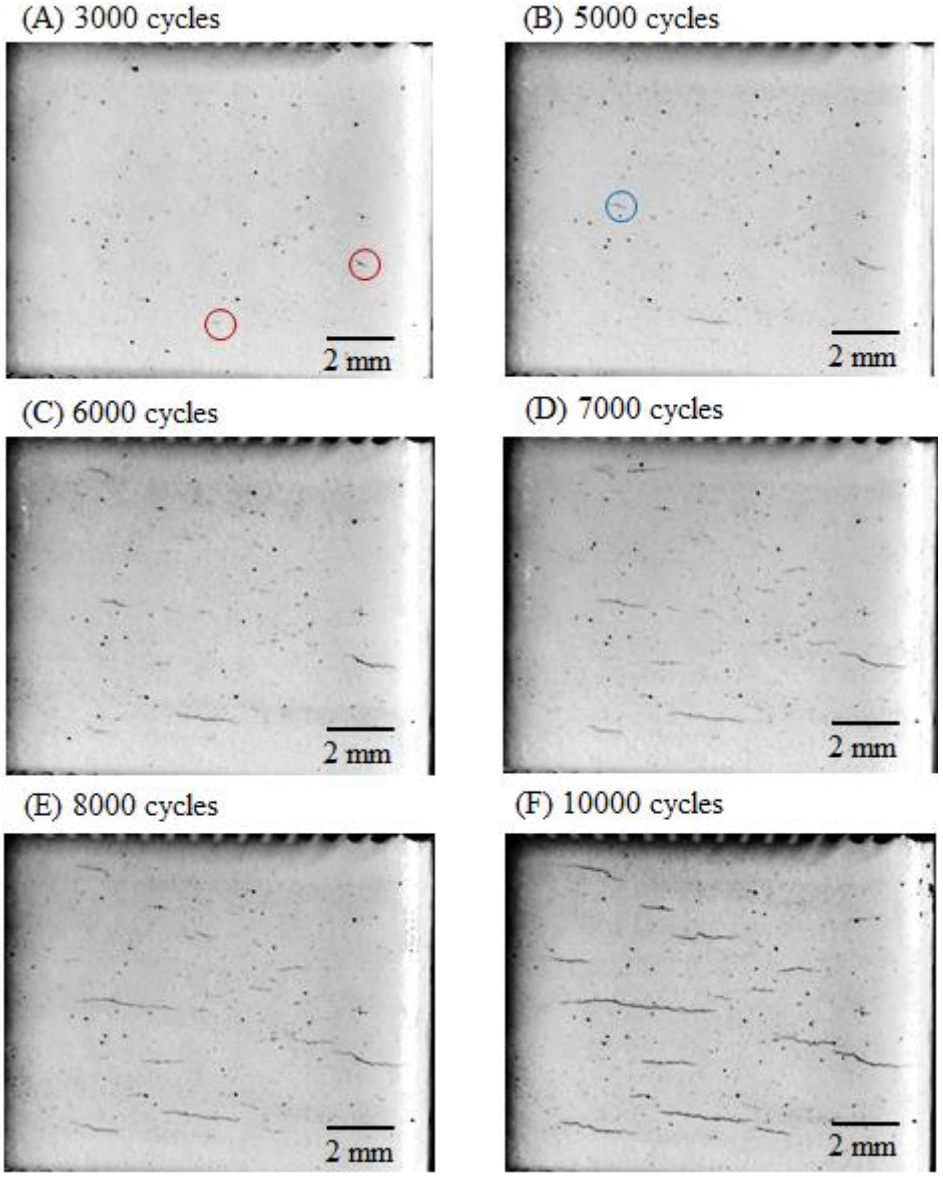

Figure 51. Coating crack development of a Coating B sample (FFB-5) under a constant strain amplitude of ± 0.24% at ambient temperature.

similar images showing fatigue cracking process of coating A cannot be produced using digital images as the colour of coating A had a low contrast to coating cracks even when enhanced by the dark ink. For coating A samples, surface replication only was used to record surface crack features.

In Figure 51A, two cracks were initially observed with lengths of about 0.2 mm at 3000 cycles, see inside of the red circles. As the cycling continued, these cracks grew in length

and at 4500 cycles another crack was found initiated at a different site, see blue circle in image B. As the test continued, the cracks on surface grew both in length and number, and eventually formed a multiple crack pattern with almost parallel cracks with different lengths. All samples shared similar cracking behaviour under cycle strains. It was also found that the number of cycles to the observation of first cracks as well as the rate that existing crack grew depended on the size of strain range. The details will be described later.

Fatigue failure of substrates also occurred. When substrate failure took place the substrates separated into two parts by a substrate crack and developed large plastic strains near the crack. In this section the substrate response to cyclic strains will be introduced first. Following this the effect of strain range on both cycle number to coating fatigue failure and crack growth rate will be introduced in detail.

4.4.1. Substrate response during fatigue test

It is well known that under cyclic strains the stress-strain behaviour of steel is different from that under static strains [144]. In the current case, the steel substrates softened during cycling, which means the maximum stresses at the maximum strains reduced compared to a substrate that is extended monotonically to the same strains. Each strain cycle from the minimum strain to the maximum strain then back to the minimum strain formed a hysteresis loop. As softening took place, the shape of hysteresis loops changed and eventually achieved a stable state. The stabilised hysteresis loops of the current substrates under fully reversed strain cycles with various amplitudes, from ± 0.25% to ± 0.6%, are shown in Figure 52.

In Figure 52, the hysteresis loops became larger as the amplitude increased, which is typical for elastic plastic materials under fully reversed strain cycles. Figure 53 shows the stabilised hysteresis loops of original substrate under zero-tension cycles with maximum strains from 0.4% to 1.05%. There hysteresis loops also become larger as the amplitude increases, and the tensile and compressive portions of the loops remain symmetric. In

the zero-tension cycles, the compression was caused by the plastic deformation generated in the loading branch of the cycles.

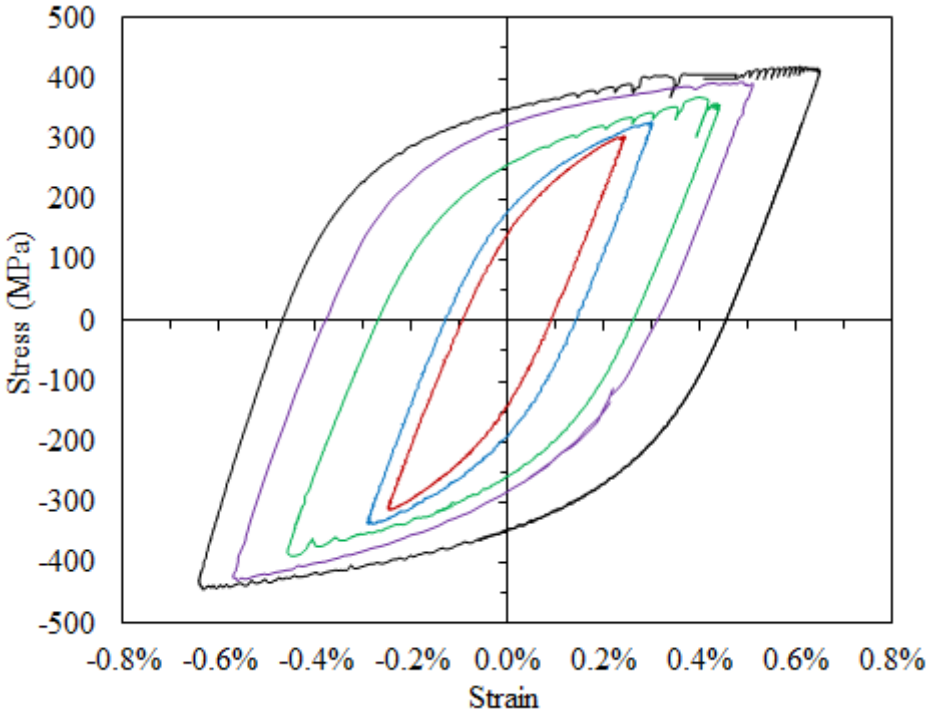

Figure 52. Stabilised hysteresis loops of original substrate under fully reversed cycles. The strain amplitudes from the inner circle outwards are ± 0.25%, ±0. 28%, ± 0.4%, ± 0.5% and ± 0.6%.

Figure 54 shows the stabilised hysteresis loops of pre-strained substrate under zero-tension cycles with maximum strains from 0.3% to 0.6%. The loops also become larger when the maximum strain increases. Different from the original substrates, the maximum and minimum stress of the loops of the pre-strained substrate appeared to be asymmetric to the horizontal axis. For the loop with the maximum strain of 0.3%, the portion of the loop in compression is only about 25% of the entire loop. As the maximum strain increased, the portion of loop in compression increased. However, till the maximum strain of 0.6%, the portion of the loop in tension still exceeds that in compression. This might be caused by the pre-straining process of the substrates.

The cyclic stress-strain curve of the steel substrate was produced using the definitions given in Suresh [144], and it is in Figure 55. The data points were half stress ranges

($\Delta\sigma/2 = \sigma_{max} - \sigma_{min}$) against half strain ranges ($\Delta\varepsilon/2 = \varepsilon_{max} - \varepsilon_{min}$). The cyclic stress-strain curve is the best fit of data points based on Ramberg-Osgood relationship [173]. In Figure 55, the static stress-strain curve of the substrate is also plotted. It can be seen that the substrate softened for half strain ranges below 0.6%, and hardened above 0.6%.

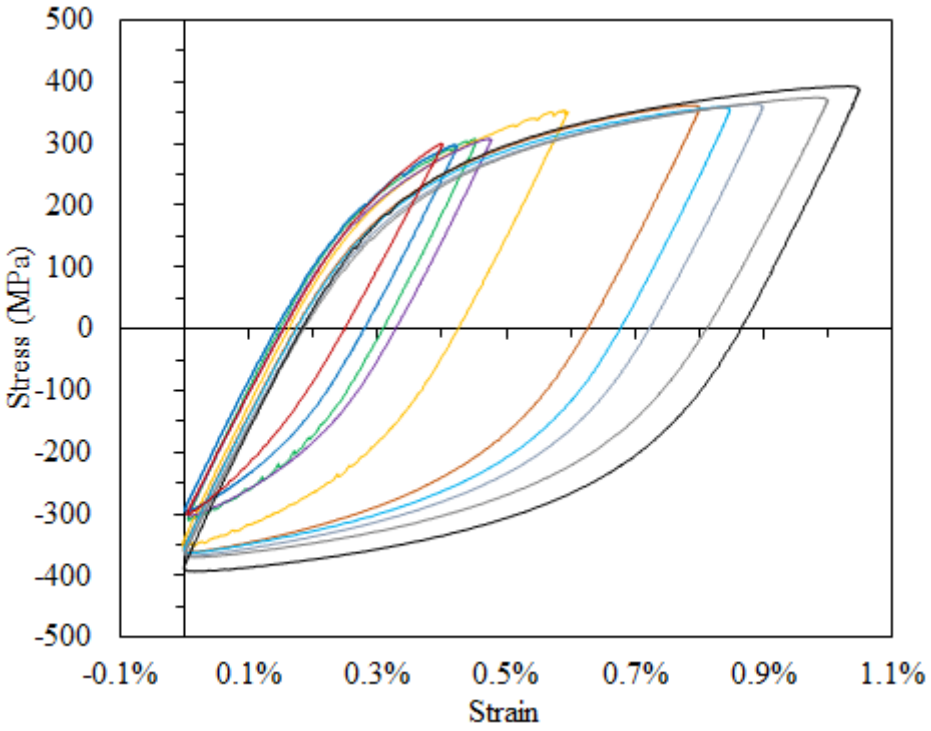

Figure 53. Stabilised hysteresis loops of original substrate under zero-tension cycles. The maximum strain from the leftmost circle rightwards are 0.4%, 0.43%, 0.45%, 0.48%, 0.6%, 0.8%, 0.9%, 1.0%, and 1.05%.

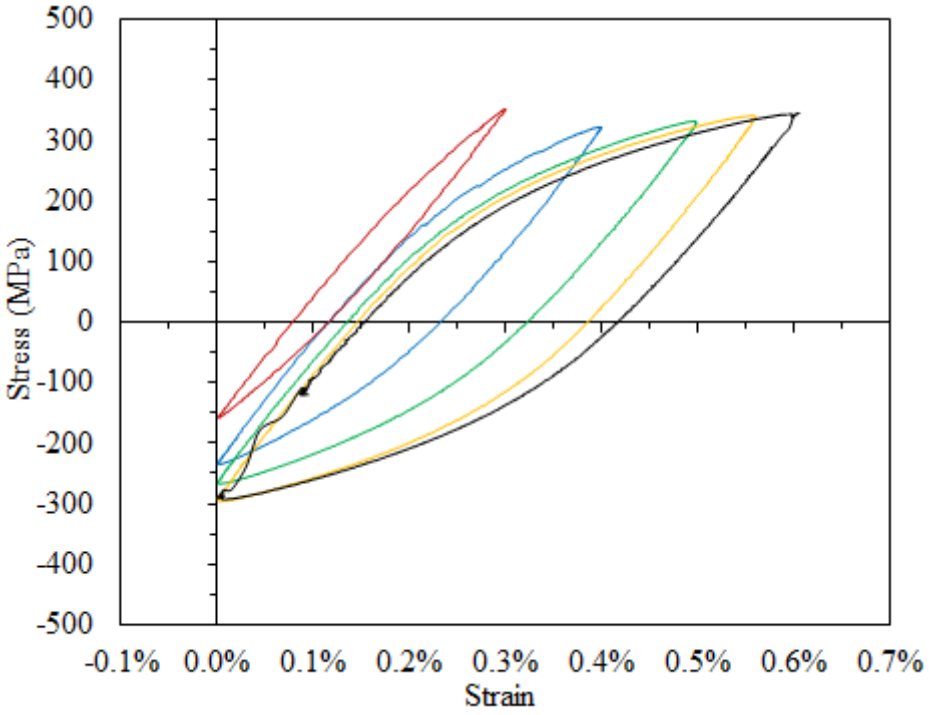

Figure 54. Stabilised hysteresis loops of pre-strained substrate under zero-tension cycles. The maximum strain from the leftmost circle rightwards are 0.3%, 0.4%, 0.5%, 0.55%, 0.6%.

4.4.2. Strain-life relationship in fatigue

Fatigue failure scenarios

One purpose of the fatigue test of substrated coatings was to characterise the fatigue lives of the coatings for different strain ranges. During the tests, it was found that the strain range dependence of the fatigue life of the substrate was different from that of the coatings, and interfered with the measurement of coating fatigue lives. Ideally, the substrate should remain intact throughout the entire test. Unfortunately, substrate failure often occurred before coating cracking took place. Figure 56A illustrates this ideal scenario, in which test was stopped where sufficient coating fatigue fractures were observed and prior to the rupture of substrate. This normally happened for coating B samples tested at high strain ranges.

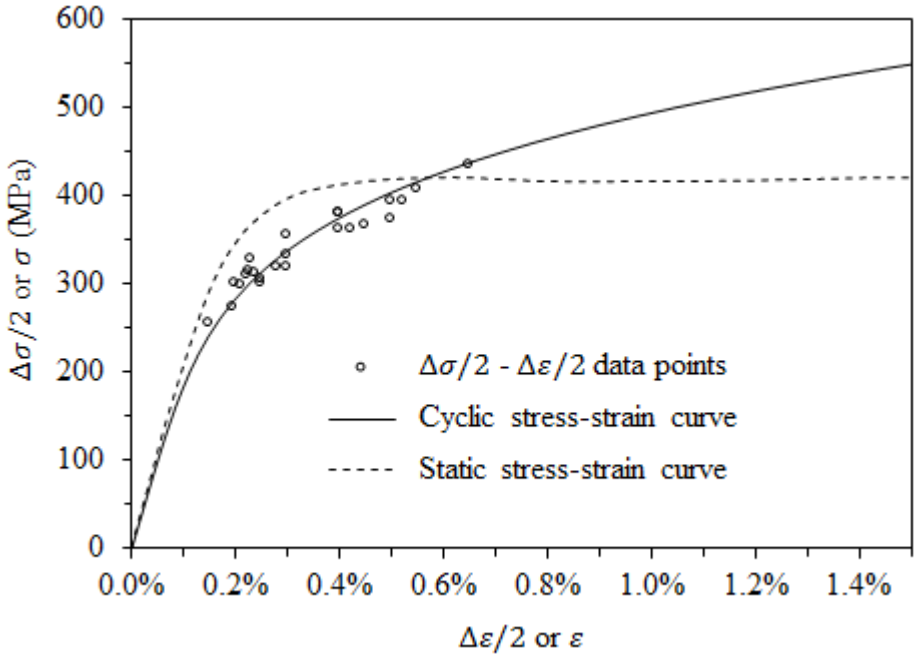

Figure 55. Cyclic stress-strain curve and static stress-strain curve of the substrate steel.

As illustrated by Figure 56B, sometimes the fatigue test was stopped due to the rupture of substrate after the first 2 mm coating crack was observed. This scenario was acceptable as it allowed the characterisation of the coating life as well as some degree of coating crack propagation after that. This happened in all successfully measured coating A samples as well as some coating B samples. However, the worst scenario, illustrated by Figure 56C, was that the rupture of substrate occurred before the appearance of the first 2 mm coating crack, sometimes even before the appearance of any observable coating cracks. This was classified as an unsuccessful test as it did not give any coating life characterisation. This normally happened in coating A samples tested at strain amplitudes (half of strain range) below 0.5%, and in coating B samples tested at strain amplitudes below 0.2%.

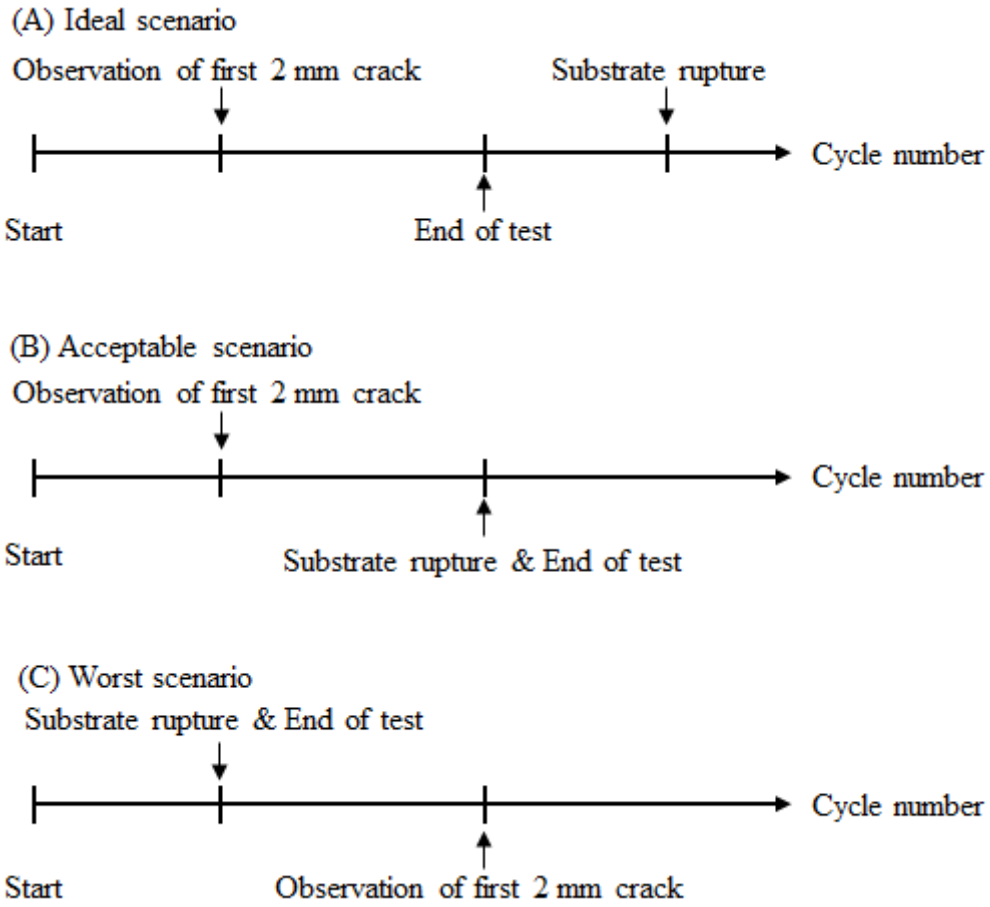

Figure 56. Illustration of (A) the ideal scenario, (B) an Acceptable scenario, and (C) the worst scenario, in the fatigue test of substrated coatings.

Strain-life relationship of the substrate in fatigue

The strain-life (ε-N) relationship of the substrate of all samples, where the substrate failure occurred, is plotted in , which shows the life of substrate increased as the strain amplitudes reduced. Full data of substrate lives can be found in Appendix iv.

The data points were obtained from samples of both coatings under fully reserved and zero-tension cycles, and that all data points fit the same trend means that the mean value or the mode of strain cycles did not affect the life of the substrate. This plot is highly important, because it defines the limit that the coating fatigue failure could be observed. For a certain strain amplitude, if the life of coating is greater than that of the substrate,

such as the worst scenario described in Figure 56C, the coating fatigue cannot be observed due to the failure of the substrate.

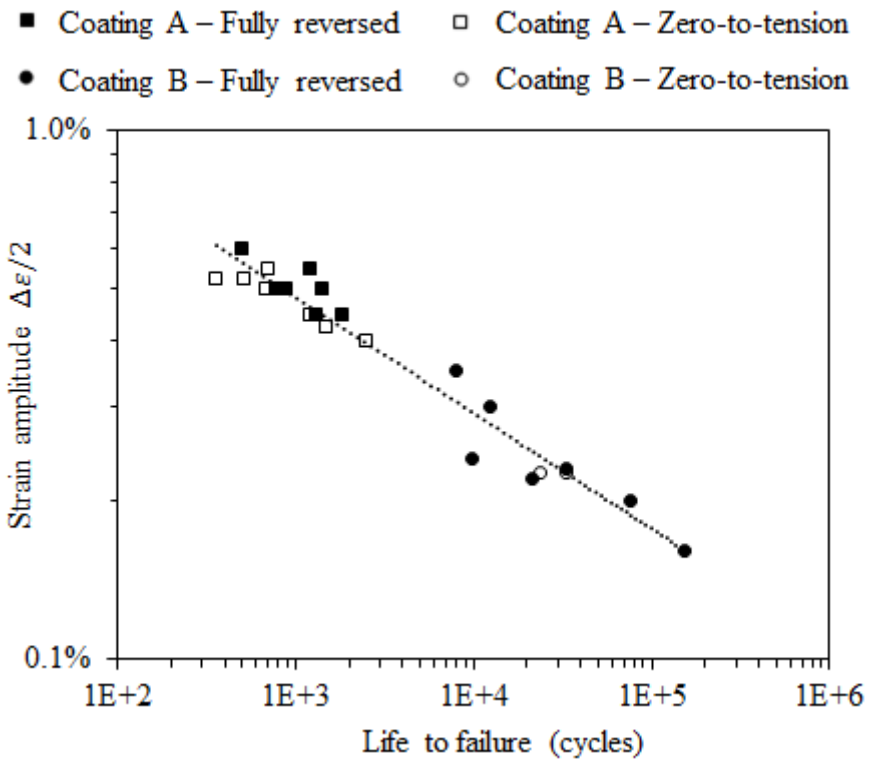

Figure 57. S-N curve of substrate at various strain amplitudes.

Strain-life relationship of the coatings in fatigue

The life of the coatings was defined as the number of cycles where the longest surface crack achieved 2 mm in length. Assuming coating surface cracks were semi-elliptical, in a 0.3 mm thick coating a crack with surface length greater than twice the thickness (0.6 mm) would have completely penetrated the coating thickness. In this work, the failure point definition should ensure a full thickness penetration.

The lengths of coating cracks at different cycles were measured primarily from the surface replica using an optical microscope. The microscope had a travelling stage with two micrometres controlling the movement in X and Y directions with a controlling resolution of 1 µm. The replicas were observed under a magnification of 100 times, and the coordinates of the two end points for each crack were recorded. The distance

between each pair of end points was used as the crack length. The measurement had an error of ± 2 μm. Note, before the first crack reached 2 mm, it might have already penetrated the thickness. Also, before the first 2 mm crack was observed, in most of the tests there had already be some cracks with smaller lengths. Full data sets of coating fatigue lives can also be found in Appendix iv. Figure 58 shows that the strain-life (ε-N) relationship of coatings A and B with original substrate under fully reversed cycles.

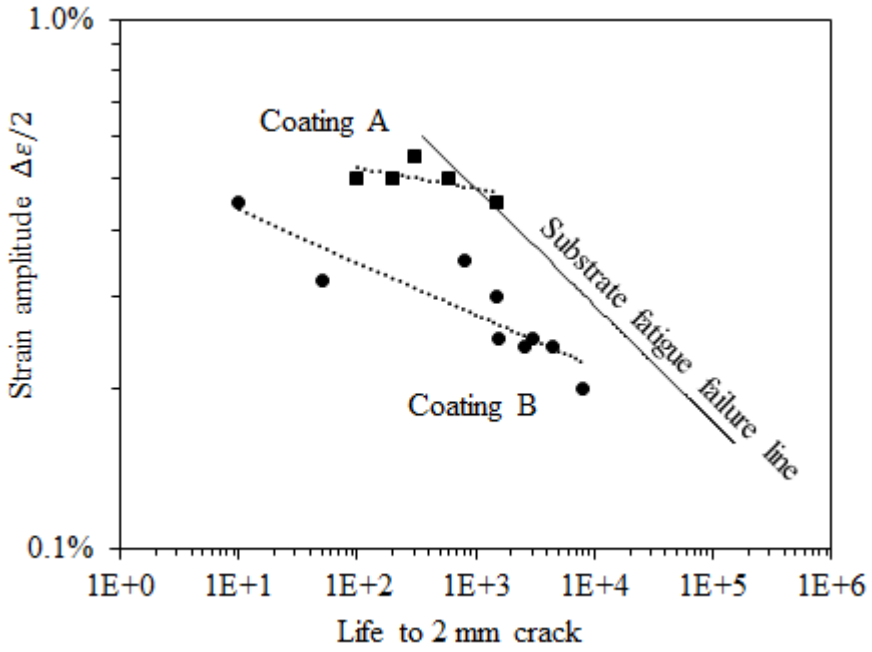

Figure 58. S-N curves of coatings A and B samples under fully reserved strain cycles. The power regression of the substrate life data is also shown.

In Figure 58, the ε-N plot for coating B is well below that of coating A under fully reversed strain cycles. At a strain amplitude of 0.45%, the life of coating A was about 2 orders of magnitude longer than that of coating B. For a life of 1500 cycles, it required an amplitude of about 0.45% to cause failure in coating A while it only required an amplitude of about 0.3% for coating B to fail. This shows that coating A was more fatigue resistant than coating B. The substrate fatigue failure line is the data fitting line shown in Figure 57. At strain amplitudes smaller than the intersections of the coating lines and the substrate failure line, the substrate life is shorter than the life to coating first 2 mm coating crack, and therefore the fatigue life of the coating cannot be measured. This is

illustrated by the worst scenario illustrated in Figure 56C. The intersections defined the lower strain amplitude limits that the fatigue of the substrate coatings could be studied. For coatings A and B, the limits were about 0.4% and 0.2% respectively.

The samples of both coatings were also tested under zero-tension cycles, and the ε-N plots of them are shown in Figure 59, in which the life data of the samples tested under fully reversed cycles is also plotted. The data points of coating A under zero-tension cycles are also well above those of coating B under zero-tension cycles, which also indicates that coating A was of greater fatigue resistance than coating A also under zero-tension cycles. Figure 59 also shows that the life of coating A samples was not affected by the mode the cycling was performed. The data points of coating A tested under zero-tension cycles are not significantly different from those of coating A tested under fully reversed cycles in the positions shown in the figure. In contrast, the data points of coating B tested under these two modes of cycling are clearly two separate sets of results. The coating B data points obtained from the fully reversed tests are above those from the zero-tension tests before a life of about 10^4 cycles, after that these two sets of data seem to merge. The life of coating B under zero-tension cycles was 2 order of magnitude shorter than that under fully reversed cycles at a strain amplitude of 0.23%, while at amplitudes smaller than about 0.2% the life of the coating was not sensitive to the cycle mode anymore.

The static failure strains of both substrated coatings, representing fatigue life at 1 cycle for the samples tested under zero-to-tension cycles, are shown as the red points in Figure 59. As the strain axis in Figure 59 is plotted as amplitude which is half of the total strain range, static strain to failure is similarly represented as half of the applied strain to cause failure. Both data points are below the extrapolated trends of the strain-life line of each corresponding coating. This means that the fatigue data predicts a greater resistance for 1 cycle. Note that the fatigue failure of the coatings were defined as the cycles to 2 mm crack, while the static failure strain was defined as the strain to first cracking onset, where the crack length was smaller than 2 mm. The discrepancy between

the static failure strains and the fatigue strain data reflects the difference in the definitions of coating failure in the static tensile and the fatigue tests.

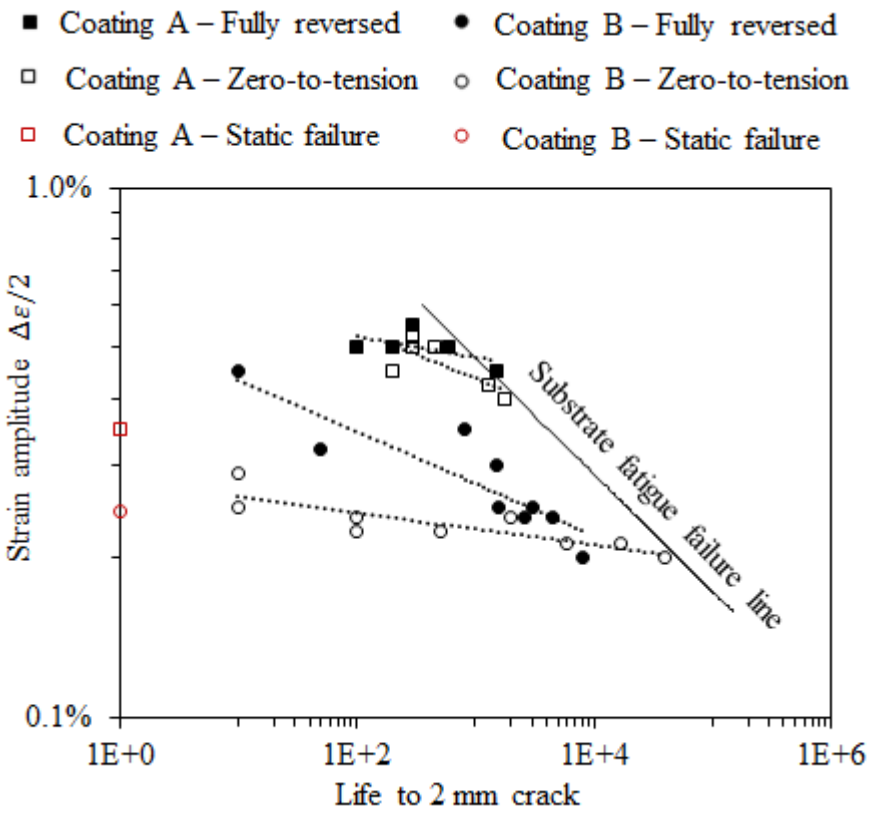

Figure 59. S-N plots of coating A and B fatigue samples under both fully reversed and zero-tension cycles at various strain amplitudes. The power regression of the substrate life data is also shown.

The fatigue life of coating B on both original and pre-strained substrates under zero-tension cycles is shown in Figure 60. In this figure, the power regressions of the plots intersect at a life about 1000 cycles. Before this number of life, the plots of coating B samples on pre-strained substrate are above the coating B samples on non-pre-strained substrate. This means the coating B on a pre-strained substrate had a longer life than that on a non-pre-strained substrate at the same strain amplitude. For the data points after the life of 1000 cycles, if the trends of the plots hold for both types of the samples, the life of coating B on a non-pre-strained substrate would be longer than that on a pre-strained substrate at the same amplitude.

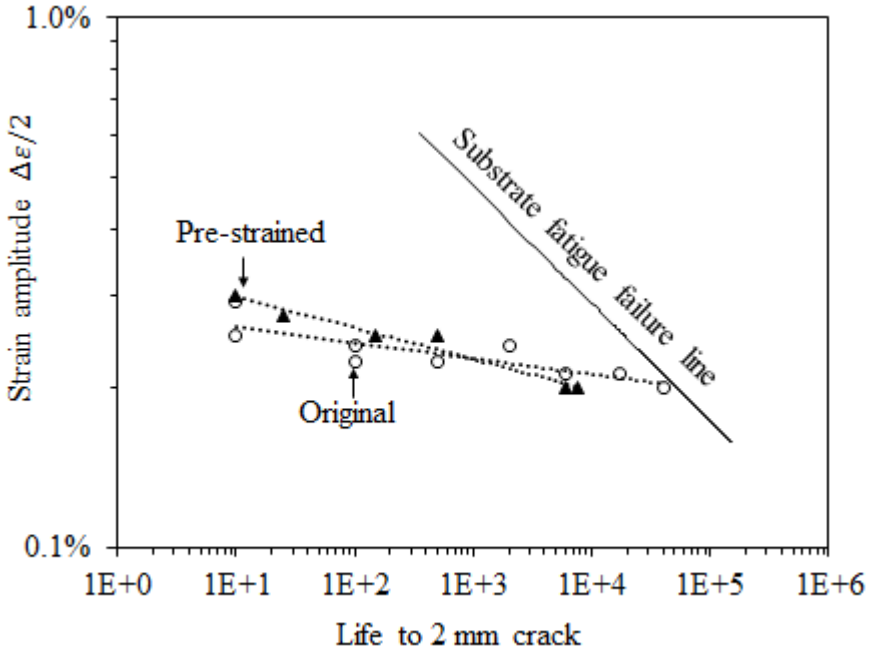

Figure 60. S-N plots of coating B samples with non-pre-strained and pre-strained substrate under zero-tension strain cycles. The power regression of the substrate life data is also shown.

Proportion of cycle to initial crack observation in the life to first 2 mm crack

Before the cycle to 2 mm crack, cracks with a length smaller than 2 mm were observed at smaller cycles. Table 9 lists the cycle to initial crack observation (N_{in}) and the cycle to first 2 mm crack (N_{2mm}) of some samples of both coatings A and B. The proportion of cycle to initial observation in the life to first 2 mm crack is defined as the ratio of N_{in} to N_{2mm}, which is also shown in the table.

It can be seen that N_{in}/N_{2mm} ranges from 11% to 100%. There is no obvious effect of strain range on the N_{in}/N_{2mm} ratios of the samples of both coatings. The average N_{in}/N_{2mm} of all coating A samples shown in Table 9 is 38% with a standard deviation of 9%, whilst the average N_{in}/N_{2mm} coating B samples is 63% with a standard deviation of 30%. The results indicate that the life of coating A was predominately determined by the propagation of fatigue cracks after initiation, while the life of coating B was predominantly determined by the life to the initiation of coating cracks. Note, there was

not any definition of the initiation of coating cracks, and the cycle number to the initial observation was also influenced by the intervals chosen to pause testing and collect data.

Table 9. Cycle number to the initial observation of coating fatigue cracks and to the first 2 mm cracks.

	Sample number	Strain range (%)	Cycle to initial observation (N_{in})	Cycle to first 2 mm crack (N_{2mm})	N_{in}/N_{2mm} ratio
Coating A	FTA - 2	0 – 0.85	600	1350	44%
	FTA - 3	0 – 0.9	50	200	25%
	FTA - 4	0 – 1.0	100	300	33%
	FTA - 5	0 – 1.0	200	450	44%
	FTA - 6	0 – 1.05	100	300	33%
	FTA - 7	0 – 1.05	200	400	50%
Coating B	FFB - 5	-0.24 – 0.24	3000	4500	67%
	FFB - 7	-0.25 – 0.25	2000	2550	78%
	FFB – 8	-0.25 – 0.25	200	1800	11%
	FFB - 10	-0.3 – 0.3	400	1500	27%
	FFB - 12	-0.35 – 0.35	800	800	100%
	FFB - 13	-0.45 – 0.45	10	10	100%
Coating B	FTBP - 1	0 – 0.4	5000	7500	67%
	FTBP - 2	0 – 0.4	3000	6000	50%
	FTBP - 3	0 – 0.5	100	150	67%
	FTBP - 4	0 – 0.5	250	500	50%
	FTBP - 5	0 – 0.55	10	25	40%
	FTBP - 6	0 – 0.6	10	10	100%

4.4.3. Crack interaction

Due to the presence of multiple coating cracks, independent cracks and their growth were found to interact with other cracks nearby. The visual examination of the digital images of coating surfaces at different stages of cycling revealed that there are 4 types of crack interaction, see Figure 61.

Type I – independent cracks are those grewing independently without other cracks in their vicinity of 1 mm radius, see Figure 61A. This was normally observed in newly initiated cracks.

Type II – coalescing cracks are those originally independent cracks coalesced with other co-linear cracks when they grew longer, see Figure 61B.

Type III – confronting cracks are those originally independent cracks where the crack tips grew into the vicinity of a co-linear crack but did not coalesce and continued to grow at a much reduced rate, Figure 61C.

Type IV – Double initiated cracks are those initiated with another initiation in vicinity and grew only to the direction away from the initiation site, see Figure 61D.

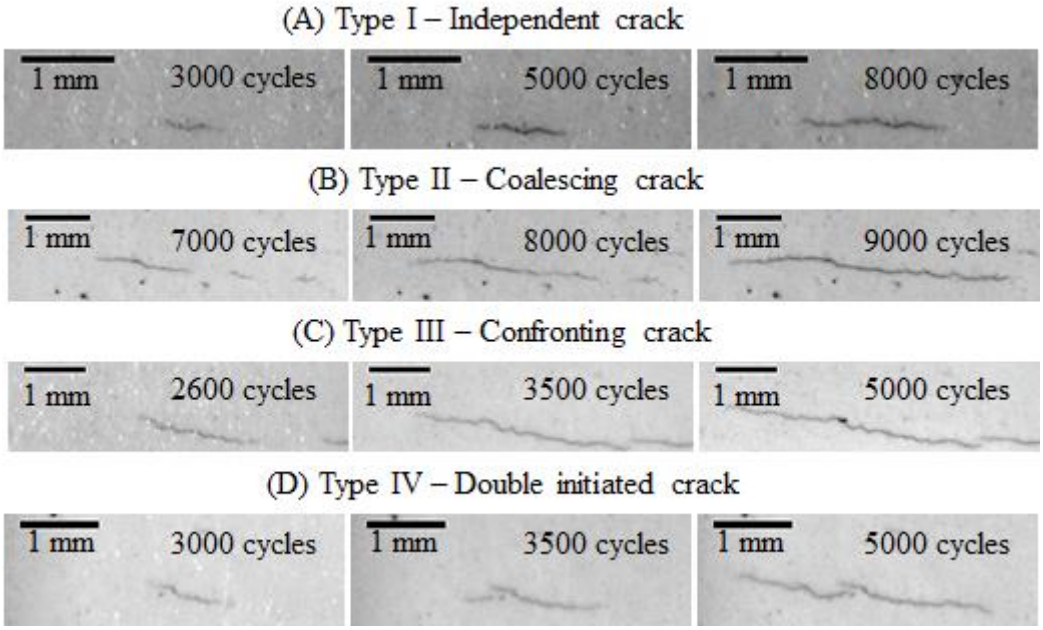

Figure 61. Four types of cracks depending on their interactions with other cracks. These images were taken from a coating B sample tested at ± 0.25% (FFB-7).

4.4.4. Single crack growth

Growth of single cracks before interaction

A typical crack length growth as a function of cycle number of an independent crack without any interaction with other cracks or crack tips is shown in Figure 62 and Figure 63. Figure 62 shows an example from a coating A sample under a fully reversed cycle of ± 0.55%, and Figure 63 shows an example from a coating B sample under a fully reversed

cycle of ± 0.6%. The cracks were initially observed at a cycle number of 250 with a length of about 0.8 mm for the coating A sample, and at a cycle number of 600 with a length of about 0.5 mm for the coating B sample. After that, these cracks grew in length with the cycle number in an effectively linear fashion. This linear relationship between crack length and cycle number was widely observed in independent cracks on all samples. The crack used as example in Figure 63 was found to eventually coalesce with another crack at 2000 cycles. Due to the coalescence, one tip of the crack merged with the tip of another crack, and therefore the figure only plots the growth when it was still independent (till 1500 cycles).

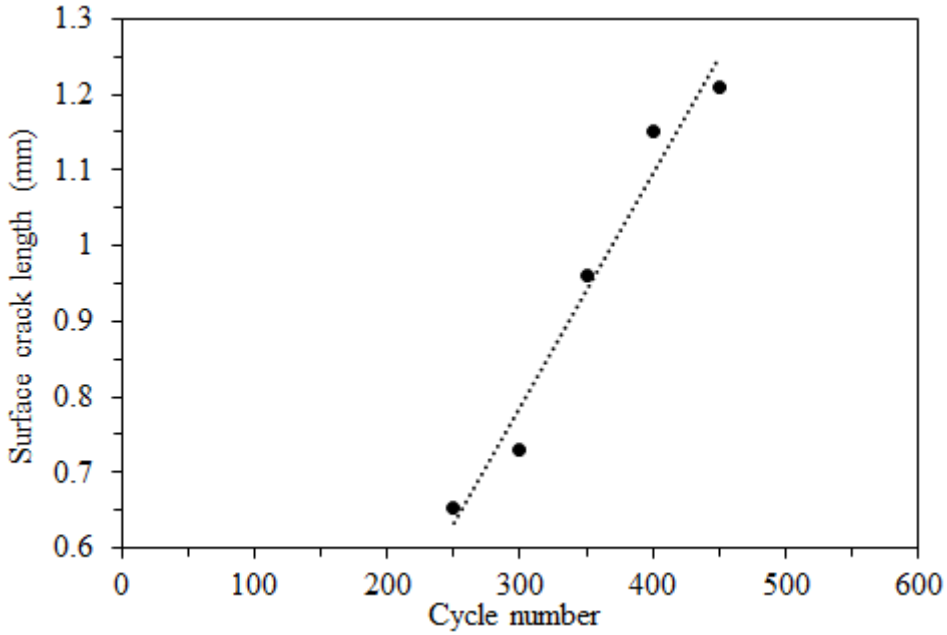

Figure 62. The growth of an independent crack on the surface of a coating A sample (FFA – 6) under fully reversed cycles with an amplitude of ±0.55%.

Growth of single cracks in interaction

A typical example of crack growing into interaction with other crack can be found in Figure 64 and Figure 65 for a coating A sample and a coating B sample respectively. In both figures, the crack length increased linearly with the cycle number before both of their crack tips grew into the vicinity of another two crack tips about 1 mm away at 300

cycles for coating A and 10000 cycles for coating B. After that, the growth rates significantly reduced, which can be seen as the reduction of the slope of the plots.

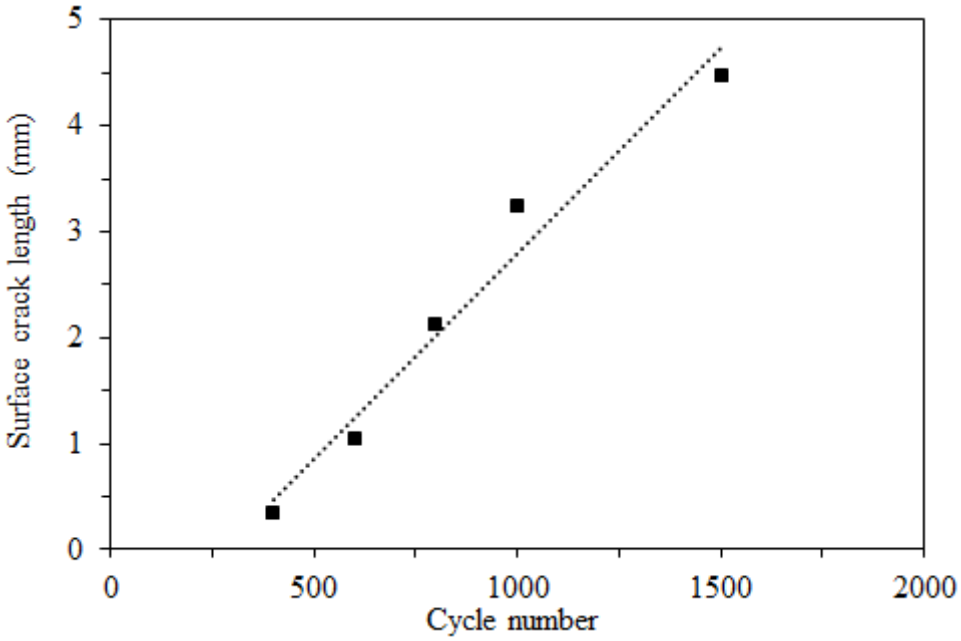

Figure 63. The growth of an independent crack on the surface of a coating B sample (FFB – 12) under fully reversed cycles with an amplitude of ±0.6%.

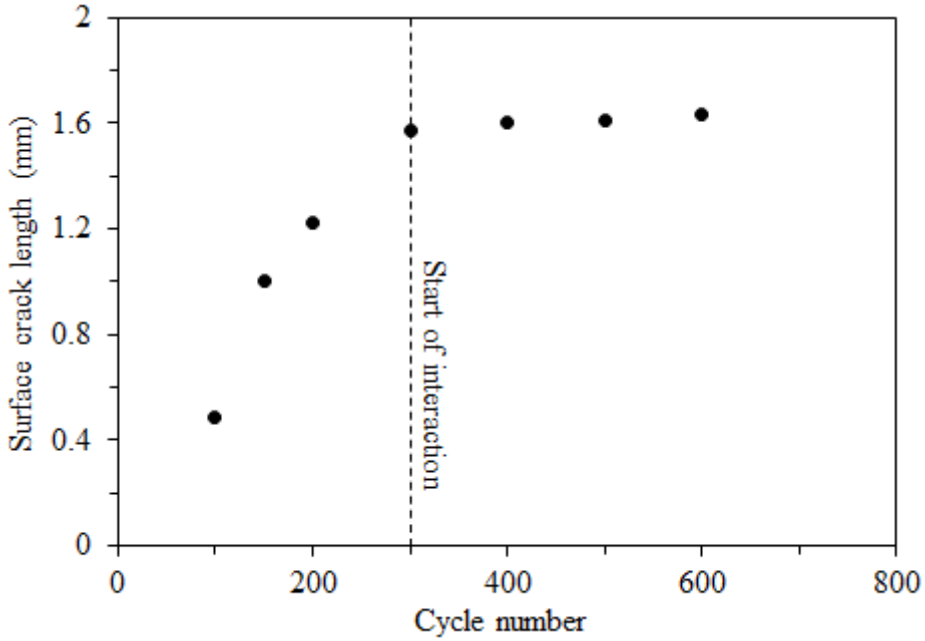

Figure 64. The growth of an independent crack confronting another two cracks on the surface of a coating A sample (FTA-5) under a zero-tension cycle from 0 to 1%.

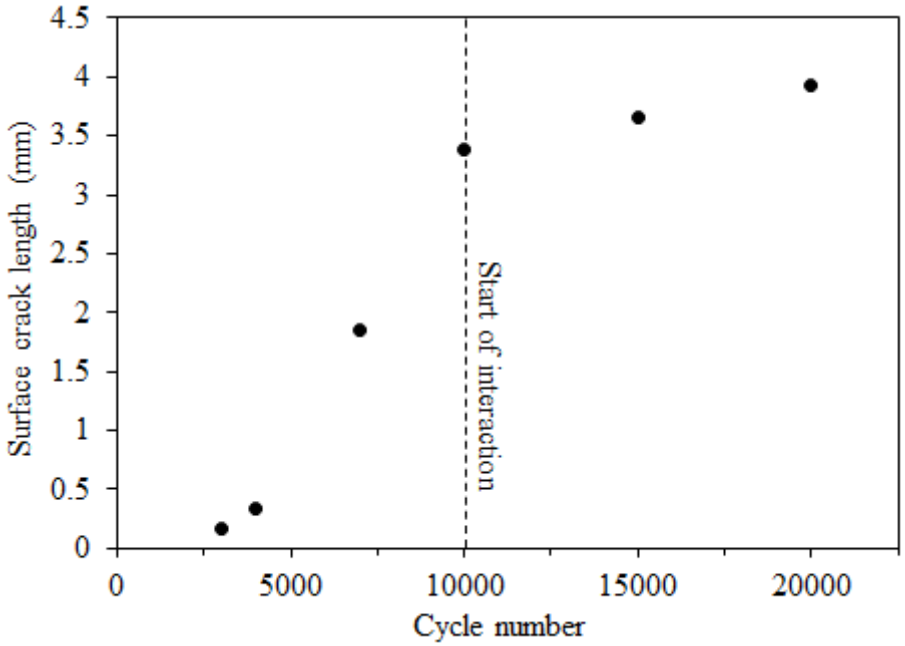

Figure 65. The growth of an independent crack confronting another two cracks on the surface of a coating B sample (FTBP-2) under a zero-tension strain cycle with a range of 0 – 0.4%.

Varying growth rates of single cracks of the same sample

The growth of single cracks on the same sample has also been investigated. In all samples, it was observed that the single cracks within the same sample grew in different rates. Figure 66 and Figure 67 shows the growth of 5 single cracks within the same coating A samples under zero-tension cyclic strains with maximum strains of 0.9% and 1.05%. Figure 68 and Figure 69 show the growth of 5 single cracks within the same coating B samples under zero-tension cyclic strains with maximum strains of 0.45% and 0.58%.

Based on these 5 cracks, 5 different crack growth rates could be calculated using the slope of the linear fits of each data set. It can be seen that each single crack shows constant crack growth rate, but there is a big variation in the fatigue crack growth rates of single cracks within each sample. The standard deviation of the crack growth rates can be as high as 90% of the mean growth rate.

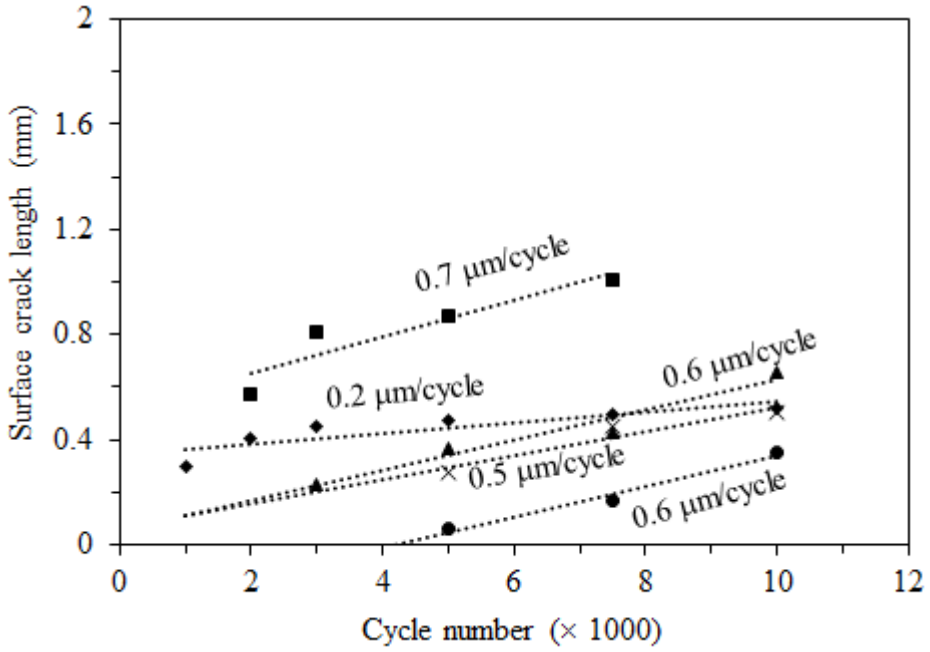

Figure 66. Growth of 5 single cracks with increasing cycle number in a coating B fatigue sample with original substrate under a strain range of 0 – 0.9% (FTA-3).

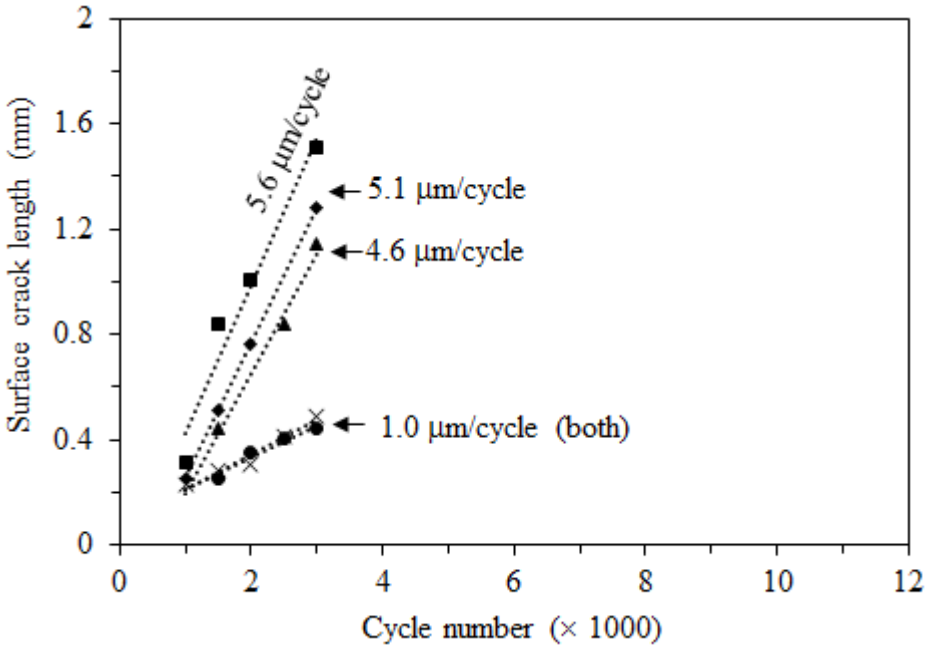

Figure 67. Growth of 5 single cracks with increasing cycle number in a coating B fatigue sample with original substrate under a strain range of 0 – 1.05% (FTA-6).

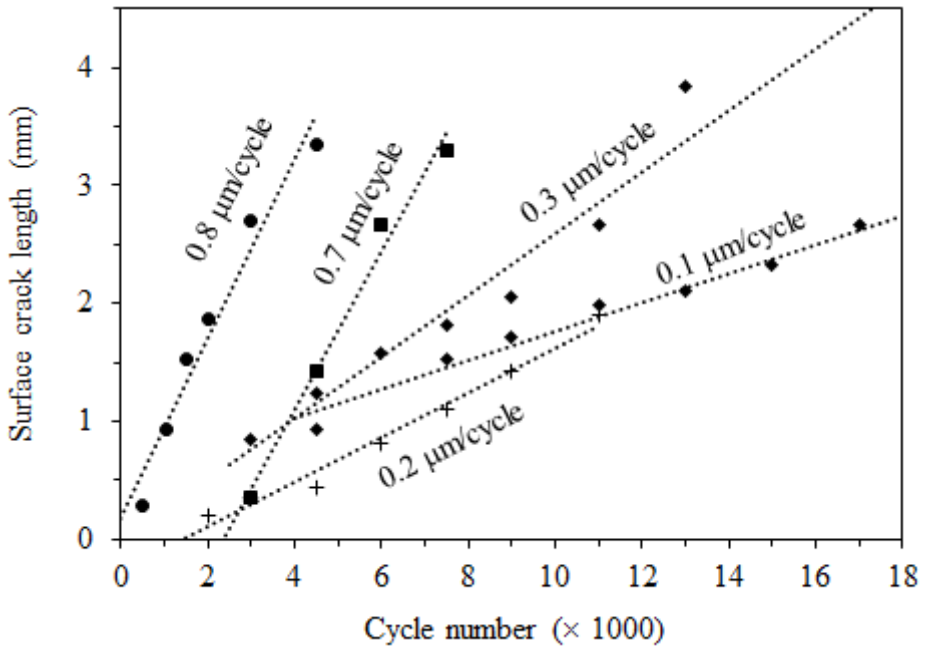

Figure 68. Growth of 5 single cracks with increasing cycle number in a coating A fatigue sample with original substrate under a strain range of 0 – 0.45% (FTB-4).

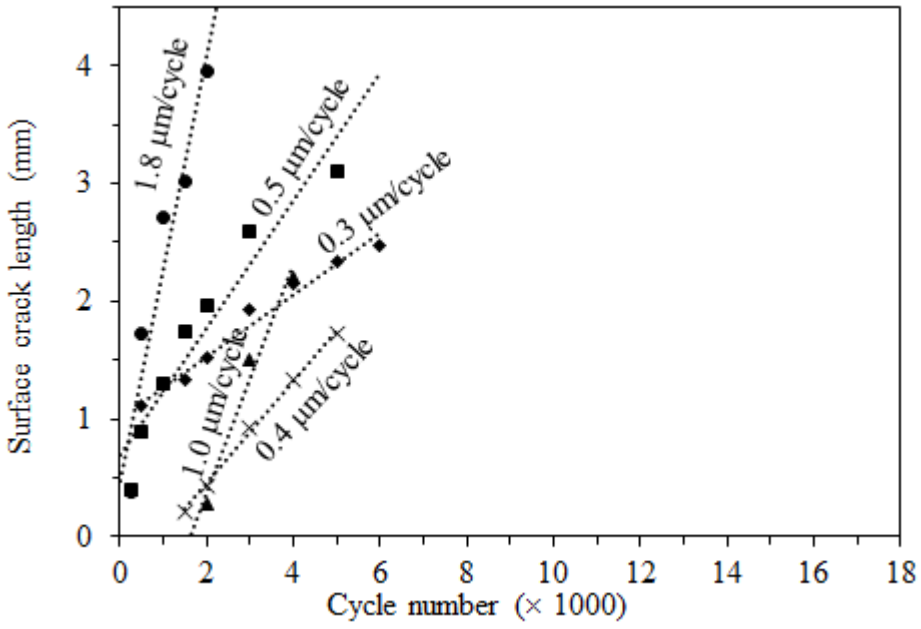

Figure 69. Growth of 5 single cracks with increasing cycle number in a coating A fatigue sample with original substrate under a strain range of 0 – 0.58% (FTB-9).

Growth of co-linear cracks in interaction

It was also found that the growth of originally co-linear and later interacting cracks, if treated as one crack, will also be of linear relationship with cycle number. The morphology of 3 such cracks under an increasing cycle number is shown in Figure 70B. Crack A was initially an independent crack until 3500 cycles, at which another two cracks B and C initiated at either tip of crack A. The crack growth plot shown in Figure 70A shows that the growth of crack A significantly slowed down upon the initiation of cracks B and C, which then grew independently at their own rates. Considering the number of crack tips growing independently after the appearance of cracks B and C was the same as before, these cracks were then treated as one crack, of which the length increase with the cycle number is also plotted in Figure 70A. The linear relationship of the total crack length of these 3 cracks with increasing cycle number indicates a constant growth rate for a constant number of crack tips not in interaction.

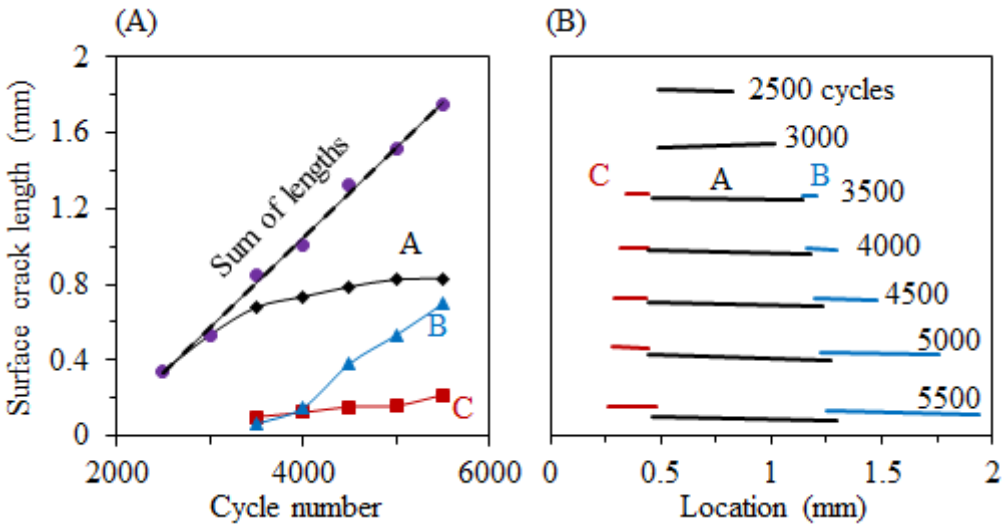

Figure 70. (A) Lengths of three interacting cracks observed on a coating B sample (FFB-8) tested at a strain amplitude of ±0.25%. (B) An illustration of the morphology of the cracks.

4.4.5. Total crack growth

Considering the multiple cracking behaviour of the coatings as well as the wide spread of single crack growth rate within each sample under cyclic strain, the fatigue damage of the coatings was quantified using the total length of the cracks (L_{total}), which is the sum of the length of all cracks measured over an area 12.5 × 8 mm^2 within the gauge length, see equation (42). Full data set of total crack development of all measured samples can be found in Appendix v.

$$L_{total} = \sum_{i}^{N} l_i \tag{42}$$

Here, l_i is the length of a single crack, and N is the number of crakcs.

Typical total crack length development

A typical total crack length evolution with increasing cycle number is shown in Figure 71A, which shows the total crack lengths of a coating B sample tested at a strain amplitude of ± 0.35%. The plot shows that the damage was first recorded at 700 cycles, and then increased almost linearly with the cycle number to 2000 cycles. After that, the increase rate of the total crack length significantly reduced. This trend reflects the surface crack development shown in Figure 71 B to E. At 800 cycles, the first crack with a length of about 1.5 mm initiated, and soon after that at 1500 cycles more cracks initiated and longer cracks also appeared. This trend continued until at 2000 cycles where long cracks formed a multiple crack pattern across the width of the sample. This pattern did not change much until the finish of the test at 4500 cycles. At the cycle number of 2000, it is believed that the total crack length reached a relatively saturated state, and thus the growth rate of total crack length significantly reduced.

For most tested samples, especially coating A samples, the substrate failed by fatigue crack growth, but the saturation of coating fatigue cracks was not observed. A typical example is given in Figure 72, which shows the total crack length of a coating A sample

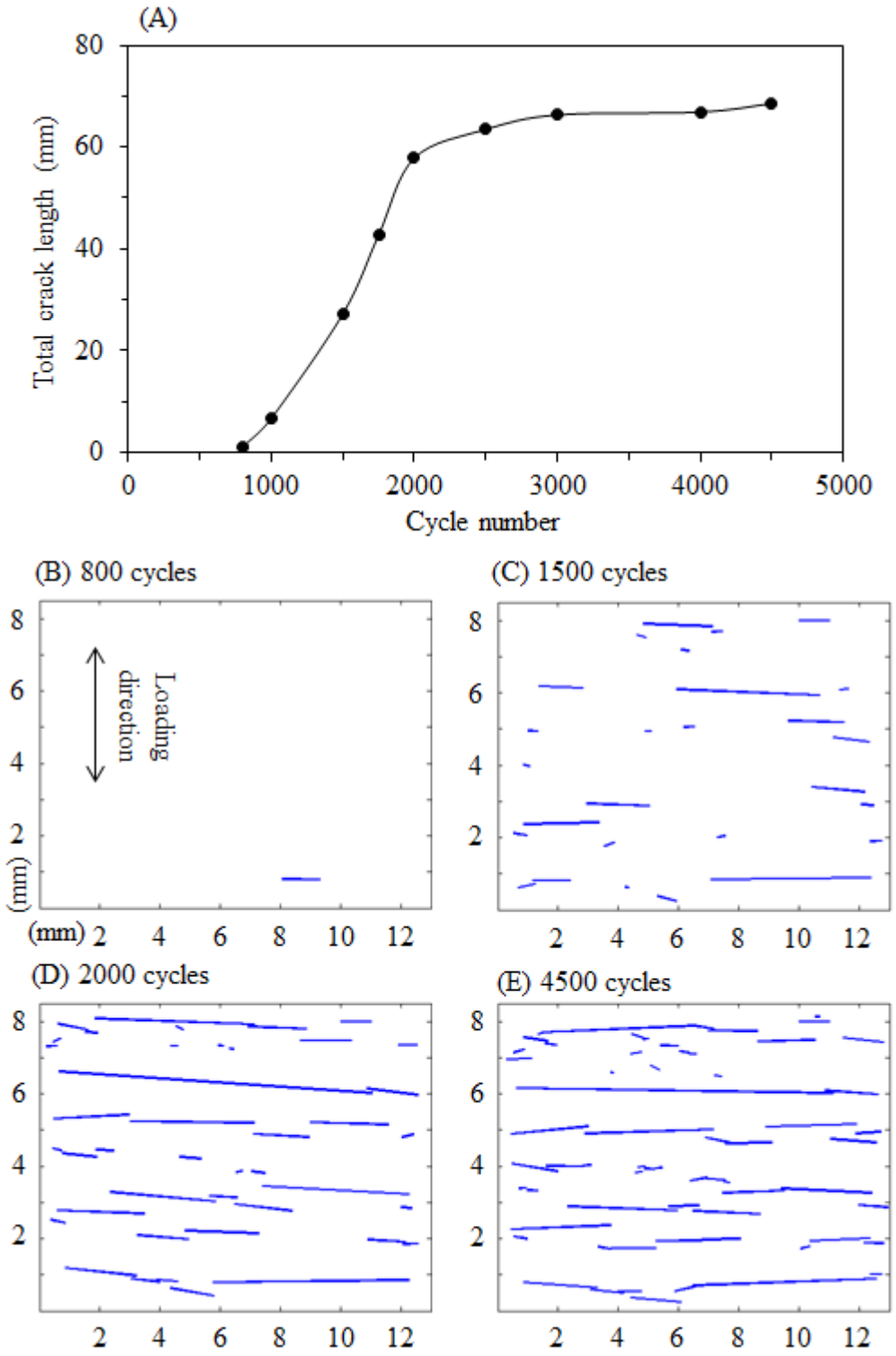

Figure 71. (A) The development of total crack length of a coating B sample (FFB-11) tested at a strain amplitude of ±0.35%, the test was stopped at 4500 cycles; (B) to (E) are the representation of surface crack morphology at 4 selected cycle numbers.

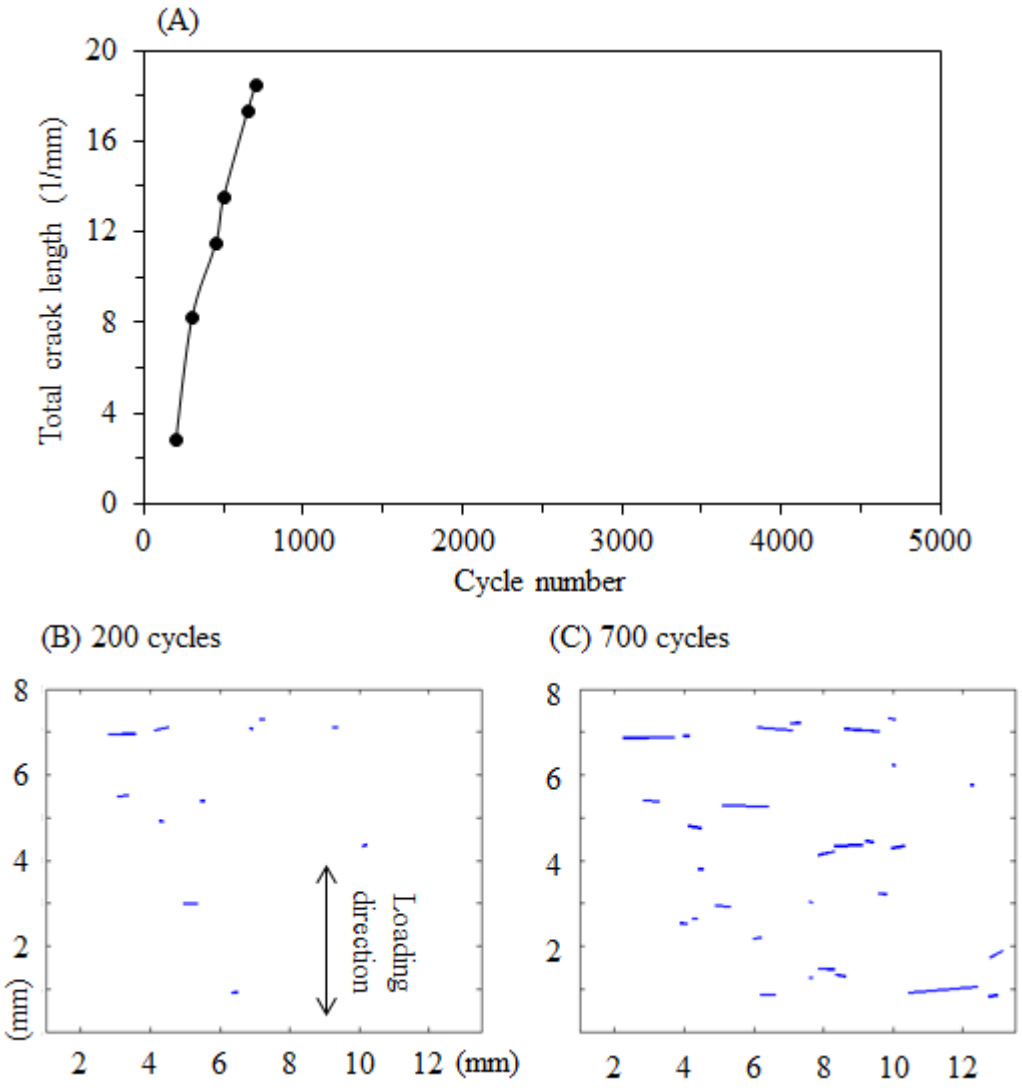

Figure 72. (A) The development of total crack length of a coating A sample (FTA-5) tested at a strain range from 0 ~ 1%. The test was stopped at about 800 cycles due to substrate failure; (B) and (C) are the illustration of surface crack morphology at 2 selected cycle numbers.

tested under zero-tension cycles with a strain range of 1%. The substrate failed at about 800 cycles before the next planned recording. The plot shown in Figure 72 shows a linear relationship between the total crack length and cycle number, indicating a constant total crack growth rate. The Figure 72 B and C show the surface crack development at the appearance of the first crack at 200 cycles and the last recording at 700 cycles, at which the cracks did not saturate the coating surface, and therefore the total crack length still grew linearly with the cycle number.

Strain range dependence of total crack length

It was found that the size of strain range had an effect on the total crack length development, Figure 73 plots the total crack length of samples of both coatings A and B under different cyclic strain magnitudes. For coating A, all the samples did not reach the saturation of surface cracks, and therefore they all appeared to be linearly proportional to the cycle number. For coating B, the sample tested at ± 0.3% did reach surface crack saturation, however in a much smoother fashion than the sample tested at ± 0.35%, and therefore did not show a drastic slope change in the plot. For the sample tested at ± 0.2%, the plot appears to be linear also because that the saturation was not achieved. For all the samples, the slopes of the linear region of the plots reflected the rate of total crack length development before surface crack saturation, and the figure shows that the samples tested under bigger strain amplitudes or ranges have steeper slopes than those tested under smaller strain amplitudes and ranges.

Total crack growth rate and correlation with strain range

A total crack growth rate was determined using the slope of the linear portion of the total crack growth development with cycle number (such as FFB – 11 shown in Figure 73B), if no saturation occurred, i.e. the total crack growth curve remained linear, the entire curve was used (such as those in Figure 73A). The full data set of total crack growth rate for all measured fatigue samples can be found in Appendix vi. Figure 74 shows the relationship between the total crack growth rate and strain range of all samples. Here, strain range is the difference between the maximum and minimum strain of a cycle.

In general, the data points of coating B are to the left of those of coating A, which means that to achieve the same total crack growth rate coating B required a smaller strain range than coating A. This indicates coating A was more resistant to fatigue crack growth than coating B. For both types of coatings, the data points of the samples tested under both fully reversed and zero-tension cycles did not show a distinctive difference. For

coating B, the state of substrate did not appear to affect the total crack growth rate either.

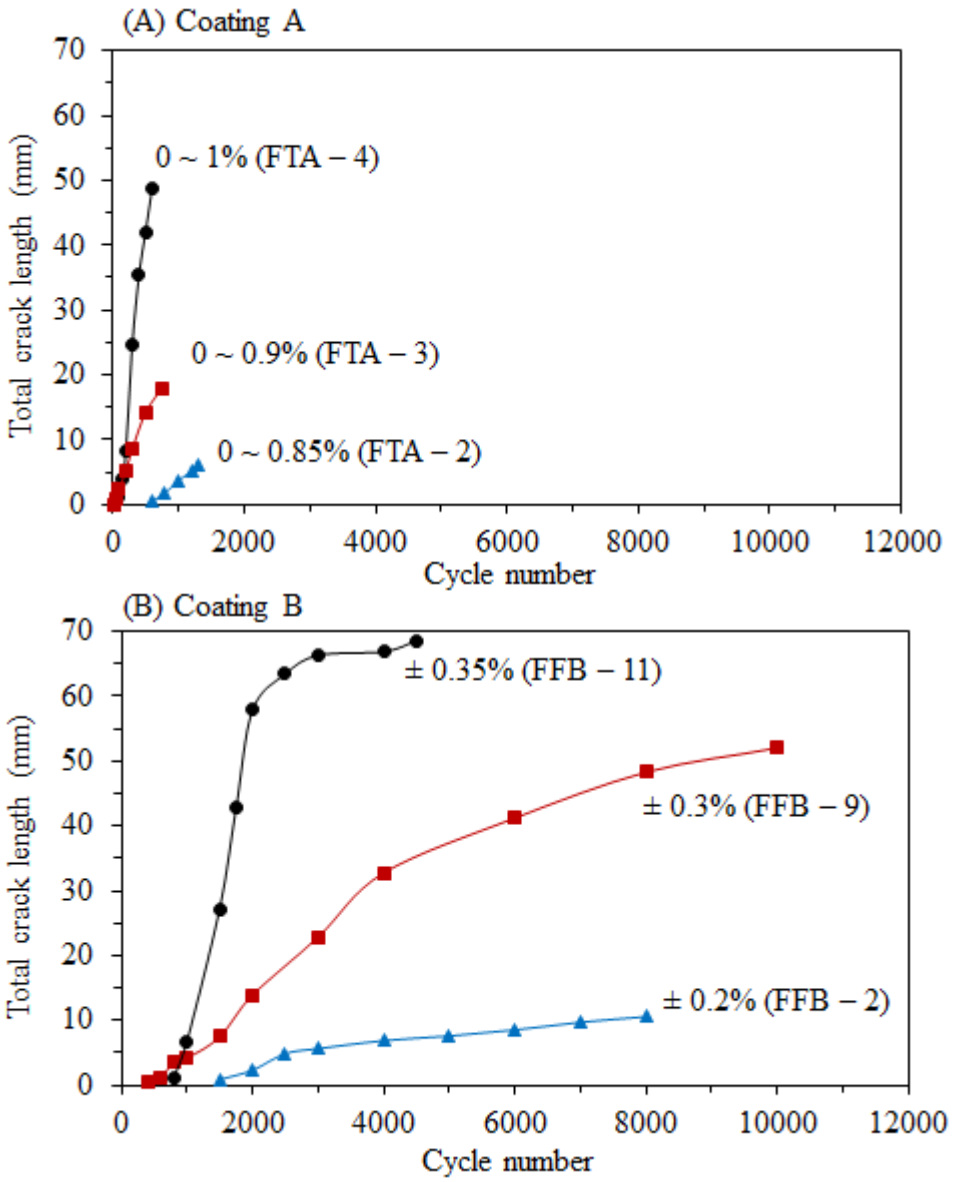

Figure 73. The total crack length development with an increasing cycle number. (A) Coating A samples under zero-tension cycles; (B) Coating B samples under fully reversed cycles

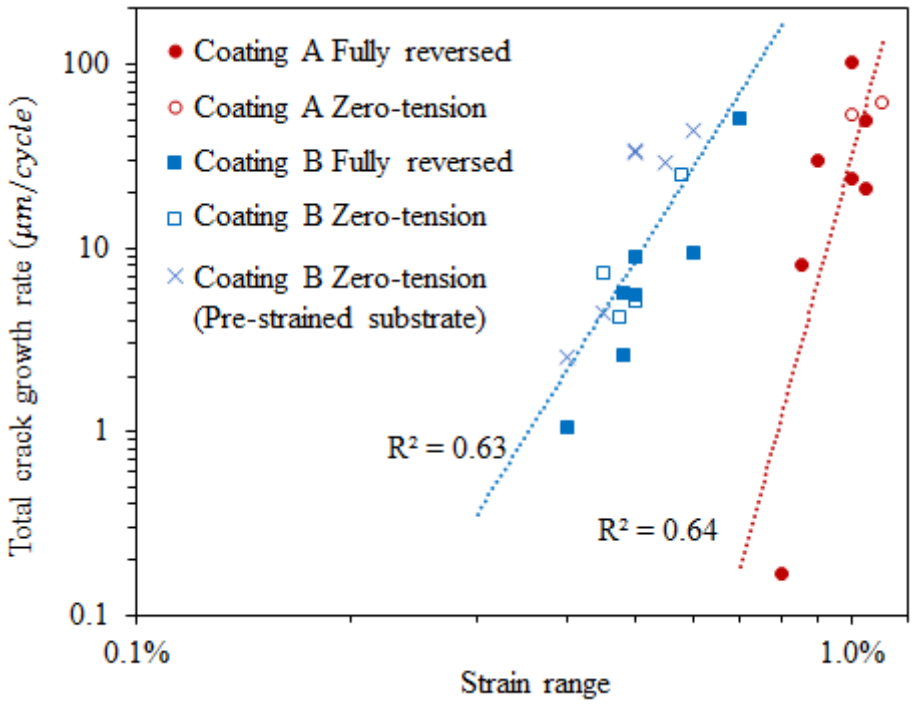

Figure 74. Total crack growth rate as a function of strain range.

The data has been fitted to a Paris' Law – like relationship by equation (43). Here $\frac{da}{dN}$ is the total crack growth rate per cycle, $\Delta\varepsilon$ is the strain range, and C and m are two empirical factors determined by fitting. The fitted lines are shown as dashed lines in Figure 74, the resultant fitting parameters C and m are shown in Table 10. The R^2 values of the fittings were 0.63 and 0.64 for coatings A and B, which indicate the scattering nature of fatigue test results. The m factor of coating A is about 2.5 times that of coating B, indicating that the sensitivity of the total crack growth rate of coating A is greater than that of coating B. This can be seen in Figure 74.

$$\frac{da}{dN} = C(\Delta\varepsilon)^m \tag{43}$$

Table 10. Resultant parameters of fitting total crack growth rate - $\Delta\varepsilon$ to equation (43).

	C ($\mu m/cycle$)	m
Coating A	1.82×10^{30}	14.4
Coating B	2.12×10^{15}	6.25

4.4.6. Crack number and average crack length quantification

In addition to the total crack length development, the number of coating cracks developed within gauge length during the fatigue tests was quantified. Here, a crack is defined as a crack with only two tips, and if two cracks coalesced the cracks were then counted as one crack. Figure 75 and Figure 76 serve as an example showing typical crack number development with increasing cycle number in coating A and coating B respectively. Full crack number data for all samples measured can be found in Appendix V.

Figure 75 and Figure 76 show that in both coatings the number of cracks increased with cycling. There is a general trend that the increase of crack number is more rapid in samples tested under greater strain ranges. A stabilisation of crack number increase was observed in both coatings, and it was more marked in coating B.

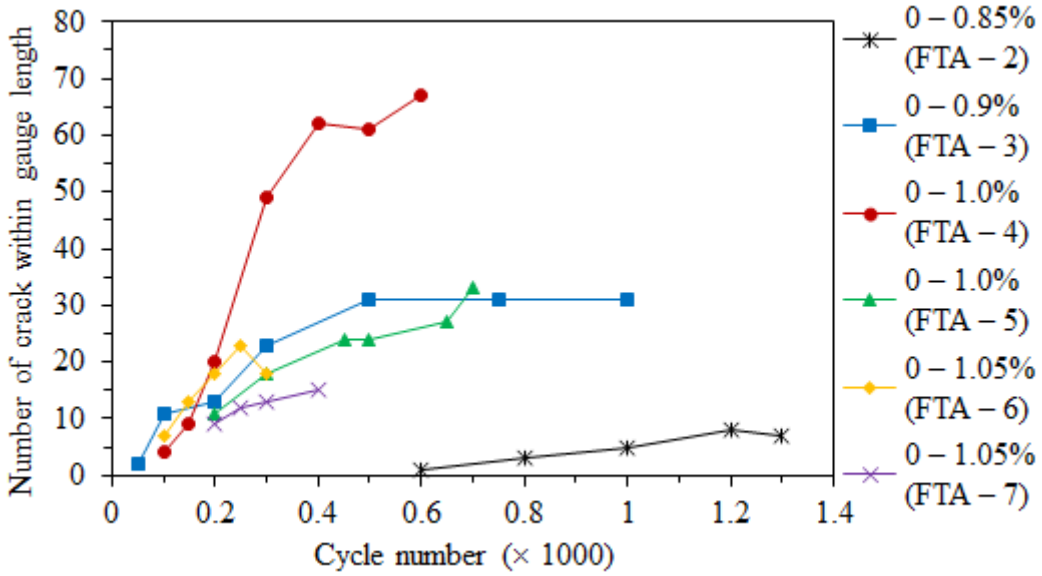

Figure 75. Number of cracks as a function of cycle number in a coating A samples under zero-tension cycles

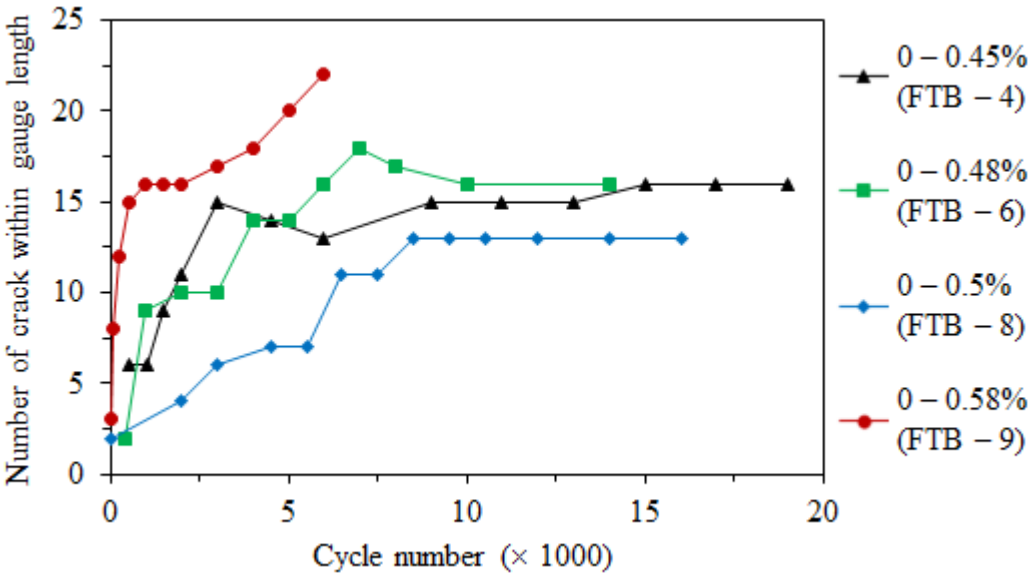

Figure 76. Number of cracks as a function of cycle number in a coating B under a zero-tension cycles.

The average crack length (L_{avg}) was calculated by dividing the total crack length (L_{total}) using the number of cracks (N_{crack}), see equation below.

$$L_{avg} = L_{total}/N_{crack} = \sum_{i}^{N} l_i \, /N_{crack} \tag{44}$$

As an example, Figure 77 and Figure 78 show the average crack length as a function of cycle number of coatings A and B samples. It can be seen that in both coatings the average crack length increased with cycle number, reflecting the growth of single cracks. However, there is no clear evidence of any effect of strain range on the development of average crack size. In comparison to coating B, the average crack length of coating A was below 1 mm throughout the tests, while the average crack length of coating B reached above 2.5 mm.

As the strain-life relationship in Figure 59 (page 102) shows that the coatings had very distinctive resistance to fatigue cracking, the characterised fatigue cycle ranges of coating A (about 2000 cycles maximum) were much more limited than that of coating B

(to a maximum about 20000 cycles), whilst the strain ranges applied to coating B samples were about only 50% of those applied to coating A sample.

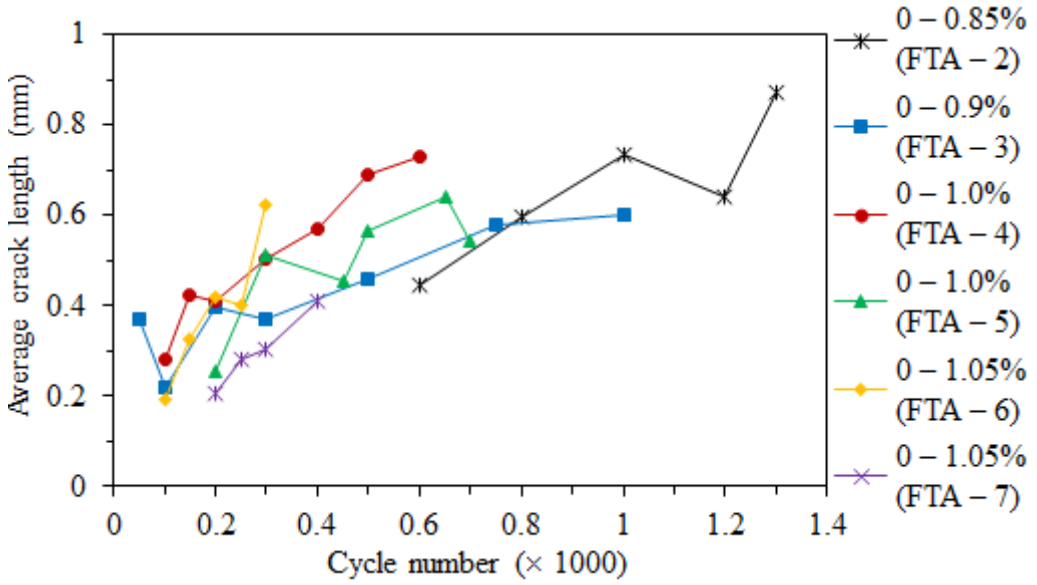

Figure 77. Development of average crack length with increasing cycles in coating A samples under zero-tension cycles.

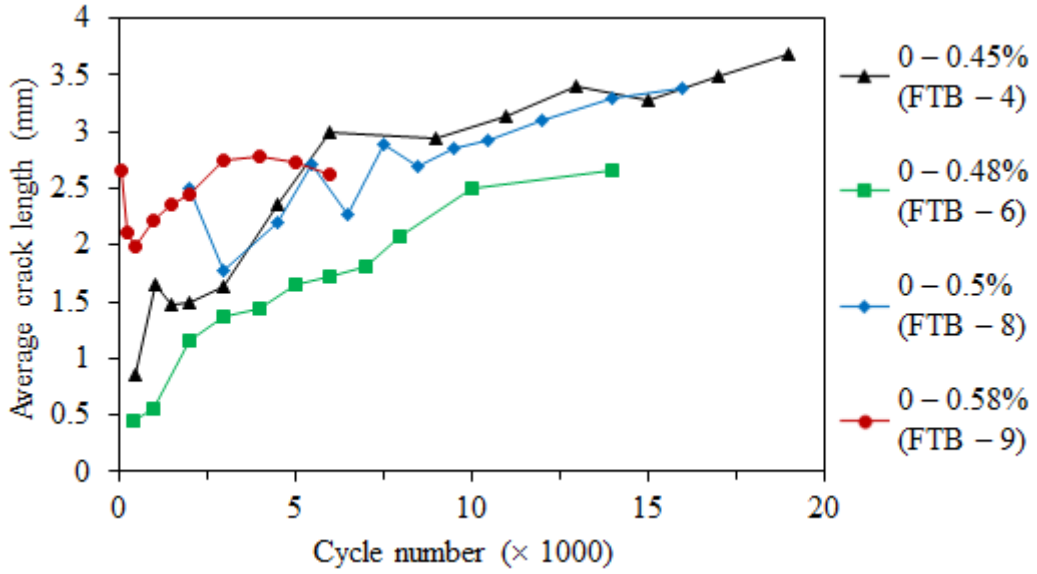

Figure 78. Development of average crack length with increasing cycles in coating B samples under zero-tension cycles.

In order to make direct comparisons, the crack number and average crack length results shown from Figure 75 to Figure 78 were re-plotted against total crack length,

which is shown in Figure 79, in which the symbols with solid lines represent coating A samples, while those with dashed lines represent coating B samples.

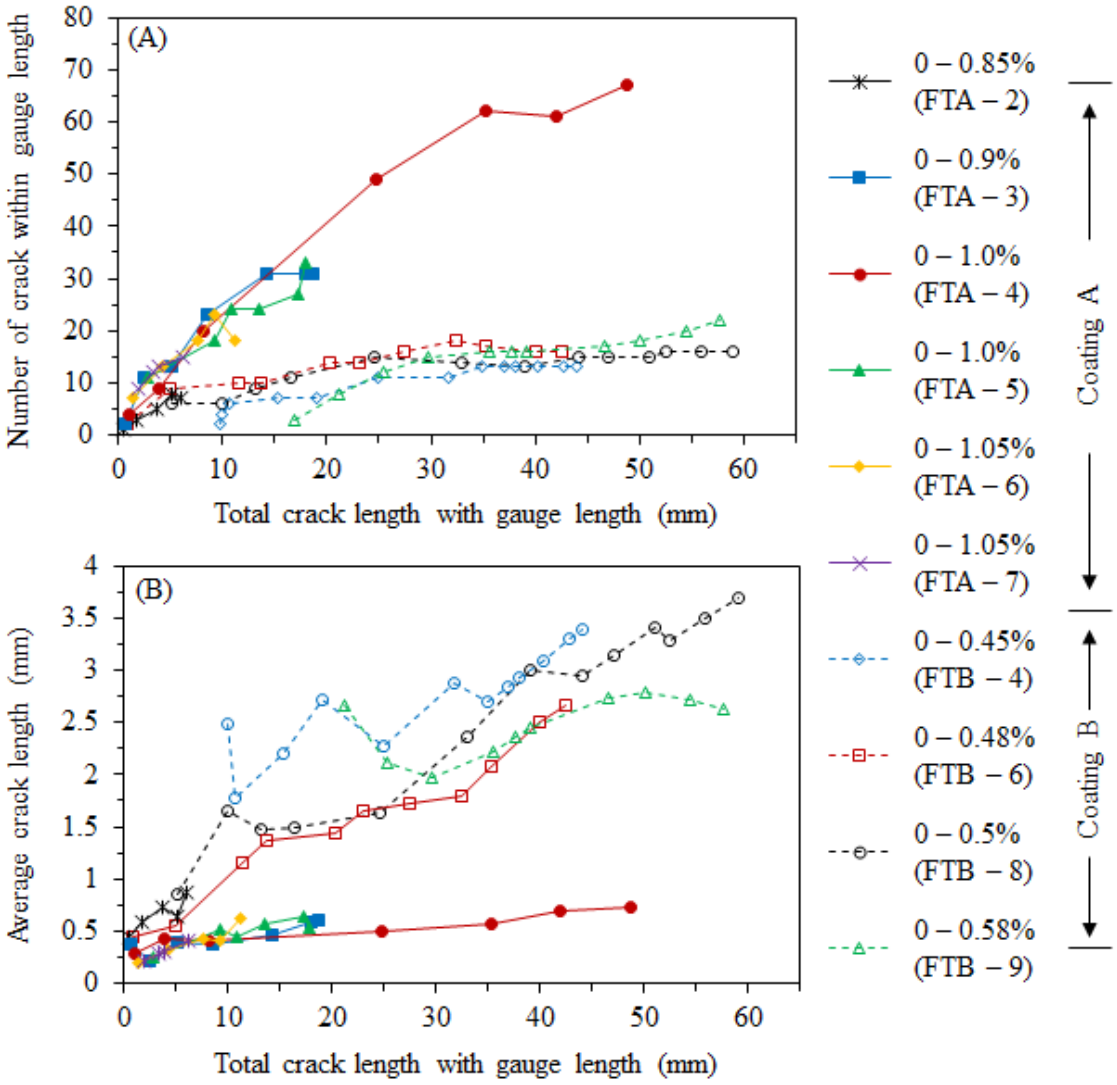

Figure 79. Number of fatigue cracks (A) and average fatigue crack length (B) as a function of total crack length in coatings A and B.

Figure 79A shows the relationship between crack number and total crack length of coatings A and B. It can be seen that in both coatings the number of cracks increases almost linearly with the total crack length. Again, no obvious effects of strain range was observed. It is clear that the development of crack number in coating A is much faster than coating B. At a total crack length of about 50 mm, the number of cracks in coating A

could be about 3 times the number of cracks in coating B. Figure 79B the relationship between average crack length and total crack length of coatings A and B. The trend of average crack length is opposite to that of the crack number. Coating B tended to develop greater average crack length than coating A, and at a total crack length of about 50 mm, the average length of fatigue cracks in coating B could be about 3 times that in coating B.

5. NUMERICAL MODELLING OF SUBSTRATED COATING SAMPLE FAILURE

As introduced before, the coating fracture is treated as two processes, namely crack penetration and channelling. For coating cracks under uniform remote normal stresses, Beuth [129] developed close-form approximations for the energy release rates of these two processes, see equations (23) - (27). Based on these equations, the energy release rates of crack penetration and channelling from a defect can be calculated when the modulus and Poisson's ratio of both coating and substrate, as well as the defect depth and coating thickness are known. These equations only deal with situations where the material properties are constant. However, the stress-strain behaviour of the coatings and substrate has shown non-linearity under an increasing strain, which means the moduli of both coating and substrate were not constant. Given this, calculations using Beuth's equations with constant elastic modulus would not be appropriate when the material deformation exceeds the linear region. In the current work, numerical modelling was performed to investigate the fracture process of substrated coating beyond the linear elastic region during the mechanical testing.

5.1. Finite element fracture mechanics model

Adopting the same treatment for coating cracking used in several previous works [128,129,174], the coating crack penetration process is treated as a 2D plane strain problem, and a 2D FE model in plane strain was developed, see Figure 80. This model simulates half of a 25 mm long and 5.5 mm thick substrate supporting a 0.3 mm thick coating covering the whole top surface of the substrate. The actual length of the model was only 12.5 mm as the other half was symmetric to the model, with the left edge serving as longitudinal centre. A vertical defect with a depth of a was introduced to the coating surface at the left edge of the model. Apart from the crack, the rest of the left edge including both coating and substrate sections was assigned with X-symmetry, which constrained movement of the left edge but allowed the crack to open under tensile stresses. As the neutral axis of the system is not in the centre of the substrate, the system

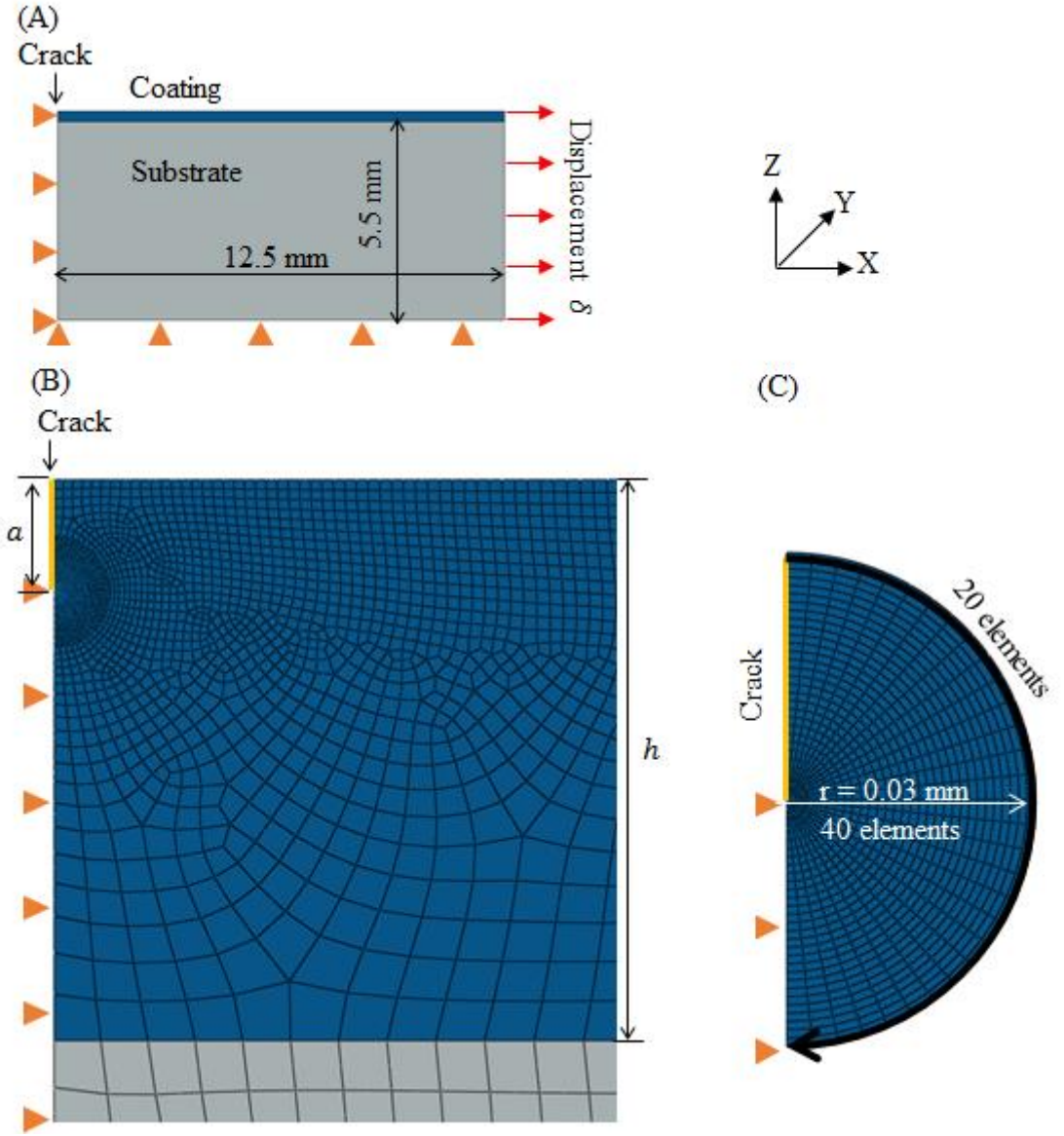

Figure 80. 2D plane strain model for the calculation of J-integral of crack penetration in coating on a 5.5 mm flat substrate. (A) shows the dimensions of the model; (B) shows the mesh near the crack; (C) shows the mesh and dimension of the crack tip contour region.

will bend under a tensile stress. Considering that the modulus and thickness of the substrate are much greater than the coating, thus any bending will be small, and the bottom of the model was assigned with Y direction constraint, this assumed the model will not bend under stress. Mechanical strain was applied uniformly on the right edge of the model. To include thermal residual stress, a temperature reduction can be applied to the model. All the elements were 8-node rectangular plane strain elements, and at the crack tip the elements were collapsed into triangle shape with two nodes at the tip.

In ABAQUS, energy release rate is calculated in terms of J-integral with linear material properties, as energy release rate and J-integral are equivalent in linear elastic situations. J-integral can be calculated directly using a contour integral method included in the software package. Details of the formulations used for calculation are clearly described by Brocks [95], and they can also been found in ABAQUS documentation [175]. It essentially uses the expression of J-integral developed by Rice [94], see equation (17). In theory, the accuracy of J calculation using contour integral depends on the size of the contour integral region. In the current model, as shown by Figure 80C the contour integral region had a radius of 0.03 mm, which was found sufficiently large to have accurate J calculation, as the J calculated using bigger contour integral regions was found unchanged. In the 2D model, only the J-integral for crack penetration (J_p), can be calculated directly using the contour integral technique.

The J-integral for the crack channelling process (J_{ch}), in which the crack growth is in the direction perpendicular to the X-Z plane shown in Figure 80, can be calculated indirectly only by using the remote stress and crack opening induced by the applied strain. The calculation procedure has been used and reported by Beuth and Klingbeil [174], of which a brief description is given as below.

Under a uniform normal stress, a crack with a depth of a in a coating with a thickness of h will open, see Figure 81A. When the crack tip channels a unit length (dl), a slice of crack will develop the profile like that shown in Figure 81A, and the slice will have a thickness of dl. Thus the energy released due to cracking can be treated as the difference between the energy stored in the un-cracked material far ahead of the crack tip and the work done (W') for the generation of the slice of crack opening far behind of the crack tip [129,174].

At each position along the y direction of the coordinate defined in Figure 81A, the crack face has an opening displacement of $\delta(y)$. A collective crack face opening Δ' can be expressed by equation (45). To achieve this Δ', a stress of $\sigma(\Delta')$ is needed. A schematic relationship between σ and Δ' can be found in Figure 81B.

$$\Delta' = \int_0^a \delta(y)\, dy \tag{45}$$

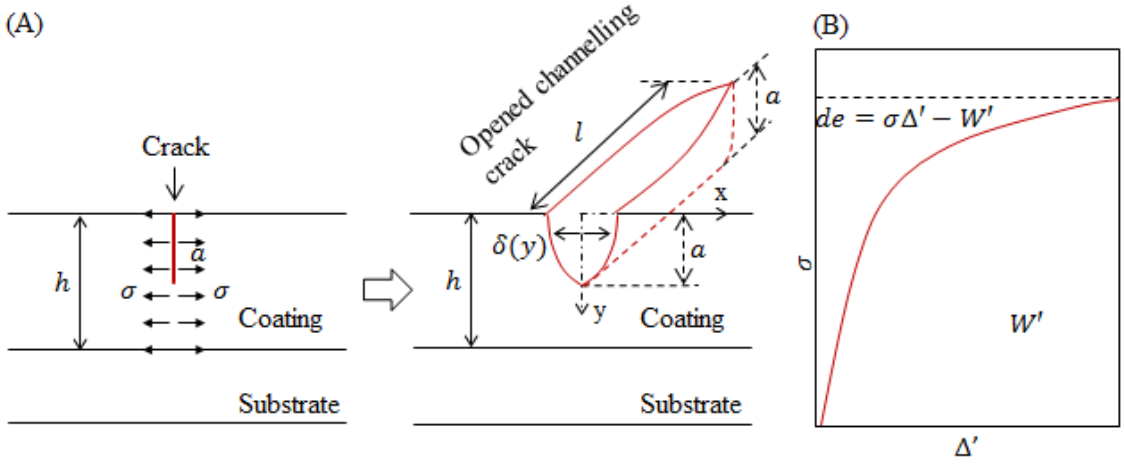

Figure 81. (A) Illustration of coating crack opening under a uniform normal stress; (B) Schematic relationship between stress and corresponding collective crack face opening displacement.

This crack opening is a cross section of a channel crack far behind the crack tip, the energy consumed for the development of the slice of crack opening W', can be expressed by equation (46).

$$W' = \int_0^{\Delta} \sigma(\Delta')\, d\Delta' \tag{46}$$

W' is essentially the area below the σ-Δ' curve. The energy stored far ahead of the crack tip can be simply found as the product of σ and Δ'. Then the energy released by the cracking (de) can be found using equation (47), and it is essentially the area above the σ-Δ' curve.

$$de = \Delta'\sigma - W' \tag{47}$$

Following above, the J-integral of crack channelling (J_{ch}) in the steady state can be expressed.

$$J_{ch} = \frac{de}{a} \tag{48}$$

5.2. Benchmarking of Linear Elastic Numerical Model

In this section, the FE fracture mechanics model will be benchmarked to Beuth's equations. As Beuth's equations are only valid for linear cases, the linear stress-strain behaviour of coating A and steel substrate were used. According to Table 2, the modulus of the coatings, 5.2 GPa, and the Poisson' ratio 0.3 was used. The substrate modulus of 200 GPa, and Poisson's ratio of 0.3 was used. A series of defect sizes a from 30 to 300 μm were investigated, and the ratio of defect size to coating thickness, a/h, was from 0.1 to 1. A uniform tensile strain of 1% was applied on the right edge of the model. The J-integral of crack penetration (J_p) and channelling (J_{ch}) for selected defect sizes were calculated using the methods described in the last section. Recall that in linear elastic case, J-integral is equivalent to energy release rate (G).

The same linear material properties, coating thickness, and defect depths were used in Beuth's equations to calculate the energy release rates of crack penetration and channelling. Using the Young's modulus and Poisson's ratios of the materials, the Dundur's parameters were determined using equations (20) and (21), and α was found to be -0.95 and β was found to be -0.27, which reflect that it was combination of a high-modulus substrate and a low-modulus coating. The Dundur's parameters were then employed into to equation (22), and the singularity exponent s was calculated to be 0.302. These parameters along with a series of a/h ratios ranging from 0 to 1 were then introduced into equations (24) and (27), which produced the values of f and g factors for different a/h ratios. The values of f and g factors can be introduced to equations (25) and (26) to calculate the energy release rates. In the current calculations the energy release rates were non-dimensionalised by rearranging equations (25) and (26) into equations (49) and (50) shown below. In these equations, $ND(G_p)$ and $ND(G_{ch})$ are non-dimensionalised energy release rates for crack penetration and channelling respectively.

$$ND(G_p) = \frac{\bar{E}_C G_p}{\pi \sigma^2 h} = f\left(\alpha, \beta, \frac{a}{h}\right)^2 \tag{49}$$

$$ND(G_{ch}) = \frac{G_{ch}\bar{E}_c}{\pi\sigma^2 h} = \frac{1}{2}\, g\left(\alpha, \beta, \frac{a}{h}\right) \quad (50)$$

The non-dimensionalisation eliminated the direct influence of coating thickness h and stress σ, and only kept the Dundur's parameters representing the coating/substrate stiffness mismatch, and a/h ratio representing the depth of crack tip relative to the interface. The non-dimensionalised values can be directly calculated by introducing the values of f and g factors into equations (49) and (50) respectively. Similarly the results produced using the FE model can also be non-diminsionalised using the middle terms of equations (49) and (50). The non-dimensionalised linear J-integrals of crack penetration and channelling as a function of a/h ratio, produced by both the FEA model and Beuth's equations are shown in Figure 82.

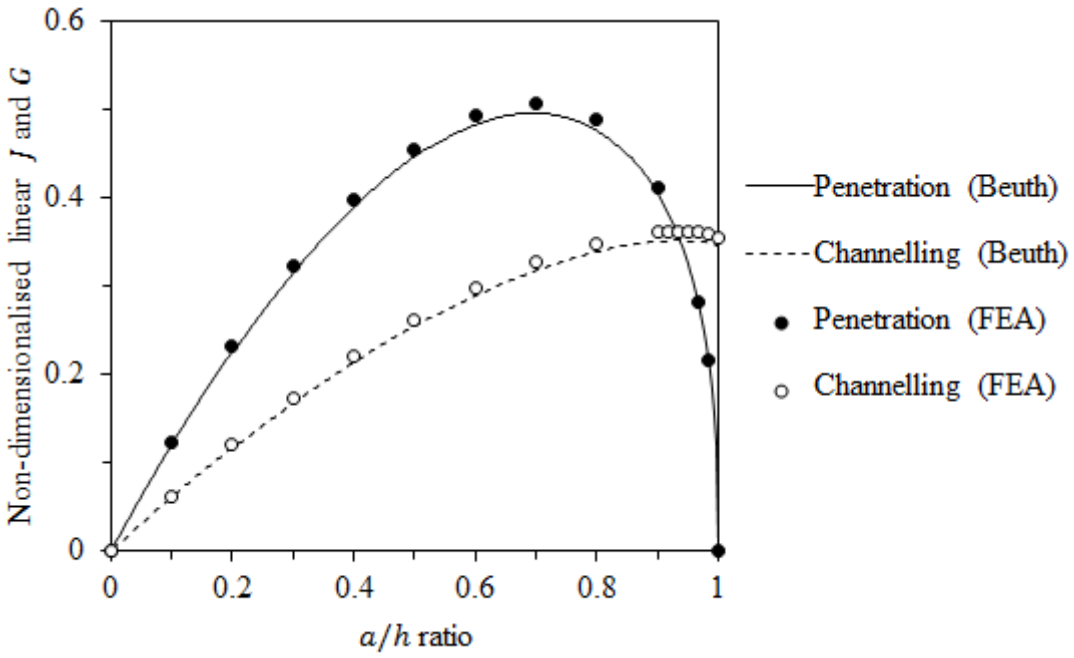

Figure 82. Non-dimensionalised J-integral of crack penetration and channelling calculated using Beuth's equations and the 2D FEA plane strain model. Linear material properties were used.

The FEA results demonstrate the same trends as the results calculated using Beuth's equations. The two sets of results show a very good match, the maximum difference between them is about 3% of the set calculated using Beuth's equations. For the results calculated using both methods, the penetration plot exhibits a near parabolic shape, it peaks at an a/h ratio of about 0.7 and decreases afterwards and approaches 0 as the

a/h ratio approaches 1. The channelling plot increases for most of the a/h range until an a/h of about 0.93, where it intersects with the penetration plots. After that, the channelling plot value slightly reduces to about 98% of the maximum. Before the penetration plots reach the peak, it is more than 70% higher than the channelling plots and becomes lower than the channelling plot after their intersection. Figure 82 indicates that for defects with a/h ratio less than 0.93 the penetration process is favoured compared to the channelling process.

5.3. Material Properties Use for Non-linear Elastic Modelling

During the substrated tensile tests, both coating and substrate experienced non-linear deformation, hence had changing stiffness mismatch at different strains, which would influence the calculation of the J-integrals [129]. To include the effect of changing stiffness mismatch, the elastic stress-strain behaviour of the materials ought to be incorporated. As J-integral is calculated using deformation plasticity, the elastic-plastic stress-strain behaviour is represented for monotonic loading as non-linear elasticity.

The non-linear stress-strain behaviour of the materials at ambient temperature (~23 °C), shown in Figure 23 (page 52) for the coatings and in Figure 36 (page 67) for the substrate, were employed in a form depicted by the Ramberg-Osgood relationship [176] as follows.

$$E\varepsilon = \sigma + \theta\left(\frac{|\sigma|}{\sigma_Y}\right)^{n-1}\sigma \tag{51}$$

Here, σ_Y is the yield stress of the material, θ is the "yield" offset, and n is the hardening exponent. The parameters θ and n can be found by fitting the expression to the known material stress-strain curves. Note, the Ramberg-Osgood relationship is normally used to describe the elastic-plastic deformation of materials, however, in the current work, it was used only to describe the material stress-strain curves for the FE analysis. The factors σ_Y, θ, and n are used as fitting parameters without physical meanings.

Given that the measured stress-strain behaviour of the coatings are similar, the coating A stress-strain behaviour at ambient temperature was adopted for both coatings. Also, in all the calculations, the deformation of substrate was considered to be uniform, and therefore only the stress-strain behaviour of the pre-strained substrate was used. Five stress-strain curves of free film samples of coating A and 5 stress-strain curves of pre-strained substrates were used to fit equation (51) using Matlab. To give the best fits, the yielding stresses of the coating and substrate were chosen as 15 and 500 MPa respectively, which achieved the best fits of the data. The results of θ and n are shown in Table 11. The stress-strain curves described by the employed Ramberg-Osgood relationships are shown in Figure 83. In ABAQUS the material deformation was described as non-linear elasticity, which under monotonically increasing stress or strain is an appropriate approximation of both coatings and substrate. Note, the actual coating strain to failure was about 0.74%, thus the stress-strain behaviour described using Ramberg-Osgood equation beyond the fracture strain is an extrapolation.

Table 11. Ramberg-Osgood parameters of the materials employed in the FEA models for non-linear analysis.

	Modulus E (GPa)	σ_Y (MPa)	θ	n
Steel substrate	200	500	1.554	23.370
Coating A	5.2	15	0.016	4.422

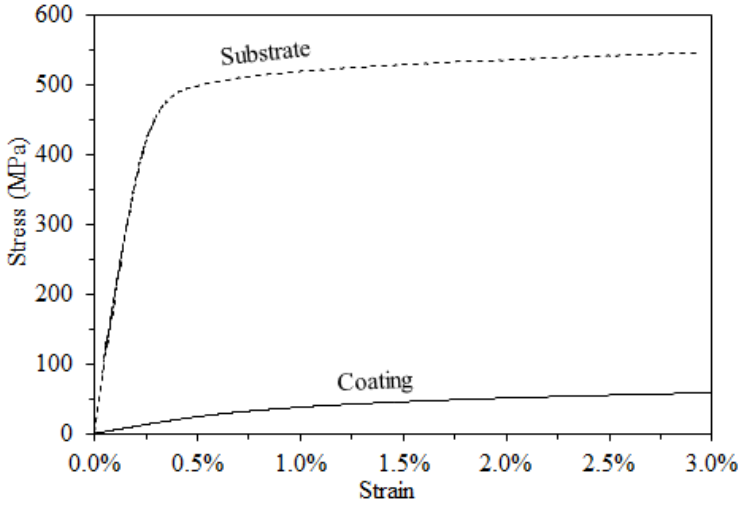

Figure 83. Stress-Strain curves of substrate and coating at 23 °C employed for numerical calculations.

5.4. Validation of Thermal Stress Calculation

In the substrated coating samples, the coatings developed thermal residual stresses after curing, see section 4.1. To model the fracture of substrated coatings, this thermal residual stress ought to be included in the calculation of J-integrals. A thermal residual stress model was set up to calculate residual stress in the current coatings at 23 °C, of which the results were compared to the experimental values.

5.4.1. Simulation of bi-layer strip deflection due to thermal stress

A 3D model simulating the coating/substrate bi-layer strip samples for thermal stress measurement was developed. The actual model simulated a quarter of the strip sample shown in Figure 84A. The edges at the centre lines were assigned with symmetry boundary conditions, see Figure 84B. The bottom edge of the transverse centre was fixed in Z direction movement, see Figure 84C, which simulated that the sample was supported on a surface with only a line contact. The average coating thicknesses of the strip samples, 0.24 mm and 0.29 mm for coatings A and B respectively, as well as the average substrate thickness of 0.21 mm were used for both coatings. All elements were 20-noded quadratic bricks. In the XY plane, the elements have the same length and width of 0.45 mm, and in Z direction (thickness direction) three elements were assigned in each layer. In ABAQUS, thermal strains/stresses can be induced by applying temperature reduction to a model with different thermal expansion coefficients being included as material properties. The deflection of the model under temperature reduction was compared to the measured values.

For the calculation of residual stress, the non-linear stress-strain curves of the materials were used. The thermal expansion coefficients of the coatings and steel substrate presented in Table 2 were used. For both coatings, temperature reductions from T_g to 23 °C were applied, for coating A it was 65 to 23 °C, and for coating B it was 69 to 23 °C. Here, the T_g was considered as the thermal stress free temperature, rather

than 100 °C, because above T_g the modulus of the coatings was so small that the thermal stress generated was negligible.

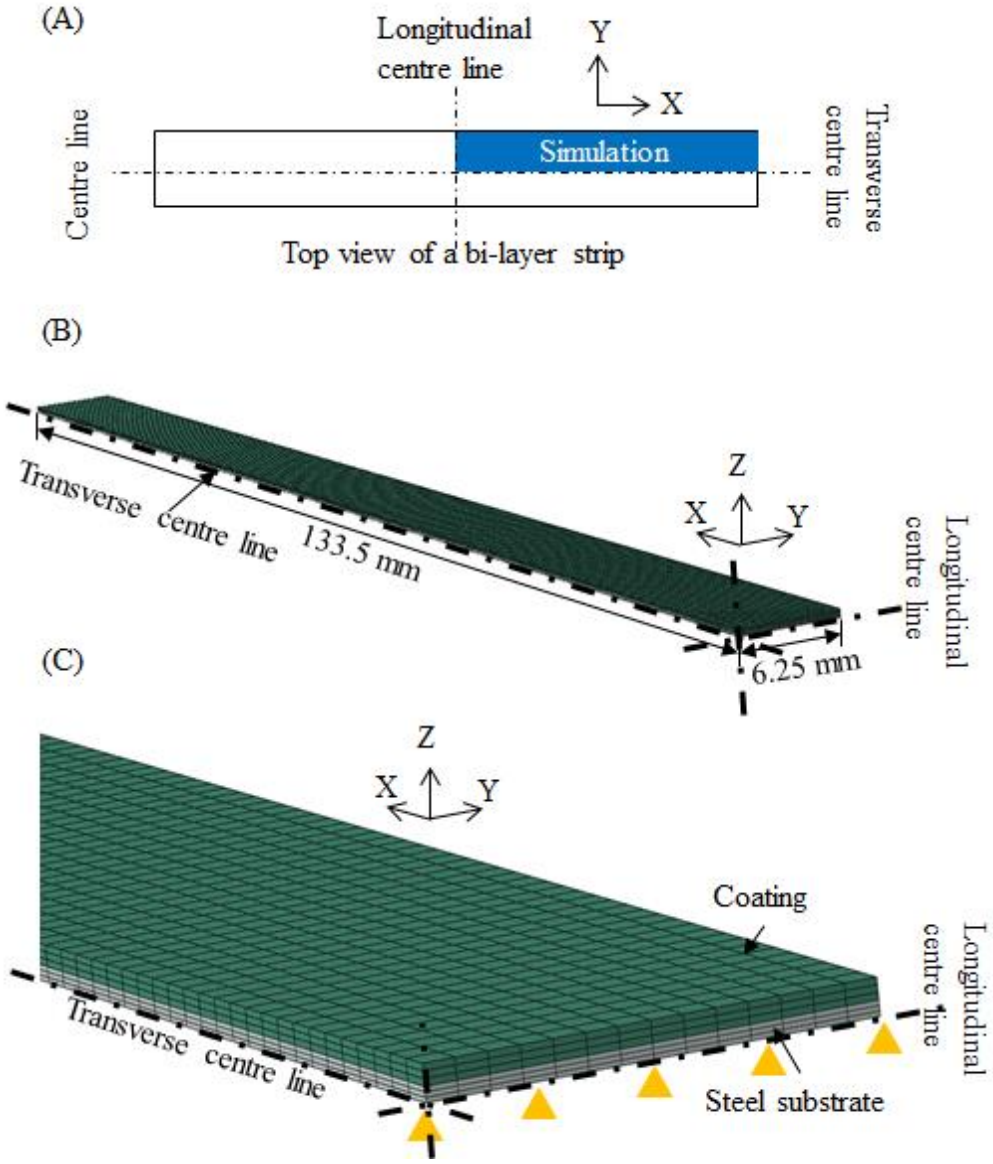

Figure 84. Illustration of the 3D model simulating a quarter of a coating/steel bi-layer strip sample. (B) shows the length and width dimension of the model; (C) shows a close-up view the centre of the model.

The deflections of the models with coatings A and B under the applied temperature reductions are shown in Figure 85. The result shows the entire 267 mm length of an actual bi-layer sample by mirroring the models. The deflections of the models were found to be 20.42 and 27.22 mm for coatings A and B respectively. The deflections along with the

material properties and other dimensions were also employed into equations (2) to (4) (page 10) to produce thermal stresses and equivalent mechanical strains, and the results are shown in Table 12, in which the measured values are also shown for comparison.

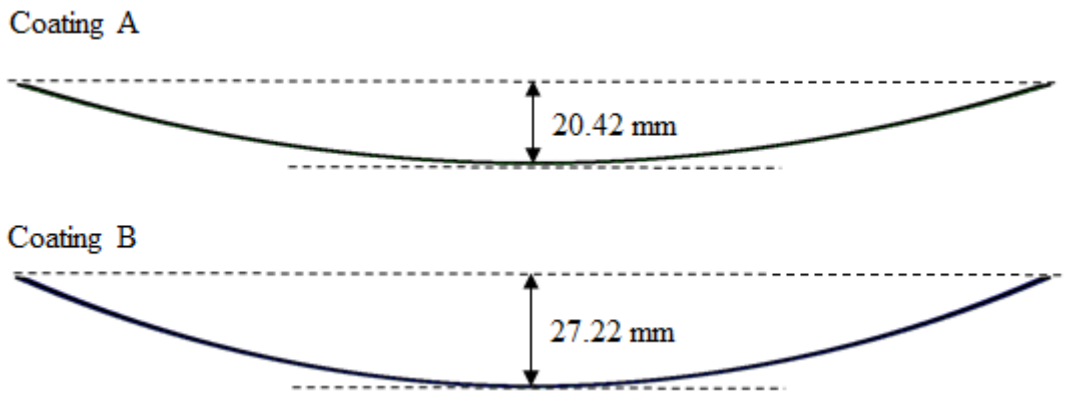

Figure 85. Deflections of the models under the applied temperature reduction from T_g to 23 °C. This figure shows the entire length of 267 mm by mirroring the models.

Table 12. Bi-layer deflections and corresponding thermal stresses and strains produced using FE modelling in comparison of experimental results.

	FE modelling			Experiment (average of 3 samples)		
Coating	Calculated Deflection (mm)	Thermal residual stress (MPa)	Thermal residual strain (%)	Measured Deflection (mm)	Thermal residual stress (MPa)	Thermal residual strain (%)
A	20.42	12.80	0.17	16.00 ± 2.23	10.93 ± 0.57	0.15 ± 0.01
B	27.22	14.67	0.20	26.11 ± 1.35	14.25 ± 1.15	0.19 ± 0.02

The results show that the deflections calculated using the FE models are greater than those measured experimentally. The deflection of coating A model is about 28% greater that the measured deflection, while the deflection of coating B model is only about 4% greater than the measured value. When the calculated deflections are converted into thermal stresses and equivalent mechanical strains, the differences between the calculated and measured values become smaller. The thermal stress and equivalent mechanical strain of coating A calculated using FE-produced deflection is about 17% greater than those measured experimentally, while the thermal stress and equivalent

mechanical strain of coating B calculated using FE-produced deflection is only about 3% greater than the experimental values. The reason why the FE model of coating A overestimated the thermal stresses might be that stress relaxation occurred in the coatings during the actual cooling process, which was not considered in the model. There are several other factors that could possibly influence the results. If the measured thermal expansion coefficient and T_g overestimated the actual values, they can produce overestimated thermal stresses. Also, the coating thickness in the models was uniform, if the measured coating thickness of the samples was overestimated compared to the average thickness along the sample length, this could also lead to an overestimated FE modelling results. In general, the FE model produced deflections similar to those measured experimentally, which provided confidence to use the measured thermal properties of the coatings in the calculation of J-integrals of coating cracks under thermally induced stresses.

5.4.2. Comparison between 2D and 3D models

Thermal stresses in coatings generated due to temperature changes are in a biaxial state, in which the stress in one direction equals the stress in a direction perpendicular to the first direction in the same plane. A 3D FE model would be the most appropriate to simulate stress development in such situations. However, in this work, the J-integrals of coating cracks under stress were evaluated using a 2D plane strain model. Thus there was a need to prove a 2D plane strain model was able to produce correctly thermal stress in the required direction. For this purpose, a 2D and a 3D model of a 0.3 mm coating on a 5.5 mm thick substrate were developed to calculate thermal stress and strain under the same temperature reduction, see Figure 86. The 2D model is essentially the FE fracture mechanics model. The 3D model simulates a quarter of a structure with a length of 25 mm and a width of 12.5 mm, which represent the gauge length of a substrated coating sample for static tensile tests. The 2D model is essentially a XY plane of the 3D model with no thickness in Z direction.

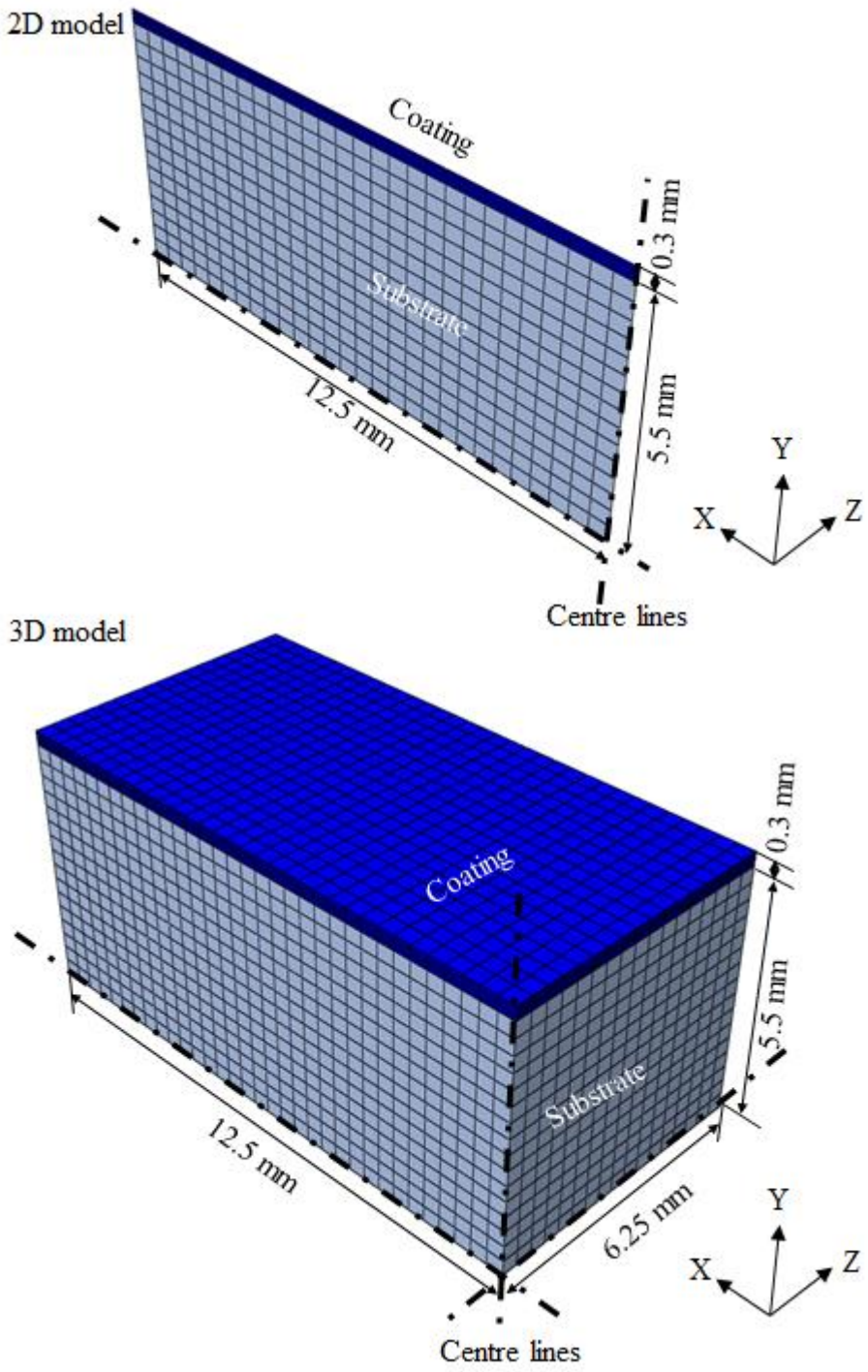

Figure 86. A 2D and a 3D model of a 0.3 thick mm coating on a 5.5 mm thick substrate. The dimensions of the 2D model are the same as those of the XY plane of the 3D model.

For the 3D model, the XY and YZ central planes were assigned with symmetries in Z and X directions respectively. Similar to the 2D model, a Y direction constraint was

assigned to the bottom surface of the 3D model, and the YZ plane at the other end was limited to keep perpendicular to the bottom surface at all time. The XY plane opposite to the central XY plane did not have any constraint, which simulated the free edge of a substrated coating sample.

For this calculation, the non-linear stress-strain behaviour of coating A and substrate was used. A temperature reduction from the T_g of coating A to 23 °C was applied. The resultant thermal stresses in X and Y directions along paths on coating surface are shown in Figure 87. The paths are illustrated by the orange arrowed lines, of which 0 corresponds to the start of the path.

Figure 87A shows that the thermal stresses in X direction produced by both models were independent from the position along the paths. This is because the models simulated infinite length, and there was no edge effect. Both models produced thermal stresses of about 13.8 MPa, while the thermal stress produced by the 2D model was 0.2% smaller than that by the 3D model. Figure 87B shows that the thermal stresses in Z direction produced by both models, and in the figure only the path in the 3D model could be defined as the 2D model had no dimension in Z direction. The thermal stress in Z direction produced by the 2D model was about 16.4 MPa, which was about 19% greater than the maximum thermal stress in Z direction produced by the 3D model. The reason for this was that the 2D model was in plane strain, which does not allow any deformation in the Z direction, thus the volumetric shrinkage of the coating was completely constrained and translated into thermal stress. In contrast, in the 3D model, part of the coating volume shrinkage was accommodated by the shrinkage of the substrate, and only the rest of coating shrinkage that exceeded the substrate shrinkage was constrained, and therefore produced smaller thermal stress. Near the edge of the 3D model (position > 4 mm), the thermal stress was found to be much smaller, and it was in compression within 0.25 mm from the edge. This was due to the edge coating being only constrained by the interface, and nothing else in the Z direction. As the position moves inward from the edge for about 2 mm, the effect of the edge became insignificant, and the thermal stress

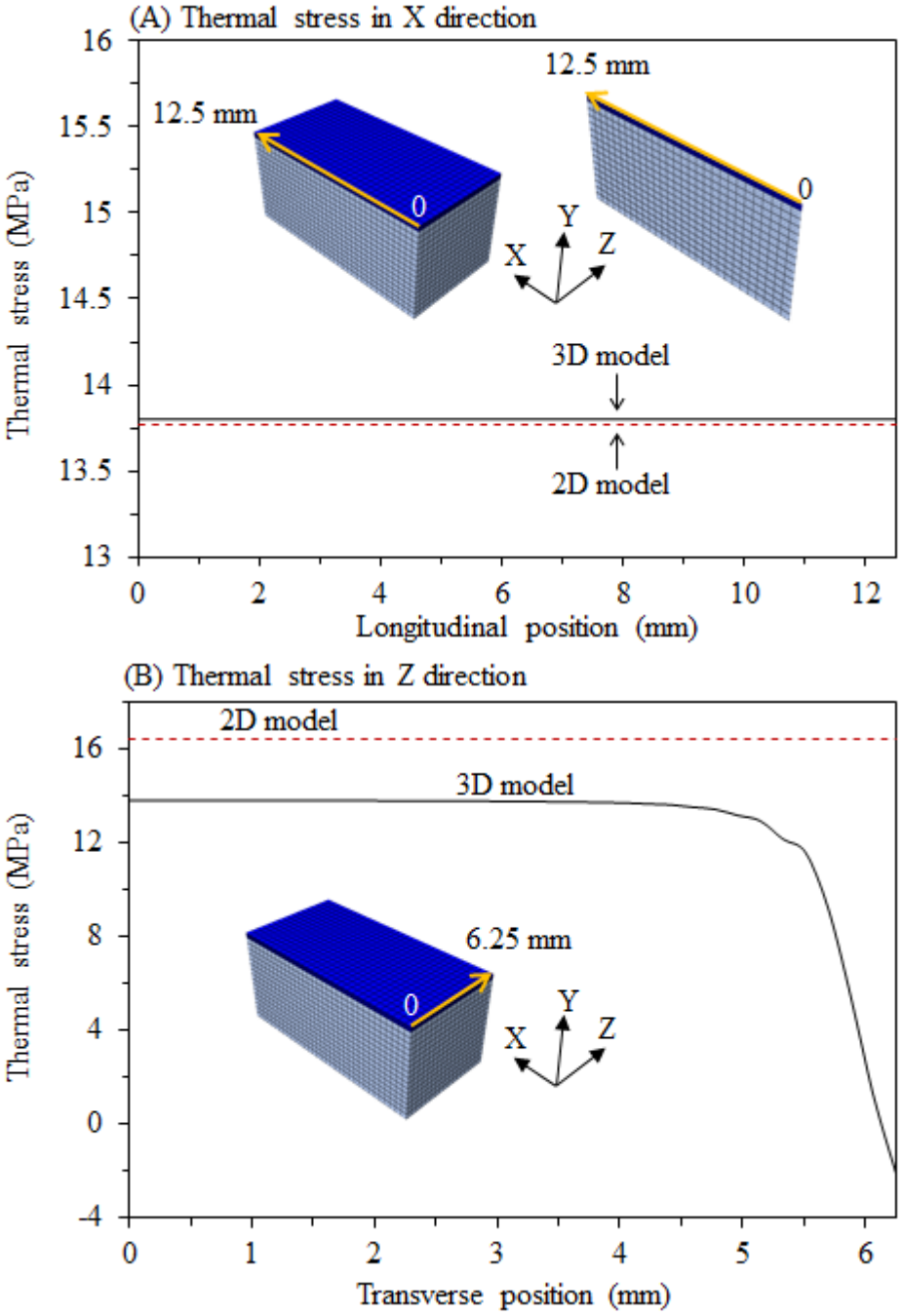

Figure 87. Thermal stresses in X and Z directions produced by the 2D and 3D models.

become constant. The maximum stress in Z direction of the 3D model equalled to that in the X direction, which indicates that the coating was under biaxial thermal stress state.

As the thermal stress in the X direction produced by the 2D model was equivalent to that produced by the 3D model, this means that the 2D model can be used to evaluate the J-integrals due to thermal strains.

5.5. Calculation of J-integrals of Coating Crack under Static Strain

To understand the stress field around defects at the cracking onset in the coatings, the Von Mises stress in coating containing a defect at the measured strains to first crack was calculated using the FE fracture mechanics model (section 5.1) incorporating the non-linear elastic stress-strain curves of the materials. To simulate the samples, the thicknesses of coating A and B were 300 and 350 µm, and the defect depths were 60 and 70 µm respectively. A temperature reduction from T_g to 23 °C was applied, introducing thermal residual strains of 0.17% and 0.2% in coatings A and B. Mechanical strains of 1.04% and 0.64% were then applied. The resultant Von Mises stress distributions around the crack tips are shown in Figure 88. The picture on the right is an enlarged view of the area around the crack tips.

In both cases, the maximum Von Mises stress reached more than 200 MPa at a location about 5 µm from the crack tips, and for the sake for presentation, the maximum stress in the colour scale is chosen to be 110 MPa to show enough contrast between different stresses. Figure 88 shows that the local stress in both coatings at the applied strains exceeds the remote nominal fracture stresses of the free films. In crack tip regions, the stresses are more 60 MPa, indicating the materials are well into the non-linear region of the stress-strain curves. Smooth stress contours were achieved. This means that the stresses calculated by the model were adequate to produce reliable J-intergrals for cracking.

5.5.1. J-integrals at measured strain to first crack

To investigate J-integral values of coating cracks at different defect depths at the measured strain to first crack of each coating, the J-integrals of crack penetration (J_p)

and channelling (J_{ch}) at various defect depths, with a/h ratios from 0 to 1 were calculated using the model. To simulate the substrated coating tensile tests, the coating thickness of the model was replaced by the average coating thickness, 0.3 mm for coating A, and 0.35 mm for coating B. The same thermal and mechanical strains applied to calculate the Von Mises stress field were applied. These strains were the strains to first crack of each coating during tensile tests measured by extensometer.

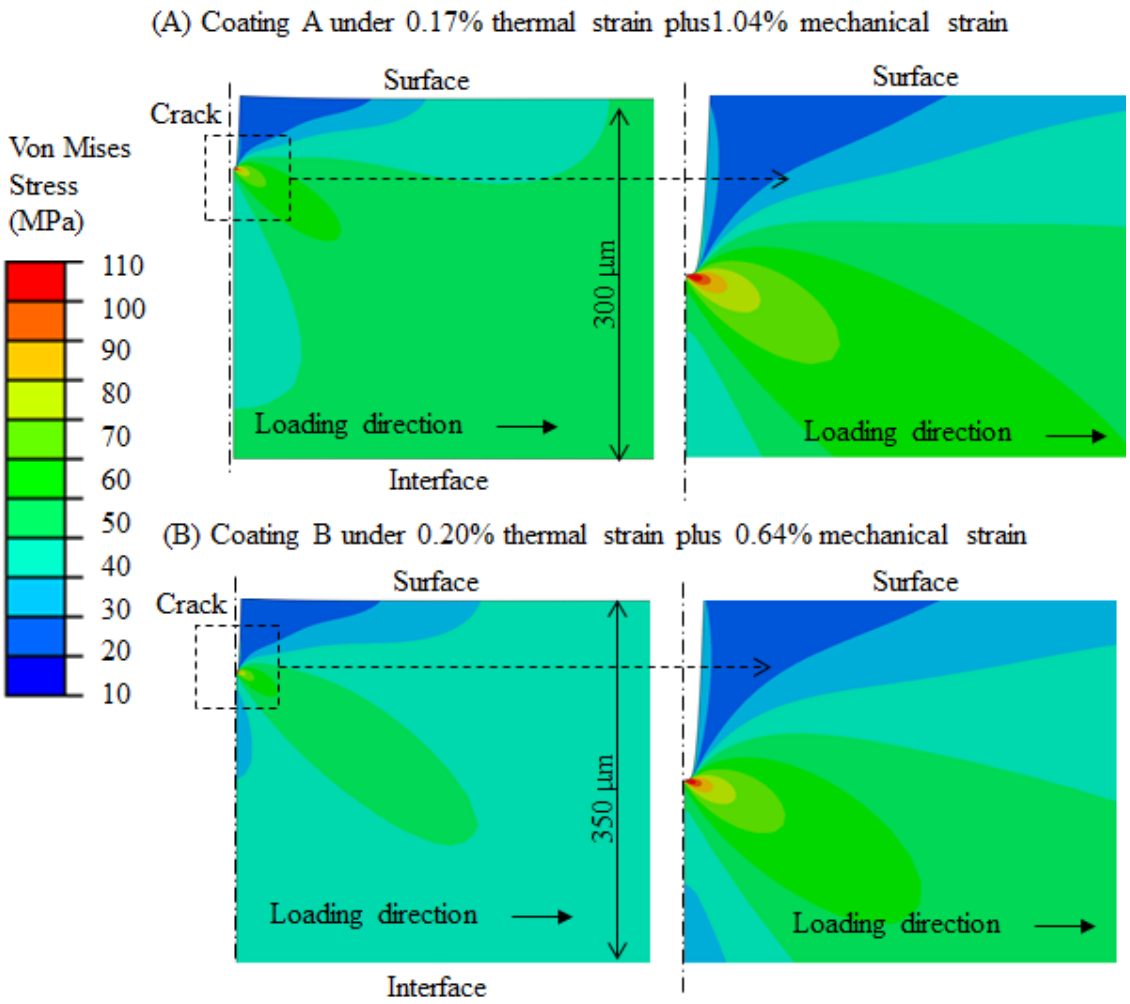

Figure 88. Von Mises stress field around coating surface crack tips. (A) 60 µm deep defect in 300 µm thick coating A; (B) 70 µm deep defect in 350 µm thick coating B, both under a combination of thermal residual and mechanical strains simulating the conditions to the onset of first cracks in the tensile tests.

Figure 89 shows the calculated defect depth dependence of J_p and J_{ch} in a substrated coating A sample at 1.04% mechanical strain, and Figure 90 shows the same in a

substrated coating B sample at 0.64% mechanical strain. The relationship between the defect size and J-integrals shown in these two figures resembles the linear case shown in Figure 82. For almost the entire range of defect depth, J_p is greater than J_{ch}, meaning penetration will always start before channelling. The J-integral for crack channelling (J_{ch}) is smaller than J_p for both coatings at defect depths below 295 and 345 µm. Although J_{ch} increases with increasing a, J_{ch} at a fixed depth will be independent of the surface crack length, according to equation (26).

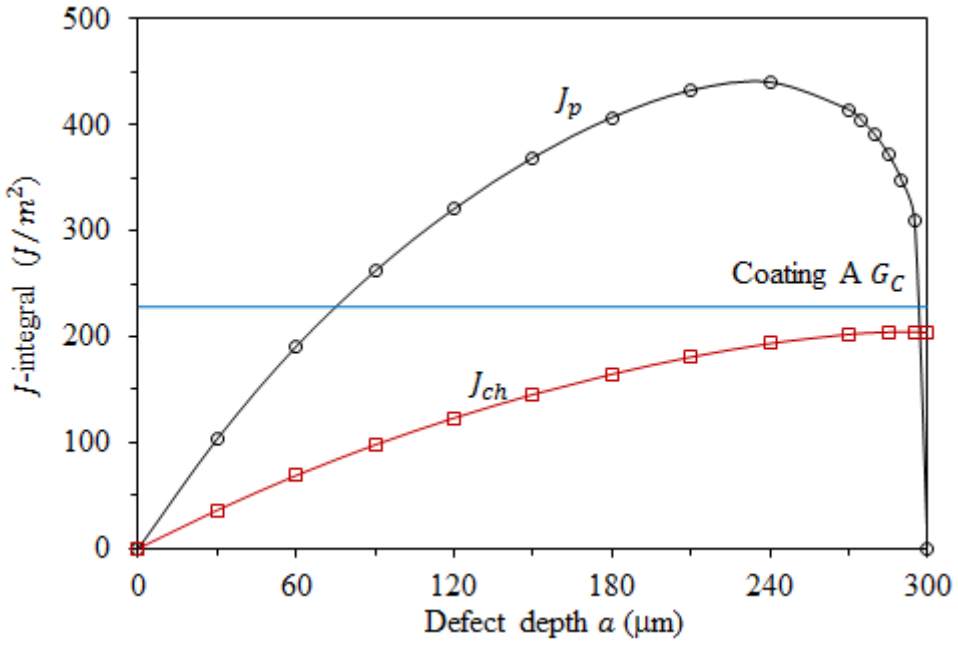

Figure 89. J_p and J_{ch} of defect with various sizes in a 300 µm thick coating A under a mechanical strain of 1.04% in the substrated coating tensile test.

The fracture toughness of the coatings in terms of critical strain energy release rate (G_C) are indicated by the horizontal lines in Figure 89 and Figure 90 for each coating. For coating A, at the measured strain to first crack of 1.04%, the J_p for defect depth between 75 µm and 290 µm is greater than the G_C value, while the J_{ch} does not reach the G_C value even for a fully penetrated crack (a = 300 µm). For coating B at the measure strain to first crack of 0.67%, the J_p for defect depth between 40 µm and 345 µm is greater than the G_C value; the J_{ch} reached the G_C for a > 110 µm, and becomes about twice the G_C for a fully penetrated crack (a = 350 µm). The development of J_p and J_{ch} with a in comparison to the fracture toughness values will give discussed in chapter 6.

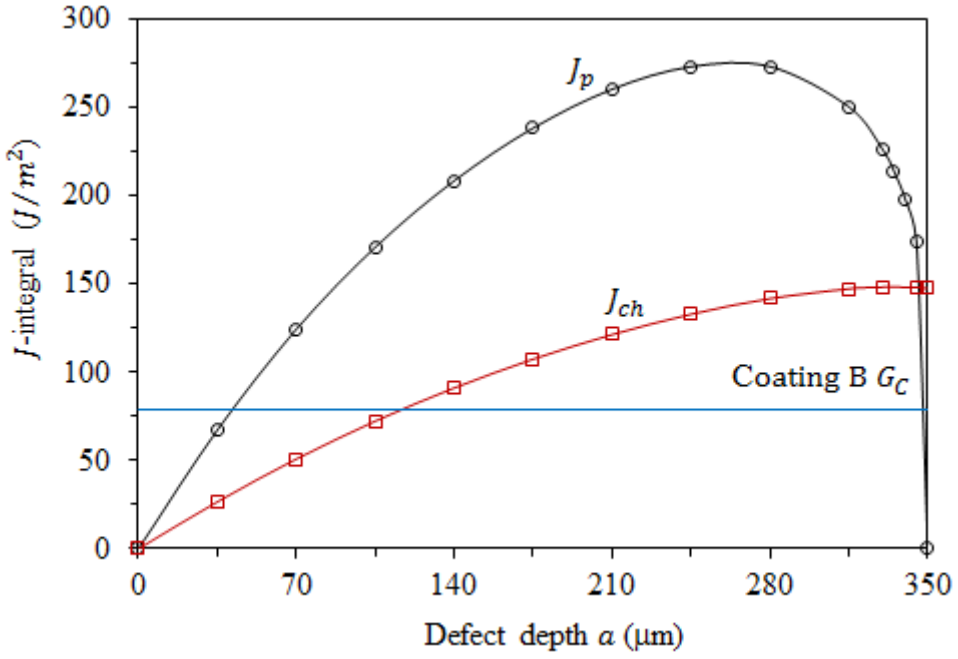

Figure 90. J_p and J_{ch} of defect with various sizes in a 350 μm thick coating B under a mechanical strain of 0.64% in the substrated coating tensile test.

Figure 89 and Figure 90 also show that the calculated J-integrals had a strong sensitivity to the defect depth. For example, the J_p of a 60 μm deep defect in coating A at 1.04% strain was twice the J_p of a 30 μm deep defect, but only about 2/3 of the J_p of a 90 μm deep defect. An estimation of the effect of defect depth on strain to first crack requires the knowledge of the strain dependence of J_p of different defect depths, this is shown in the next section.

5.5.2. Defect depth dependence of J_p under increasing strain

The development of J_p at different defect depth during substrated coating tensile tests was calculated. For coating A, defect depths of 30, 60, and 90 μm, and for coating B defect depths of 40, 70, and 100 μm were studied. A temperature reduction from the T_g to 23 °C was applied first, followed by a mechanical strain to 3%.

The development of J_p of defects with the three studied depths in coatings A and B as a function of increasing mechanical strain is shown in Figure 91 and Figure 92. In both

coatings, an increase or a decrease in defect size caused significant increase or decrease in J_p. For example, in coating A at a strain of 1%, the J_p of the 60 μm defect was about 90% greater than that of the 30 μm defect, and was about 70% of the J_p of the 90 μm deep defect. A similar situation can be found in coating B.

The fracture toughness (G_C) of the coatings are also indicated in Figure 91 and Figure 92. It can be seen that the mechanical strain required for the J_p to achieve the G_C increases with decreasing defect depth. In the order of decreasing defect depth, the mechanical strain required are 0.93%, 1.18% and 1.83% for coating A, and are 0.33%, 0.43% and 0.64% for coating B. The indication of the defect depth dependence of the J-integrals on the ductility of substrated coatings will be discussed later.

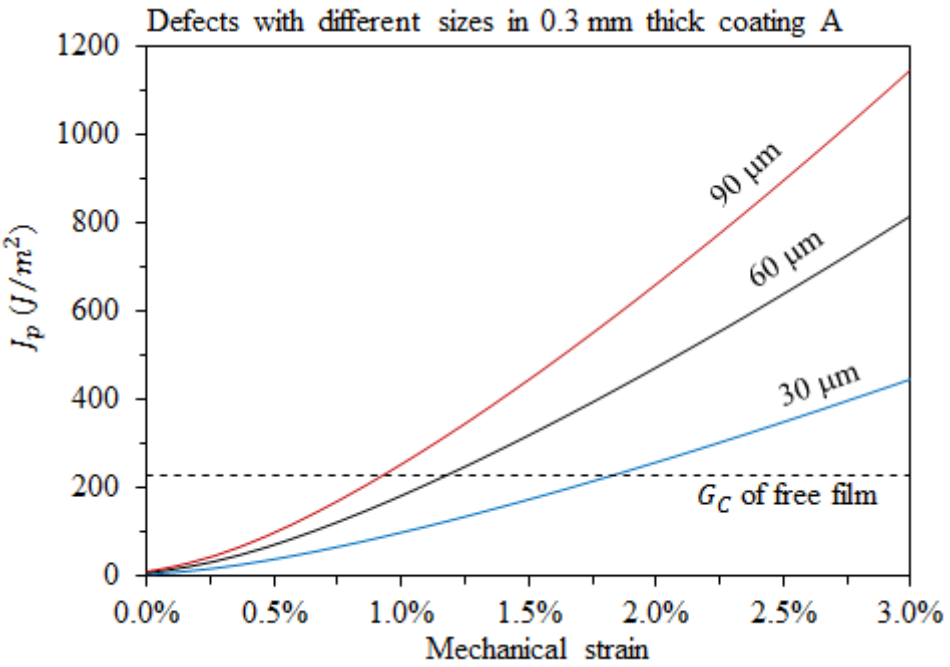

Figure 91. Development of J_p of defects with 3 different sizes in a 0.3 mm thick coating A under an increasing mechanical strain.

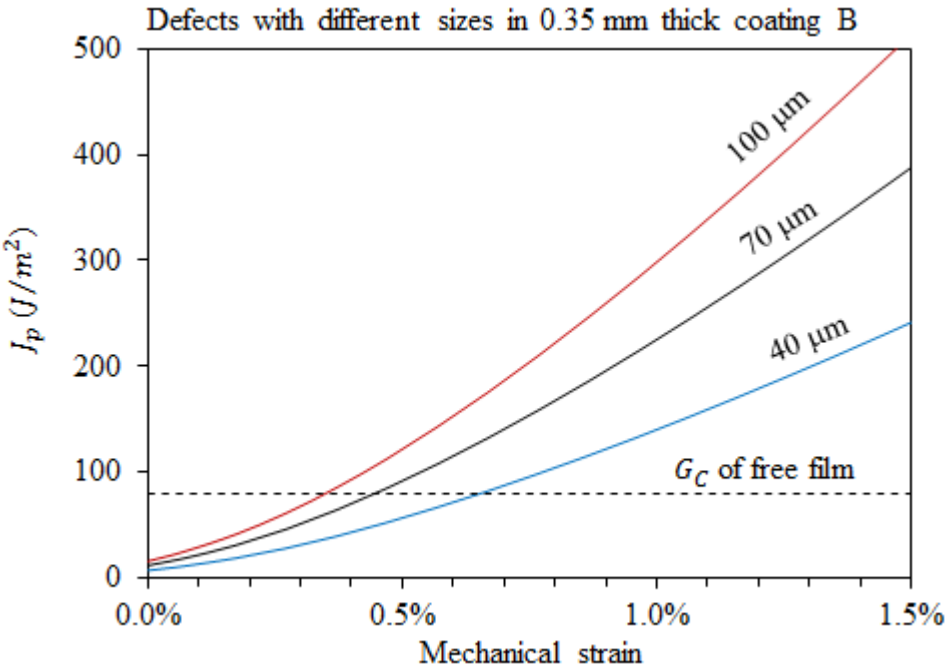

Figure 92. Development of J_p of defects with 3 different sizes in a 0.35 mm thick coating B under an increasing mechanical strain.

5.5.3. J-integral calculated with different coating thicknesses

The effect of coating thickness on J-integral of crack penetration (J_p) was investigated over a range of coating thickness from 0.1 to 1.5 mm. In this calculation, a fixed crack depth of 60 µm and only coating A were considered. A temperature reduction from the T_g to 23 °C was applied first, followed by a mechanical strain to 3%.

The J_p under an increasing mechanical strain in coating A with different thicknesses is shown in Figure 93. It can be seen that bigger coating thicknesses led to the steeper increase of J_p, and the effect of coating thickness was found to become smaller as the coating thickness increases. At a strain of 3%, the difference between the J_p of 0.1 mm and 0.2 mm thick coatings was about 170 J/m^2, while the difference between J_p of the 0.6 mm and 0.2 mm thick coatings was only about 150 J/m^2. Indeed, as the coating thickness reached 0.9 mm, the effect of further thickness increase become so small that the plots representing thicknesses 0.9, 1.2, and 1.5 mm practically overlap together.

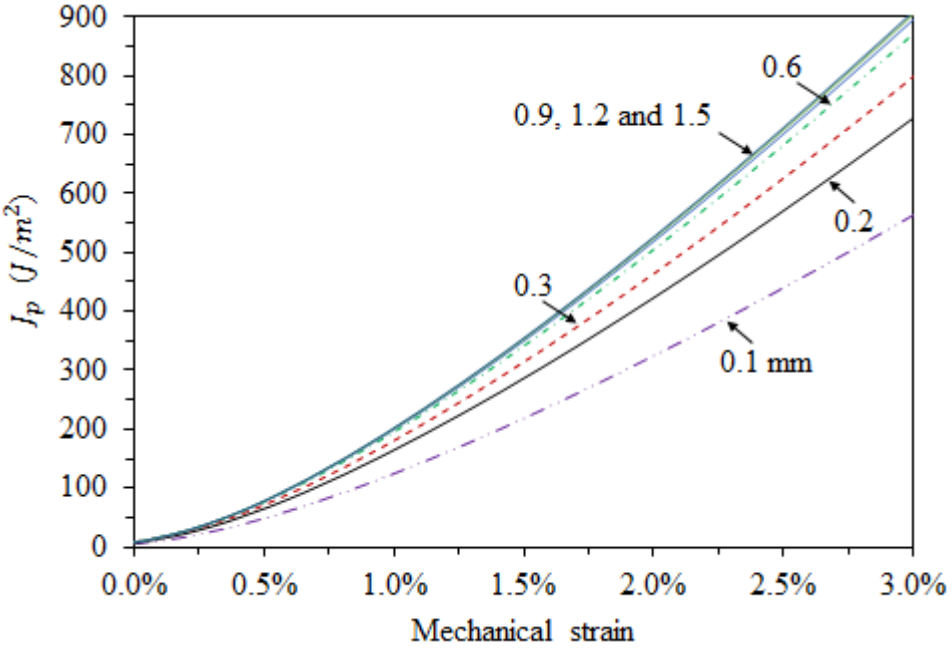

Figure 93. J_p of a 60 µm deep defect under increasing mechanical strain in coating A with different thickness.

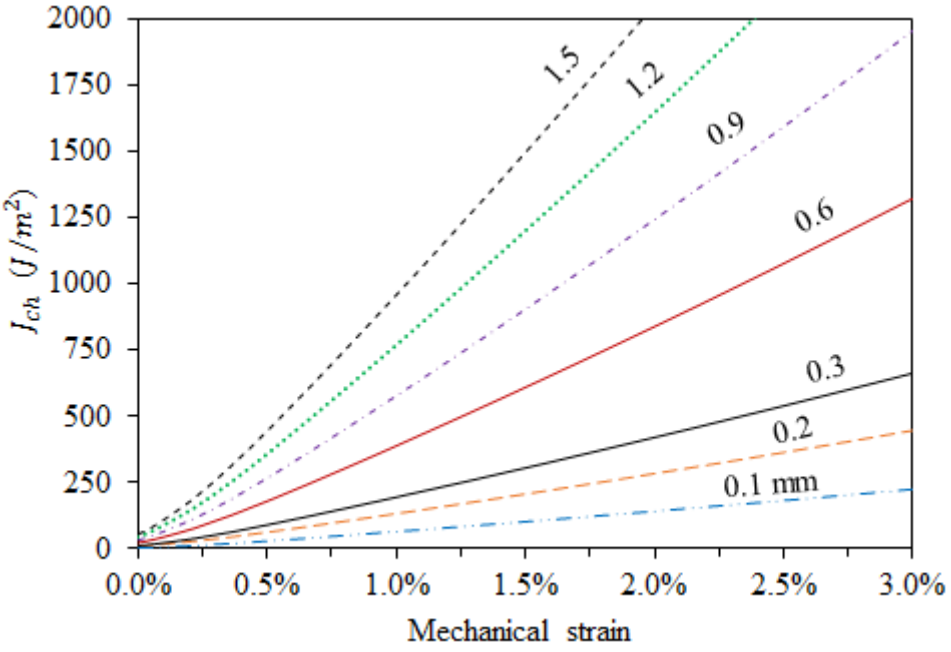

Figure 94. J_{ch} of a through-thickness crack under increasing mechanical strain in coating A with different thicknesses.

The effect of coating thickness on J-integral of crack channelling (J_{ch}) was also investigated. The same model and coating thicknesses were used, while only through

thickness cracks were considered. The calculated J_{ch} under an increase mechanical strain in coating A with different thicknesses is shown in Figure 94. Similar to the effect of coating thickness on J_p, the J_{ch} of thicker coatings was found greater than that of thinner coatings. Unlike, the effect of thickness on J_p, the increase of J_{ch} due to coating thickness increase was significant. To demonstrate this, the dependences of J_p and J_{ch} on coating thickness at a constant mechanical strain of 1.04% are shown in Figure 95. The stabilisation of J_p at about 210 J/m^2 above 0.9 mm can be clearly seen, while the increase of J_{ch} due to coating thickness increase showed a linear relationship, and J_{ch} overtook J_p at a coating thickness of 0.3 mm.

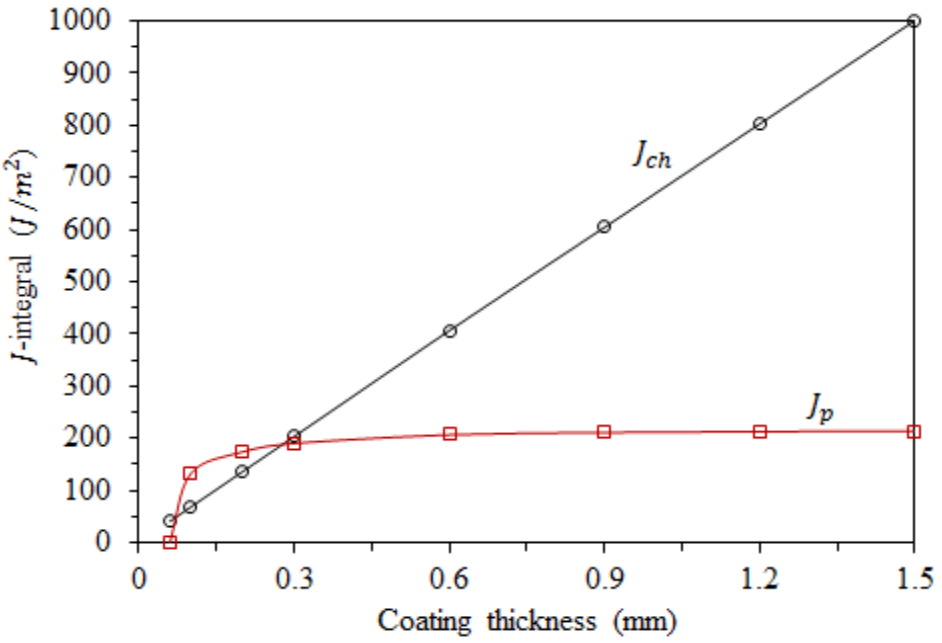

Figure 95. Thickness dependence of J_p of a 60 μm deep crack and J_{ch} of a through-thickness crack under increasing mechanical strain of 1.04% in coating A with different thicknesses.

The fundamental reason why J_p becomes insensitive to thickness increase above 0.9 mm is that the defect depth in comparison to the coating thickness becomes tiny. Thus, the thickness increase will not have noticeable effect on J_p as the substrate interface is moving away from the defect tip. The linear dependence of J_{ch} of through-thickness crack on coating thickness can be explained as follows using the channelling crack energy balanced described in section 5.1. Suppose two through-thickness coating cracks O and

T are in separate coatings with thicknesses, h_o and h_t, and $h_t = nh_o$ with $n > 1$, meaning $h_t > h_o$. The through-thickness cracks under the same normal stress (σ) in these two coatings will have geometrically similar cross-section profiles. Because of this, the crack opening along crack T (δ_t) will also be n times that of crack O (δ_o), thus according to (45) the collective displacement of crack T (Δ'_t) will be n^2 times that of crack O (Δ'_o). As the energy stored in front of a channelling crack is $\sigma \cdot \Delta'$ (section 5.1), the energy stored in front of crack T will be n^2 times that stored in from of crack O. Similarly, according to equation (46) the work down (W') for crack T opening will also be n^2 times that of crack O. Thus, the energy released ($\sigma \cdot \Delta' - W'$) due to a unit channelling growth of crack T (de_t) will also be n^2 times that of crack O (de_o). According to equation (48), $J_{ch} = de/h$ for through-thickness cracks, the ratio of the J-integral for the channelling of crack T (J_{ch_t}) to that of crack O (J_{ch_o}) can be expressed.

$$\frac{J_{ch\_t}}{J_{ch\_o}} = \frac{\frac{de_t}{h_t}}{\frac{de_o}{h_o}} = \frac{de_t}{de_o} \cdot \frac{h_o}{h_t} = n^2 \cdot \frac{1}{n} = n \tag{52}$$

Equation (52) clearly shows that J_{ch_t} to J_{ch_o} ratio is the same as h_t to h_o ratio, and thus explains the linear dependence of J_{ch} on thickness.

6. DISCUSSION OF COATING FRACTURE IN EXPERIMENTS

This chapter will discuss the coating fracture behaviour observed in the mechanical tests under both static and cyclic strains. During mechanical testing, coating fracture was primarily caused by mechanical strains in addition to a thermal residual strain. This is different from WBT coating failure in service where thermal strain is predominant. Following this chapter, the numerical calculations regarding the coating failure under thermal strains in service will be introduced, and then the relevance of the current experimental work to the coating failure in service will be discussed.

6.1. Properties of Coatings and Substrate

The temperature dependence (Figure 24) of all these properties of the coatings has been widely observed in other polymeric materials [33] including some WBT coatings [10] tested at various temperatures. The increased temperature leads to the expansion of the free volume between the molecular chains, which causes a reduced resistance of the molecular chain movement under deformation, and it is then reflected by the increase of the ductility and the decrease of modulus of the material [33].

The measured modulus of steel of about 200 GPa is typical, and can be found in textbooks or reference books [177]. The high strain bands developed in non-pre-strained substrated (Figure 35) should be Lüder's bands [178]. This is also typical, and widely found in low-carbon steel, and some aluminium alloys [178].

Due to the non-linear stress-strain behaviour of the coating and substrate, the stiffness mismatch will vary depending on the strain. Defining the effective stiffness as the tangent modulus at different strains, the effective stiffness of coatings and substrate as a function of strain can be produced using the stress-strain curves of the coating and substrate, see Figure 96. As the Dundur's parameter α quantifies the stiffness mismatch, the effective stiffness of the coatings and substrate was employed in equation (20) (page 25) to calculate α at various strains, which is also shown in Figure 96.

The effective stiffness of both coatings and substrate reduces as the strain increases. Below 0.2% strain, the effective stiffness of the coatings and substrate was the same as the Young's modulus; while at 3% strain, the effective stiffness of the coatings and substrate reduced to 0.6 and 1 GPa respectively. The reduction of the effective stiffness of the substrate was much greater than that of the coatings, leading to the reduction of stiffness mismatch. Below 0.2% strain, the Dundur's parameter α was about -0.95, and as the strain increased to about 1%, α increased to about -0.2. As the reduction of substrate effective stiffness was about 43 times the reduction of coating effective stiffness, the increase of α should be primarily caused by the change of substrate effective stiffness.

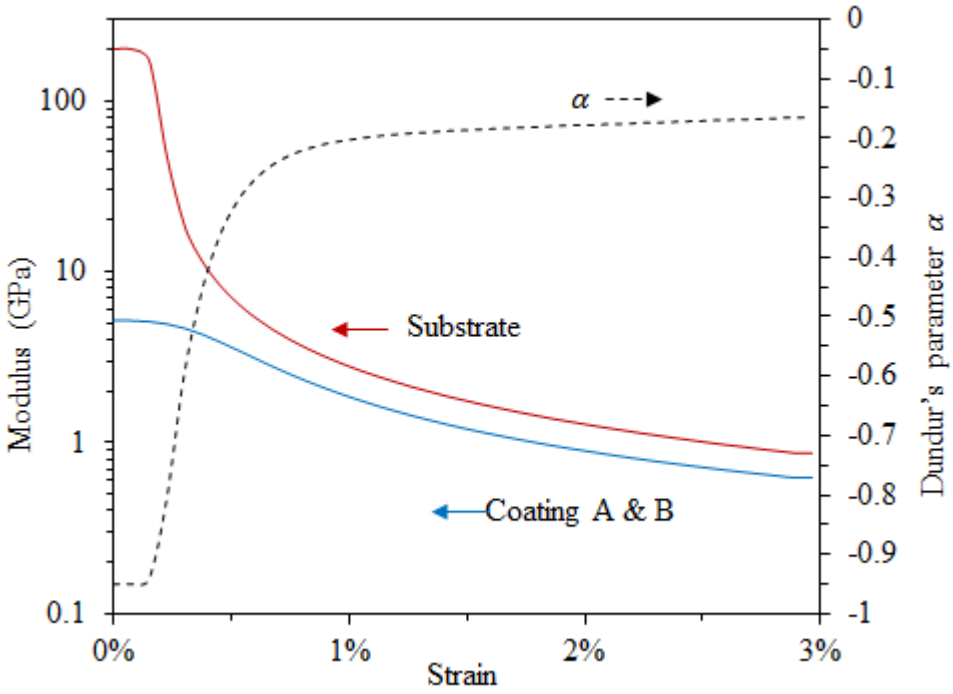

Figure 96. Strain dependence of the effective stiffness of coatings and substrate, and corresponding Dundur's parameter α.

The effects of coating/substrate stiffness mismatch on the fracture of coatings have been theoretically explored by several researchers [129,174,179,180], and it has been found that an increase of α encourages coating fracture. Therefore the adoption of non-linear stress-strain behaviour of the materials in the FE analysis of J-integrals for coating

cracking shown was more appropriate than assuming the materials were linear-elastic. In service, substrates will not experience stresses beyond yielding point, and therefore the modulus will remain constant, thus α will also remain roughly constant at about -0.95.

6.2. Fracture of Coating Free films

The stress-strain curves of un-notched free films at ambient temperature (Figure 23 on page 52) suggests that at the fracture of free films of both coatings A and B the deviation from linear elasticity was small. Thus, it can be assumed that the fracture toughness (G_C) of the coating free films at the fracture strain of the un-notched samples were the same as those measured using the double notched samples. Using the G_C, the defect size in the un-notched free films can be estimated. There were three types of defects that might be present in the un-notched free film samples, and they were: 1) through-thickness edge defect, 2) semi-circular surface defect, and 3) internal defect, see Figure 97, which illustrates these possible defects in a section of a free film. As internal defects have smaller K or G to initiate cracking in comparison to the other two types of defects for the same sizes [93], thus they were unlikely to cause failure. The sizes of defects as in surface semi-circular and through-thickness edge defects were estimated.

Strain energy release rate for a semi-circular surface defect (G_{surf}) with $a = c$ and a through-thickness edge defect (G_{edge}) in mode I can be expressed by the equations (53) [181] and (54) [167] respectively. Here, σ is the remote normal stress, E_c is the coating modulus. The other symbols are shown in Figure 97. f_{surf} and f_{edge} are geometry correction factors, which are shown following the respective equations.

$$G_{surf} = \frac{\pi\sigma^2 a}{2.464E_c} {f_{surf}}^2 \tag{53}$$

$$f_{surf} = [1.04 + 0.202\left(\frac{a}{h}\right)^2 - 0.106\left(\frac{a}{h}\right)^4][\sec\left(\frac{\pi c}{2W}\sqrt{\frac{a}{h}}\right)]^{0.5}$$

$$G_{edge} = \frac{\pi\sigma^2 a}{E_c} f_{edge}(a/W)^2 \tag{54}$$

$$f_{edge}(a/W) = \sqrt{\frac{2W}{\pi a} tan\frac{\pi a}{2W}} \cdot \frac{0.752 + 2.02\left(\frac{a}{W}\right) + 0.37(1 - \sin\frac{\pi a}{2W})^3}{cos\frac{\pi a}{2W}}$$

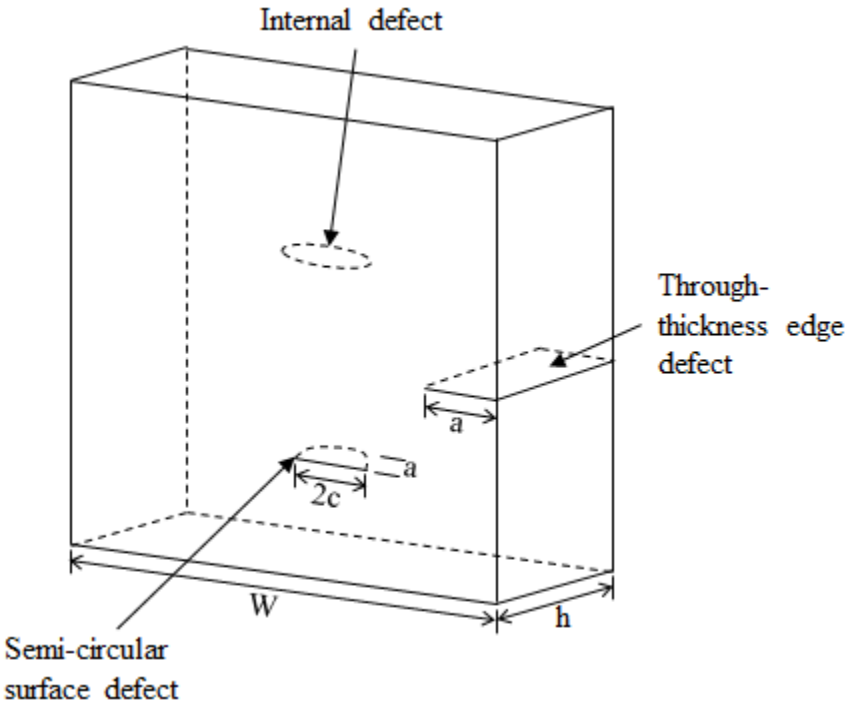

Figure 97. Schematic of possible defects in un-notched free film samples.

Using the equations above, the relationship between the energy release rate (G) and defect size (a) for both surface semi-circular and through-thickness edge cracks at the failure strain of the coatings can be produced. For the calculation, a nominal thickness h of 0.3 mm and a nominal width W of 12 mm were used. Figure 98 and Figure 99 show the results for free films of coatings A and B respectively. In both figures, G_{surf} and G_{edge} is shown by a red solid line and a dashed line respectively; the defect size a for the surface semi-circular defect ranges from 0 to 0.29 mm, as a needs to be smaller than the thickness (0.3 mm) in order to remain in a surface crack.

The J -integral of through-thickness edge defects (J_{edge}) was also calculated numerically using a 2D plane stress free film model (see appendix viii) incorporating both linear and non-linear stress-strain curves of the coatings shown in section 5.3 (page130). The results are also shown in Figure 98 and Figure 99 for each coating. The J_{edge} values calculated using linear elastic stress-strain curves are shown by empty square data points. The results are the same as the G_{edge} produced using equation (54). The J_{edge} values produced using non-linear stress-strain curves are shown by solid black circles linked by a black solid line, and they are found to be 6% and 9% greater than the G_{edge} for coatings A and B respectively. The small difference between J_{edge} and G_{edge} indicates that the effect of non-linearity at crack tip on strain energy release rate was small.

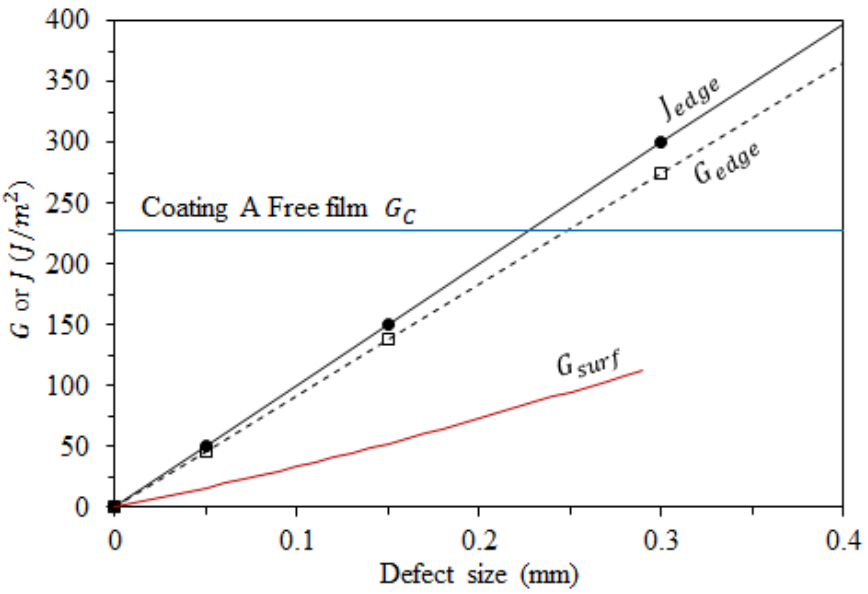

Figure 98. Strain energy release rate (G) and J-integral (J) as a function of defect size at the measured failure strain (0.67%) of coating A free film at ambient temperature. The empty squares are data points calculated using FE method incorporating linear elastic stress-strain behaviour.

Normally, when J-integral is used to predict fracture, a fracture toughness measured in terms of critical J-integral at fracture (J_C) is required. Given that the effect of stress-strain non-linearity on the cracking drive forces is found to be small, it is assumed here that the J_C of the coatings is the same as the G_C, and the measured G_C values will be used as the fracture toughness values of the coatings throughout this thesis.

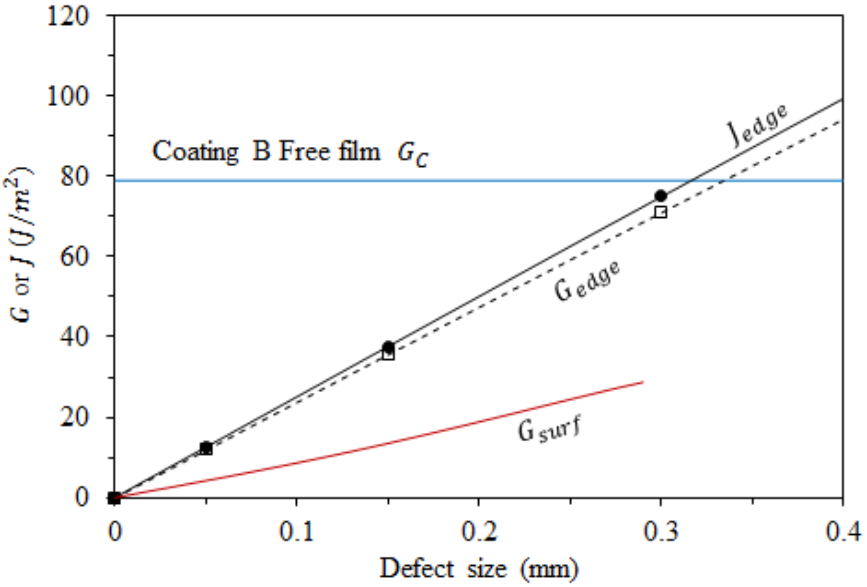

Figure 99. Strain energy release rate (G) and J-integral (J) as a function of defect size at the measured failure strain (0.34%) of coating B free film at ambient temperature. The empty squares are data points calculated using FE method incorporating linear elastic stress-strain behaviour.

It can be seen that for both coatings, the maximum G_{surf} was still much less than the G_C, meaning that defects in the form of semi-circular surface defect should not be the source that initiated the fracture of free films. In comparison, the G_{edge} of through-thickness edge defect exceeded the G_C as the defect size a exceeded 0.25 mm and 0.34 mm in coatings A and B respectively. Using J_{edge}, the a of through-thickness edge defect giving the current fracture strains was found to be 0.23 mm and 0.32 mm for coatings A and B respectively.

The estimated defect sizes in both coatings had a small difference of about 0.09 mm, this may indicate that the defects were introduced in the same way. The predicted sizes of these defects were much greater than the possible surface defects observed from the locally bent free films (Figure 31 and Figure 32 on page 62) by a factor of about 3 to 4. During the tensile tests, the entire gauge length was stressed equally, and fracture would occur from the defects with the largest available strain energy release rate within the

bulk. In the current case, the defects might be through-thickness edge defects introduced due to sample cutting.

6.3. Fracture of Substrated Coatings

The observation of coating cracking in mechanical tests similar to that performed in the current work can be found in a number of publications [14,16,147–155]. Previous work has shown that the nominal strain to first crack of substrated coatings could be either greater [182,183], in agreement of the current test results, or smaller [161] than free film fracture strain. It is unclear why there should be this anomaly, since the substrated coatings contained residual tensile strains of about 0.2%, due to which the ductility of the substrated coating ought to be consistently smaller than the free films.

A fracture mechanics approach [129,135] predicts that the strain to first crack of substrated coatings will depend on 1) defect size, 2) coating thickness, 3) residual stress level. There is a further factor of substrate inhomogeneous strain distribution (Figure 35 on page 66), which can result in local strain at the onset of cracking being much greater than the nominal strain measured using the entire gauge length (Table 8). For similar tests in the future, the yield behaviour of substrates ought to be reported. It is not clear yet how other substrates would behave. A reliable measurement of strain to fracture should be made only based on local strains or on nominal strains of pre-strained substrates. This however is a laboratory issue only, because in reality the failure of the current coatings is primarily caused by thermal stress/strains, and substrate will not yield. The discussion that follows will assume homogeneous substrate deformation.

In addition, there is also a difference between the defects in free films and substrated coatings. Free films are likely to have edge defects introduced due to sample cutting during manufacturing. In contrast, substrated coatings are unlikely to have crack initiating defects away from the edges, as there is no need to cut them from a bigger sheet. That cracking initiation in substrated coatings always occurred away from sample edges (Figure 42) is a good demonstration. The defect size of free film depends on the

manufacturing process, and the defect size of substrated coatings may vary depending on the size of fillers. The strain dependence of the energy release rate of these two types of defects may be highly different. Thus, it is recommended to use the failure strain of one type of sample to predict the failure strain of the other.

6.3.1. Fracture mechanics prediction of substrated coating fracture behaviour

Different from cracks in monolithic service applications, where the crack drive force (G or J) increases monotonically with crack depth [93], the J_p for crack penetration is not monotonic with an increasing crack depth (Figure 89 and Figure 90). This behaviour in substrated coatings reflects the increased constraining effect of the substrate as the crack tip approaches the coating/substrate interface [129]. At the measured strain to failure, Figure 89 and Figure 90 predict that penetration will start at defect depths (a) of about 75 μm and 40 μm in coatings A and B, because the fracture toughness is reached by J_p. The penetration crack will propagate unstably and stop before reaching the interface, as J_p falls below the toughness.

In the case of coating A, J_{ch} does not exceed the measured G_C when the penetration process is complete, meaning channelling will not start at the measured strain to first crack. This is illustrated by the crack front 1 shown in Figure 100A, which shows a penetrated crack before the onset of channelling at an applied strain of 1.04%. As the applied strain increased further, and J_{ch} exceeds G_C, the crack front 1 will spread to crack front 2, leading to a large surface crack length increase.

In the case of coating B, J_{ch} exceeds the measured G_C as the surface crack unstably penetrates to an a greater than 110 μm. This indicates that crack channelling should start immediately after the onset of penetration in coating B without the need of any further increase in applied strain. Figure 100B illustrates this process. The difference between the channelling cracking behaviour of the coatings may explain the more abrupt crack opening observed for the first crack in coating B (Figure 46), as a greater crack opening can be caused by immediate crack channelling after penetration initiated.

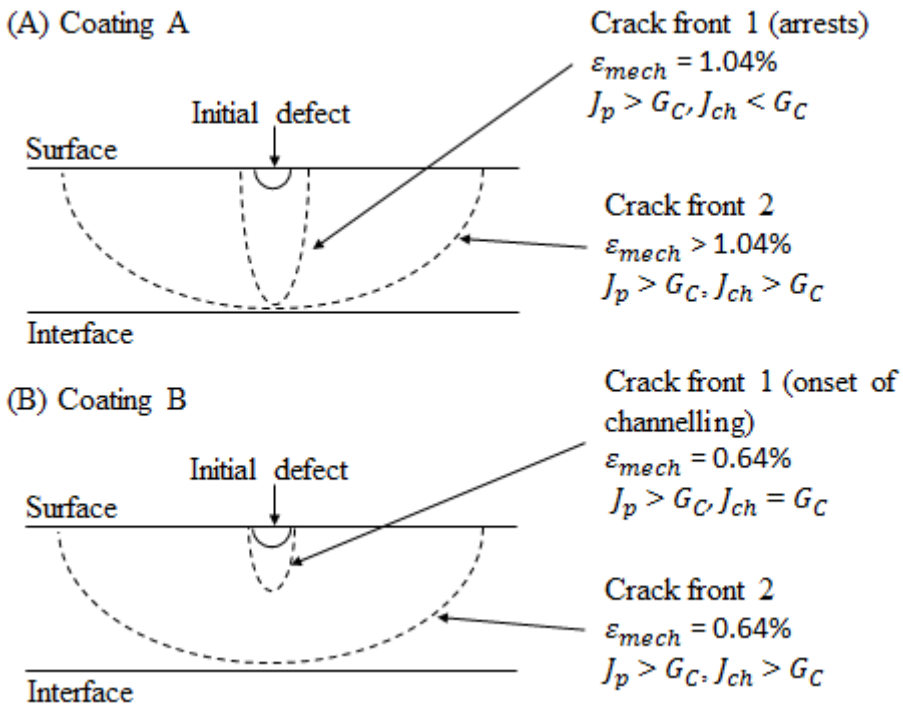

Figure 100. Illustration of cracking process in substrated coatings A and B.

In this work, the penetration and channelling of cracks were treated as two independent 2D processes. In reality, a single surface crack will contain both penetration and channelling components, as shown in Figure 100. The respective values of J_p and J_{ch} will depend on the crack front profile. In linear elastic fracture mechanics of monolithic materials, the effect of surface crack geometry on stress intensity around the crack front has been studied intensively [184], whilst for shape similar to the original coating defect with depth similar to half of surface length, stress intensity is approximately equal all the way along the crack front. For the shape adopted in crack front 1 shown in Figure 100A with depth considerably greater than surface crack length, the largest stress intensity would be at the surface, equivalent to J_{ch}. Assuming this behaviour can be extrapolated to the behaviour of cracks in coatings, the initial J_{ch} may be insufficient for channelling crack extension. However, the crack penetration will change the crack front profile which in turn will increase J_{ch} at the surface relative to J_p.

As J_{ch} is independent of the surface crack length (l), channelling cracks should propagate across the entire sample width once the coating toughness is reached.

However, this was not observed, and instead the crack channelling in the current substrated coating samples required an increasing strain to proceed, see Figure 42 (page 81). There are two reasons that might have caused this.

Firstly, the current coatings were not linearly elastic, and it is conceivable that crack tip blunting occurred at the tips of channelling cracks. Kinloch and Williams [121] have reported that crack tip blunting in test samples with constant stress intensity factors (similar to channelling cracks in coatings) was likely to occur for epoxy resins with yield stresses less than 50 MPa. In this case, the crack growth requires a continuously increasing strain, as the increase of crack length enhanced the crack blunting, thus also increased the effective critical stress intensity factor as crack length increased. The current coatings with yielding stresses smaller than 50 MPa are in this category. Thus, this might be the reason that channelling crack growth required a continuous strain increase. Secondly, the current coatings are microscopically heterogeneous with fillers within the scale of the crack. It is very likely that the front of channelling crack was pinned at the fillers [124,125], thus the fracture toughness was effectively increased.

6.3.2. Effect of defect depth on strain to first crack

Coating cracking in the current samples should start by surface defect penetration, of which the strain to the onset is strongly influenced by defect depth via its effect on J-integral for penetration (J_p). Figure 91 (page 142) and Figure 92 have already demonstrated a high sensitivity of coating ductility to the defect size, and a reduction in defect size can lead to an increased coating ductility.

Photographs in Figure 31 and Figure 32 (page 62) suggest that the fillers in the current coatings were associated with filler or agglomeration of fillers with clean surfaces. As fillers de-bond from the surrounding resins they could act as defects [26], and the size of de-bonded filler could determine the size of defect. Song *et al.* [161] have already shown that a larger filler, which could also be a large defect, leading to the reduction of the fracture strain of some epoxy based coatings. As the strain to penetration onset is

predicted to reduce significantly with the small increase of defect sizes, WBT coatings adopting smaller fillers could therefore have a reduced defect size and an increased ductility.

Note, the onset of penetration will not necessarily lead to channelling as the the J-integral for channelling (J_{ch}) in the coatings could still be smaller than the coating toughness, such as the case of coating A shown in Figure 89.

6.3.3. Effects of coating thickness on strain to first crack

Another important parameter in the application of coatings is the coating thickness. For different applications of coatings, different thickness ranges are usually recommended, and excessive coating thickness normally leads to pre-mature failure of the coatings [58,78]. The thickness dependence of J-integrals of coating cracking has been explored in the section 5.5.3 (page 143).

Figure 95 indicates that the effect of coating thickness the initiation of crack penetration is significant only below a thickness about 0.3 mm. An increase of thickness from 0.3 mm to 1.5 mm will only lead to a 12% increase in the J_p, translating to a 12% reduction in strain to first crack. However, it has been well understood [185] that an increase in thickness will lead to the increase of residual stress of epoxy coatings after curing. This suggests that for the current coatings, if the thickness increases to, for example, 1.5 mm, the reduction of strain to first crack should be greater than just 12% due to the increased residual stress.

Using Figure 95 the effect coating thickness on the onset of crack channelling can be inferred. Between h of 0.07 and 0.3 mm the J_{ch} of a though-thickness crack is smaller than the J_p, which means that as J_p reaches the coating fracture toughness and penetration takes place, forming a through-thickness crack, of which the J_{ch} will still be smaller than the toughness, and thus channelling will not start until further strain/stress is applied. This is similar to the case shown in Figure 100A for coating A. As h exceed 0.3 mm, J_{ch} will exceed J_p. In this case, once penetration occurs and forms a through-

thickness crack, the J_{ch} will also be greater than the coating toughness, which will lead to channelling cracking immediately. This is similar to the case of coating B shown in Figure 100B. This indicates the cracking behaviour observed on the current coating A samples may be changed by increasing coating thickness h, as an increased thickness encourages channelling to occur immediately after penetration starts.

Since the change of coating thickness will lead to the change of a/h ratio for a constant a, reduction of thickness towards defect size will lead to the increase of a/h ratio. When a/h ratio is greater than 0.93, meaning nearly through-thickness crack, the J-integral for channelling (J_{ch}) will be greater than the J-integral for penetration (J_p) (Figure 82). This means that cracking will commence by channelling, and thus the strain to failure will be determined by strain to channel. This means by changing coating thickness, the cracking initiation mode can be altered. Experimental evidence for this has been provided by Chai [179], who successfully predicted the thickness dependence of the measured strain to failure of a type of epoxy coating on metallic substrate using 2D models, and found a critical coating thickness, below which the strain to failure depended only on the channelling J_{ch}.

For the current coatings, such critical thickness can be calculated using the a/h ratio of 0.93. As the defect depths in coatings A and B were about 60 and 70 µm, the critical thickness for these coatings would be 65 and 75 µm respectively, below which the cracking initiation mode should always be channelling. However, WBT coatings in service are often several hundred micrometres in thickness, this means the cracking initiation mode in service should be crack penetration. As thickness increase above 300 µm will have insignificant effect on crack initiation strain, the initiation strain will primarily depend on defect size. This again highlights the importance of minimising defect size.

6.3.4. Contribution of thermal residual stress to coating cracking

As the thermal expansion coefficients of the coatings were greater than that of the substrate (Table 4 on page 56), tensile thermal residual stress/strain was developed in

the substrated samples. The possible contribution of the thermal residual stress in the static fracture of the coatings has been evaluated by calculating the J-integral for penetration (J_p) with and without the presence of thermal residual stress. Figure 101 shows the development of the J-integral for penetration (J_p) of a 60 μm deep defect in a 0.3 mm thick coating A and a 70 μm deep defect in a 0.35 mm thick coating B *with* and *without* initial thermal residual stress under an increasing mechanical strain. For both coatings, the J_p without initial residual stress is smaller than that with initial stress at all strains. In the absence of residual stress, it requires a mechanical strain of 1.42% and 0.72% for the respective defects in coatings A and B to achieve a J_p the same as the free film fracture toughness (G_C). These strains are about 20% and 70% greater than the predicted strains with residual stresses. This indicates that the contribution of thermal residual stress to the static fracture of substrated coating B should be greater than that to coating A.

This also implies that the strain to first crack of coating B is more sensitive to the thermal residual stress than that of coating A. Thus a change of thermal residual stress, such as stress relaxation in the substrated samples might increase the measured strain to failure more significantly in coating B than in coating A.

6.3.5. Fracture mechanics prediction of substrated coating fracture strain

The discussion before this section focuses on the dependence of J_p and J_{ch} on defect depth, coating thickness, and residual stress. By comparing these two J values to fracture toughness, the fracture behaviour of coatings A and B samples can be explained. With known defect depth, coating thickness, residual stress, as well as fracture toughness, predictions of the strain to failure of the coatings can also be made. Figure 102 shows the development of J-integral of penetration (J_p) of a 60 μm deep defect in a 0.3 mm thick substrated coating A and a 70 μm deep defect in a 0.35 mm thick substrated coating B under increasing mechanical strain with initial thermal residual stress at 23 °C.

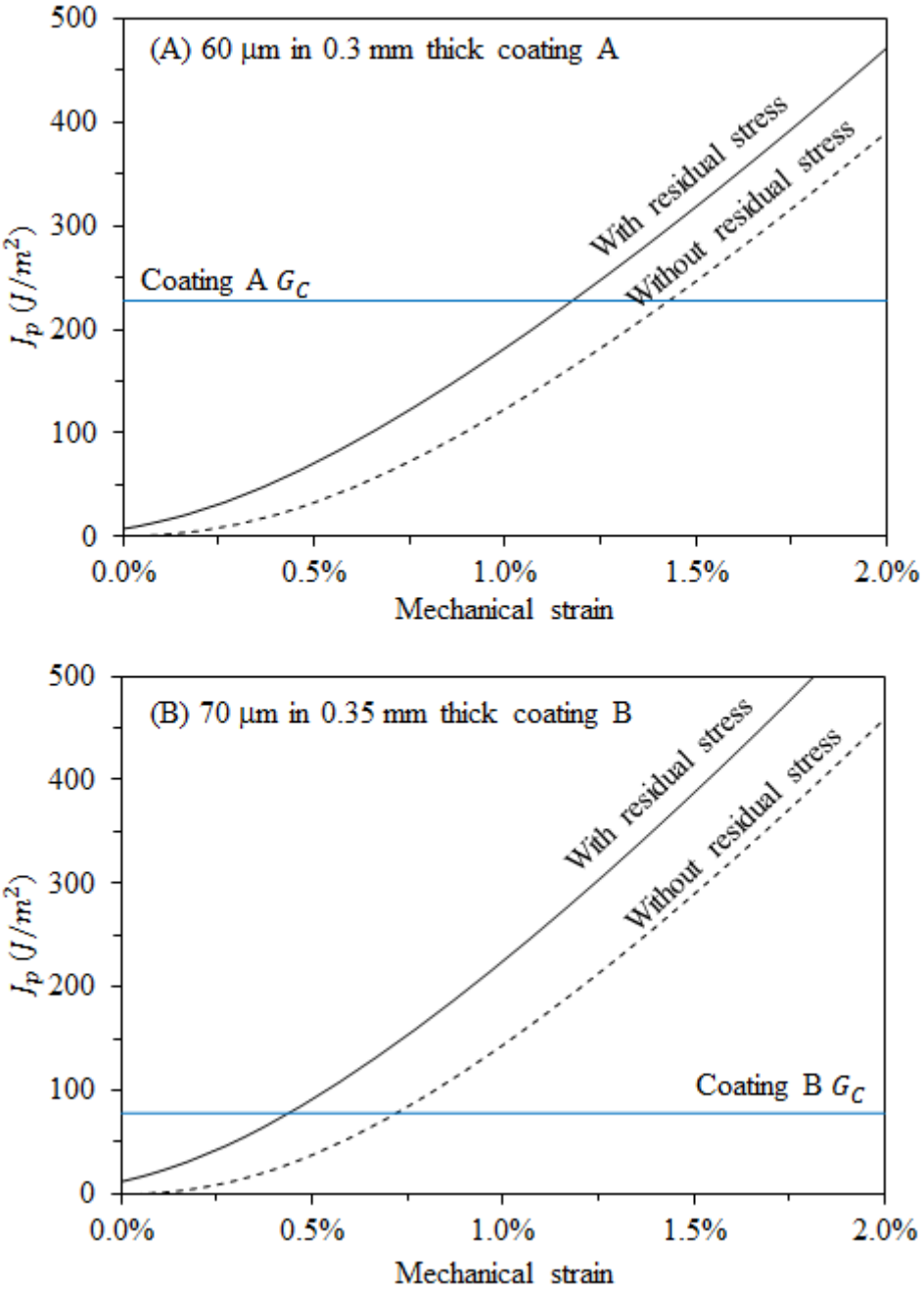

Figure 101. Development of J-integral of penetration (J_p) under increasing mechanical strain with and without initial thermal residual stress.

These defect depths (a) are the mean values of the measured defect depths in the coatings. It can be seen that the J_p of the defects reach the measured fracture toughness (G_C) of free films at mechanical strains of 1.18% and 0.43% for coatings A and B. As crack penetration occurs as J_p reaches G_C, these critical mechanical strains can be seen as a prediction of the fracture strain of each coating during the tensile tests. These predicted values are about 10% greater and 30% smaller than the measured strain to first crack of substrated coatings A and B.

The discrepancy between predicted values and measured values of strain to first crack may originate from the following factors.

1) The coating stress-strain curves used for the J calculations were approximated using extrapolation of the known free film stress-strain relationships. There may be an error in the calculated J values at strains beyond the fracture strain of the coating free films.
2) The thermal residual stress calculated in the FE models may be an overestimate of the actual residual stress level. There may be possible relaxation of the residual stress in the sample after re-heating and before being tested.

The extent of the influence of these factors is difficult to assess without further research. However, the current results predict 1) a smaller strain to first crack of coating B on substrate than coating A; 2) greater ductility than free film samples even with residual stress included. These predictions are consistent with the observations.

6.4. Fracture of Substrated Coatings under Cyclic Strains

Only two pieces of published work regarding fatigue of substrated polymeric coatings were found [156,186], the fatigue cracking of epoxy coating under cyclic thermal stresses was observed in these works, but neither reported any quantitative studies of fatigue crack growth in the coatings. The current work is believed to be the first quantitative investigation into the fatigue failure of WBT coatings.

In this section, the fatigue lives of the substrated coatings to the first 2 mm surface crack under cyclic mechanical strains will be compared. After that, the coating fatigue crack growth in terms of single crack length and total crack length will be discussed separately.

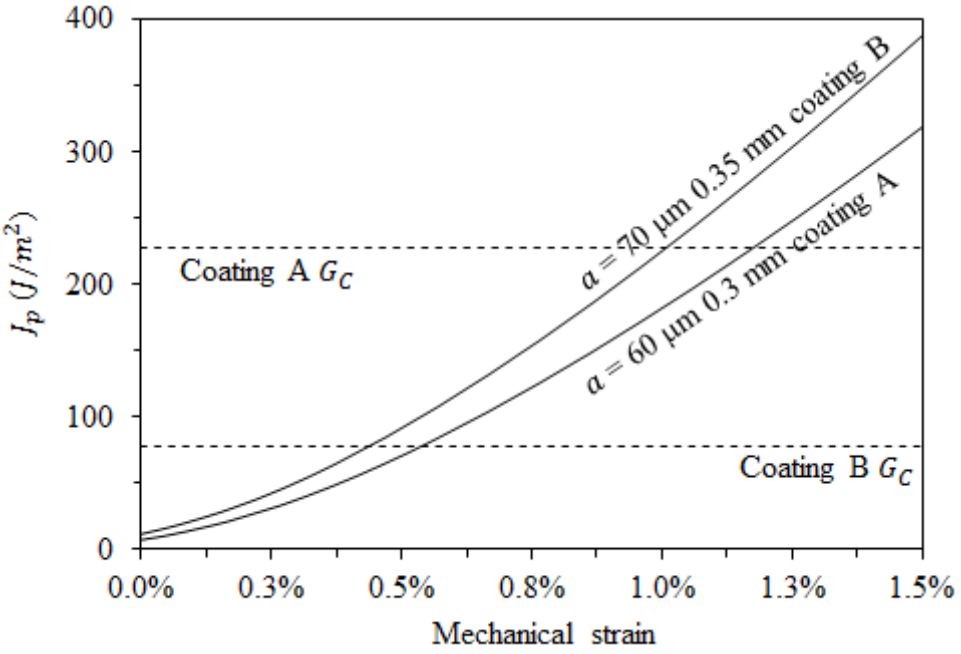

Figure 102. Development of J-integral of penetration (J_p) of defects with depth of a in coatings A and B under an increasing mechanical strain with initial thermal residual stress at 23 °C.

6.4.1. Fatigue crack development from surface defect

The thumb-nail shape feature at the coating surface (section 3.3.1) along with the observation of the association between coating fatigue cracks and surface spots (Figure 51) strongly suggests that the fatigue cracks might initiate from the surface thumb-nail features. These cracks then propagate longer progressively under strain cycles with maximum strains less than the static strain to failure of the coatings. Figure 103 shows an ideal fatigue case of crack development that is similar to the static case.

In this ideal case, a fatigue crack penetrates towards the interface with an elliptical crack front geometry, the surface crack length (l) will be twice the depth of the crack. As the crack fully penetrates the entire thickness, l will equal twice the coating thickness (h)

for a semi-circular crack. After that, the crack will not penetrate into the substrate, but will channel sideways.

The details of the crack shapes in coatings A and B might differ from this ideal scenario. The relationship between the crack depth and surface crack length during fatigue was not able to be observed. However, as fracture mechanics predicts that penetration crack will not reach the interface (Figure 82), it is highly possible that the surface crack length might be smaller than twice the coating thickness when the coating is fully penetrated, in another words the surface crack length being less than 0.6 mm when a 0.3 mm thick coating is fully penetrated. Therefore, the current definition of the first 2 mm surface crack as the criterion of fatigue failure will overestimate the cycles to the full penetration of coating.

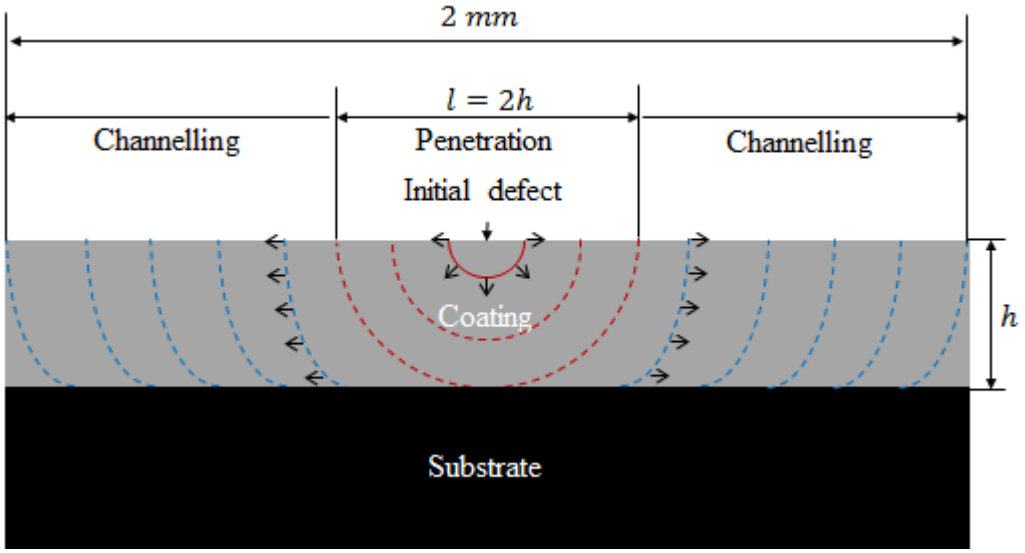

Figure 103. Schematic of the fracture surface of a first 2 mm fatigue crack in the current coating.

6.4.2. Comparison between the fatigue lives of the coatings

Previous research [187–189] regarding the effect of fracture toughness on fatigue life has already shown that monolithic epoxy-based composites with greater fracture toughness exhibited greater fatigue lives under the same loading conditions. Thus it is

not surprising to see in the current work that the substrated coating A was clearly more fatigue resistant than the substrated coating B in terms of lives to the first 2 mm crack.

Effect of R ratio

To understand the R ratio dependence of the fatigue lives of coating B, the measured lives are plotted with strain amplitude and corresponding maximum strain. Figure 104A shows the original strain-life relationship of coating B in terms strain amplitude ($\Delta\varepsilon/2$), and Figure 104B re-plots the data using maximum strain (ε_{max}).

In Figure 104A, the power-fit lines of the data show that the lines come together at lower strains with larger lives, while in Figure 104B the lines come together at larger strains with smaller lives, and the lines extrapolate to a maximum strain of about 0.5% for a life of 1 cycles, which is the same as the measured strain to failure of coating B on non-pre-strained substrate. This indicates that at smaller strains the coating life is more prone to be dominated by the cyclic component, while at larger strains the life is more prone to be dominated by the static component. In comparison, the strain-life relationship of coating A (Figure 59, page 102) was insensitive of the R ratio, this might indicate that the life of coating A is dependent on the cyclic component.

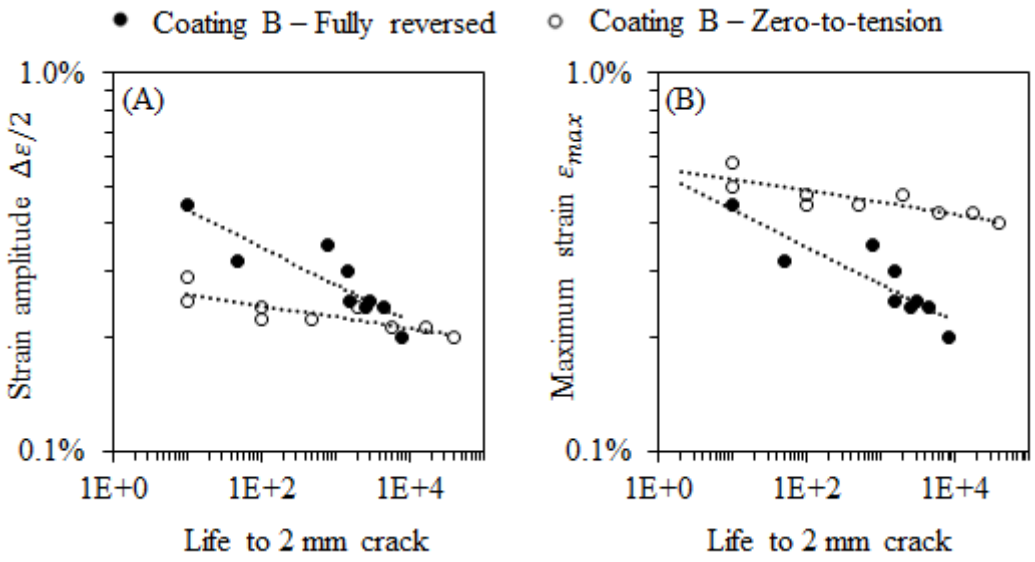

Figure 104. Replot of strain-life behaviour of coating B under fully reversed and zero-tension cycles using strain amplitude (A) and maximum strain (B) as vertical axis.

Effect of substrate uneven deformation

The difference between the fatigue resistances of coating B samples on pre-strained and non-pre-strained substrates (Figure 60) may be due to the Lüder's bands developed in the non-pre-strained substrates. The effect of these bands on the fatigue cracking should be similar to that on static cracking (Table 8). The fatigue samples with non-pre-strained substrates would have experienced larger strain cycles locally above the Lüder's bands, and thus developed fatigue cracks at shorter lives than the samples with pre-strained substrates under the same nominal strain cycles. Although, the local deformation of original substrate under 0.7% strain was not directly observed, it is likely that the yielding of the substrate leads to local high strains causing earlier initiation of cracks.

6.4.3. Coating fatigue crack development

Growth of single crack

Fracture mechanics of coating cracks predicts that the J-integral for crack channelling (J_{ch}) is invariant of surface crack length [129]. Thus it is expected that the fatigue crack growth rate of single coating cracks would be constant. Based the literature survey conducted by the author, it is the first time that this behaviour is observed experimentally (section 4.4.4).

Xia and Hutchinson [134] theoretically demonstrated that as the tips of two coating cracks approach each other, the strain energy release rates of both tips will reduce as the distance between the tips is smaller than a critical distance (H_c), which can be expressed as,

$$H_c = 2\pi G(\alpha, \beta)h \tag{55}$$

here, $G(\alpha, \beta)$ is a non-dimensionalised value of a through-thickness crack which reflects the material dissimilarity, h is coating thickness. $G(\alpha, \beta)$ can be determined using equation (27). For the current coating A and B samples, with thicknesses of 0.3 and 0.35

mm, the H_c can be determined as 1.29 and 1.5 mm respectively using equation (55). When the growth rate reduction of single cracks was observed in the current work, such as those shown in Figure 63 (page 107) and Figure 64, the cracks were found within the H_c of other surrounding cracks. Therefore it is highly possible that the slowing down of single crack growth was due to interaction with other nearby cracks. Looking at a greater scale, the slowdown of single crack growth due to interaction can also explain the slowdown of total crack length development as a reflection of the majority of single cracks being in interaction.

It was unexpected to observe that the fatigue crack growth rates of single cracks within the same sample varied significantly from crack to crack, see Figure 66 (page 109) to Figure 69. This may be caused by 1) microstructural inhomogeneity; 2) thickness variation; 3) crack interaction; 4) a combination of all these above.

Number of cracks and average crack length

The faster growth of number of cracks in the coatings at greater strain ranges (Figure 75 and Figure 76) is expected. Because given the distribution of defect sizes in the coatings, larger strains will lead to the crack initiations from both large and small defects, while at a small strain crack will only initiate from large defects.

To understand the difference between the developments of the number and average of cracks in coatings A and B (Figure 79), a possible explanation may be given using the magnitude of J -integral of crack channelling (J_{ch}) with respect to that of crack penetration (J_p). Figure 105 shows the J_p of a surface defect and J_{ch} of a through thickness crack in coating A and B at different static strains.

It can be seen that over the entire tested maximum strains, in coating A the J_{ch} was about 16% greater than the J_p, while in coating B the J_{ch} was about 55% greater than the J_p. In comparison to coating A, the drive force for channelling of coating B relative to the drive force of penetration is much greater. Thus in coating B the propagation of already

existing cracks should be more dominant over the initiation of new cracks, which leads to the appearance of smaller number of cracks with longer lengths.

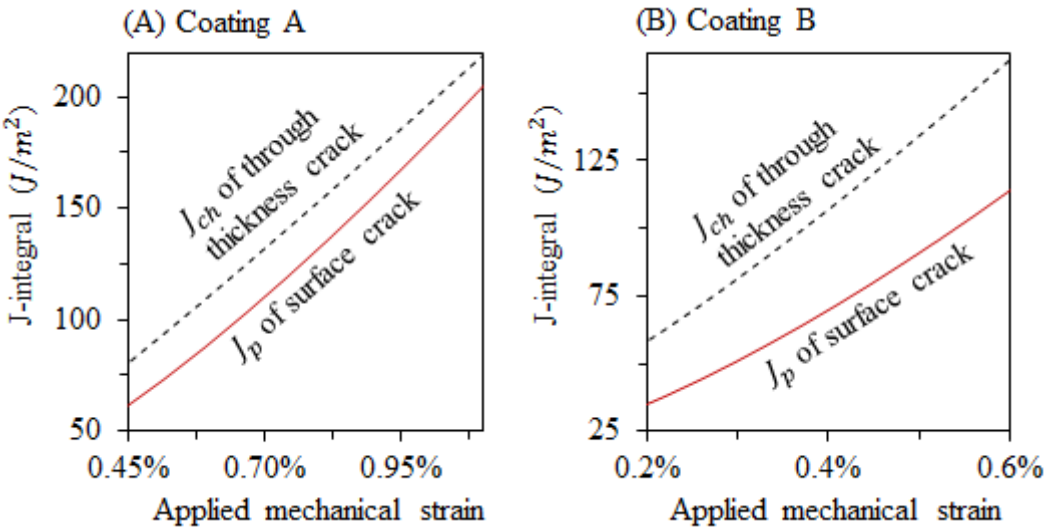

Figure 105. (A) Static strain dependence of the J_p of a 60 µm deep defect and the J_{ch} of a through-thickness defect in a 0.3 mm thick coating A on substrate; (B) Static strain dependence of the J_p of a 70 µm deep defect and the J_{ch} of a through-thickness defect in a 0.35 mm thick coating B on substrate.

6.4.4. Calculation of J-integral Range in Fatigue Tests

In the studies of fatigue crack growth of metallic materials, the correlation between crack growth rate and stress intensity range ($\Delta K = K_{max} - K_{min}$) under linear elastic conditions is usually constructed [144]. K_{max} and K_{min} stand for the stress intensity factors at the maximum and minimum stresses. Fatigue crack growth rate (da/dN) is normally correlated with ΔK using the Paris Law [146], see equation (34) on page 35. Crack growth rate can be predicted with known ΔK. As the stress-strain curves of coating A and B exhibited non-linearity over the applied strain ranges, J-integral range (ΔJ) needed to be used to correlate with crack growth rate instead of ΔK. Good correlation between the total crack growth rate of the coatings and cyclic strain range has been shown in Figure 74 on page 117. As it has been discussed that coating thickness influence the J-integrals of cracks in coatings at the same strain (section 6.3.3), thus a correlation between ΔJ and total crack growth rate would generalise the current fatigue crack

development results and expand the applicability of the current data to the coatings in other configurations such as different thickness.

For metallic materials undergoing large cyclic plastic deformation, many, such as Dowling [190,191], demonstrated that growth rate of long [190,192,193] and short [191,194] cracks can be correlated with J-integral range (ΔJ). In contrast to ΔK, ΔJ does not equal to $J_{max} - J_{min}$ [195]. Similar to J under static loading, ΔJ can be treated as a J-integral under cyclic loading [196]. For ΔJ of a crack under a cyclic normal stress, an expression similar to the static J-integral expression (equation (17) on page 19) developed by Rice [94] has been developed by Lamba [196], see equations below.

$$\Delta J = \oint (\phi(\Delta\varepsilon)dy - \Delta T_i \frac{\partial u_i}{\partial \mathrm{x}} ds) \tag{56}$$

$$\phi(\Delta\varepsilon) = \int_0^{\Delta\varepsilon} \Delta\sigma \cdot \mathrm{d}(\Delta\varepsilon) \tag{57}$$

Here, the symbol Δ refers to the change of the parameter between two states, and all the other symbols are consistent with those in equation (17). The term $\phi(\Delta\varepsilon)$ shown in equation (57) is the change of strain energy density between the two states. Figure 106 shows an arbitrary cyclic hysteresis loop. The two states of this loop are the top and bottom turning points, at the maximum and minimum strains.

Using the bottom turning point as the origin of a new coordinate, with the changes of stress ($\Delta\sigma$) and strain ($\Delta\varepsilon$) as Y and X axis respectively, the change of strain energy density $\phi(\Delta\varepsilon)$ can be seen as the area below either the loading, see the shaded area in Figure 106. By this definition, J-integral range (ΔJ) were calculated numerically [195] or analytically [190,191]. Dowling [191] dealt with the growth of single semi-circular surface short crack on smooth surface of monolithic A533B steel samples during low-cycle fatigue, and developed an approximation to calculate the ΔJ based on the loading path of the stress-strain hysteresis loop, see equation below.

$$\Delta J \approx 3.2\Delta W_e a + 5\Delta W_p a \tag{58}$$

Here, ΔW_e and ΔW_p are the changes in the elastic and plastic portions of strain energy respectively, and can be calculated with known hysteresis loops; a is the surface crack length, which implies that ΔJ of such cracks will be crack length dependent. Treatment of fatigue crack growth in coatings on a plastic deforming substrate has not yet been developed.

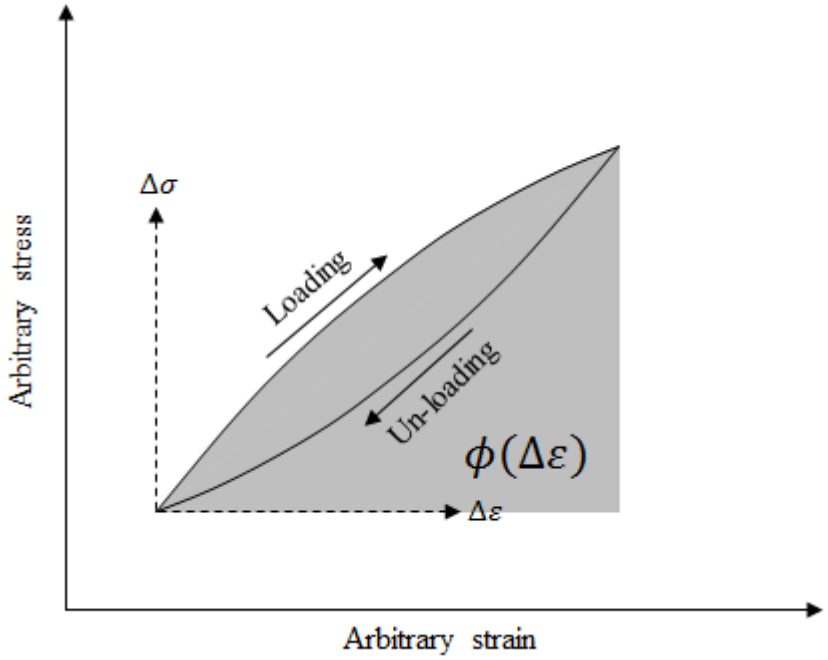

Figure 106. Illustration of an arbitrary cyclic hysteresis loop and the definition of the change of strain energy density.

As the total crack growth rate was measured only from coating crack channelling, the calculation of ΔJ of the coating under cyclic strains only considered the crack channelling of through-thickness cracks, thus the J-integral range for channelling (ΔJ_{ch}) The calculation of ΔJ_{ch} requires the knowledge of the hysteresis loops of the coatings under strain cycles. This could not be measured experimentally. To approximate the hysteresis loops of the coatings during fatigue, it will be assumed that the coatings were cyclically stable and the cyclic stress-strain curve was the same as the monotonic stress-strain curve as being described using Ramberg-Osgood relationship shown in section 5.3 (page 129). It has been widely observed in many metallic materials in a stable state during fatigue tests, the unloading path of a hysteresis loop has geometric shape the same as

the loading path being rotated for 180°, and both of them are twice the size of the cyclic stress strain curve of the fatigue cycle [197]. This phenomenon is widely recognised as the Masing's hypothesis or rule [198]. In this work, the Masing's hypothesis is adopted. Figure 107 shows an approximated hysteresis loop of a substrated coating A sample under a fully reversed load with a strain range of 1.2% for R = -1.

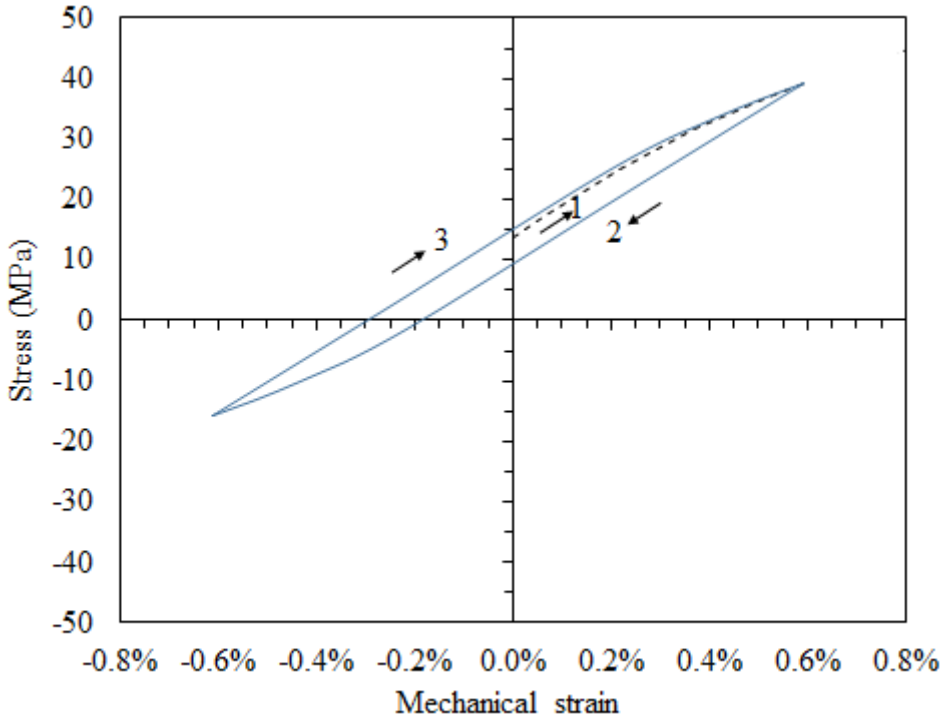

Figure 107. Estimated hysteresis loop of substrated coating A sample (FFA – 7) under a fully reversed cycle with a strain range of 1.2%.

The change of stress in the figure is associated with the change of mechanical strain only. The initial loading curve 1 starts with a thermal residual stress of 14 MPa and ends at the upper turning point at the maximum strain of 0.6%. Following that, the strain reduces to the lower turning point at minimum strain of -0.6% with the minimum stress of about -16 MPa, and forms the unloading branch shown by curve 2. After that, the strain travels 1.2% strain back to the upper point, see curve 3, and forms a complete hysteresis loop with the unloading path. Hysteresis loops of the coatings under other strain amplitudes can be produced in the same way. Note in reality, hysteresis loops often shift as a response to the change in material [144].

6.4.4.1. J-integral range calculation

In this work, the load increasing paths of hysteresis loops were used to calculate ΔJ_{ch}. Shifting the lower turning point to the origin at 0 stress and strain, the change of stress and strain of the cycle will be the maximum stress and strain of the shifted upper turning point. Thus using the shifted loading paths as the stress-strain curve, the J-integral at the maximum stress/strain (upper turning point) calculated in a single loading would be the ΔJ_{ch} of the cycle.

During the fatigue tests, the substrates also had large plastic deformation. As discussed in section 6.1 (page 147), the effective stiffness of both substrate and coating changes during straining, resulting in changes in stiffness mismatch. As the J-integral of channelling (J_{ch}) is influenced by stiffness mismatch via Dundur's parameters α and β, see equation (26) (page 28), the loading paths of substrate hysteresis loops ought to be incorporated in the calculations as well. Figure 108 shows the load increasing paths of the measured substrate hysteresis loops under different strain cycles in terms of stress range ($\Delta\sigma$) – strain range ($\Delta\varepsilon$) curves, in which the lower turning points of all curves were shifted to the origin. Given the similar shapes of all the curves, a representative curve was produced using the Ramberg-Osgood fitting of all the curves, and the fitted parameters are shown in Table 13. The loading path of the coatings in terms of stress range ($\Delta\sigma$) – strain range ($\Delta\varepsilon$) were essentially the coating static stress-strain curve being enlarged by a factor of 2, of which the Ramberg-Osgood parameters for the coatings are also shown in Table 13. The parameters apart from the modulus in Table 13 are different from Table 11. The reason is that these parameters represent the loading path of the hysteresis loops of the materials, which are different from static stress-strain curves. The n parameter of the substrate under cyclic strain is about 1/3 of that under static strain. This indicates the cyclic softening behaviour of the steel substrate during fatigue. The reason why σ_Y of the coatings is twice that in Table 11 is that the loading branch of the coating hysteresis loop is geometrically double the coating static stress-strain curves.

Table 13. Ramberg-Osgood parameters for the cyclic stress-strain behaviour of substrates.

Cycle type	Modulus E(GPa)	σ_Y (MPa)	θ	n
Substrate	200	400	0.015	8.75
Coating A & B	5.2	30	0.016	4.422

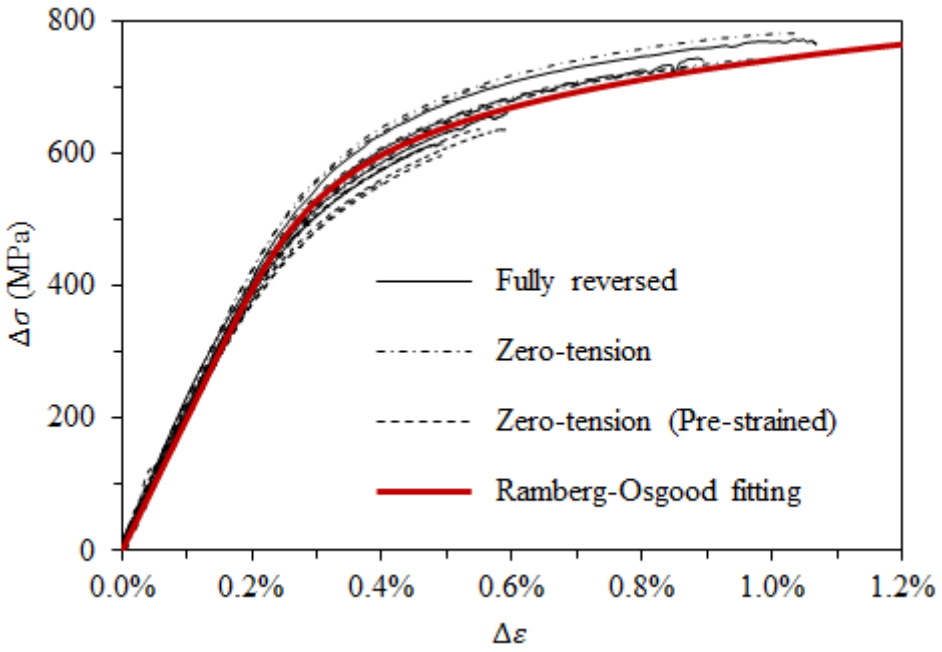

Figure 108. $\Delta\sigma$-$\Delta\varepsilon$ curves derived from the load increasing paths of the hysteresis loops of substrate under both fully reversed and zero-tension cycles with different strain ranges from 0.3% to 1.05%.

The same FE models used for the calculation of J-integral of coating cracks under static strains was used, see section 5.1 (page 123). The ΔJ_{ch} was calculated in the same way as the J_{ch} under static strain was calculated. The calculation of ΔJ_{ch} under cyclic strains had two major differences from the calculation of J under static strains. First, the material properties reflected only the changes of stress and strain during cycling. Second, since the thermal residual strain did not contribute in the change of J-integral, no temperature reduction was applied. For both coatings, a maximum strain of 1.5% was applied to the models. From 0 to 1.5% strain, 30 numerical calculation steps were assigned with an equal increment of 0.05% strain. This calculated the ΔJ_{ch} for different strain ranges up to 1.5%. The results are shown in Figure 109.

In the fatigue tests of the coatings, the strain ranges were all smaller than 1.5%. The ΔJ_{ch} of coating B appeared to be 17% greater than that of coating A due to the average thickness of coating B being 50 μm bigger than that of coating A. It needs to be noted here that ΔJ_{ch} is the same as J_{ch} that the value is independent of surface crack length. For a fixed strain range, the ΔJ_{ch} value is constant.

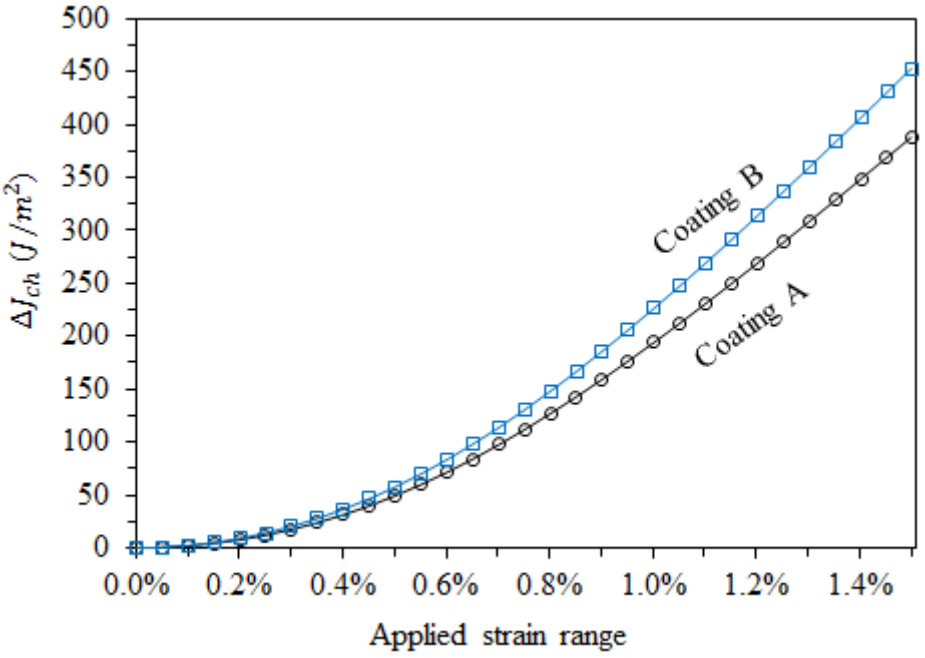

Figure 109. The development of ΔJ_{ch} as a function of strain range calculated by FEA.

6.4.5. Correlation between J-integral range and total crack growth rate

For each coating, the ΔJ_{ch} at each tested strain range was interpolated from Figure 109. Figure 110 shows the total crack growth rate plotted against ΔJ_{ch}. Similar to the correlation between the strain range and total crack growth rate (Figure 74 on page 117), the total crack growth rate increased with the increase of ΔJ_{ch}, and the data points of the samples tested do not show strong dependence on the R ratio. To correlate total crack growth rate (da/dN) with ΔJ_{ch}, the Paris' law can be rewritten [93,144], see equation (59).

$$\frac{da}{dN} = C(\Delta J_{ch})^m \tag{59}$$

Here, C and m are empirical constants to be determined experimentally. Both the data sets of coatings A and B were fitted to equation (59), and the resultant parameters C and m are shown in Table 14.

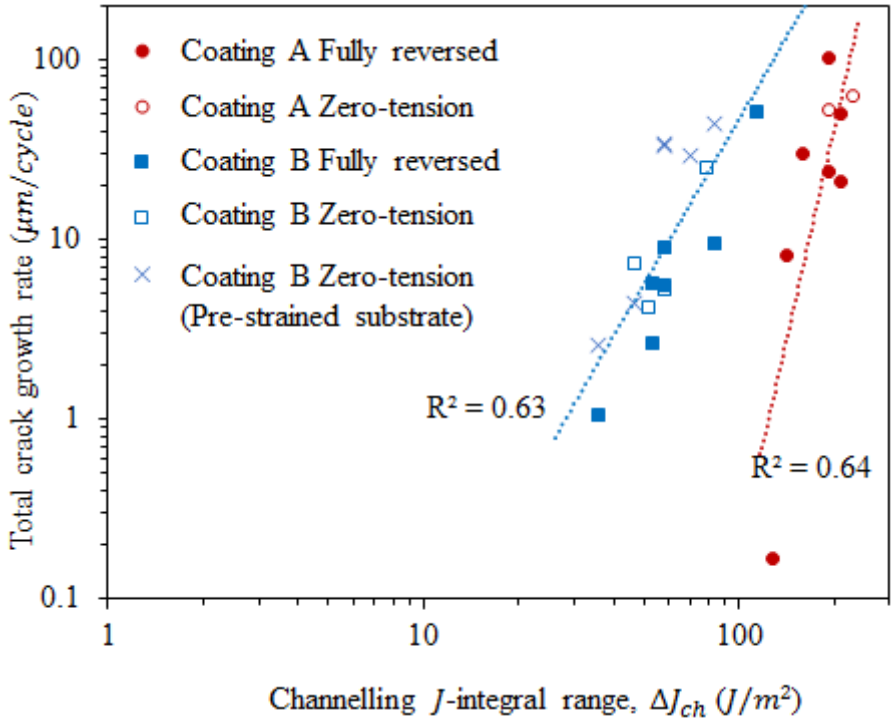

Figure 110. The correlation between total crack growth rate and ΔJ of both coatings under cyclic strains.

Table 14. Resultant parameters of fitting total crack growth rate - ΔJ to equation (59).

	C (μm/cycle)	m
Coating A	5.30×10^{-17}	7.77
Coating B	3.97×10^{-5}	3.03

Good correlations between the J-integral range (ΔJ_{ch}) and total crack growth rate have been shown, and coating B showed an inferior resistance to total crack growth to coating A. Note, the R^2 values of the correlations shown in Figure 110 are the same as the power-law correlations between total crack growth rate and strain range (Figure 74 on page 117). This means that the correlation using ΔJ_{ch} does not reduce the scatter of the data.

At a ΔJ_{ch} of about 100 J/m^2, the total crack growth rate of coating B is about 250 times that of coating A. Hsieh [188] experimentally demonstrated that the fatigue crack growth rates in carbon/epoxy composites is greater in the composites with smaller fracture toughness. Thus, as the fracture toughness of coating B is only about 34% the toughness of coating A, that coating B has a greater total crack growth rate than coating A is consistent with the results of Hsieh [188].

However, the total crack length development of coatings encompasses the initiation and propagation of multiple cracks, see Figure 51 (page 92), and this is different from the case for monolithic materials, in which only a single fatigue crack is investigated [144]. Whether the dependence of the total crack growth rate on ΔJ_{ch} of these coatings can be used to predict the fatigue crack growth of the coatings in other configurations, such as different coating thickness and different substrate geometry, requires further investigation. Nevertheless, the ΔJ_{ch} – total crack growth rate data can still be used to predict the total crack growth rate of the coatings with similar thickness to the current thicknesses of the current test samples. These results are valuable for future studies into the thickness effect on the total crack growth behaviour of the coatings under cyclic strains.

6.5. Recommendations on Coating Design

The results have implications on the design of coating formulation, the application of coatings in service, as well as the fracture investigation into new formulations.

It has been concluded that the strain to first crack of WBT coatings is affected by fracture toughness, residual stress, and defect size. The superior ductility and fatigue resistance of coating A derives from its greater toughness in comparison to coating B. This highlights the crucial role of improving toughness in designing coating formulations against cracking. As CTE strongly affects the residual stress level in coatings, hence affects the ductility, new formulations also ought to reduce the CTE in order to reduce residual stress. Since debonded filler/matrix interface could act as a crack initiator, the maximum

size of the fillers used in coatings could also be the maximum defect size. Thus, reducing the size of fillers in new formulations may also improve the strain to first crack.

From the application point of view, coating thickness is the only factor can be controlled by coating users. As thicker coatings tend to have greater J-integrals for cracking, coating users should try to keep the coating thickness as small as sufficient anti-corrosion performance can be maintained.

It has been demonstrated in the current work, that the free film tensile fracture strains underestimated the fracture strain of the coatings on substrates. Only when fracture toughness was used, the predictions of strains to first crack of substrated coatings being greater than the free film fracture strains are consistent with the observations. The reason for this observation may be that the defects in the free films may be different from those in substrated coatings in both location and size, as the sample manufacturing methods were different. This highlights that future studies of WBT coating fracture should adopt a toughness-based approach. This is because that the fracture of coatings is influenced by various factors, and the strength or ductility measured from one type of sample is likely to be transferrable for other sample geometries or service conditions.

7. CALCULATION OF J-INTEGRALS OF COATING CRACKING UNDER THERMAL STRAINS

In service, the failure of WBT coatings is mainly caused by thermal strains with associated stresses generated due to temperature cycles, which is intrinsically different from the current mechanical tests at a constant ambient temperature, where the coating failure was caused by mechanical strains. Thus it is crucial to understand the relevance of the current coating mechanical tests to coating failure in service. If thermal and mechanical strains are equivalent in terms of the effect on cracking, the J-integrals for coating cracking at the same thermal and mechanical strain should also be the same.

For this purpose, finite element analysis of J-integrals of coating cracking purely due to thermally induced stress/strain was performed. The results are compared to the J-integrals of coating cracking during the mechanical tests, which has been calculated in section 5.5 (page 138). In this chapter, the material properties used for the FE analysis under thermal strains are introduced first, followed by an introduction to the models used. The procedures and results of calculations are described in separate subsections.

7.1. Material Properties Used for Calculation

The modulus of epoxy is temperature-dependent [33], thus when calculating thermal stress at different temperatures a temperature-dependent stress-strain behaviour of the material ought to be used. In the current calculations the modulus of the coatings was assumed to be temperature dependent. As the measured stress-strain curves of the coating free films at -10 °C were linear (Figure 23 on page 52), it is also assumed that the stress-strain curves used for calculation are linearly elastic at a fixed temperature.

The temperature dependence of both coating elastic modulus from 70 to -10 °C has been shown in Figure 24 (page 53). The modulus between each pair of adjacent data points was interpolated linearly. Deng *et al*. [199] have shown that the temperature dependence of the modulus of a silica-filled epoxy below T_g to about – 80 °C was almost linear. Based on this, the temperature dependence of the modulus of both current coatings below – 10 °C was approximated using the linear trend formed by the modulus

at -10 and 23 °C, and as coatings A and B had the same moduli at these two temperatures, it was also assumed these coatings had the same modulus below – 10 °C, see Figure 111.

Figure 29 (page 59) shows the dimension change of both coatings due to temperature reduction below T_g to – 50 °C are linear. Thus in the calculations the thermal expansion coefficients were also treated as constant, and the same as those used in Chapter 5. In addition to this, the glass transition temperature and Poisson's ratios were the same as those used in Chapter 5.

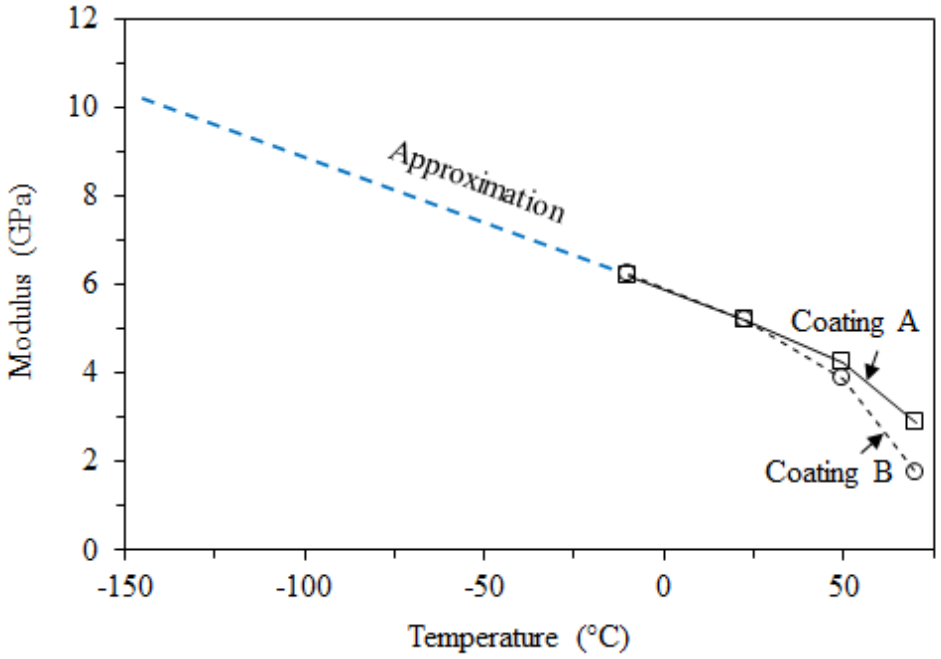

Figure 111. Temperature dependence of modulus of the coatings and the approximation below – 10 °C.

7.2. Finite Element Models for the Calculation of J-integrals under thermal strain

Figure 112 shows the right half of a T section model symmetric to the left vertical edge, and this model simulates a cross-section of fillet weld joint. The coating and substrate are shown in red and grey respectively. The model itself is also symmetric to the centre line. The transition between the vertical and horizontal arms is a central flat region forming 135° inner angles with each arms. The two ends of the central flat region connect with each arms with a surface curvature with a radius of curvature of 2 mm. The

coating layer was designed to be constant in thickness (h) along the substrate surface. The elements used in the model were all 2D plane strain quadratic quadrilateral CPE8 elements, which consist of 8 nodes for each element. To simulate such structure in a much larger ballast tank structure, symmetry boundary conditions were assigned to the left and bottom edges of the model, and the top and right edges were constrained to be permanently horizontal and vertical respectively.

Previously, Zhang et al. [156] and Kim and Lee [3] performed calculations of thermal stress in epoxy coatings on steel fillet weld joints with geometries similar to the current model using FE analysis, and found that the maximum stress/strain developed at the surface curvature region of the coatings. Current work also focused on this region. A magnified view of the top corner is shown in Figure 112B, which also shows a fine mesh in this region.

When the J-integral was calculated, a surface crack with a depth of a was introduced to the centre of coating surface curvature at the top corner, and it was aligned in the radial direction. Figure 112C shows the location of and the mesh around the crack. For the calculation of J-integral for crack penetration (J_p), the contour integral technique was used, and the contour at a crack tip had a radius of 30 μm. To calculate the J-integral for crack channelling (J_{ch}), the same method based on crack opening displacement, described in section 5.1 (page 123), was used.

7.3. Calculation of J-integral of Penetration in Coating on Flat Steel Substrate

To investigate the effect of thermal strains on the cracking of the coatings, the J-integral of crack penetration (J_p) under pure thermal strains was calculated. The model of coating on flat steel substrate was used. The coating thicknesses of 0.3 mm and 0.35 mm for coatings A and B respectively, and the defect depths of 60 and 70 μm were introduced to simulate current samples. Temperature reduction from the T_g to minimum temperatures of – 150 and – 100 °C were applied to coatings A and B respectively. When

tensile thermal stress is developed in the coatings, substrate compressive stress occurs in order to keep the coating/substrate system in load balance.

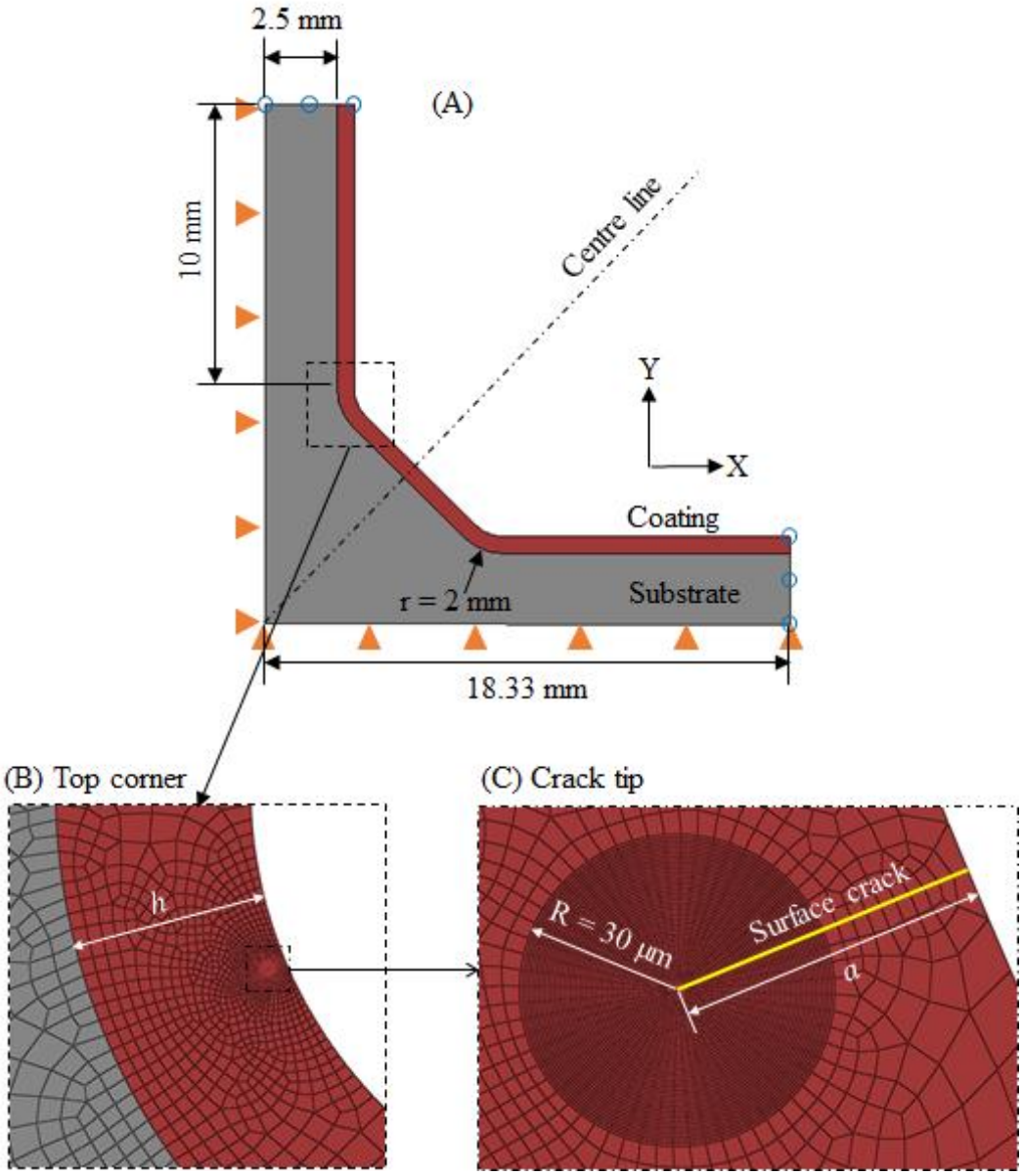

Figure 112. 2D plane strain welded joint model with 0.6 mm thick coating as an example. (A) Boundary conditions; (B) Mesh in the coating around the crack; (C) Crack tip contour and mesh.

It was found that the greatest compressive stress developed in the substrate in the studied temperature range was - 9 MPa, which is trivial and means that the substrate deformation was within the elastic limit. This is different from the substrate stress during

the mechanical tensile testing, in which large unidirectional tensile strain up to 3% was applied to the substrate, inducing a mechanical stress up to 600 MPa, which was well beyond the elastic limits. The resultant J_p is plotted against thermal strain and temperature in Figure 113 for coating A and Figure 114 for coating B.

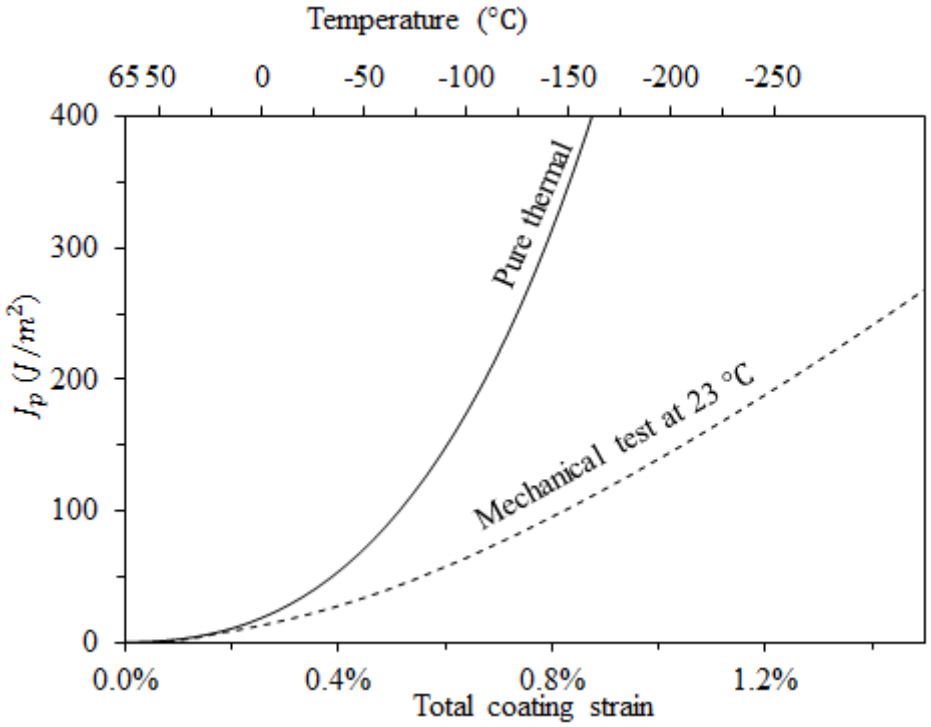

Figure 113. J_p of a 60 μm deep surface defect in a 0.3 mm thick coating A as a function of total coating strains generated by temperature reduction and during the mechanical testing.

The J_p of a defect with the same size generated during mechanical testing at 23 °C was extracted from Figure 91 (page 142) and Figure 92 for coatings A and B, and it is also plotted against total coating strain in the figure for each coating. Note, here total coating strain for the pure thermal case is thermal strain, while for the mechanical test case the total coating strain includes the thermal residual strain of about 0.2% at 23 °C, and the additional total coating strain was induced by the mechanical straining of the substrate.

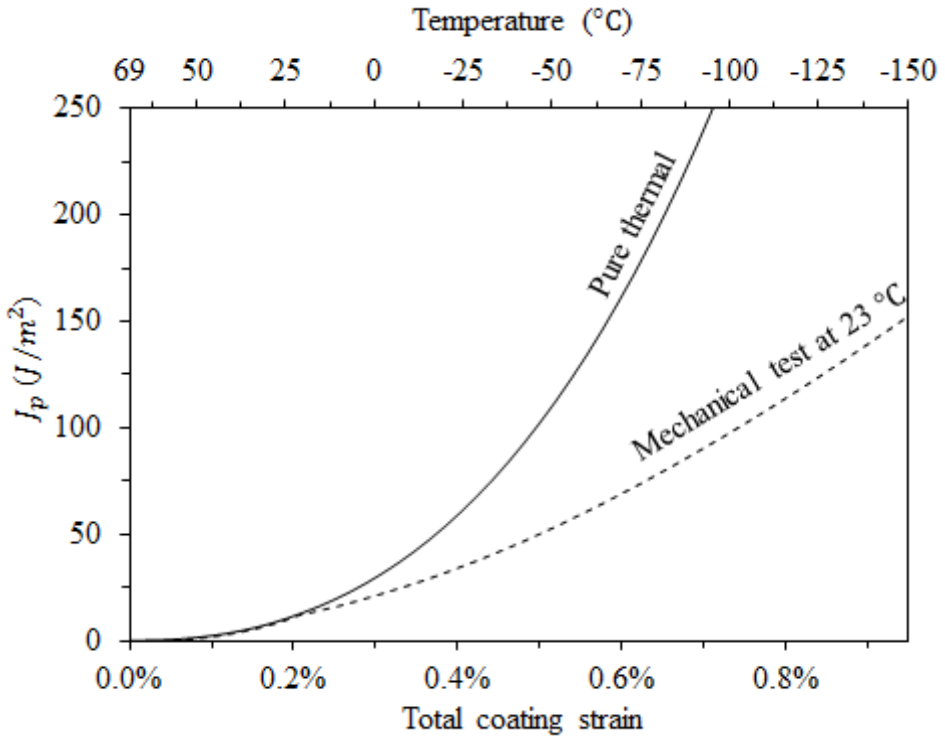

Figure 114. J_p of a 70 µm deep surface defect in a 0.35 mm thick coating B as a function of total coating strains generated by temperature reduction and during the mechanical testing.

It is clear that at the same total coating strains greater than about 0.2% thermal strains induce greater J_p than mechanical strain, and the gap widens with increasing total coating strain. As penetration will start when J_p exceeds coating fracture toughness, the results predict that the total coating strain to fracture under pure thermal strains of the current substrated coating samples will be smaller than the total coating strain to failure during mechanical tensile tests at 23 °C of coatings A and B respectively.

Based on equation (25), the ratio of penetration J-integral of a defect in a substrated coating caused by pure thermal strain due to temperature reduction (J_p^{th}), to that caused by mechanical straining during mechanical testing at 23 °C (J_p^{ms}) is shown as below.

$$\frac{J_p^{th}}{J_p^{ms}} = \frac{\sigma_{th}}{\sigma_{ms}} \cdot \frac{f_{th}^2(\alpha, \beta, \frac{a}{h})}{f_{ms}^2(\alpha, \beta, \frac{a}{h})} \tag{60}$$

Here, σ_{th} and σ_{ms} are the coating stresses at the same total coating strain caused by a pure thermal strain and by a mechanical strain respectively. The f_{th}^2 and f_{ms}^2 are two dimensionless factors in these two cases respectively. As introduced before this factor is a function of the stiffness mismatch of the coating and substrate, quantified by Dundur's parameters (α, β), and the crack depth to coating thickness ratio (a/h). As in the current case, the a/h in the pure thermal case and mechanical tests is the same, 0.2, the f^2 factor is only a function of the stiffness mismatch. Equation (60) shows the J_p^{th} to J_p^{ms} ratio is mainly affected by the stresses and stiffness mismatch.

7.3.1. Effect of source of stress on J-integral

Figure 115 shows the stress in a substrated coating A due to thermal strain under temperature reduction and due to mechanical straining during mechanical test. The data for the purely thermal case was extracted from the calculation of J-integrals under thermal strain shown in section 7.3 (page 179), and the data for the mechanical straining case was extracted from the calculation of J-integrals during mechanical tests shown in section 5.5 (page 138).

Figure 115 shows that the trends of the development of coating stresses under thermal strain and during mechanical tests are similar to that of the development of J_p shown in Figure 113. At a total coating strain of 0.7% for instance, the stress produced by thermal strain is about 100 MPa, while the stress produced by mechanical straining is only about 35 MPa. This gives a σ_{th}/σ_{ms} of about 2.86, which means even if for the same f_{th}^2 and f_{ms}^2, the J_p^{th} caused thermally would be 2.86 times the J_p^{ms} produced in mechanical testing.

There are two major reasons why there should a difference between σ_{th} and σ_{ms}. Firstly, the development of thermal strain was achieved by reduced temperature. As the coating modulus used for thermal stress calculation increases with the reduction of temperature. For example, at the predicted total coating strain of 0.7% to thermal failure of coating A, a -110 °C is required, at this temperature the modulus used for thermal

stress calculation can be found to be about 9.3 GPa in Figure 111 (page 178). While during mechanical straining, the temperature was constant 23 °C, the modulus of the coating was only 5.2 GPa, see Figure 96 (page 148). Secondly, the development of thermal stress is biaxial, according to Hook's law for plane stress [200] the stress in one direction is amplified by the perpendicular direction, and thus the modulus of the coating under thermal strain needs also to be factored by $1/(1-\upsilon)$, as υ is 0.3 this further increases the coating modulus under thermal strains.

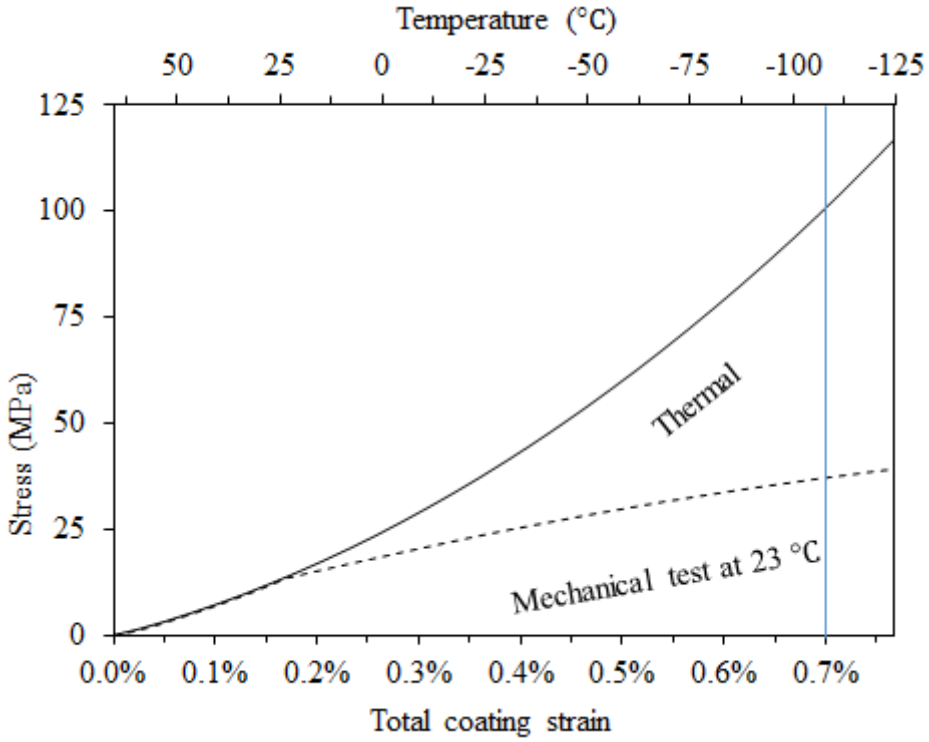

Figure 115. Stress in coating A under pure thermal strain due to temperature reduction and by mechanical straining during mechanical test at 23 °C.

7.3.2. Effect of stiffness mismatch on J-integral

During mechanical straining the substrate plastically deformed, and in the calculation of J_p^{ms} the effect of material non-linear deformation on coating/substrate stiffness mismatch due to both reduced coating and substrate stiffness (Figure 96 on page 148) was considered. While during the calculation of J_p^{th} under pure thermal strains, the

substrate did not experience yielding, thus the modulus would remain unchanged as 200 GPa, and the modulus of coating increased as temperature was reduced.

Again using substrated coating A sample as an example, at the same total coating strain of 0.7%. In the thermal case, a temperature of – 110 °C is needed, and the modulus of coating A is about 9.3 GPa, while the substrate modulus is 200 GPa. The f_{th}^2 (a/h = 0.2) can be calculated using using equations (21) (page 25), (22), and (24), and it is 0.245. At a total coating strain of 0.7% during mechanical tests, the effective stiffness (tangential modulus) of coating and substrate can be found to be 3.1 and 6.2 GPa, and the f_{ms}^2 can be calculated to be 0.247. This will give an f_{th}^2/f_{ms}^2 ratio of 0.994.

It can also be found that the σ_{th}/σ_{ms} ratio is about 3 times the f_{th}^2/f_{ms}^2 ratio, this means the difference between the calculated J_p^{th} and J_p^{ms} may be mainly due to the effect of the different source of the stress. In other words, that main reason why the coatings are predicted to be more prone to cracking under thermal strains might be that the thermal strains could induce greater stresses than mechanical strains. Note, here only the case where a/h = 0.2 is investigated. At an increased a/h ratio, the effect of stiffness mismatch (i.e. f_{th}^2/f_{ms}^2 ratio) might be greater.

7.4. Analysis of Coating on Fillet Welds

7.4.1. Stress analysis of coating on fillet welds

The stress in the current coatings on fillet welds due to temperature reductions was calculated using the model of coating on fillet weld introduced earlier. Three different coating thicknesses, 0.3, 0.6 and 0.9 mm were investigated. Temperature reductions from the T_g to 23 °C and 0 °C were applied to coatings A and B respectively. The temperature 23 °C represents an as-cured state before being in service, and the temperature 0 °C represents the minimum temperature the coating could experience in service. An assessment of the thermal stress and related J -integrals at these temperatures can suggest the integrity of the coating in these two scenarios.

As an example, Figure 116A shows the stress/strain distribution along the surface of coating A at a temperature of 0 °C. As the structure was symmetric, the stress distribution of only half of the entire surface was shown. The location is normalised by the coating surface length of half of the model, and marked by a path shown in the same figure. It can be seen from the figure that 1) the coating thickness does not have any effect on the thermal stress and strain along the flat portion of the structure; 2) the maximum local thermal stress and strain are at the midpoint of the coating surface curvature directly above the weld corners; 3) the maximum stress/strain in thicker coatings are greater than thinner coatings. For a thickness of 0.9 mm, the maximum stress/strain on the curvature is about 100% great than the stress/strain in the flat region.

As it can also been seen from the diagram of Figure 116B, there is a noticeable stress gradient through the coating thickness at the weld corners, while no noticeable through-thickness stress gradient is seen in the flat portion of the weld. Figure 117 shows the through-thickness stress distribution of coating A from the midpoint of coating surface curvature to the midpoint of interface curvature. The locations along the path is normalised by thickness, the coating surface is 0 and the interface is 1. It can be seen from the figure that 1) the strain decreases from surface towards interface; 2) a greater thickness leads to a greater strain gradient; 3) the strains at the interface for all thicknesses are about 0.26%.

The stress gradient in the coating at the weld corners as well as its sensitivity to coating thickness are not seen in coatings on the flat region. This means that the stresses in the coating test samples with flat substrates should be different from those on weld corners in service.

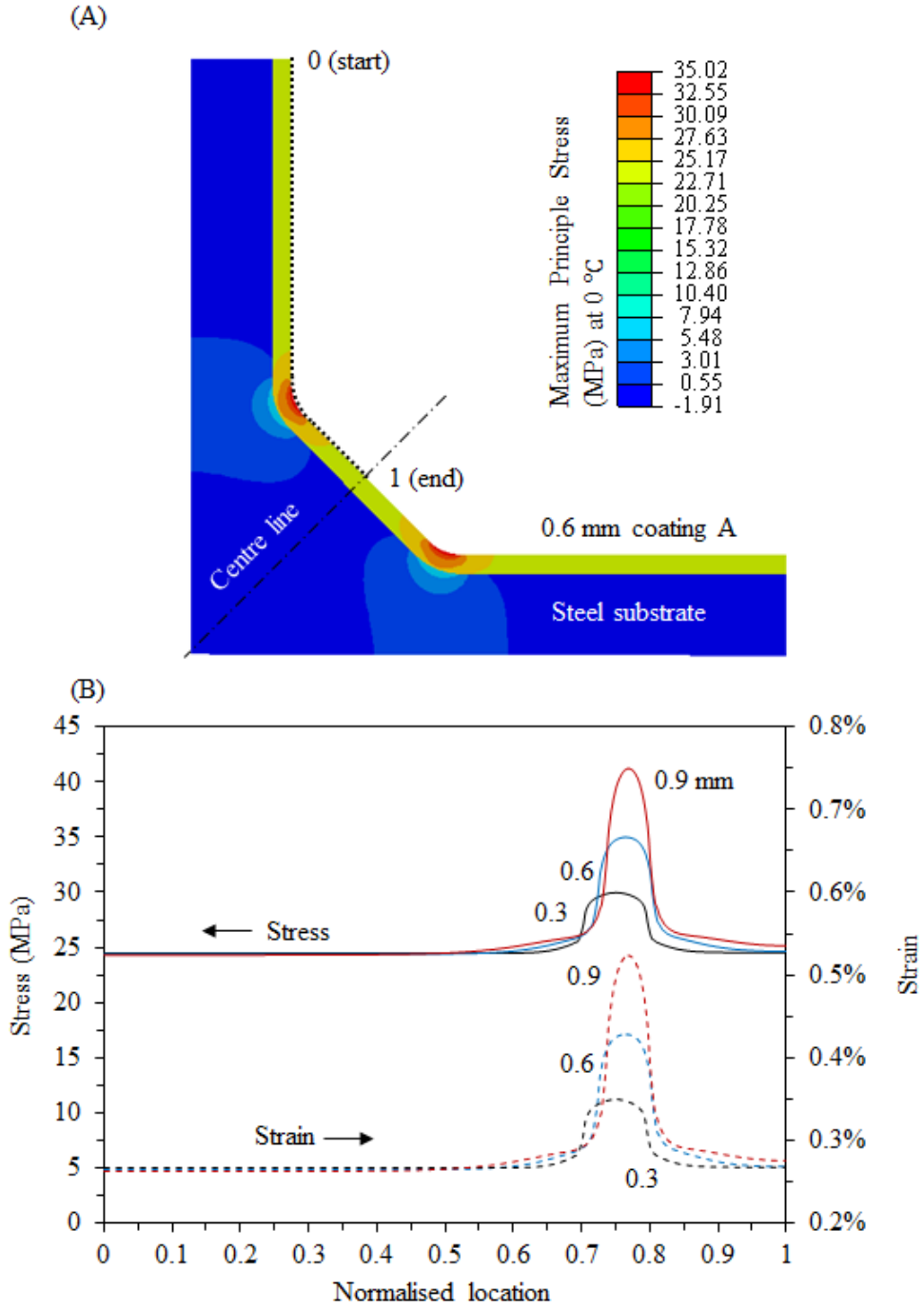

Figure 116. Estimated stress and strain distribution along the surface of coating A with thicknesses of 0.3, 0.6, and 0.9 mm on a fillet weld at 0 °C.

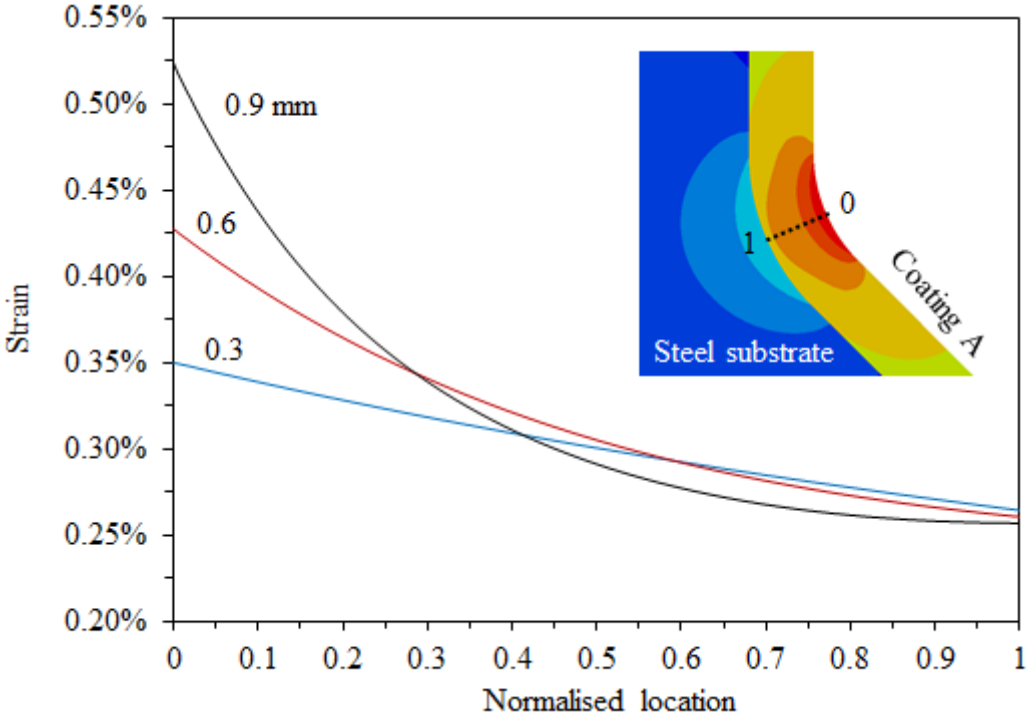

Figure 117. Estimated strain distribution along the through-thickness paths in coating A with thicknesses of 0.3, 0.6, and 0.9 mm on a fillet weld at 0 °C.

7.4.2. Calculation of J-integrals of defects in coatings on fillet weld at two critical temperatures

To investigate the process of cracking the current coating under thermal stresses, the J-integrals of penetration (J_p) and channelling (J_{ch}) of surface defects with various depths (a) in the current coatings on the fillet welds under thermal stresses/strains induced by temperature reductions from T_g to two critical temperatures, 23 and 0 °C, were calculated. Three coating thicknesses (h), 0.3, 0.6, and 0.9 mm were investigated. The defects with a/h ratios from 0.1 to a through-thickness depth were incorporated.

In result, the J_p and J_{ch} as a function of defect depth in coating A are shown in Figure 118 for 23 °C and Figure 119 for 0 °C, and the J_p and J_{ch} as a function of defect depth in coating B are shown in Figure 120 for 23 °C and Figure 121 for 0 °C. The trend of J_p and J_{ch} calculated using the model of coating on fillet welds under thermal strains are similar to those calculated for coatings on flat substrate during mechanical testing shown in Figure 89 on page 140.

It can be seen from Figure 118 to Figure 121 that for coatings on the corner of fillet welds:

1) The J_p values are greater than the J_{ch} for crack depths with a/h ratios below about 0.9. This also means that for the current defect sizes of 60 and 70 μm in coatings A and B respectively, the penetration will start first in coating, with thickness greater than 0.3 mm, on fillet welds.
2) For the same coating type with the same thickness, the J_p and J_{ch} are greater at 0 °C than those at 23 °C. This should be due to greater thermal strains induced at 0 °C.
3) For the same coating type at the same temperature, the J_p and J_{ch} estimated for a greater thickness are larger than those estimated for a smaller thickness. This should be due to greater thermal strains caused by increased thickness as shown by Figure 116 (page 187).
4) For coatings with the same thickness at the same temperature, the J_p and J_{ch} of coating B are greater than those of coating A. This should be due to the thermal expansion coefficient and T_g of coating B being slightly greater than those of coating A, leading to greater thermal strains in coating B.

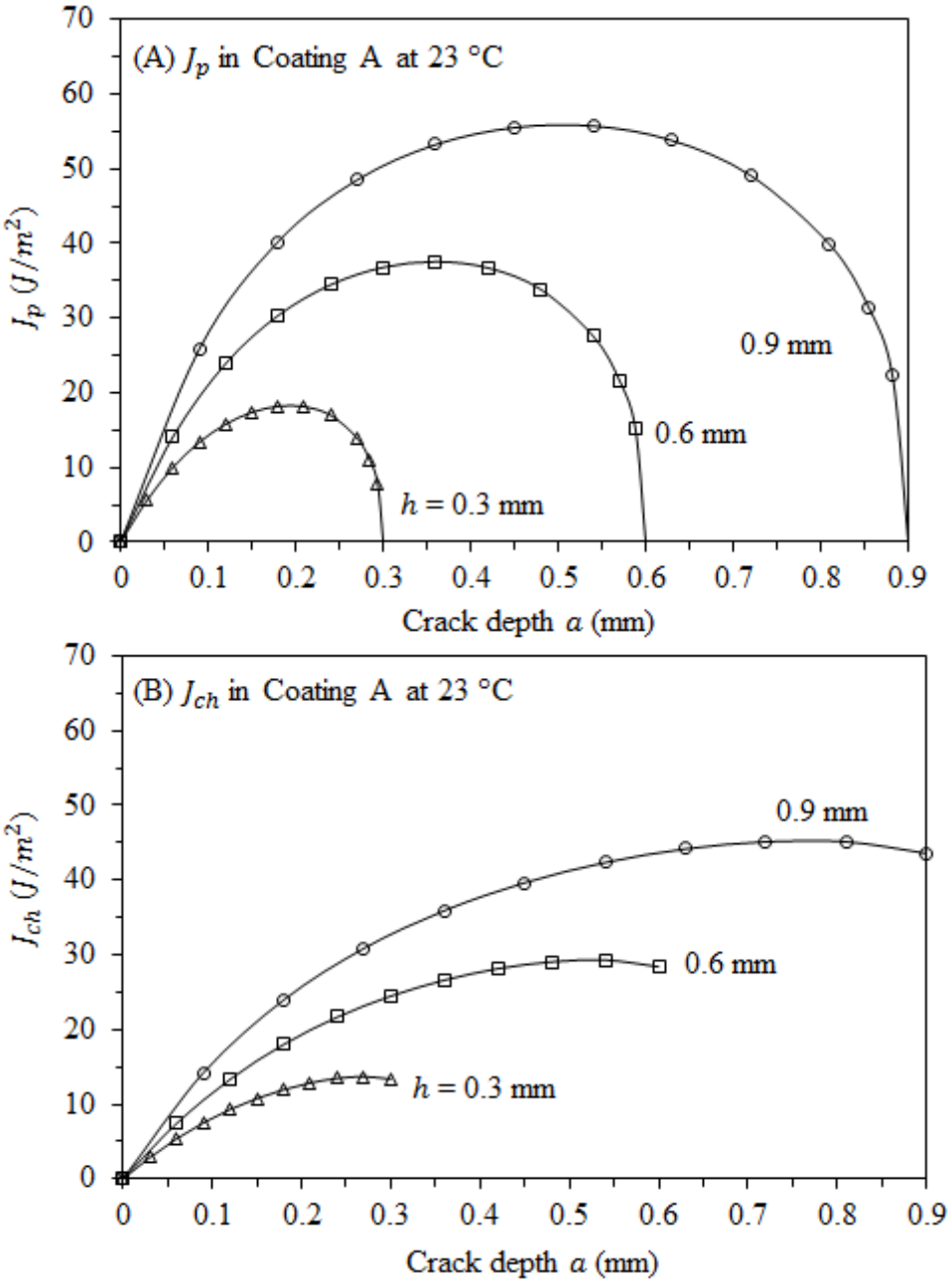

Figure 118. J_p and J_{ch} of cracks in coating A with different thickness on fillet welds joint under temperature reductions from T_g to 23 °C.

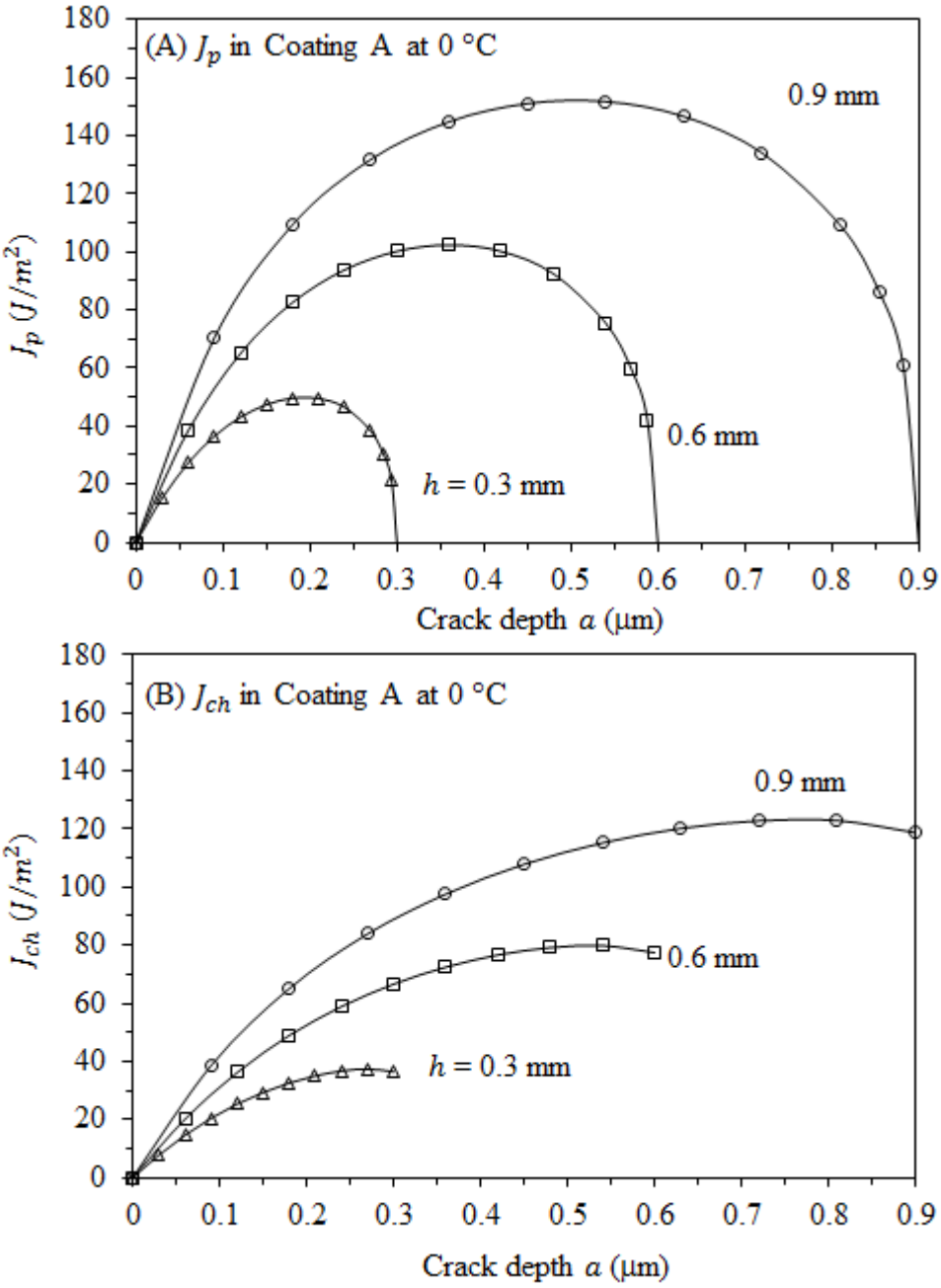

Figure 119. J_p and J_{ch} of cracks in coating A with different thickness on fillet welds joint under temperature reductions from T_g to 0 °C.

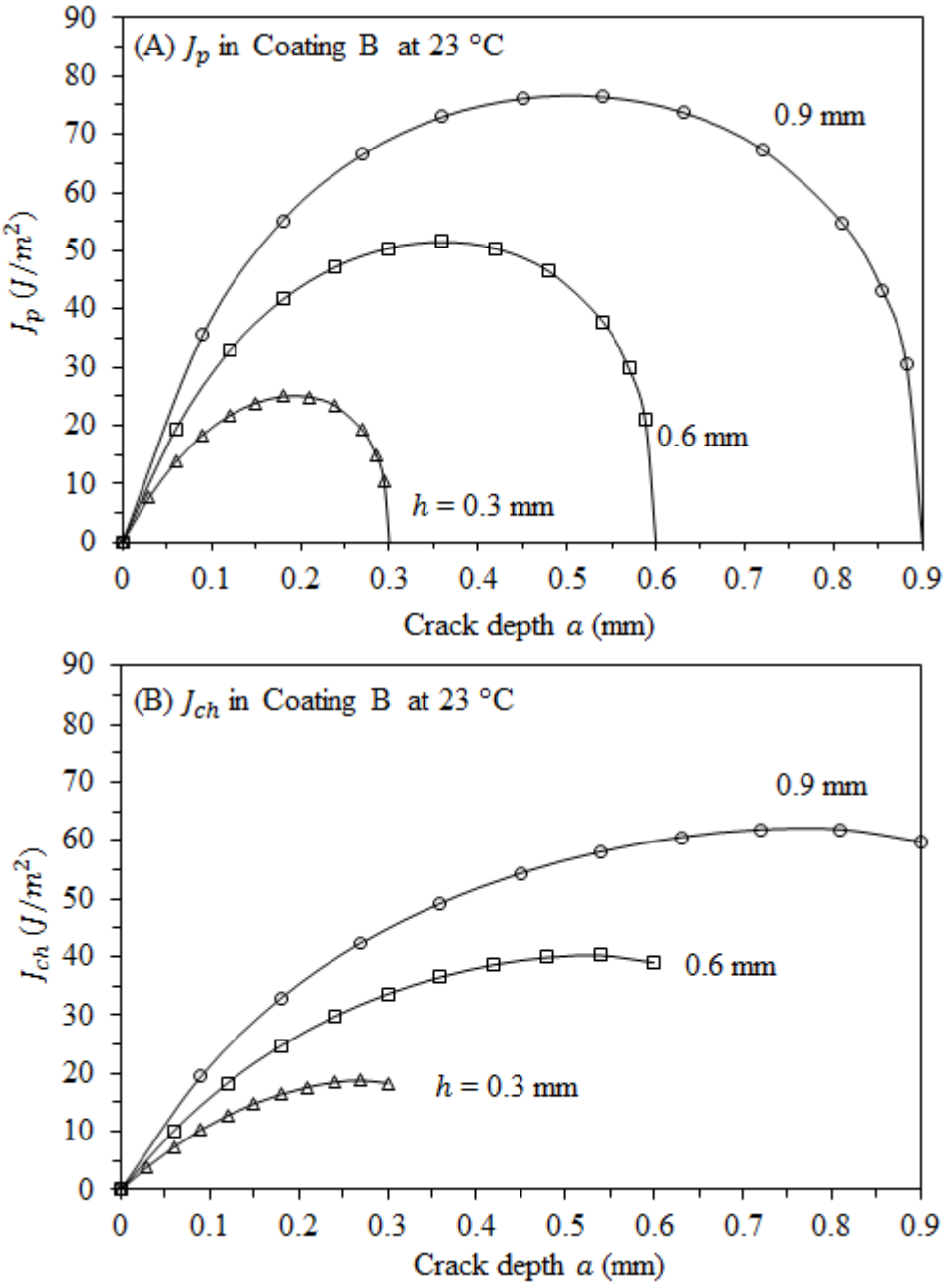

Figure 120. J_p and J_{ch} of cracks in coating B with different thickness on fillet welds joint under temperature reductions from T_g to 23 °C.

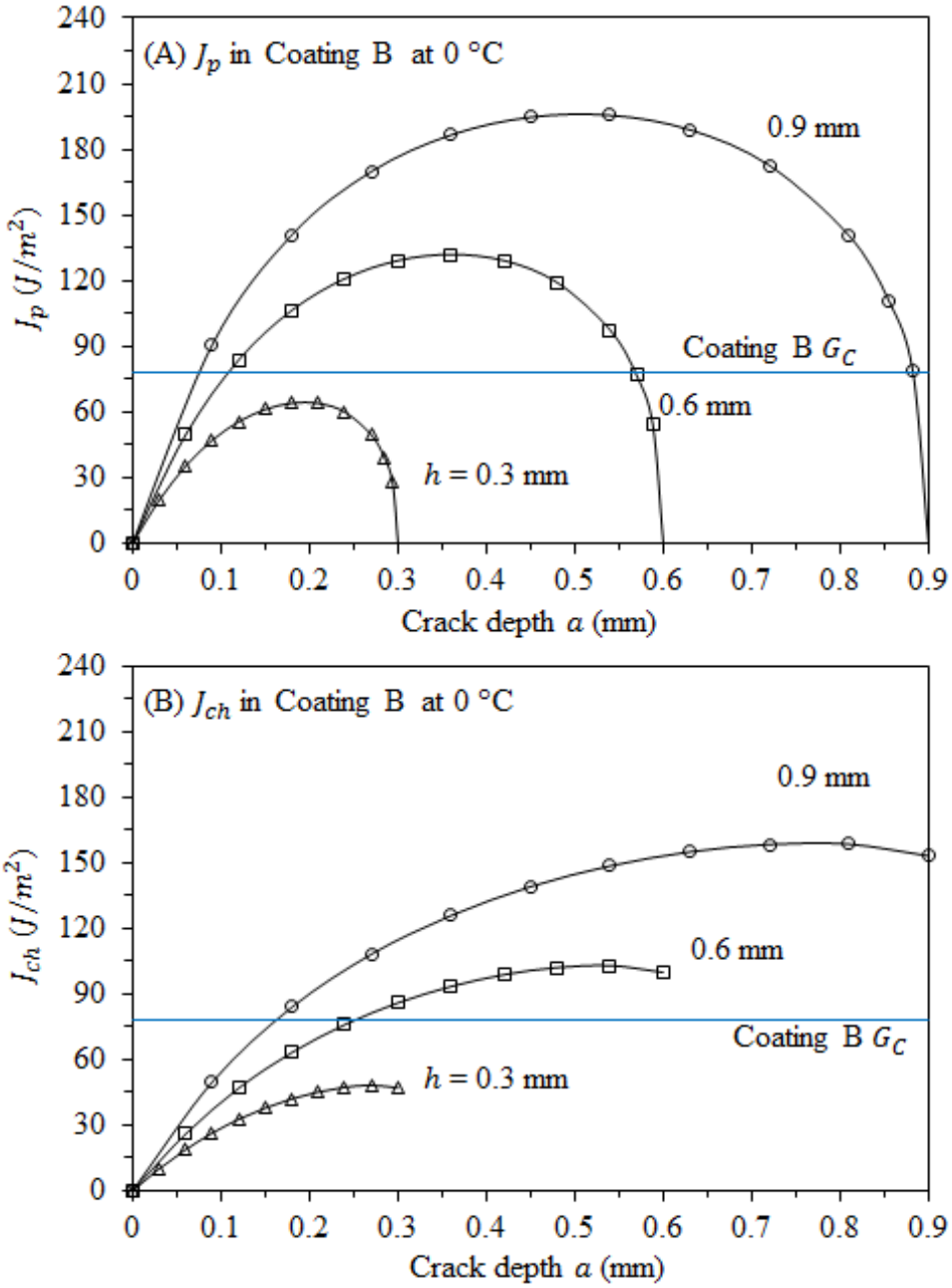

Figure 121. J_p and J_{ch} of cracks in coating B with different thickness on fillet welds joint under temperature reductions from T_g to 0 °C.

The thermal strain concentration at the surface of the coating on the corners of fillet welds is reflected by the J-integrals of crack penetration (J_p). For example, the calculated J_p of a 60 μm deep defect in 0.3 mm thick coating A on the corner of fillet welds at 23 °C can be found in Figure 118 (page 190) to be about 10 J/m^2, which is 43% greater than the J_p (7 J/m^2) of the same coating on a flat substrate with the same defect depth and thickness. This predicts in terms of J-integral of coating cracking that coatings on the corners of fillet welds in WBTs are more likely to have fracture than those on the flat regions. This agrees with the observation of WBT coating failure in service [2]. It was also found that at the same temperature the J_p in 0.6 and 0.9 mm thick coatings can be 60% to 120% greater than that in a 0.3 mm thick coating. This predicts that on fillet welds thicker coatings are more vulnerable to failure than thinner coatings, which is also in agreement with experimental and service observation [3].

The calculations of J_p as a function of defect depth (Figure 118 on page 190 to Figure 121) have also shown that the maximum J_p of defects of all sizes in coating A on fillet welds at 0 °C are smaller than the measured fracture toughness (G_C) of coating A (228 $\mathrm{J/m^2}$), this predicts that coating A with a thickness up to 0.9 mm will not have static fracture in service. The same situation is also predicted for coating B (G_C=78 $\mathrm{J/m^2}$) with thickness up to 0.9 mm at 23 °C, and thickness up to 0.6 mm at 0 °C. Thus, any failure of these in service might be caused by thermal fatigue due to temperature cycles. The prediction of the coating fracture on fillet welds at 0 °C is based on the fracture toughness (G_C) measured at ambient temperature. As the temperature difference is only about 23 °C, it is assumed that the G_C at 0 °C is the same as that at 23 °C.

As shown in Figure 121A, at 0 °C the J_p of a 78 μm deep defect in a 0.9 mm thick coating B reaches the measured fracture toughness (G_C) of about 78 J/m^2. As the measured defect depth in coating B was about 70 μm, the result predicts that a 0.9 mm thick coating B on the curvature of the fillet weld may have static cracking at 0 °C in service. Similar to that predicted in coatings on flat substrate subjected to mechanical

straining, once static cracking occurs in coating B the crack is predicted to propagate unstably to a depth of about 0.88 mm, at which the J-integral of crack channelling (J_{ch}) will also be well above the G_C (Figure 121B), leading to channelling immediately after penetration takes place.

Figure 121A also shows that in 0.6 mm coating B at 0 °C the J_p will reach the measured fracture toughness (G_C) when the crack depth reaches 108 μm. Assuming that the initial defect size is the same as the measured defect depth (70 μm), the coating will not experience static cracking at 0 °C. However, as the defect penetrates deeper by thermal fatigue, and reaches 108 μm, static fracture will be allowed. This predicts that for this coating the failure in this case might be a combination of an initial thermal fatigue crack propagation and subsequent unstable static fracture when the fatigue crack reaches the critical depth.

Predictions of fatigue lives of coatings in service can be made when more definitive information is available, such as coating fatigue crack initiation process, effects of coating thickness on fatigue cracking and fatigue crack growth rates. It needs to be mentioned again that the fracture toughness values used for the predictions were measured at ambient temperature. A more accurate prediction may be made when the fracture toughness at 0 °C known.

8. CONCLUSIONS

Based on the experimental and numerical results obtained in the work, the following conclusions can be drawn:

(1) Tensile testing of free films of a brittle and a tough epoxy coating established that the tensile strength, the stiffness, and the strain to failure were all temperature dependent. For coating A, stiffness decreased from 6.2 GPa at -10 °C to about 3 GPa at 70 °C, tensile strength decreased by 13 MPa from -10 to 70 °C. In contrast, ductility increased from 0.67% to 1.35%. For coating B, stiffness decreased from 6.2 to 1.7 GPa from -10 to 70 °C, tensile strength decreased by 6 MPa from – 10 to 70 °C, and ductility increased from 0.34% to 1.5%.

(2) Toughness measurement using double edge notched coating samples for the same two coatings gave toughness values (K_C) at 23 °C of 1.07 $MPa\sqrt{m}$ for coating A and 0.64 $MPa\sqrt{m}$ for coating B.

(3) Measurements of thermal residual stress in coatings at ambient temperature using bi-layer beam methods showed that coating A developed a thermal stress of 11 MPa and a thermal strain of 0.15%; coating B developed a thermal stress of 15 MPa and a thermal strain of 0.19%.

(4) Observations of the cracking process during tensile testing of substrated coatings showed first coating cracks initiated at a critical nominal strain. Further increases in strain led to rapid growth of the original crack and initiation of new cracks across the gauge section. Eventually further initiation of cracks stopped and saturation of multiple parallel cracks occurred. The critical strain to first crack of coatings A and B were 0.70% and 0.49%. This is significantly greater than the strains to failure measured on the free films

(5) Digital image correlation observation of substrate yielding and coating crack development revealed that in the original condition the substrate exhibited heterogeneous yielding causing local concentration of strain. This initiated cracking

at local strain levels greater than global strains measured via an extensometer. These differences were eliminated by pre-straining the substrate. The critical strain to first crack of coatings A and B on pre-strained substrates at ambient temperature were 1.04% and 0.64%.

(6) Fracture surface observation on free films using SEM showed the presence of near-surface anomalies associated with second phase/particles. They were characterised by locally smooth fracture surfaces, indicating low energy fracture. Their sizes were about 60 and 70 μm deep in coatings A and B.

(7) The observed fracture behaviour of substrated coatings is consistent with a model that coating fracture initiation occurs when the applied J at a defect tip exceeds the measured coating toughness value. Using measured values of free film coating toughness and defect size together with non-linear tensile stress-strain properties of the coatings and the steel substrate; a calculation of J integral made by the fracture model allowed prediction of substrated coating strain to first crack. The prediction was within 10% of the experimental value for coating A and 30% of the experimental value for coating B. The model predicts that the coating strain to failure will be determined by defect size, coating thickness as well as residual strains.

(8) Observations of the cracking process of substrated coatings under cyclic mechanical strains showed fatigue cracks initiated at discrete locations on the sample gauge length. Further cycling led to the propagation of coating fatigue cracks and initiation of further parallel cracks. At long lives, fatigue testing of the coating was terminated by fatigue cracking of steel substrate.

(9) Using a definition of coating failure where the longest crack achieves 2 mm surface length, for the same life coating A required double the applied strain range compared with coating B. The life of coating A was insensitive to the mean strain, while coating B showed some sensitivity at very small fatigue lives.

(10) Observations of coating surface fatigue crack behaviour showed single cracks grew at constant growth rates independent of surface length, while the growth rates of

single cracks within the same sample varied significantly, and the standard deviation can be as high as 90% of mean growth rate. Interaction of cracks occurred as single cracks grew longer, the growth rates of interacting single cracks reduced greatly.

(11) The use of individual crack growth rates as a means of quantifying surface cracking development was not possible. Instead, quantification of total crack length (sum of all single cracks within gauge length) showed an initial linear relationship between the total crack length and cycles number.

(12) Measurement of surface crack numbers and average crack length showed that coating A developed a larger number of cracks with smaller average length than coating B for the same total crack length. The number of cracks in coating A was about 3 times greater than that in coating B at the same total crack length. Although the crack patterns of the coatings appeared to be different, they are not crucial in terms of coating cracking in service. Because the anti-corrosion capability of the coatings will be compromised once a through-thickness crack forms regardless of the pattern of the cracks. In the light of this, the fatigue lives of the coatings are the crucial criterion to rank coating integrity in service.

(13) A linear correlation was found between the logarithmic total crack growth rates (da/dN) and logarithmic applied strain ranges $(\Delta\varepsilon)$, following an equation of $\frac{da}{dN} = c(\Delta\varepsilon)^m$. An approach has been developed to calculate the J-integral range of channelling (ΔJ_{ch}). A linear correlation was found between the total crack growth rates (da/dN) and logarithmic ΔJ_{ch}, following an equation of $\frac{da}{dN} = c(\Delta J_{ch})^m$. It was found that at the same ΔJ_{ch} the $\frac{da}{dN}$ of coating B can be about 250 times the $\frac{da}{dN}$ of coating A. The fitted m parameter was about 3 and 8 for coatings A and B, implying fatigue cracking would be highly sensitive to applied strain range and ΔJ_{ch}.

(14) The correlation between ΔJ_{ch} and $\frac{da}{dN}$ incorporates both thermal and mechanical strains as well as the effects of coating thickness and substrate geometry, and it is

more generalised and thus more applicable than a strain range based correlation for applications outside of a laboratory.

(15) Calculations of J-integrals of coating crack penetration (J_p) under thermal strains showed that thermal strain induced greater J_p values than mechanical straining. This predicts that the thermal strain required to the failure of coatings A and B are 50% and 30% smaller than strain required from mechanical straining, implying coatings are more likely to fracture under thermal strains.

9. FUTURE WORK

Based on the finding of the current work, some aspects worthy of further study are recommended as below:

(1) Incorporation of full range stress-strain data for fracture mechanics analysis

The current work used approximated strain-strain curve to calculate the J-integrals of coating defects under strain beyond the known stress-strain data. This inevitably introduced errors in the results. It would be worthwhile to use sufficient stress-strain data that contains the entire range of strains that are required. To overcome the problem of being too brittle in tension, the full range stress-strain curve can be determined indirectly using shear testing [179]. This will improve the accuracy of the prediction of the fracture coating on substrates.

(2) Three-dimensional modelling of crack penetration

The current work used a simplified 2D model to analyse the penetration process of coating surface defects, which is in fact a 3D problem. The 2D model neglected the influence of crack front shape the cracking process. It is recommended that a 3D crack penetration model should be developed to investigate the stress intensity factor along the crack front, and determine the change of crack front during penetration, and how this influence coating ductility. The modelling result can be compared to experimental work. This will also allow more accurate prediction of coating failure.

(3) Effect of thermal ageing on fracture

It is known that thermal ageing changes the material properties of epoxy coatings, and in a long term it increases residual stress and reduces toughness. The effect of thermal ageing on fracture can be studied by artificially ageing samples using temperatures slightly below T_g. The amount of ageing can be quantified using thermal analysis techniques, and it can be correlated to fracture behaviour. As WBT coatings

experience thermal ageing in service, this work will allow predictions of coating failure in a long term.

(4) Effect of filler on fracture

The current work suggests that the size of fillers in coatings may determine the defect size, as de-bonded filler/resin interfaces can act as crack initiators. Further work can look into the effect of filler size on the coating ductility. Since a change in filler size may as well modify the mechanical properties and the anti-corrosion capability of the coatings. A clear mapping of the effect of filler size on coating properties, anti-corrosion capability, and ductility needs to be established. This will allow the selection of optimum filler sizes.

(5) Thermal fatigue of coatings with different thicknesses

The current work investigated the fatigue of the coatings under mechanical strain cycles. It is known that WBT coatings in service encounter thermal strain cycles. The FE analysis of thermal strain induced J-integral perform in this work showed that the coatings should be more susceptible under thermal strains than mechanical strains. The FE results also showed that thicker coatings are more likely to fail than thinner ones. This highlights the importance of performing thermal fatigue tests on coatings with different thicknesses. This can be done using welded joints sprayed with coatings with different thicknesses. The temperature ranges – life data can be obtained for different coating thicknesses. Also, using finite element models the temperature ranges can be converted to other quantities such as strain/stress range, strain energy ranges, and energy release rate ranges. By correlating these different parameters to the life data, one might be able to establish the factor controlling coating life.

REFERENCES

[1] Towers R, Eliasson J. The future of ballast tank coatings. Naval Architect 2008;25:57.

[2] Wang G, Spencer JS, Saidarasamoot S, Thuanboon S, Olson DL, Mishra B. Tanker Corrosion. In: Kutz M, editor. Handbook of Environmental Degradation of Materials, Norwich, NY: William Andrew Publishing; 2005, p. 523–45.

[3] Lee D, Kim B. Investigation of coating failure on the surface of a water ballast tank of an oil tanker. Journal of Adhesion Science and Technology 2005;19:879.

[4] Oosterbroek M, Lammers RJ, Ven LG, Perera DY. Crack formation and stress development in an organic coating. Journal of Coatings Technology 1991;63:55.

[5] Perera DY. On adhesion and stress in organic coatings. Progress in Organic Coatings 1996;28:21.

[6] Mills G, Eliasson J. Factors influencing early crack development in marine cargo and ballast tank coatings. Journal of Protective Coatings and Linings 2006;23:10.

[7] Weldon DG. Why coatings work and why they fail. Failure Analysis of Paints and Coatings, Revised Edition, Chichester: John Wiley & Sons, Ltd; 2009, p. 9–37.

[8] Nichols ME, Darr CA. Effect of weathering on the stress distribution and mechanical performance of automotive paint systems. Journal of Coatings Technology 1998;70:141.

[9] Nichols ME. Anticipating paint cracking: the application of fracture mechanics to the study of paint weathering. Journal of Coatings Technology 2002;74:39.

[10] Song E, Chung M, Lee C, Lee S, Lee H. Why do we have cracks in epoxy coatings for water ballast tanks? NACE Corrosion, San Diego: NACE International; 2006, p. 25–35.

[11] Eve S, Huber N, Last A, Kraft O. Fatigue behavior of thin Au and Al films on polycarbonate and polymethylmethacrylate for micro-optical components. Thin Solid Films 2009;517:2702.

[12] Zhang GP, Volkert CA, Schwaiger R, Monig R, Kraft O. Fatigue and thermal fatigue damage analysis of thin metal films. EuroSime 2006 - 7th International Conference on Thermal, Mechanical and Multiphysics Simulation and Experiments in Micro-Electronics and Micro-Systems 2006;47.

[13] Sim GD, Lee YS, Lee SB, Vlassak JJ. Effects of stretching and cycling on the fatigue behavior of polymer-supported Ag thin films. Materials Science and Engineering A 2013;575:86.

[14] Zhou M, Yao WB, Yang XS, Peng ZB, Li KK, Dai CY. In-situ and real-time tests on the damage evolution and fracture of thermal barrier coatings under tension: A coupled acoustic emission and digital image correlation method. Surface and Coatings Technology 2014;240:40.

[15] Zhu DM, Choi SR, Miller RA. Development and fatigue testing of ceramic thermal barrier coatings. Surface and Coatings Technology 2004;188:146.

[16] Mao WG, Dai CY, Yang L, Zhou YC. Interfacial fracture characteristic and crack propagation of thermal barrier coatings under tensile conditions at elevated temperatures. International Journal of Fracture 2008;151:107.

[17] Rouw AC. Model epoxy powder coatings and their adhesion to steel. Progress in Organic Coatings 1997;34:181.

[18] Ochi M, Takemiya K, Kiyohara O, Nakanishi T. Effect of the addition of aramid-silicone block copolymer on the phase structure and toughness of cured epoxy resins modified with RTV silicone. Polymer 2000;41:195.

[19] Hare CH. Protective coatings: fundamentals of chemistry and composition . Pittsburgh, Pa: Technology Publ. Co.; 1994.

[20] Sørensen PA, Kiil S, Dam-Johansen K, Weinell CE. Anticorrosive coatings: A review. Journal of Coatings Technology Research 2009;6:135.

[21] Knudsen OØ, Bardal E, Steinsmo U. Effect of Barrier Pigments on Cathodic Disbonding. Journal of Corrosion Science and Engineering 1999;2:15.

[22] Kouloumbi N, Tsangaris GM, Vourvahi C, Molnar F. Corrosion resistance and dielectric properties of an iron oxide filled epoxy coating. Journal of Coatings Technology 1997;69:53.

[23] Nikravesh B, Ramezanzadeh B, Sarabi AA, Kasiriha SM. Evaluation of the corrosion resistance of an epoxy-polyamide coating containing different ratios of micacaeous iron oxide-al pigments. Corrosion Science 2011;53:1592.

[24] Funke W. Towards environmentally acceptable corrosion protection by organic coating. Anti-Corrosion Methods and Materials 1984;31:4.

[25] Landel RF, Nielsen LE. Mechanical properties of polymers and composites. Second Edi. Boca Raton, FL: CRC Press; 1993.

[26] Rothon RN. Particulate-Filled Polymer Composites (2nd Edition). Shrewsbury: Smithers Rapra Technology; 2003.

[27] Ahmed S, Jones FR. A review of particulate reinforcing theories for polymer composites. Journal of Materials Science, 1990;25:4933.

[28] Móczó J, Pukánszky B. Polymer micro and nanocomposites: Structure, interactions, properties. Journal of Industrial and Engineering Chemistry 2008;14:535.

[29] Pukánszky B. Interfaces and interphases in multicomponent materials: Past, present, future. European Polymer Journal 2005;41:645.

[30] Perera DY. Effect of pigmentation on organic coating characteristics. Progress in Organic Coatings 2004;50:247.

[31] Perera DY, Eynde D V. Internal stress in pigmented thermoplastic coatings. Journal of Coatings Technology 1981;53:40.

[32] Zosel A. Mechanical behaviour of coating films. Progress in Organic Coatings 1980;8:47.

[33] Michael Rubinstein RHC. Polymer Physics. Oxford: OUP Oxford; 2003.

[34] Theocaris PS, Spathis GD. Glass-transition behavior of particle composites modeled on the concept of interphase. Journal of Applied Polymer Science 1982;27:3019.

[35] Drzal L. The interphase in epoxy composites. Epoxy Resins and Composites II 1986;75:1.

[36] Prime RB. Chapter 5 - Thermosets. In: Turi E, editor. Thermal Characterization of Polymeric Materials, Academic Press; 1981, p. 435–569.

[37] Toussaint A. Influence of pigmentation on the mechanical properties of paint films. Progress in Organic Coatings 1974;2:237.

[38] Kraus G, Gruver JT. Thermal Expansion, Free Volume, and Molecular Mobility in a Carbon Black-Filled Elastomer. Rubber Chemistry and Technology 1971;44:1297.

[39] Zicherman JB, Holsworth RM. Instrumental approaches to powder coatings characterization. Journal of Paint Technology 1974;46:55.

[40] Bajaj P, Jha NK, Kumar A. Effect of coupling agents on thermal and electrical properties of mica/epoxy composites. Journal of Applied Polymer Science 1995;56:1339.

[41] Droste DH, Dibeneditto AT. The glass transition temperature of filled polymers and its effect on their physical properties. Composites 1970;1:255.

[42] Pinheiro MDFF, Rosenberg HM. Thermal expansion of epoxy-resin/particle composites - a size effect. Composites 1981;12:152.

[43] Zhuang GQ, Yang YM, Li BY. Reinforced effect of wollastonite on phenolphthalein poly(ether ketone). Journal of Applied Polymer Science 1997;65:649.

[44] Croll SG. Origin of Residual Internal Stress in Solvent-Cast Thermoplastic Coatings. Journal of Applied Polymer Science 1979;23:847.

[45] Vaessen D. Effects of phase separation on stress development in polymeric coatings. Polymer 2002;43:2267.

[46] Cairncross RA, Francis LF, Scriven LE. Competing drying and reaction mechanisms in the formation of sol-to-gel films, fibers, and spheres. Drying Technology 1992;10:893.

[47] Vrentas JS, Vrentas CM. Evaluation of a sorption equation for polymer-solvent systems. Journal of Applied Polymer Science 1994;51:1791.

[48] Alsoy S, Duda JL. Drying of Solvent Coated Polymer Films. Drying Technology 1998;16:15.

[49] Stolov A, Xie T, Penelle J, Hsu SL. Simultaneous measurement of polymerization kinetics and stress development in radiation-cured coatings: A new experimental approach and relationship between the degree of conversion and stress. Macromolecules 2000;33:6970.

[50] Lange J, Toll S, Månson JAE, Hult A. Residual stress build-up in thermoset films cured above their ultimate glass transition temperature. Polymer 1995;36:3135.

[51] Lange J, Månson JAE, Hult A. Build-up of structure and viscoelastic properties in epoxy and acrylate resins cured below their ultimate glass transition temperature. Polymer 1996;37:5859.

[52] Lange J, Toll S, Månson JAE, Hult A. Residual stress build-up in thermoset films cured below their ultimate glass transition temperature. Polymer 1997;38:809.

[53] Wen M, Scriven LE, McCormick A V. Differential scanning calorimetry and cantilever deflection studies of polymerization kinetics and stress in ultraviolet curing of multifunctional (meth)acrylate coatings. Macromolecules 2002;35:112.

[54] Payne JA, Francis LF, McCormick A V. The effects of processing variables on stress development in ultraviolet-cured coatings. Journal of Applied Polymer Science 1997;66:1267.

[55] Vaessen DM, Ngantung FA., Palacio MLB, Francis LF, McCormick AV. Effect of lamp cycling on conversion and stress development in ultraviolet-cured acrylate coatings. Journal of Applied Polymer Science 2002;84:2784.

[56] Cook WD. Thermal aspects of the kinetics of dimethacrylate photopolymerization. Polymer 1992;33:2152.

[57] Sato K. The internal stress of coating films. Progress in Organic Coatings 1980;8:143.

[58] Francis LF, McCormick AV, Vaessen DM, Payne JA. Development and measurement of stress in polymer coatings. Journal of Materials Science 2002;37:4717.

[59] Hoffman RW. Mechanical Properties of Non-Metallic Thin Films. Physics of Nonmetallic Thin Films, Boston, MA: Springer; 1976, p. 273–353.

[60] Hoffman RW. Stress distributions and thin film mechanical properties. Surface and Interface Analysis 1981;3:62.

[61] Kobatake Y, Inoue Y. Mechanics of adhesive joints - Part I. Residual stresses. Applied Scientific Research, Section A 1957;7:53.

[62] Ulfvarson A, Vikgren K. Anticorrosion protection systems - Improvements and continued problems. Proceedings of MARSTRUCT 2009, 2nd International Conference on Marine Structures-Analysis and Design of Marine Structures, 2009, p. 199–206.

[63] Croll SG. Effect of solvents on residual strain in clear epoxy coatings. Journal of the Oil and Colour Chemists' Association 1980;63:230.

[64] Stoney GG. The Tension of Metallic Films Deposited by Electrolysis. Proceedings of the Royal Society A: Mathematical, Physical and Engineering Sciences 1909;82:172.

[65] Kamata K, Aizawa N, Moriyama M. Microhardness and internal stress of Si3N4-SiC films prepared by plasma CVD. Journal of Materials Science Letters 1986;5:1055.

[66] Nakamura Y, Tabata H, Suzuki H, Iko K, Okubo M, Matsumoto T. Internal stress of epoxy resin modified with acrylic core-shell particles prepared by seeded emulsion polymerization. Journal of Applied Polymer Science 1986;32:4865.

[67] Jou JH, Hsu L. Stress analysis of elastically anisotropic bilayer structures. Journal of Applied Physics 1991;69:1384.

[68] Benabdi M, Roche AA. Mechanical properties of thin and thick coatings applied to various substrates. Part I. An elastic analysis of residual stresses within coating materials. Journal of Adhesion Science and Technology 1997;11:281.

[69] Röll K. Analysis of stress and strain distribution in thin films and substrates Analysis of stress and strain distribution in thin films and substrates. Journal of Applied Physics 1976;3224:3224.

[70] Yan G, White JR. Residual stress development in a bi-layer coating. Polymer Engineering & Science 1999;39:1856.

[71] Ringsberg JW, Ulfvarson AYJ. On mechanical interaction between steel and coating in stressed and strained exposed locations. Marine Structures 1998;11:231.

[72] Bockenheimer C, Fata D, Possart W. New aspects of aging in epoxy networks. I. Thermal aging. Journal of Applied Polymer Science 2004;91:361.

[73] Bockenheimer C, Fata D, Possart W. New aspects of aging in epoxy networks. II. Hydrothermal aging. Journal of Applied Polymer Science 2004;91:369.

[74] Hutchinson JM. Physical aging of polymers. Progress in Polymer Science 1995;20:703.

[75] Perera DY. Physical ageing of organic coatings. Progress in Organic Coatings 2003;47:61.

[76] Perera DY, Schutyser P. Effect of physical aging on thermal stress development in powder coatings. Progress in Organic Coatings 1994;24:299.

[77] Kong ESW. Physical aging in epoxy matrices and composites. Epoxy Resins and Composites IV, Springer; 1986, p. 125–71.

[78] Hare CH. Internal stress: part I. Journal of Protective Coatings and Linings 1996;13:65.

[79] G'Sell C, McKenna GB. Influence of physical ageing on the yield response of model DGEBA/poly(propylene oxide) epoxy glasses. Polymer 1992;33:2103.

[80] Aref-Azar A, Biddlestone F, Hay JN, Haward RN. The effect of physical ageing on the properties of poly(ethylene terephthalate). Polymer 1983;24:1245.

[81] Yang AC, Wang RC, Lin JH. Ductile-brittle transition induced by aging in ploy(phenylene oxide) thin films. Polymer 1996;31:5751.

[82] Liu W, Shen J, Lu F, Xu M. Effect of physical aging on fracture behavior of polyphenylquinoxaline films. Journal of Applied Polymer Science 2000;78:1275.

[83] Struik LCE. Mechanical behaviour and physical ageing of semi-crystalline polymers: 4. Polymer 1989;30:815.

[84] Truong VT, Ennis BC. Effect of physical aging on the fracture behavior of crosslinked epoxies. Polymer Engineering and Science 1991;31:548.

[85] Griffith A. The Phenomena of Rupture and Flow in Solids. Philosophical Transactions of the Royal Society A: Mathematical, Physical and Engineering Sciences 1921;221:163.

[86] Irwin GR. Fracture dynamics. Fracturing of Metals, Cleveland: American Society for Metals; 1948, p. 147–66.

[87] Orowan E. Fracture and strength of solids. Reports on Progress in Physics 1949;12:309.

[88] Irwin GR. Onset of fast crack propagation in high steel and aluminium alloys. Sagamore Research Conference Proceedings, vol. 2, 1956, p. 289–305.

[89] Westergaard HM. Bearing and Cracks. Transation ASME Series E, Journal of Applied Mechanics 1939;B9:A49.

[90] Irwin GR. Analysis of stresses and strains near the end of cracking traversing a plate. Journal of Applied Mechanics 1957;24:361.

[91] Sneddon IN. The Distribution of Stress in the Neighbourhood of a Crack in an Elastic Solid. Proceedings of the Royal Society A: Mathematical, Physical and Engineering Sciences 1946;187:229.

[92] Williams ML. On the stress distribution at the base of a stationary crack. Journal of Applied Mechanics 1957;24:109.

[93] Anderson TL. Fracture mechanics: fundamentals and applications. Boca Raton, FL: CRC press; 2005.

[94] Rice JR. A Path Independent Integral and the Approximate Analysis of Strain Concentration by Notches and Cracks. Journal of Applied Mechanics 1968;35:379.

[95] Brocks W, Scheider I. Numerical Aspects of the Path-Dependenceof the J-Integral in Incremental Plasticity How to Calculate Reliable J-Values in FE Analyses. International Journal of Fatigue 2001:1.

[96] Scheirs J. Compositional and Failure Analysis of Polymers - A Practical Approach. Chichester: Wiley; 2000.

[97] Williams JG, Pavan A, editors. Fracture of Polymers, Composites and Adhesives. vol. 32, Oxford: Elsevier; 2003.

[98] Argon AS. The Physics of Deformation and Fracture of Polymers. Cambridge: Cambridge University Press; 2013.

[99] Grellmann W, Seidler S, Barenblatt G. Deformation and Fracture Behaviour of Polymers. vol. 56. Berlin: Springer; 2003.

[100] Bandyopadhyay S. Review of the microscopic and macroscopic aspects of fracture of unmodified and modified epoxy resins. Materials Science and Engineering: A 1990;125:157.

[101] Al-Turaif HA. Effect of nano TiO2 particle size on mechanical properties of cured epoxy resin. Progress in Organic Coatings 2010;69:241.

[102] Unnikrishnan KP, Thachil ET. Toughening of epoxy resins. Designed Monomers and Polymers 2006;9:129.

[103] Huang Y, Hunston DL, Kinloch a J, Riew CK. Mechanisms of toughening thermoset resins. Advances in Chemistry Series 1993;233:1.

[104] Wu JS, Mai YW. Ductile fracture and toughening mechanisms in polymers. Materials Forum 1995;19:181.

[105] Garg AC, Mai YW. Failure mechanisms in toughened epoxy resins—A review. Composites Science and Technology 1988;31:179.

[106] Morgan RJ, Mones ET, Steele WJ. Tensile deformation and failure processes of amine-cured epoxies. Polymer 1982;23:295.

[107] Morgan RJ, O'Neal JE. The microscopic failure processes and their relation to the structure of amine-cured bisphenol-A-diglycidyl ether epoxies. Journal of Materials Science 1977;12:1966.

[108] Morgan RJ, O'neal JE. The Durability of Epoxies. Polymer-Plastics Technology and Engineering 1978;10:49.

[109] Wronski AS, Pick M. Pyramidal yield criteria for epoxides. Journal of Materials Science 1977;12:28.

[110] Wronski AS, Parry T V. Fracture of a plasticized epoxide under superposed hydrostatic pressure. Journal of Materials Science 1982;17:2047.

[111] Narisawa I, Murayama T, Ogawa H. Internal fracture of notched epoxy resins. Polymer 1982;23:291.

[112] Andrews EY, editor. Developments in Polymer Fracture. vol. 1. San Francisco: Applied Science Publishers; 1979.

[113] Mijovic JS, Koutsky JA. Effect of Postcure Time on the Fracture Properties and Nodular Morphology of an Epoxy Resin. Journal of Appled Polymer Science 1978;23:1037.

[114] Bascom WD, Cottington RL, Jones RL, Peyser P. The fracture of epoxy-and elastomer-modified epoxy polymers in bulk and as adhesives. Journal of Applied Polymer Science 1975;19:2545.

[115] Gledhill RA, Kinloch AJ. Mechanics of crack growth in epoxide resins. Polymer Engineering and Science 1979;19:82.

[116] Scott JM, Wells GM, Phillips DC. Low temperature crack propagation in an epoxide resin. Journal of Materials Science 1980;15:1436.

[117] Bandyopadhyay S, Morris CEM. Evidence of microscopic crack jumping in an epoxy resin. Micron (1969) 1982;13:269.

[118] Yamini S, Young RJ. Stability of crack propagation in epoxy resins. Polymer 1977;18:1075.

[119] Sultan JN, McGarry FJ. Effect of rubber particle size on deformation mechanisms in glassy epoxy. Polymer Engineering and Science 1973;13:29.

[120] Ming Lee S. Double torsion fracture toughness test for evaluating transverse cracking in composites. Journal of Materials Science Letters 1982;1:511.

[121] Kinloch AJ, Williams JG. Crack blunting mechanisms in polymers. Journal of Materials Science 1980;15:987.

[122] Moloney AC, Kausch HH, Stieger HR. The fracture of particulate-filled epoxide resins. Journal of Materials Science 1984;19:1125.

[123] Evans AG. The strength of brittle materials containing second phase dispersions. Philosophical Magazine 1972;26:1327.

[124] Spanoudakis J, Young RJ. Crack propagation in a glass particle-filled epoxy resin. Journal of Materials Science 1984;19:487.

[125] Kinloch AJ, Maxwell DL, Young RJ. The fracture of hybrid-particulate composites. Journal of Materials Science 1985;20:4169.

[126] Dundurs J. Edge-Bonded Dissimilar Orthogonal Elastic Wedges Under Normal and Shear Loading. Journal of Applied Mechanics 1969;36:650.

[127] Suga T, Elssner G, Schmauder S. Composite Parameters and Mechanical Compatibility of Material Joints. Journal of Composite Materials 1988;22:917.

[128] Gecit MR. Fracture of a surface layer bonded to a half space. International Journal of Engineering Science 1979;17:287.

[129] Beuth JL. Cracking of thin bonded films in residual tension. International Journal of Solids and Structures 1992;29:1657.

[130] Zak AR, Williams ML. Crack Point Stress Singularities at a Bi-Material Interface. Journal of Applied Mechanics 1963;30:142.

[131] Gille G. Strength of thin films and coatings. Current Topics in Materials Science 1985;12:420.

[132] Hu MS, Evans AG. The cracking and decohesion of thin films on ductile substrates. Acta Metallurgica 1989;37:917.

[133] Nakamura T, Kamath SM. Three-dimensional effects in thin film fracture mechanics. Mechanics of Materials 1992;13:67.

[134] Xia ZC, Hutchinson JW. Crack patterns in thin films. Journal of the Mechanics and Physics of Solids 2000;48:1107.

[135] Hutchinson JW, Suo Z. Mixed Mode Cracking in Layered Materials. Advances in Applied Mechanics 1991;29:63.

[136] Malyshev BM, Salganik RL. The strength of adhesive joints using the theory of cracks. International Journal of Fracture Mechanics 1965;1-1:114.

[137] Cook TS, Erdogan F. Stresses in bonded materials with a crack perpendicular to the interface. International Journal of Engineering Science 1972;10:677.

[138] Erdogan F, Biricikoglu V. Two bonded half planes with a crack going through the interface. International Journal of Engineering Science 1973;11:745.

[139] Goree JG, Venezia WA. Bonded elastic half-planes with an interface crack and a perpendicular intersecting crack that extends into the adjacent material. International Journal of Engineering Science 1977;15:1.

[140] He MY, Evans AG, Hutchinson JW. Crack deflection at an interface between dissimilar elastic materials: Role of residual stresses. International Journal of Solids and Structures 1994;31:3443.

[141] Mei H, Pang Y, Huang R. Influence of interfacial delamination on channel cracking of elastic thin films. International Journal of Fracture 2007;148:331.

[142] Hsueh CH, Yanaka M. Multiple film cracking in film/substrate systems with residual stresses and unidirectional loading. Journal of Materials Science 2003;38:1809.

[143] Hsueh CH, Wereszczak AA. Multiple cracking of brittle coatings on strained substrates. Journal of Applied Physics 2004;96:3501.

[144] Suresh S. Fatigue of Materials. Cambridge: Cambridge University Press; 1998.

[145] Schijve J, editor. Fatigue of Structures and Materials. Dordrecht: Springer Netherlands; 2009.

[146] Paris P, Erdogan F. A Critical Analysis of Crack Propagation Laws. Journal of Basic Engineering 1963;85:528.

[147] Kim SR, Nairn JA. Fracture mechanics analysis of coating/substrate systems. Engineering Fracture Mechanics 2000;65:595.

[148] Nairn JA, Sung-Ryong K. A fracture mechanics analysis of multiple cracking in coatings. Engineering Fracture Mechanics 1992;42:195.

[149] Yanaka M, Miyamoto T, Tsukahara Y, Takeda N. In situ observation and analysis of multiple cracking phenomena in thin glass layers deposited on polymer films. Composite Interfaces 1998;6:409.

[150] Evans AG, Drory MD, Hu MS. The cracking and decohesion of thin films. Journal of Materials Research 1988;3:1043.

[151] Chen BF, Hwang J, Chen IF, Yu GP, Huang JH. A tensile-film-cracking model for evaluating interfacial shear strength of elastic film on ductile substrate. Surface and Coatings Technology 2000;126:91.

[152] Zou J, Wang R. Crack initiation, propagation and saturation of TiO2 nanotube film. Transactions of Nonferrous Metals Society of China 2012;22:627.

[153] Wu DJ, Mao WG, Zhou YC, Lu C. Digital image correlation approach to cracking and decohesion in a brittle coating/ductile substrate system. Applied Surface Science 2011;257:6040.

[154] Xu Y, Mellor BG. Application of acoustic emission to detect damage mechanisms of particulate filled thermoset polymeric coatings in four point bend tests. Surface and Coatings Technology 2011;205:5478.

[155] Xu Y, Mellor BG. Characterization of acoustic emission signals from particulate filled thermoset and thermoplastic polymeric coatings in four point bend tests. Materials Letters 2011;65:3609.

[156] Zhang B, Kim B, Lee D. Stress analysis and evaluation of cracks developed on the coatings for welded joints of water ballast tanks. Corrosion 2005, Houston: NACE International; 2005, p. 1–10.

[157] Kim BJ, Shin HAS, Jung SY, Cho Y, Kraft O, Choi IS. Crack nucleation during mechanical fatigue in thin metal films on flexible substrates. Acta Materialia 2013;61:3473.

[158] Kraft O, Schwaiger R, Wellner P. Fatigue in thin films: Lifetime and damage formation. Materials Science and Engineering A 2001;319-321:919.

[159] Sim GD, Won S, Lee SB. Tensile and fatigue behaviors of printed Ag thin films on flexible substrates. Applied Physics Letters 2012;101:191907.

[160] Sim GD, Hwangbo Y, Kim HH, Lee SB, Vlassak JJ. Fatigue of polymer-supported Ag thin films. Scripta Materialia 2012;66:915.

[161] Song EH, Lee SG, Lee H, Kim DY. Effect of Coating Formulation On Crack Resistance of Epoxy Coatings. Corrosion 2011, Houston: NACE International; 2011, p. 1–10.

[162] Espinosa HD, Peng B. A new methodology to investigate fracture toughness of freestanding MEMS and advanced materials in thin film form. Journal of Microelectromechanical Systems, vol. 14, 2005, p. 153–9.

[163] Lloyd's Register. Rules and Regulations for the Classification of Offshore Units Draft for the Consideration of the Offshore Technical Committee Energy. London: Lloyd's Register; 2014.

[164] ASTM E8M. Standard Test Methods for Tension Testing of Metallic Materials. ASTM International, West Conshohocken, PA: ASTM International; 2011.

[165] British Standards Institute. BS ISO 527-1 Plastics — Determination of tensile properties — Part 1 : General principles. ISO standard, vol. 44, 2012.

[166] ASTM. D5045-14 Standard Test Methods for Plane-Strain Fracture Toughness and Strain Energy Release Rate of Plastic Materials 1. ASTM International, West Conshohocken: ASTM International; 2014.

[167] Tada H, Paris PC, Irwin GR. The Stress Analysis Handbook of Cracks Handbook. New York: ASME Press; 2000.

[168] British Standards Institute. BS ISO 11359-2 Thermomechanical analysis (TMA) Part 2 : Determination of coefficient of linear thermal expansion and glass, BSI; 1999.

[169] ASTM. E111-4 Standard Test Method for Young's Modulus, Tangent Modulus, and Chord Modulus. ASTM International, West Conshohocken, PA: 2010.

[170] Hase TPA. Measurements and their uncertainties : a practical guide to modern error analysis. Oxford University Press; 2010.

[171] Cverna F. ASM Ready Reference: Thermal properties of metals. Material Park, OH: ASM International; 2002.

[172] British Standards Institute. ISO 8501-1 Preparation of steel substrates before application of paints and related products - visual assessment of surface cleanliness - part 1: Rust grades and preparation grades of uncoated steel substrates and of steel substrates after overa. BSI; 2007.

[173] ASTM. E606 Standard Practice for Strain-Controlled Fatigue Testing. ASTM International, West Conshohocken, PA: 2012.

[174] Beuth JL, Klingbeil NW. Cracking of thin films bonded to elastic-plastic substrates. Journal of the Mechanics and Physics of Solids 1996;44:1411.

[175] ABAQUS Documentation. vol. 6.11. Providence, RI, USA: Dassault Systemes Simulia Corp; 2011.

[176] Ramberg W, Osgood WR. Description of stress-strain curves by three parameters. Washington, DC: NASA; 1943.

[177] Duggan T V. Mechanics of solids. In: Parrish A, editor. Mechanical Engineer's Reference Book, New York, NY: Elsevier; 1973, p. 727–56.

[178] Deighton M. Deformation and fracture mechanics of engineering materials. vol. 5. New York: Wiley; 1984.

[179] Chai H. Channel cracking in inelastic film/substrate systems. International Journal of Solids and Structures 2011;48:1092.

[180] Ambrico JM, Begley MR. The role of initial flaw size, elastic compliance and plasticity in channel cracking of thin films. Thin Solid Films 2002;419:144.

[181] Newman JC, Raju IS. Stress-intensity factor equations for cracks in three-dimensional finite bodies subjected to tension and bending loads. Computational Methods in the Mechanics of Fracture 1984;2:311.

[182] Xiang Y, Li T, Suo Z, Vlassak JJ. High ductility of a metal film adherent on a polymer substrate. Applied Physics Letters 2005;87:161910.

[183] Lu N, Wang X, Suo Z, Vlassak J. Metal films on polymer substrates stretched beyond 50%. Applied Physics Letters 2007;91:221909.

[184] Raju IS, Newman JC. Stress-intensity factors for a wide range of semi-elliptical surface cracks in finite-thickness plates. Engineering Fracture Mechanics 1979;11:817.

[185] Knudsen O, Frydenberg T, Johnsen R. Development of internal stress in organic coatings during curing and exposure. Corrosion, NACE International; 2006, p. 2–11.

[186] Shaffer EO, McGarry FJ, Hoang L. Designing reliable polymer coatings. Polymer Engineering & Science 1996;36:2375.

[187] Bortz DR, Heras EG, Martin-Gullon I. Impressive fatigue life and fracture toughness improvements in graphene oxide/epoxy composites. Macromolecules 2012;45:238.

[188] Hsieh TH, Kinloch AJ, Taylor AC, Kinloch IA. The effect of carbon nanotubes on the fracture toughness and fatigue performance of a thermosetting epoxy polymer. Journal of Materials Science 2011;46:7525.

[189] Yu N, Zhang ZH, He SY. Fracture toughness and fatigue life of MWCNT / epoxy composites. Materials Science and Engineering: A 2008;494:380.

[190] Dowling NE, Begley JA. Fatigue crack growth during gross plasticity and the J-integral. ASTM Special Technical Publication 1976:82.

[191] Dowling NE, Impellizzeri LF. Crack Growth During Low-Cycle Fatigue of Smooth Axial Specimens. ASTM Special Technical Publication 1977:97.

[192] Lambert Y, Saillard P, Bathias C. Application of the J Concept to Fatigue Crack Growth in Large-Scale Yielding. ASTM Special Technical Publication 1988:318.

[193] Banks-Sills L, Volpert Y. Application of the cyclic to fatigue crack propagation of Al 2024-T351. Engineering Fracture Mechanics 1991;40:355.

[194] Hoffmeyer J, Seeger T, Vormwald M. Short fatigue crack growth under nonproportional multiaxial elastic – plastic strains. International Journal of Fatigue 2006;28:972.

[195] Ochensberger W, Kolednik O. A new basis for the application of the J-integral for cyclically loaded cracks in elastic–plastic materials. International Journal of Fracture 2014;189:77.

[196] Lamba HS. The applied to cyclic loading. Engineering Fracture Mechanics 1975;7:693.

[197] Milella PP. Fatigue and Corrosion in Metals. Milano: Springer Milan; 2013.

[198] Masing G. Self-stretching and hardening for brass. 2nd International Congress on Applied Mechanics, Zurich: 1926, p. 332-5.

[199] Deng S, Hou M, Ye L. Temperature-dependent elastic moduli of epoxies measured by DMA and their correlations to mechanical testing data. Polymer Testing 2007;26:803.

[200] Gere JM, Goodno BJ. Mechanics of Materials. 8th ed. Stamford: Wiley; 2012.

[201] Sutton MA, Orteu JJ, Schreier HW. Image correlation for shape, motion and deformation measurements: Basic concepts, theory and applications. New York, NY: Springer; 2009.

Appendix i – Fracture toughness data

Table A 1. Load to fracture of fracture toughness samples with different thicknesses and notch lengths.

	Label	Width (mm)	thickness (mm)	Notch length (mm)	Fracture load (N)
Coating A	TA - 1	11.60	0.48	1.16	85.28
	TA - 2	11.78	0.29	1.26	52.84
	TA - 3	11.66	0.40	1.39	72.03
	TA - 4	11.72	0.32	2.01	49.54
	TA - 5	11.68	0.33	2.09	47.54
	TA - 6	11.63	0.40	2.34	53.51
	TA - 7	11.75	0.36	2.97	35.84
	TA - 8	11.71	0.30	3.28	30.49
	TA - 9	11.58	0.49	3.86	39.60
	TA - 10	11.61	0.46	4.07	38.38
Coating B	TB - 1	11.66	0.39	1.04	42.66
	TB - 2	11.81	0.40	1.10	44.59
	TB - 3	11.88	0.38	1.13	45.85
	TB - 4	11.83	0.40	2.35	29.77
	TB - 5	11.76	0.33	2.45	22.43
	TB - 6	11.81	0.35	2.70	23.37
	TB - 7	11.82	0.40	3.40	25.72
	TB - 8	12.11	0.39	3.58	23.53
	TB - 9	11.85	0.40	4.29	17.08
	TB - 10	11.83	0.40	4.06	15.85

Appendix ii – Mechanical properties of free films

Table A 2. Mechanical properties of Coating A free films at various temperatures.

Temperature: -10 °C			
Sample number	Young's modulus (GPa)	Fracture stress (MPa)	Fracture strain (%)
1	6.2	32.7	0.62
2	6.7	31.9	0.58
3	5.9	38.3	0.72
4	6.3	38.3	0.74
5	5.7	33.9	0.58
Temperature: 23 °C			
1	5.4	32.7	0.74
2	5.4	32.3	0.72
3	4.9	29.7	0.65
4	5.2	25.4	0.59
5	5.0	28.5	0.66
Temperature: 50 °C			
1	4.9	25.6	0.74
2	4.3	21.5	0.79
3	4.1	21.6	0.71
4	4.0	23.8	0.81
5	4.0	18.4	0.93
Temperature: 70 °C			
1	3.2	22.2	1.29
2	2.7	18.6	1.33
3	2.8	19.1	1.43

Table A 3. Mechanical properties of Coating B free films at various temperatures.

Temperature: -10 °C			
Sample number	Young's modulus (GPa)	Fracture stress (MPa)	Fracture strain (%)
1	5.7	18.6	0.33
2	6.2	16.9	0.26
3	6.3	17.1	0.28
4	6.2	15.4	0.25
5	6.9	14.8	0.21
Temperature: 23 °C			
1	5.1	16.9	0.31
2	5.7	17.9	0.33
3	4.6	13.6	0.26
4	5.0	19.0	0.40
5	5.4	18.8	0.42
Temperature: 50 °C			
1	3.8	16.1	0.56
2	4.1	15.4	0.50
3	3.6	17.3	0.69
4	3.7	15.7	0.53
5	4.1	16.2	0.53
Temperature: 70 °C			
1	1.8	12.0	1.37
2	1.8	12.2	1.50
3	1.6	11.5	1.63

Appendix iii – Ductility of substrated coatings at room temperature

Table A 4. Strain to the onset of first crack of coatings A and B on original and pre-strained substrated at ambient temperature. For both coatings, label ending with letter 'P' or 'N' refer to sample with pre-strained or original substrate respectively.

	Strain at the onset of first crack - Coating A			
Label	Strain by extensometer	Strain by DIC		
		Virtual gauge length (mm)	Gauge extension at onset (mm)	Strain
STAP - 1	0.99%	0.54	0.0066 ± 0.0002	1.22%
STAP - 2	1.10%	0.52	0.0064 ± 0.0002	1.23%
STAP - 3	0.99%	0.54	0.0061 ± 0.0002	1.13%
STAP - 4	1.05%	0.54	0.0069 ± 0.0001	1.28%
STAP - 5	1.08%	0.54	0.0065 ± 0.0002	1.20%
STAN - 1	0.79%	0.48	0.0061 ± 0.0004	1.27%
STAN - 2	0.62%	0.52	0.0066 ± 0.0001	1.27%
STAN - 3	0.70%	0.51	0.0055 ± 0.0001	1.08%
	Strain at the onset of first crack - Coating B			
Label	Strain by extensometer	Strain by DIC		
		Virtual gauge length (mm)	Gauge extension at onset (mm)	Strain
STBP - 1	0.54%	0.52	0.0035 ± 0.0002	0.67%
STBP - 2	0.73%	0.49	0.004 ± 0.0002	0.82%
STBP - 3	0.68%	0.49	0.0035 ± 0.0002	0.71%
STBP - 4	0.52%	0.54	0.0037 ± 0.0003	0.69%
STBP - 5	0.71%	0.64	0.0048 ± 0.0002	0.75%
STBN - 1	0.56%	0.49	0.0034 ± 0.0002	0.69%
STBN - 2	0.31%	0.6	0.0035 ± 0.0005	0.58%
STBN - 3	0.61%	0.57	0.004 ± 0.0003	0.70%

Appendix iv – Fatigue lives of coating on substrate

Table A 5. Fatigue lives of coating and substrate measured from coating A on original substrate under fully reversed cycles.

Label	Coating thickness (µm)	Strain range (%)	Strain amplitude (%)	Cycle to coating failure	Cycle to substrate failure
				2 mm	
FFA – 1	338	-0.45 ~ +0.45	0.45	1500	1800
FFA – 2	337	-0.45 ~ +0.45	0.45	-	1286
FFA – 3	334	-0.5 ~ +0.5	0.5	100	1400
FFA – 4	333	-0.5 ~ +0.5	0.5	200	772
FFA – 5	310	-0.5 ~ +0.5	0.5	600	870
FFA – 6	278	-0.55 ~ +0.55	0.55	300	1200
FFA – 7	305	-0.6 ~ +0.6	0.6	-	500

Table A 6. Fatigue lives of coating and substrate measured from coating A on original substrate under zero-tension cycles.

Label	Coating thickness (µm)	Strain range (%)	Strain amplitude (%)	Cycle to coating failure	Cycle to substrate failure
				2 mm	
FTA – 1	283	0 ~ 0.80	0.40	1750	2451
FTA – 2	280	0 ~ 0.85	0.425	1350	1468
FTA – 3	273	0 ~ 0.90	0.45	200	1193
FTA – 4	273	0 ~ 1.00	0.5	300	674
FTA – 5	282	0 ~ 1.00	0.5	450	784
FTA – 6	299	0 ~ 1.05	0.525	300	357
FTA – 7	278	0 ~ 1.05	0.525	400	512
FTA – 8	289	0 ~ 1.10	0.55	-	699

Table A 7. Fatigue lives of coating and substrate measured from coating B on original substrate under fully reversed cycles.

Label	Coating Thickness (μm)	Strain range (%)	Strain amplitude (%)	Cycle to coating failure	Cycle to substrate failure
FFB – 1	371	-0.16 ~ 0.16	0.16	-	151952
FFB – 2	362	-0.2 ~ 0.2	0.2	8000	75434
FFB – 3	384	-0.22 ~ 0.22	0.22	-	21539
FFB – 4	365	-0.23 ~ 0.23	0.23	-	32896
FFB – 5	330	-0.24 ~ 0.24	0.24	4500	-
FFB – 6	383	-0.24 ~ 0.24	0.24	2600	9800
FFB – 7	352	-0.25 ~ 0.25	0.25	3000	-
FFB – 8	340	-0.25 ~ 0.25	0.25	1550	-
FFB – 9	396	-0.30 ~ 0.30	0.3	1500	8568
FFB – 10	357	-0.32 ~ 0.32	0.32	50	-
FFB – 11	332	-0.35 ~ 0.35	0.35	800	5253
FFB – 12	350	-0.45 ~ 0.45	0.45	10	858

Table A 8. Fatigue lives of coating and substrate measured from coating B on original substrate under zero-tension cycles.

Label	Coating Thickness (μm)	Strain range (%)	Strain amplitude (%)	Cycle to coating failure	Cycle to substrate failure
FTB – 1	380	0 ~ 0.40	0.2	40000	-
FTB – 2	351	0 ~ 0.425	0.213	6000	-
FTB – 3	362	0 ~ 0.425	0.213	17000	-
FTB – 4	417	0 ~ 0.45	0.225	500	23983
FTB – 5	415	0 ~ 0.45	0.225	100	32896
FTB – 6	318	0 ~ 0.48	0.24	1000	-
FTB – 7	353	0 ~ 0.48	0.24	100	-
FTB – 8	370	0 ~ 0.50	0.25	10	-
FTB – 9	347	0 ~ 0.58	0.29	1	-

Table A 9. Fatigue lives of coating and substrate measured from coating B on pre-strained substrate under zero-tension cycles.

Label	Coating Thickness (μm)	Strain range (%)	Strain amplitude (%)	Cycle to coating failure	Cycle to substrate failure
FTBP – 1	336	0 ~ 0.40	0.20	7500	-
FTBP – 2	339	0 ~ 0.40	0.20	6000	-
FTBP – 3	341	0 ~ 0.50	0.25	150	-
FTBP – 4	321	0 ~ 0.50	0.25	400	-
FTBP – 5	337	0 ~ 0.55	0.275	25	-
FTBP – 6	316	0 ~ 0.60	0.30	10	-

Appendix v– Development of total crack length, number of cracks and number of non-interacting crack tips in the coatings during fatigue tests.

Coating A – Fully reversed

Coating A - FFA - 5			
Fully reversed: ± 0.5%			
Cycle number	Total crack length (mm)	Number of cracks	Number of non-interacting tip
200	2.33	10	12
300	20.51	56	9
500	29.91	79	5
700	47.54	90	5
900	52.83	93	2
1100	61.62	99	0
1300	74.64	127	0

Coating A - FFA - 6			
Fully reversed: ± 0.6%			
Cycle number	Total crack length (mm)	Number of cracks	Number of non-interacting tip
250	3.62	12	20
300	6.28	21	28
350	10.03	32	43
400	15.27	37	37
450	16.58	50	48

Coating A – Zero-tension

Coating A - FTA - 2			
Zero-tension: 0-0.85%			
Cycle number	Total crack length (mm)	Number of cracks	Number of non-interacting tip
600	0.45	1	2
800	1.78	3	6
1000	3.68	5	8
1200	5.12	8	12
1300	6.09	7	12

Coating B - FTA - 3			
Zero-tension: 0-0.9%			
Cycle number	Total crack length (mm)	Number of cracks	Number of non-interacting tip
50	0.74	2	4
100	2.40	11	13
200	5.18	13	15
300	8.56	23	24
500	14.17	31	34
750	17.97	31	33
1000	18.64	31	34

Coating B - FTA - 4			
Zero-tension: 0-1%			
Cycle number	Total crack length (mm)	Number of cracks	Number of non-interacting tip
100	1.13	4	4
150	3.81	9	4
200	8.17	20	9
300	24.74	49	8
400	35.33	62	11
500	41.97	61	8
600	48.78	67	4

Coating B - FTA - 5			
Zero-tension: 0-1%			
Cycle number	Total crack length (mm)	Number of cracks	Number of non-interacting tip
200	2.81	11	18
300	9.23	18	22
450	10.89	24	28
500	13.53	24	28
650	17.32	27	34
700	17.89	33	40

Coating B - FTA - 6			
Zero-tension: 0-1.05%			
Cycle number	Total crack length (mm)	Number of cracks	Number of non-interacting tip
100	1.36	7	7
150	4.24	13	7
200	7.58	18	6
250	9.25	23	7
300	11.23	18	7

Coating B - FTA - 7			
Zero-tension: 0-1.05%			
Cycle number	Total crack length (mm)	Number of cracks	Number of non-interacting tip
200	1.87	9	10
250	3.38	12	16
300	3.95	13	18
400	6.18	15	18

Coating B – Fully reversed

Coating B - FFB-2			
Fully reversed: ± 0.2%			
Cycle number	Total crack length (mm)	Number of cracks	Number of non-interacting tip
1500	0.87	3	4
2000	2.32	5	4
2500	4.87	9	4
3000	5.64	9	6
4000	6.88	8	5
5000	7.59	10	8
6000	8.54	11	9
7000	9.70	10	9
8000	10.57	11	9

Coating B - FFB-5			
Fully reversed: ± 0.24%			
Cycle number	Total crack length (mm)	Number of cracks	Number of non-interacting tip
3000	0.35	2	4
3500	0.65	3	6
4000	0.90	3	6
4500	1.36	3	6
5000	1.99	4	8
6000	4.52	10	18
7000	7.81	14	17
8000	10.66	16	19
9000	14.84	17	17
10000	17.43	18	17

Coating B - FFB-7			
Fully reversed: ± 0.25%			
Cycle number	Total crack length (mm)	Number of cracks	Number of non-interacting tip
2000	0.27	13	26
3000	11.21	26	32
4000	17.98	23	30
5000	22.79	28	25
6000	25.80	31	28

Coating B - FFB-8			
Fully reversed: ± 0.25%			
Cycle number	Total crack length (mm)	Number of cracks	Number of non-interacting tip
200	0.19	2	4
300	0.50	2	4
500	1.91	5	10
1000	6.08	17	12
1550	13.26	24	15
2000	17.31	26	11
2500	21.34	25	11
3000	25.85	27	13
3500	30.60	30	12
4000	34.03	29	9
4500	37.69	31	8
5000	40.05	34	8

Coating B - FFB-9			
Fully reversed: ± 0.3%			
Cycle number	Total crack length (mm)	Number of cracks	Number of non-interacting tip
400	0.51	3	4
600	1.05	4	8
1000	4.20	8	16
1500	7.46	11	16
2000	13.90	19	15
3000	22.84	26	14
4000	32.75	27	14
6000	41.22	29	5
8000	48.30	27	2
10000	52.03	27	3

Coating B - FFB-11			
Fully reversed: +- 0.35%			
Cycle number	Total crack length (mm)	Number of cracks	Number of non-interacting tip
800	2.32	2	4
1000	6.73	4	6
1500	27.22	26	25
1750	42.76	38	21
2000	57.86	41	8
2500	63.45	44	8
3000	66.31	42	8
4000	67.62	50	6
4500	68.54	63	5

Coating B – Zero-tension

Coating B - FTB - 4			
Zero-tension: 0 - 0.45%			
Cycle number	Total crack length (mm)	Number of cracks	Number of non-interacting tip
500	5.16	6	8
1058	9.91	6	10
1500	13.23	9	14
2000	16.47	11	14
3000	24.53	15	20
4500	32.97	14	14
6000	38.99	13	8
9000	44.11	15	10
11000	47.09	15	9
13000	51.01	15	9
15000	52.54	16	9
17000	55.84	16	9
19000	59.03	16	7

Coating B - FTB - 6			
Zero-tension: 0 - 0.48%			
Cycle number	Total crack length (mm)	Number of cracks	Number of non-interacting tip
400	0.90	2	4
1000	4.94	9	8
2000	11.47	10	5
3000	13.69	10	9
4000	20.25	14	10
5000	23.06	14	6
6000	27.44	16	10
7000	32.42	18	11
8000	35.27	17	6
10000	40.03	16	4
14000	42.48	16	4

Coating B - FTB - 8			
Zero-tension: 0 - 0.5%			
Cycle number	Total crack length (mm)	Number of cracks	Number of non-interacting tip
10	9.81	2	0
2000	9.96	4	2
3000	10.61	6	6
4500	15.37	7	8
5500	19.00	7	8
6500	24.95	11	14
7500	31.69	11	9
8500	34.98	13	7
9500	37.01	13	7
10500	38.05	13	7
12000	40.24	13	7
14000	42.83	13	7
16000	44.06	13	6

Coating B - FTB - 9			
Zero-tension: 0 - 0.58%			
Cycle number	Total crack length (mm)	Number of cracks	Number of non-interacting tip
10	16.96	3	1
100	21.25	8	3
250	25.40	12	9
500	29.67	15	13
1000	35.55	16	10
1500	37.72	16	12
2000	39.10	16	9
3000	46.58	17	11
4000	50.05	18	12
5000	54.43	20	13
6000	57.66	22	12

Coating B – Zero-tension (pre-strained substrate)

Coating B - FTBP - 1			
Zero-tension: 0 - 0.4%			
Cycle number	Total crack length (mm)	Number of cracks	Number of non-interacting tip
5000	2.01	2	4
7500	9.81	8	14
10000	17.49	8	12
15000	27.57	9	7
30000	36.01	9	7

Coating B - FTBP - 2			
Zero-tension: 0 - 0.4%			
Cycle number	Total crack length (mm)	Number of cracks	Number of non-interacting tip
3000	2.92	4	6
4000	6.73	7	14
7000	21.98	12	18
10000	33.07	11	10
15000	39.24	10	6
20000	41.56	10	3

Coating B - FTBP - 3			
Zero-tension: 0 - 0.5%			
Cycle number	Total crack length (mm)	Number of cracks	Number of non-interacting tip
250	0.86	2	4
500	8.89	6	6
1000	25.40	16	17
1500	35.27	23	18
2000	43.91	26	15
3000	51.82	25	11

Coating B - FTBP - 4			
Zero-tension: 0 - 0.5%			
Cycle number	Total crack length (mm)	Number of cracks	Number of non-interacting tip
100	1.32	2	4
150	2.57	2	4
250	6.57	7	12
500	15.25	9	18
1000	30.43	13	15
1500	37.44	12	13
2000	41.96	13	7
2500	44.35	13	7

Coating B - FTBP - 5			
Zero-tension: 0 - 0.55%			
Cycle number	Total crack length (mm)	Number of cracks	Number of non-interacting tip
10	0.81	1	2
25	3.45	2	4
100	6.90	3	6
250	11.37	7	12
500	18.02	17	14
750	25.39	18	16
1000	28.96	19	16
1500	35.59	21	15
2000	39.55	24	10

Coating B - FTBP - 6			
Zero-tension: 0 - 0.6%			
Cycle number	Total crack length (mm)	Number of cracks	Number of non-interacting tip
10	21.82	11	15
250	31.28	16	19
500	40.88	24	12
750	51.10	25	7
1000	54.20	24	9
1500	59.22	22	5
2000	61.49	23	7

Appendix vi – Total crack growth rate of coatings A and B under various cyclic strains

Table A 10. Total crack growth rate of coatings A and B under various cyclic strains

Coating Type	Sample label	R ratio	Strain range	Total crack growth rate (µm/cycle)
Coating A	FFA – 5	-1	1.00%	53.0
	FFA – 6	-1	1.10%	61.9
	FTA – 1	0	0.80%	0.2
	FTA – 2	0	0.85%	8.1
	FTA – 3	0	0.90%	29.9
	FTA – 4	0	1.00%	102.4
	FTA – 5	0	1.00%	23.8
	FTA – 6	0	1.05%	49.5
	FTA – 7	0	1.05%	20.8
Coating B	FFB – 2	-1	0.40%	1.0
	FFB – 5	-1	0.48%	2.6
	FFB – 6	-1	0.48%	5.6
	FFB – 7	-1	0.50%	5.5
	FFB – 8	-1	0.50%	9.0
	FFB – 9	-1	0.60%	9.4
	FFB – 11	-1	0.70%	50.9
	FTB – 4	0	0.45%	7.4
	FTB – 6	0	0.48%	4.2
	FTB – 8	0	0.50%	5.2
	FTB – 9	0	0.58%	24.9
	FTBP – 1	0	0.40%	2.5
	FTBP – 2	0	0.45%	4.4
	FTBP – 3	0	0.50%	34.3
	FTBP – 4	0	0.50%	32.8
	FTBP – 5	0	0.55%	29.4
	FTBP – 6	0	0.60%	43.8

Appendix vii- Digital Image Correlation

In the current work, a Dantec digital image correlation (DIC) system was used intensively to measure strain distribution on sample surfaces. A comprehensive reference book of DIC technique has been produced by Sutton[201]. A DIC system is a digital image based technique that is capable of measuring the strain distribution of the surface of a deformed sample. To facilitate the correlation, sample surfaces are normally required to have a random black-and-white speckle pattern, normally made by spraying black paint dots on to a thin white primer that covers the required area. During tests, DIC system captures the images of speckled surface continuously and records the deformation process. Normally the images are post-processed by a computer software after testing. For the Dantec system used in the current work, an ISTRA 4D software was used. In post-processing, the software divide the observed surface into a grid made of equally-sized square facets. Each facet has a characteristic grey value given by the speckle pattern it contains, and the location of the facet was tracked by the software. The deformation and displacement of each facet are calculated by comparing the deformed facets to their initial non-deformed states in a reference image. Based on the analysed deformation and displacement, the strains in any required directions can be calculated within the software.

For the tests under static loads in this work, a 3D DIC configuration was adopted. Two identical digital cameras with a resolution of 1 MP were used to capture the image of a sample surface simultaneously. A typical setup is shown in Figure 122. The cameras had an angle of about 30° between them and were placed in front of samples. The relative location of the cameras was calibrated using a standard target recognisable to the software. The manufacturer claims that the Dantec DIC system has spatial resolution of 0.1 pixel.

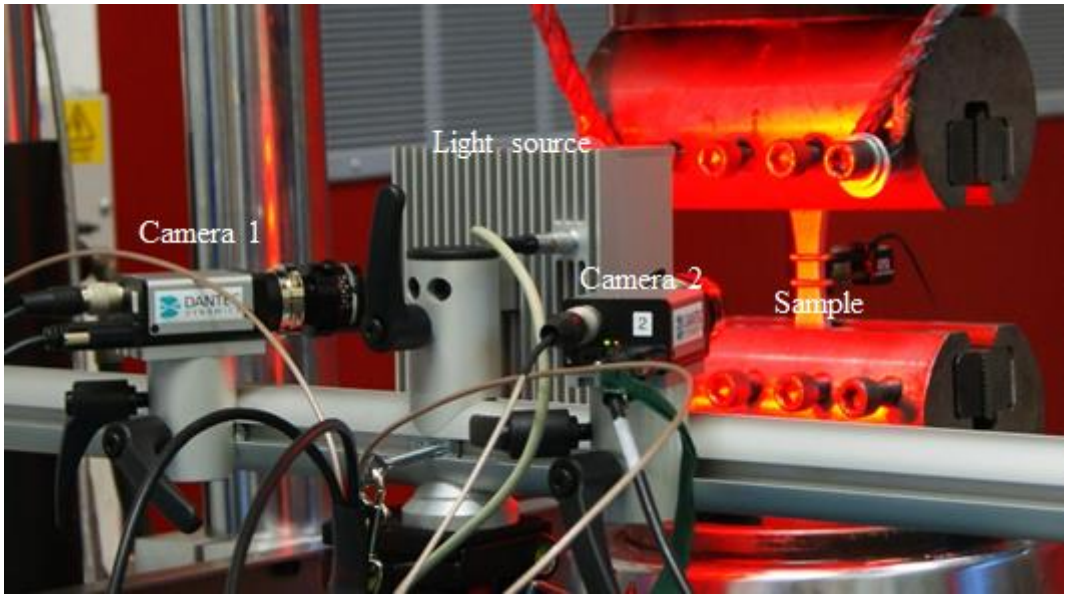

Figure 122. A photo of a typical DIC system setup for mechanical testing.

Appendix viii- Free film model for edge crack J-integral calculation

For the calculation of J-integral of edge crack in free film samples, a 2D plane stress free film model was built using ABAQUS. Figure 123 shows the model with a 150 µm long edge crack meshed with 2D plane strain elements. The model has a length of 29 mm, simulating half of the free film gauge length of 58 mm. The width of the model is 12 mm. The bottom edge of the model represented the centre of the gauge length, and a symmetry boundary condition was assigned for the calculations. A crack perpendicular to the length (indicated by the red line) was assigned to the right side of the bottom of the model. No boundary condition was assigned along the crack to allow crack opening under tensile strain.

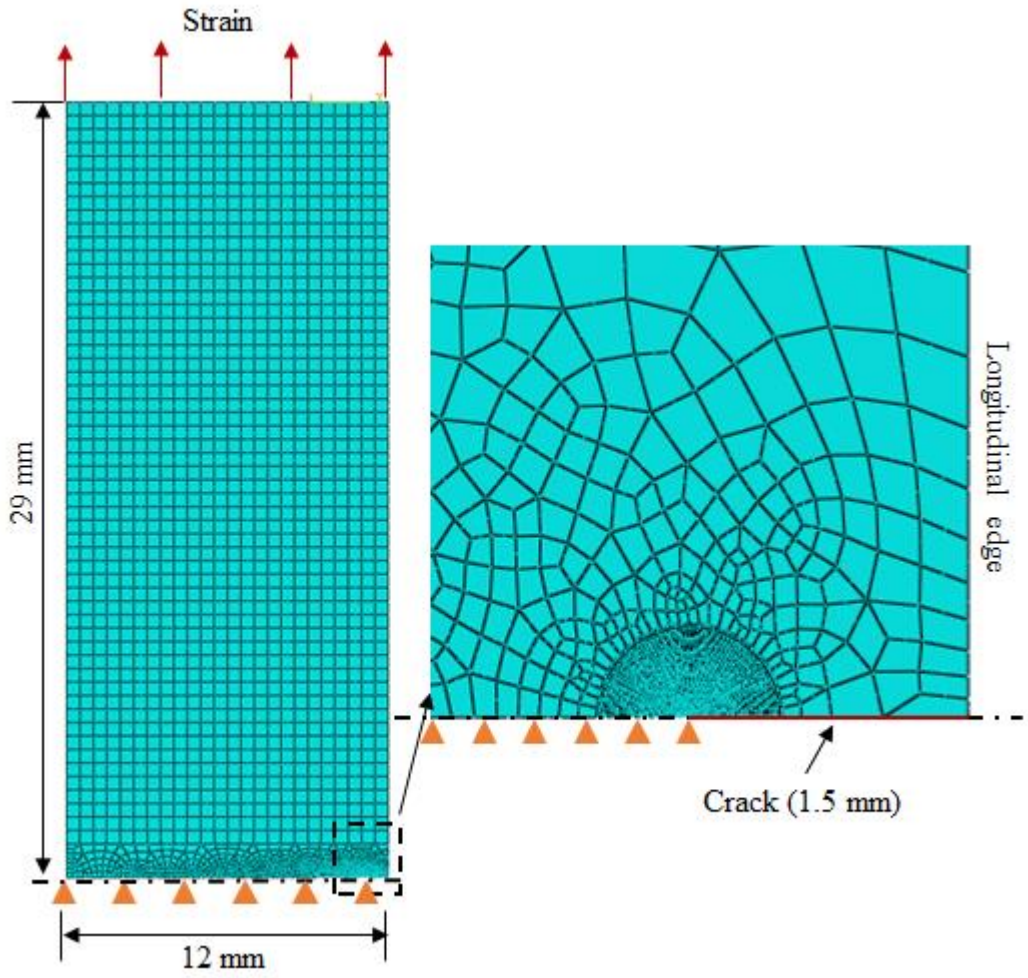

Figure 123. 2D Free film model with edge crack.

At the crack tip, a contour integral region with a radius of 0.05 mm was defined and meshed with 40 elements in the radial direction. Mechanical strain was applied by applying displacement on the top edge of the model, and the J-integral at the crack tip was calculated using the contour integral technique within ABAQUS.